Theoretical and Experimental Investigation of Spectral Cone-Beam CT as an Isocentric Imaging Modality for Proton Radiotherapy Planning

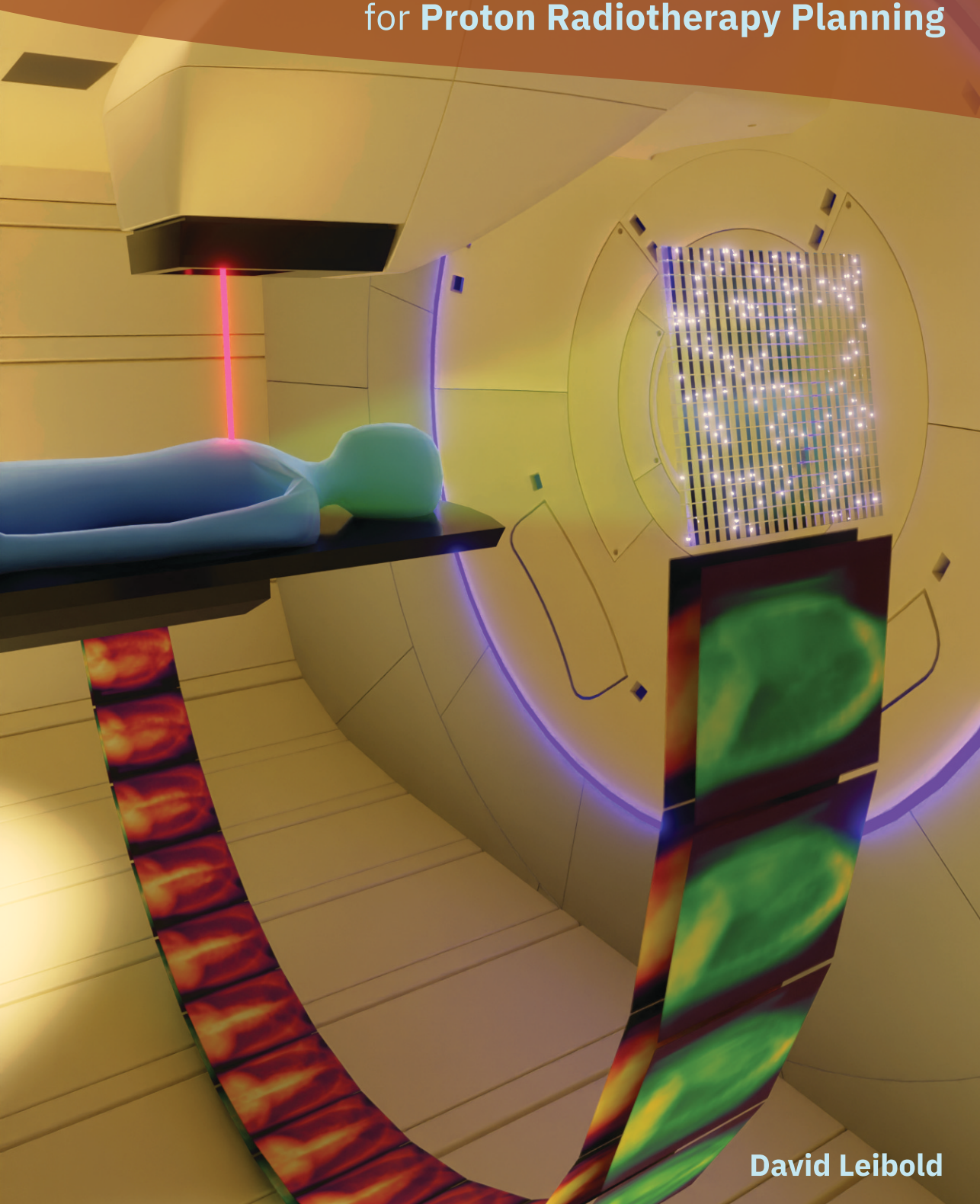

David Leibold

Theoretical and Experimental Investigation of Spectral Cone-Beam CT as an Isocentric Imaging Modality for Proton Radiotherapy Planning

Theoretical and Experimental Investigation of Spectral Cone-Beam CT as an Isocentric Imaging Modality for Proton Radiotherapy Planning

Dissertation

for the purpose of obtaining the degree of doctor
at Delft University of Technology
by the authority of the Rector Magnificus Prof. Dr. ir. H. Bijl,
chair of the Board for Doctorates,
to be defended publicly on
Monday, 9 March 2026 at 15:00 o'clock

by

DAVID LEIBOLD

This dissertation has been approved by the (co)promotors.

Composition of the doctoral committee:

Rector Magnificus	Chairperson
Dr. ir. D.R. Schaart	Delft University of Technology, promotor
Dr. ir. M.C. Goorden	Delft University of Technology, copromotor

Independent members:

Prof. Dr. M.S. Hoogeman	Delft University of Technology / Erasmus University Medical Center
Prof. Dr. C.R.N. Rasch	Delft University of Technology / Leiden University Medical Center
Prof. Dr. K. Taguchi	Johns Hopkins University, USA
Dr. V.T. Taasti	Aarhus University, Denmark
Dr. F.M. Vos	Delft University of Technology / Erasmus University Medical Center

The research described in this thesis was partially funded by VARIAN, A SIEMENS HEALTHINEERS COMPANY, grant number 2018016.

Keywords: Cone-beam CT; Proton therapy; Photon-counting detectors; X-ray imaging.

Printed by IPSKAMP PRINTING.

Cover art by © D. Leibold; for description see last page.

ISBN/EAN: 978–94–6518–246–9

An electronic version of this dissertation is available at https://repository.tudelft.nl/

Table of Contents

Summary

Proton radiotherapy is a cancer therapy that uses ionising radiation in the form of protons, offering an alternative and complement to conventional radiotherapy with high energy X-rays. In comparison to X-rays, proton beams have a finite range in tissue and deposit dose more locally. As a consequence, proton radiotherapy has the potential to deliver a higher dose to the tumour while better sparing surrounding healthy tissue. However, the delivered dose distribution in the case of protons is much more sensitive to changes in patient anatomy compared to X-rays, which therefore requires an accurate knowledge of proton stopping power ratio (SPR) values of the tissues to be treated.

In the standard workflow of proton therapy, patients are scanned using an X-ray fan-beam computed tomography scanner (CT scanner) before the commencement of a treatment series, lasting between days to several weeks. The fan-beam CT scan is used to delineate the anatomy of the patient, to extract SPR values, and to create a treatment plan. At the beginning of each session of a treatment series, the patient is positioned using in-room imaging modalities such as X-ray cone-beam CT (CBCT) to ensure correct alignment, and to check for anatomical changes such as tumour growth/shrinkage or patient weight gain/loss. CBCT is not, however, used to create or update the treatment plan directly due to its insufficient image quality caused mainly by X-ray scatter. The aim of this thesis is to explore whether CBCT can be modified such that it could be used for directly updating or creating treatment plans of the day, or even for online adaptive proton radiotherapy. The modifications addressed specifically in this thesis aim at extracting spectral information from the X-ray spectrum, in contrast to conventional CBCT systems that merely register the total energy in the incident spectrum.
Such a spectral CBCT system can be realised by either using a detector able to extract spectral information from the X-ray beam, or by imprinting spectral information on the source, or a combination thereof. An example for the type of detectors able to extract spectral information are so-called photon-counting detectors (PCDs), which are able to count and register the energy of individual X-ray photons.

An assessment of detector performance can help to gauge their suitability for application in radiotherapy. Such an assessment based on a quality metric is conventionally evaluated in the regime where a PCD is subjected to a photon fluence rate low enough for it to behave linearly. Depending on the imaging task, however, fluence rates up to $3.4 \cdot 10^8$ $\mathrm{mm}^{-2}\mathrm{s}^{-1}$ might be reached. Unless the detector pixel size is sufficiently small or the characteristic detector response time is sufficiently short, the rate of incoming photons is then so high that the average time between photons is no longer large compared to the characteristic detector response time, and the signals of individual photons will start to overlap. This so-called pile-up causes PCDs to behave non-linearly. In Chapter 2, we intend to investigate how the image quality metrics change under pile-up, which is demonstrated using specific examples in a simulation study. For this, we employ small-signal analysis to approximate the non-linear behaviour as linear around a given operating point.

In Chapter 3 we take on a broader view, comparing six spectral CBCT setups in a simulation study, including but not limited to PCD-based setups. Each setup is optimised with respect to extracting SPR values, and we take care of including a realistic CBCT scatter model. Furthermore, we compare setups assuming ideal detectors as well as assuming a more realistic

detector response. In case of ideal detectors, a single source combined with a PCD performs best. Under the assumption of a realistic detector detector response, we find that setups based on a kVp-switching source perform best. Interestingly, a kVp-switching source with an energy-integrating detector outperforms a kVp-switching source with a PCD, which we attribute to the severe degradation of the registered spectrum in state-of-the-art PCDs based on room-temperature semiconductors due to charge sharing. We furthermore show that mitigating the charge sharing in PCDs may offer substantial improvements. Moreover, we find that a higher source voltage or a higher spectral separation between source spectra are beneficial for SPR extraction.

In Chapter 4 we experimentally investigate the extraction of SPR values with a clinical CBCT setup inside a proton radiotherapy gantry. Three phantoms are scanned and (emulated) dual-energy CBCT acquisitions are compared to single-energy ones. Our results indicate that dual-energy CBCT achieves a lower bias and better robustness when extracting SPR values compared to single-energy CBCT, and allows for better differentiation between tissues. This first study is still limited in scope and we discuss various options for follow-up research.

Hence, we present an overview over pathways to increase the ability of spectral CBCT to extract SPR values, and we are cautiously optimistic about possible future developments that may enable CBCT to be used for daily treatment updates or even online adaptive treatment in proton radiotherapy.

Samenvatting

Protonentherapie is een kankerbehandeling waarbij gebruik wordt gemaakt van ioniserende straling in de vorm van protonen. Het biedt een alternatief en aanvulling op conventionele radiotherapie met hoogenergetische röntgenstralen. In vergelijking met röntgenstralen hebben protonenbundels een eindige dracht in weefsel en geven ze meer lokaal dosis af. Daardoor kan met protonentherapie een hogere dosis aan de tumor worden toegediend en tegelijkertijd het omliggende gezonde weefsel beter worden gespaard. De dosisverdeling bij protonen is echter veel gevoeliger voor veranderingen in de anatomie van de patiënt dan bij röntgenstraling, waardoor een nauwkeurige kennis van de zogenoemde energieverliesratio (Engels: stopping power ratio, SPR) van de te behandelen weefsels vereist is.

In de standaard workflow van protonentherapie worden patiënten gescand met behulp van een fan-beam röntgencomputertomografiescanner (CT-scanner) voordat een behandelingsreeks begint, die enkele dagen tot enkele weken kan duren. De fan-beam CT-scan wordt gebruikt om de anatomie van de patiënt in kaart te brengen, SPR-waarden te extraheren en een behandelingsplan op te stellen. Aan het begin van elke sessie van een behandelingsreeks wordt de patiënt gepositioneerd met behulp van beeldvormingsmodaliteiten in de behandelkamer, zoals cone-beam CT (CBCT), om een correcte uitlijning te garanderen en om te controleren op anatomische veranderingen, zoals tumorgroei/krimp of gewichtstoename/verlies van de patiënt. CBCT wordt echter niet gebruikt om het behandelingsplan op te stellen of bij te werken vanwege de te lage beeldkwaliteit, die voornamelijk wordt veroorzaakt door verstrooiing van röntgenstraling. Het doel van dit proefschrift is om te onderzoeken of CBCT zodanig kan worden aangepast dat het kan worden gebruikt voor het bijwerken of opstellen van behandelplannen voor die dag, of zelfs voor online adaptieve protonentherapie. De aanpassingen die specifiek in dit proefschrift aan de orde komen, zijn gericht op het extraheren van spectrale informatie uit het röntgenspectrum, aangezien conventionele CBCT-systemen alleen de totale energie in het invallende spectrum registreren.
Een dergelijk spectraal CBCT-systeem kan worden gerealiseerd door gebruik te maken van een detector die spectrale informatie uit de röntgenbundel kan halen, door spectrale scheiding in de bron aan te brengen, of door een combinatie daarvan. Een voorbeeld van detectoren die spectrale informatie uit een röntgenbundel kunnen halen, zijn zogenoemde fotonen tellende detectoren (Engels: photon-counting detectors, PCD's), die het aantal en de energie van individuele röntgenfotonen kunnen registreren.

Een beoordeling van de prestaties van detectoren kan helpen om te bepalen of ze geschikt zijn voor toepassing in de radiotherapie. Een dergelijke beoordeling op basis van een beeldkwaliteitsmaatstaf wordt gewoonlijk uitgevoerd in een regime waarin een PCD wordt blootgesteld aan een foton fluentietempo dat laag genoeg is om lineair gedrag van de PCD te garanderen. Afhankelijk van de beeldvormingstaak kunnen echter fluentietempo's tot $3{,}4 \cdot 10^8$ mm^{-2}s^{-1} worden bereikt. Tenzij de pixelgrootte van de detector voldoende klein is, of de karakteristieke responstijd van de detector voldoende kort, is het tempo waarop fotonen op de detector vallen dan zo hoog dat de gemiddelde tijd tussen twee fotonen niet langer groot is in vergelijking met de karakteristieke responstijd van de detector, waardoor de signalen van individuele fotonen elkaar gaan overlappen. Deze zogenoemde pile-up zorgt ervoor dat PCD's zich niet-lineair gaan gedragen. In Hoofdstuk 2 willen we onderzoeken hoe de beeldkwaliteitsmaatstaf verandert bij pile-up, wat wordt gedemonstreerd aan de hand van specifieke voorbeelden in een simulatie-

studie. Hiervoor gebruiken we kleine-signaalanalyse om het niet-lineaire gedrag te benaderen als lineair rond een bepaald punt.

In Hoofdstuk 3 verbreden we onze blik en vergelijken we zes spectrale CBCT-systemen in een simulatiestudie, waaronder op PCD's gebaseerde systemen. Elk systeem is geoptimaliseerd voor het extraheren van SPR-waarden, en we zorgen ervoor dat we een realistisch CBCT-verstrooiingsmodel meenemen. Verder vergelijken we systemen met ideale detectoren en met een realistischere detectorrespons. In het geval van ideale detectoren presteert een enkelvoudige bron in combinatie met een PCD het beste. Onder de aanname van een realistische detectorrespons vinden we dat systemen op basis van een kVp-schakelende bron (Engels: kVp-switching source) het beste presteren. Interessant is dat een kVp-switching source met een conventionele energie-integrerende detector beter presteert dan een kVp-switching source met een PCD, wat wij toeschrijven aan de ernstige verslechtering van het geregistreerde spectrum in state-of-the-art PCD's op basis van kamertemperatuur halfgeleiders als gevolg van het zogenoemde ladingsdeling effect (Engels: charge sharing). Verder laten we zien dat het verminderen van charge sharing in PCD's aanzienlijke verbeteringen kan opleveren. Bovendien vinden we dat een hogere bronspanning of een grotere spectrale scheiding tussen bronspectra gunstig is voor SPR-extractie.

In Hoofdstuk 4 onderzoeken we experimenteel de extractie van SPR-waarden met een klinisch CBCT-systeem in een protonentherapiekliniek. Er worden drie fantomen gescand en (geëmuleerde) dual-energy CBCT-scans worden vergeleken met single-energy scans. Onze resultaten geven aan dat dual-energy CBCT een lagere bias en betere robuustheid heeft bij het extraheren van SPR-waarden in vergelijking met single-energy CBCT, en een betere differentiatie tussen weefsels mogelijk maakt. Deze eerste studie is nog beperkt in omvang en we bespreken verschillende opties voor vervolgonderzoek.

Daarom presenteren we een overzicht van manieren om het vermogen van spectrale CBCT om SPR-waarden te extraheren te vergroten, en zijn we voorzichtig optimistisch over mogelijke toekomstige ontwikkelingen die ertoe kunnen bijdragen dat CBCT kan worden gebruikt voor dagelijkse behandelingsupdates of zelfs online adaptieve behandeling bij protonentherapie.

Chapter 1

Introduction

1

1.1 Thesis Objective

Cancer is the second leading cause of death worldwide [10, 28], with radiotherapy as one of the main treatment options besides chemotherapy, surgery and targeted therapy. Radiotherapy based on high energy X-rays (typically in the order of a few megaelectronvolt) has been in use for several decades, and is still the most commonly employed form of radiotherapy [11]. All forms of radiotherapy aim at inducing cell death in cancer cells via the ionising properties of the employed radiation, which either inflicts DNA damage directly or indirectly via the creation of free radicals within a cell [31]. While as an unavoidable side effect also healthy cells suffer from radiation damage, radiotherapy tries to mitigate this by, first, using a dose distribution that delivers the highest dose to the tumour while reducing dose to healthy tissue, and second, by utilising the property of healthy tissue of being better at repairing radiation damage than cancer cells, under the condition that the damage is not too severe. The second strategy is the reason for the practice of fractionating the radiation treatment, that is, delivering the total dose to the tumour over multiple treatment sessions distributed over several days to weeks [52].

While X-rays have the desired property of being an ionising form of radiation, the distribution of deposited dose over the penetration depth of X-rays follows roughly an exponential decay (Figure 1.1). As a result, tissues lying closer to the X-ray source receive a higher dose than the tumour, and tissues lying behind the tumour (as seen from the source) also receive a dose greater than zero. Though unfavourable, modern X-ray radiotherapy mitigates this by applying beams from multiple angles and with varying intensity, leading to a highly conformal dose distribution.

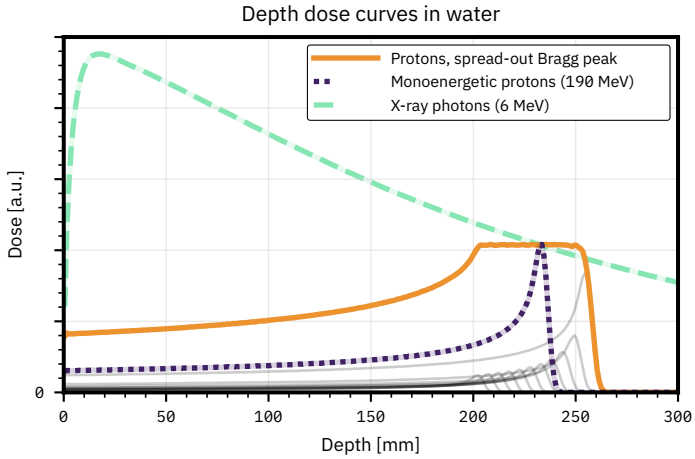

Figure 1.1: Dose vs. depth in water for X-ray photons and protons in a water volume (dose in arbitrary units, data obtained from simulation). The water volume starts at a depth of 0 mm and extends in positive direction; photons/protons move in positive direction. In the case of protons, both the data for a single monoenergetic beam is shown (dotted dark purple line) as well as a so-called spread-out Bragg peak (solid orange line) that consists of a combination of proton beams with discrete energies and varying intensities (constituent beams indicated as solid grey lines).
The depicted dose is the dose integrated over the whole cross-section of a pencil beam, binned with 1 mm step size. Individual proton beams are monoenergetic; for photons, a 6 MeV linac spectrum is assumed.

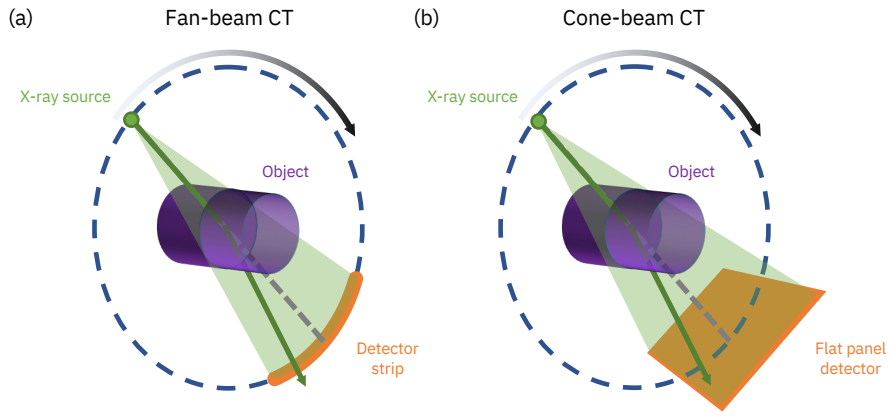

Figure 1.2: Schematic comparing (a) a fan-beam CT geometry with (b) a cone-beam CT geometry. Fan-beam CT uses a detector strip, whereas cone-beam CT uses a flat-panel detector with comparable lengths on both sides. In both cases, a single X-ray is depicted that scatters inside the object and therefore changes its direction, leaving the plane spanned by the rotating source; if it had not scattered, it would have followed the grey dashed line. In case of the fan-beam CT, the scattered X-ray is not detected by the detector strip, whereas it is still registered by the flat-panel detector, stressing the increased sensitivity of cone-beam CT to X-ray scatter.

In 1946, Wilson [53] was the first to introduce the idea of using protons or, more generally, heavy ions for therapeutic purposes due to their favourable property of exhibiting a finite range, and due to their property of depositing the highest dose within a small region close to the end of their range, called the Bragg peak, as shown in Figure 1.1. As is evident from the figure, protons (and other ions) deliver less dose to tissue in front of the tumour and no dose at all to tissue situated behind the tumour (as seen from the proton source) compared to X-rays. Utilising the fact that the range of protons is energy-dependent, protons with varying energy and intensity are combined to yield the desired dose distribution [29].

As can be appreciated in the aforementioned figure, a change in tissue properties leading to a, say, 1 mm shift in the depicted dose distributions does not change the dose delivered by X-rays over a given depth interval significantly. In stark contrast to X-rays, however, the same change in tissue properties can lead to a significant change in dose delivered by a single, monoenergetic proton beam. In other words, proton therapy is very sensitive to changes in the absorption properties of the traversed material, and in particular more sensitive to such changes than conventional X-ray radiotherapy. In clinical practice, safety margins are therefore used to account for uncertainties in the extracted proton stopping power ratio[1] (SPR) values of tissues and for uncertainties related to patient positioning [32].

Before the actual start of a fractionated proton radiotherapy treatment series, fan-beam X-ray computed tomography scanners (CT scanners,[2] see Figure 1.2a) are used to acquire a *planning (CT) scan*. Fan-beam CT scanners use a detector strip and an appropriately shaped, eponymous X-ray beam, rotating around the patient. The energy range of diagnostic X-rays used for

[1] *Stopping power* denotes the energy loss per path length in a given material and knowledge thereof is necessary to determine the range and deposited dose of protons. Dividing the stopping power of a material by the stopping power of water yields the *stopping power ratio* of a material, relative to water.

[2] *Computed tomography* refers to the technique of computing the internal structure of an object via acquiring multiple projections of it. This technique is not limited to fan-beam X-rays or even X-rays in particular. In the field of medical imaging, however, the term *CT scanner* is commonly used for scanners performing fan-beam X-ray computed tomography.

1

Figure 1.3: Photograph (top) of a treatment room at the Holland Proton Therapy Centre, Delft, The Netherlands and its schematic (bottom). In this photo, the patient couch is situated below the nozzle steering the proton beam. To the left and right of the nozzle two flat-panel detectors are attached, which, together with the two X-ray sources, form the CBCT systems (only one X-ray beam is shown). The rotating gantry containing the steering magnets for the proton beam is covered by panels and not visible. *With permission of HPTC.*

this purpose is in the range of 30 – 150 keV. The CT scan is then used for anatomical (including tumour) delineation, SPR extraction and treatment planning [7, 31]. Fan-beam CT is used since, firstly, it provides sufficient soft tissue contrast,[3] secondly, it is the most accurate X-ray imaging modality used in clinical practice, and thirdly, since the underlying physics of X-ray attenuation and proton attenuation are closely, although not directly, related.

At the start of each treatment fraction, patients need to be positioned such that their orientation matches the state during the planning CT scan. Imaging modalities inside the treatment room can be used to confirm the patient position, which includes modalities such as in-room CT, in-room CT on rails, simple flat-panel radiography, or cone-beam CT (CBCT) mounted either to the gantry or a robotic arm [21] (Figure 1.3 shows the treatment room of a proton radiotherapy centre, note the two flat-panel detectors attached to the proton nozzle). CBCT uses a flat-panel detector with sides of comparable length and an X-ray cone-beam, rotating around the patient (Figure 1.2b). In any case, these imaging modalities are merely used to check the patient position and whether the patient's anatomy of the day deviates significantly from the state during the planning CT (due to, e.g., tumour growth/shrinkage, weight gain/loss), in which case a new scan with a fan-beam CT and replanning might be indicated [21, 41]. CBCT is not used directly for treatment planning, although it has been reported to be used to deform planning CT images to the CBCT of the day [17, 20, 22, 38, 48]. The reason that CBCT is not used directly for treatment planning is that CBCT, compared to fan-beam CT, suffers from poor soft tissue contrast due to the greater influence of scatter as well as from a larger influence of patient motion due to its longer rotation times [43] (see Figure 1.4 for a comparison of image quality between fan-beam and cone-beam CT).
However, compared to fan-beam CT, CBCT offers the possibility to image the patient in treatment position without moving the patient couch, which neither fan-beam CT nor magnetic resonance imaging are capable of, and it is a comparably cheap modality. If the image quality of CBCT could be improved, its images might be of a quality sufficient enough to be used for treatment plan updates, direct treatment planning or even real-time tumour tracking, enabling a more efficient workflow. While this requires as a prerequisite the development of fast and automatic auto-contouring and treatment planning software which is actively investigated [15, 30, 34], the work presented in this thesis focuses on improving image quality as the basis for all subsequent steps.

Two possible, complementary pathways to an improved CBCT image quality are conceivable: either via improved reconstruction software which might, for example, include an improved scatter model, or via improved hardware, which could involve the inclusion of anti-scatter grids [1, 19, 33, 36, 39, 57] or setups that extract spectral information from X-rays instead of just measuring their intensity, with the latter being the current standard for CBCT. A number of studies for fan-beam CT have already shown that a better accuracy and robustness can be achieved with spectral fan-beam CT instead of single-energy fan-beam CT [5, 25, 27, 35, 45, 46, 54, 55, 56]. It is reasonable to expect that the same holds true for CBCT.
This thesis focuses on the hardware aspect and investigates spectral CBCT for its use in proton therapy. The objectives of this work are to investigate (1) which figure(s) of merit can be used to compare spectral CBCT setups, (2) which spectral CBCT setup is best suited for SPR extraction as well as to optimise the parameters of such a setup, and (3) to test SPR extraction experimentally using a clinical CBCT system.

[3] The gold standard for soft tissue contrast is magnetic resonance imaging; note that dual-energy fan-beam CT can achieve better soft tissue contrast compared to single-energy fan-beam CT.

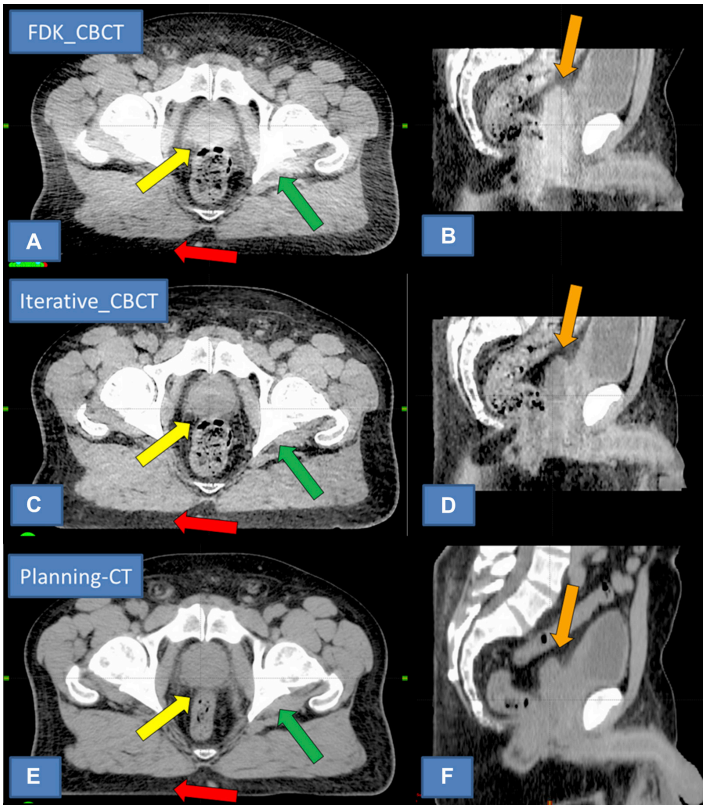

Figure 1.4: Comparison of reconstructed images of a prostate patient, either acquired with a CBCT (top and centre row) or with a fan-beam CT (bottom row). In the case of CBCT, the images were reconstructed using the conventional FDK algorithm (top row, see Section 1.2.5) as well as an iterative algorithm (centre row). Left column: axial plane; right column: sagittal plane. Arrows point to features for comparison between imaging modalities. This figure is taken from the work by Gardner et al [14]; their article is licensed under the CC BY-NC-ND 4.0 license. ©2019 Gardner et al.

1.1.1 Thesis Outline

One possibility to implement a spectral CBCT setup is via a photon-counting detector (PCD) instead of the currently used energy-integrating detectors (EIDs) (see Section 1.2.4). In order to characterise the performance of PCDs, a range of quality metrics is available. However, these are usually evaluated under the assumption that the incident X-ray fluence rate is such that the average time between photons is large compared to the detector's response time, ensuring a linear behaviour of the detector. If the rate of photons is such that the average time between photons is comparable to the detector's response time, non-linear effects become significant. Chapter 2 intends to investigate how non-linear behaviour could be incorporated into detector performance metrics.

Chapter 3 addresses the question which of the many possible implementations of a spectral CBCT setup is best suited for proton radiotherapy with respect to its ability to extract proton SPR values, and it compares different available as well as conceivable future detector technologies.

Chapter 4 presents the results of an experimental study conducted at a proton therapy clinic, emulating spectral CBCT acquisitions and investigating the accuracy and robustness with which SPR values can be extracted.
Finally, the thesis is concluded in Chapter 5, summarising the findings and presenting an outlook on future developments in the field of spectral CBCT.
A brief compilation of background knowledge can be found in the following.

1.2 Essential Background Knowledge

1.2.1 X-Ray Physics

The interaction mechanisms of X-rays with matter relevant in the context of this work are the photoelectric effect, (inelastic) Compton scattering and (elastic) Rayleigh scattering. Please note that this discussion is limited to the energy range of X-rays used in (CB)CT imaging (30 – 150 keV), unless specified otherwise. As a consequence, pair production, requiring energies ≥ 1022 keV, is excluded here. For further reference we refer the reader to Bushberg et al [8],

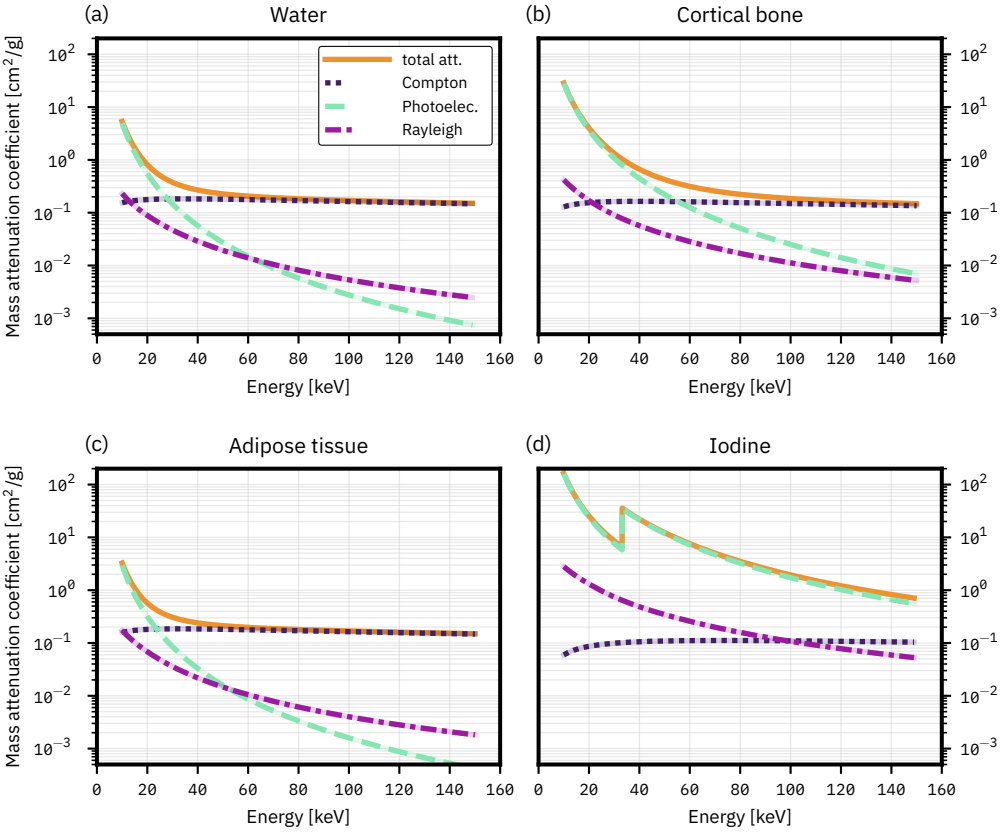

Figure 1.5: Contributions of the photoelectric effect as well as Compton and Rayleigh scattering to the total mass attenuation (μ/ρ_{mass}) of photons in (a) water, (b) cortical bone, (c) adipose tissue and (d) iodine. The tissue definition of cortical bone and adipose tissue was taken from the ICRU report 46 [18], mass attenuation coefficients were retrieved from the NIST XCOM database [23].

1

Hubbell [16] and Seibert et al [42].

The photoelectric effect refers to the complete absorption of an incoming (X-ray) photon and the transfer of its full energy to a bound electron, ejecting the electron and hence ionising the atom. The probability of interaction is highest for those electrons that have a binding energy just slightly lower than the photon. Two consequences arise from this: Firstly, for the strongest bound electrons, i.e., those in the K-shell, this leads to a steep rise in absorption probability once the photon energy is higher than their binding energy. The resulting prominent feature in the X-ray attenuation as a function of energy is, in the example of K-shell electrons, called a *K-edge* (see Figure 1.5d for an example: iodine features a K-edge at an energy of around 33 keV). Secondly, for elements with low atomic number with lower K-shell binding energies, the interaction probability for the photoelectric effect is low and their K-edges lie outside the energy range of interest and are not observed.[4] For example, the K-edge of calcium, the heaviest element of all elements in the human body with an abundance ≥ 0.1 mass percent, has a K-edge at 4.04 keV.
Once an electron is ejected, its vacancy is filled by an electron from one of the outer shells, emitting in turn a photon in this process (called *(X-ray) fluorescence*). The energy of X-ray photons emitted during this process are specific to each element due to the energy differences between orbitals, and are hence called *characteristic X-rays*.
Assuming the absence of absorption edges in the selected energy range, the probability of photoelectric interaction per unit mass is approximately proportional to Z^3/E^3, with Z as the atomic number and E the X-ray energy. Hence, the difference in attenuation between different elements, and hence the contrast between various tissues, is largest at low energies. Note, however, that the larger attenuation at lower energies does, at the same time, decrease the number of photons being able to reach the detector, therefore decreasing the signal-to-noise ratio. Furthermore, due to the dependence on Z^3, photoelectric interaction is the main interaction process for elements with higher atomic number.

During (inelastic) Compton scattering, a photon transfers part of its energy to an electron. Compton scattering is more likely for electrons with lower binding energy, and hence involves the weakly bound outer electrons of atoms. The energy transfer is typically larger than the binding energy of the electron, hence ionising the atom. Based on the momentum transferred to the electron, the outgoing photon changes its angle; the resulting Compton scatter is the main source of scatter in X-ray imaging. In the energy range used in medical X-ray imaging, the magnitude of Compton scattering can be considered approximately constant over energy, and since the probability scales with electron density, the probability of Compton scatter normalised by mass is approximately independent of the atomic number. For elements with low atomic number, Compton scattering is the dominant interaction mechanism.

Rayleigh or coherent scattering refers to elastic photon scattering. Rayleigh scattering is more prominent for low X-ray energies such as those used in mammography (15 – 30 keV), however, for (CB)CT the effect of Rayleigh scattering is usually negligible (see Figure 1.5).

1.2.2 X-Ray Generation

X-ray sources currently used in medical imaging generate X-rays by accelerating electrons to high energies and onto a target anode. Upon impinging on the anode, electrons subsequently generate X-rays via two processes: Bremsstrahlung (breaking radiation) and characteristic X-rays. The latter are produced when an incoming electron removes an electron from one of the

[4] Note that the K-edge is the absorption edge with the highest energy; if the K-edge lies below the energy range of interest, so will all other absorption edges.

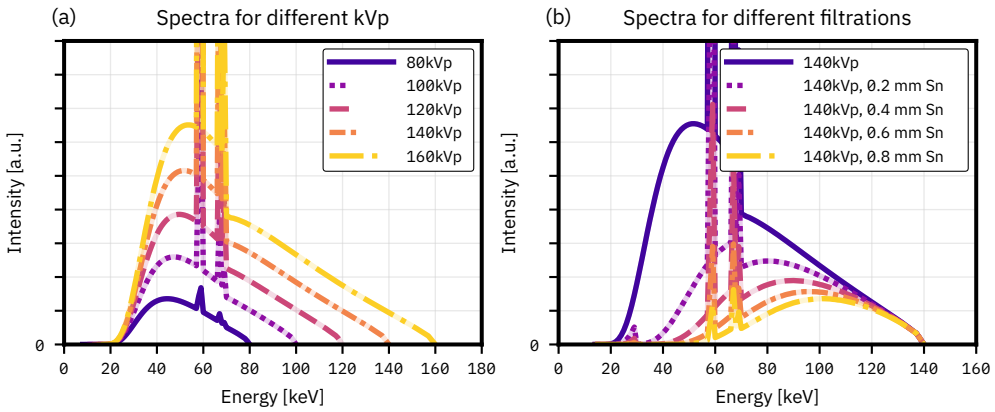

Figure 1.6: Simulated X-ray spectra, showing (a) the effect of different source voltages ranging from 80 – 140 kVp while keeping the filtration fixed, and (b) the effect of different thicknesses of additional tin (Sn) filtration after the source for a fixed source voltage of 140 kVp.
The intrinsic source filtration is 0.8 mm Be, 0.89 mm Ti; the anode angle is set to 7 degrees; normalisation is set individually for each curve to show trends more clearly, and is not intended to show relative differences in intensity.

inner shells of the anode atoms, creating a vacancy that is subsequently filled by electrons from higher orbitals (see Section 1.2.1). In case of the commonly used anode material tungsten, the following characteristic lines can be observed in the emitted X-ray spectrum:

K_α (KL_1, KL_2, KL_3):	between 57 – 59 keV,
K_β (KM_1 – KM_5):	around 67 keV,
K_γ (KN_1 – KN_5):	around 69 keV.

The second process of Bremsstrahlung refers to electrons that come sufficiently close to atomic nuclei in the anode. Subjected to the strong attraction of a core, this acceleration of electrons leads to the emission of electromagnetic radiation, more specifically, X-rays.
The generation of X-rays via this process is very inefficient: Only about 1 % of electrons impinging on the anode cause the creation of X-rays via Bremsstrahlung, and the vast majority of created X-ray photons are either filtered out by the X-ray tube's window or by the beam shaper, leading to an energy conversion efficiency in the order of 0.03 % [6].
The emitted X-ray Bremsstrahlung spectrum is quite broad and polychromatic. The upper limit for the X-ray energy in the spectrum is determined by the energy of the incoming electrons; the low energy X-rays are removed via filtration by the anode itself and the X-ray tube window as well as potential additional filters. The combination of a broad Bremsstrahlung spectrum and characteristic X-ray peaks yields the X-ray spectra depicted in Figure 1.6.

The main parameter for tuning the X-ray spectrum is the applied voltage between the cathode and anode of the source, as it determines the upper limit of X-ray energies emitted as well as the mean energy of the spectrum. The applied voltage, commonly given in units of keV (kiloelectronvolt), is denoted kVp (kilovolt peak). The source current, that is, the current of electrons flowing between the tube's cathode and anode, is proportional to the emitted number of photons and hence an important quantity in terms of radiation dose. Additional filtration can be applied to enhance the filtration of low energy photons and to shift the mean energy to higher energies; increasing the mean energy is referred to as a *hardening* of the spectrum.

1

1.2.3 X-ray Transport and Image Acquisition

There exists no closed-form expression that fully describes X-ray transport with respect to the spatial and energy distribution of scattered X-rays passing through a medium. Based on known physics models, however, Monte-Carlo simulations can be used to obtain the desired distributions [2, 40]. The only quantity accessible to a closed-form expression is the number of primary, i.e., non-scattered X-rays, which can be described via the Lambert-Beer law:[5] It states that the reduction per unit length in the number I of non-scattered, monoenergetic photons, counted over an infinitesimal cross-section A and passing through a medium, is proportional to the number of non-scattered photons:

$$\frac{\mathrm{d}I}{\mathrm{d}x} = \mu \cdot I \quad , \tag{1.1}$$

The proportionality constant μ hence describes the fraction of photons removed from the monoenergetic X-ray beam per unit thickness, and it is called the *(linear) attenuation coefficient*, usually given in units of 1/cm.

The equivalent integral expression for the general case of a monoenergetic beam with cross-section A and energy E along a straight line $\mathbf{s}$ from point $\mathbf{r} = \mathbf{0}$ to the point (x, y, z), emitting the number of photons $I_0(x, y, z, E)$ from point $\mathbf{r} = \mathbf{0}$ towards (x, y, z), and an attenuation coefficient $\mu(\mathbf{r}, E)$ at every point $\mathbf{r}$ in the volume, yields $I(x, y, z, E)$, i.e., the number of unattenuated photons arriving at $\mathbf{r} = (x, y, z)$ with energy E and within the cross-section A:

$$I(x, y, z, E) = I_0(x, y, z, E) \cdot \exp\left(- \int_{\mathbf{0}}^{(x,y,z)} \mu(\mathbf{r}, E) \, \mathrm{ds} \right) \quad , \tag{1.2}$$

where $\int_{\mathbf{0}}^{(x,y,z)} \mu(\mathbf{r}, E) \, \mathrm{ds}$ is called the *line integral* of the linear attenuation coefficient. Note that this expression neglects any scatter contribution.

Equation 1.2 can be used to calculate the spectrum $\mathbf{\Phi}(x, y, z, E) \equiv I(x, y, z, E)$ of unattenuated photons, emitted from an X-ray source located at $\mathbf{r} = \mathbf{0}$ reaching a pixel with cross-section A at point (x, y, z) during acquisition time. Assuming an ideal detector, the incident spectrum is equal to the spectrum of deposited events in a pixel, i.e., $\boldsymbol{\varphi}^{\text{depos}}(E) \equiv \mathbf{\Phi}(E)$.

1.2.4 X-Ray Detectors

X-rays can deposit energy in matter via one of the mechanisms described in Section 1.2.1. Conventional X-ray detectors measure the total deposited energy and are hence called *energy-integrating detectors*. Their detected signal $\mathbf{m}$ can be described via

$$\mathbf{m} \sim \int_0^\infty \boldsymbol{\varphi}^{\text{depos}}(E') \cdot E' \, \mathrm{d}E' \quad . \tag{1.3}$$

In contrast, *photon-counting detectors* determine the energy of every energy deposition caused by incoming X-ray photons and increment a counter in the corresponding energy bin [51]. Hence, in each energy bin k ranging from energy $E_{k,1}$ up to $E_{k,2}$, their detected signal is

$$\mathbf{m}_k \sim \int_{E_{k,1} \leq E' < E_{k,2}} \boldsymbol{\varphi}^{\text{depos}}(E') \, \mathrm{d}E' \quad . \tag{1.4}$$

EIDs either use a semiconductor such as amorphous silicon for X-ray absorption and conversion to an electrical signal (so-called *direct conversion*), or they use a scintillator such as caesium iodide to convert X-ray photons into optical photons (so-called *indirect conversion*), which

[5] The *Lambert-Beer* law is also called *Beer-Lambert* law or *Beer–Bouguer–Lambert* law.

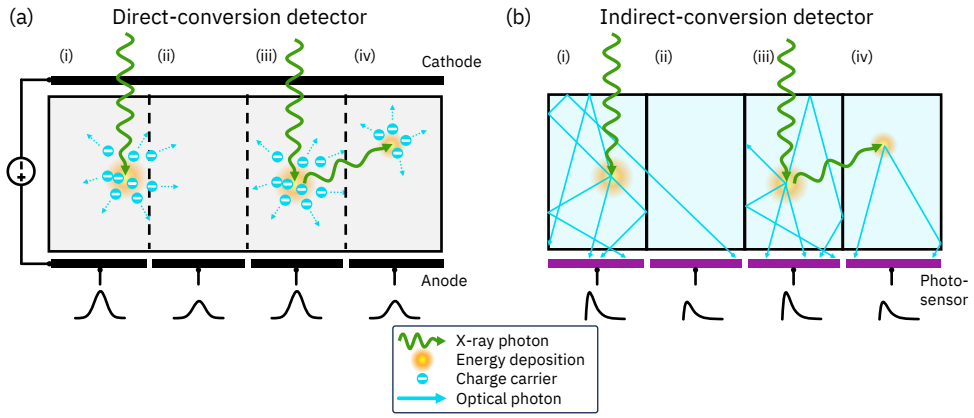

Figure 1.7: Schematics of a direct-conversion detector (a) and an indirect-conversion detector (b). Panels (i – ii) show inter-pixel cross-talk due to leakage of charge carriers (a) or optical light (b) originating from (i), leading to a detector pulse in a neighbouring pixel (ii). Panels (iii – iv) show inter-pixel cross-talk due to X-ray cross-talk: An X-ray is partially absorbed (iii) and, via X-ray scatter or X-ray fluorescence, deposits additional energy in a neighbouring pixel (iv) leading to a detector pulse therein. Schematic not to scale.

can then be detected by an array of photosensors [58]. EIDs cannot distinguish between individual photons, and their signal is proportional to the total deposited energy.

PCDs employed in clinical systems are direct-conversion detectors based on a semiconductor such as CdTe or CZT [24, 37, 47] or silicon [4, 13]; research into indirect-conversion PCDs is ongoing [49, 50]. The main challenge of direct-conversion PCDs lies in detrimental cross-talk effects, increasing in strength with decreasing pixel size; the main challenge of indirect-conversion PCDs lies in the miniaturisation of pixels, as well as in the fast decay of scintillation light necessary to detect the large amount of X-ray photons per unit time.
Multiple photons that deposit energy inside the PCD within a time that is comparable to or smaller than the detector's response time can lead to overlapping detector pulses, called *pulse pile-up* [9]. This can distort the number and/or energy of registered events.

The aforementioned inter-pixel cross-talk consists of two components: First, X-ray cross-talk occurs when, due to Compton scatter or X-ray fluorescence, an incident X-ray photon scatters into a neighbouring pixel and deposits part of its energy in two pixels simultaneously (Figure 1.7, ii – iii). Second, after an energy deposition has occurred, the deposited energy is converted into either charge carriers (direct-conversion detectors, Figure 1.7a) or optical photons (indirect-conversion detectors, Figure 1.7b), which can leak into neighbouring pixels. More specifically, the semiconducting material of state-of-the-art direct-conversion detectors for medical imaging applications is itself not pixelated, only the anode deposited on top of it, which enables charge carrier leakage between pixels (so-called *charge sharing*).

1.2.5 Image Reconstruction

For computed tomography, (X-ray) projections are acquired of the object from multiple angles. A graph of all projections, sorted by the acquisition angle, is called a *sinogram* (Figure 1.8a). In order to transform the sinogram such that it is more easily comprehensible and interpretable by humans, the sinogram is reconstructed, which is to say, the attenuation map $\mu(\mathbf{r})$ of the underlying object is estimated. It might also be desirable to instead create maps of the un-

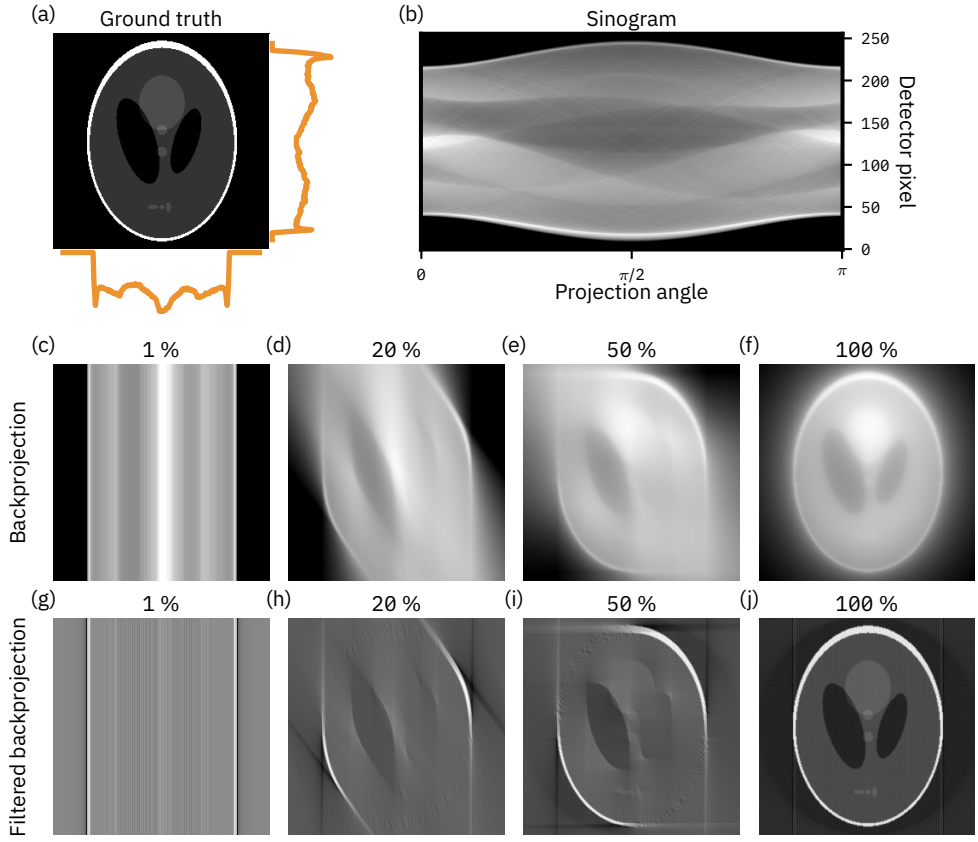

Figure 1.8: (a) Ground truth of a phantom along with the intensity profile created by parallel-beam projections at angles of 0 (up – down) and $\pi/2$ (left – right). (b) Sinogram. (c – f) Reconstruction based on simple backprojection, using either the first 1 %, 20 %, 50 % or 100 % of available projections. (g – j) Reconstruction based on filtered backprojection, using either the first 1 %, 20 %, 50 % or 100 % of available projections.

derlying object in a basis of a few different materials (such as water and bone), called material decomposition. Realistic CT acquisitions, however, pose an underdetermined inverse problem that cannot be solved analytically. The conventional reconstruction for CBCT, assuming a monoenergetic X-ray spectrum and the absence of scatter, is a frequency filtered backprojection based on the algorithm by Feldkamp, Davis and Kress (FDK) [12] (Figure 1.8j). Advances in computational methods and speed made iterative algorithms possible [26] as well as deep-learning-based reconstruction [44]; see Figure 1.4 for a comparison between CBCT images reconstructed via the FDK algorithm and via an iterative algorithm. Iterative algorithms offer the possibility to perform both reconstruction and material decomposition simultaneously while better utilising the available data, and are hence expected to perform better than FDK-based reconstruction algorithms [59].

1.2.6 Dual-Energy Imaging

In their seminal paper on the principle of dual-energy X-ray imaging, Alvarez and Macovski [3] use a small basis of energy-dependent interaction functions f_i to express the linear attenuation coefficient μ, that is: $\mu(E) = \sum_i a_i f_i(E)$; more specifically, they use a basis combining photoelectric effect and Compton scattering, while neglecting Rayleigh scattering:

$$\begin{aligned} \mu(E) &= a_{\text{photoel}} \cdot f_{\text{photoel}}(E) + a_{\text{Compton}} \cdot f_{\text{Compton}}(E) \\ \mu(E) &= K_{\text{photoel}} \cdot \rho_{\text{elec}} \cdot Z^n \cdot \frac{1}{E^3} + K_{\text{Compton}} \cdot \rho_{\text{elec}} \cdot f_{\text{KN}}(E) \end{aligned} \tag{1.5}$$

with ρ_{elec} as the electron density and $n \approx 3$. K_{photoel} and K_{Compton} are proportionality factors approximately independent of Z, and $f_{\text{KN}}(E)$ is the Klein-Nishina equation describing the Compton interaction cross-section; in first approximation, we can assume $f_{\text{KN}}(E)$ to be independent of energy (see Figure 1.5).

In order to obtain the two unknown parameters ρ_{elec} and Z in Equation 1.5 of an unknown material, two independent measurements of the attenuation coefficient at different energies are required. This can be achieved either by employing different X-ray source spectra, or by a detector capable of extracting spectral information from the registered X-ray spectrum, or a combination thereof. In this work, we use the more general term *spectral* CT to denote setups capable of extracting spectral information, since a setup might perform measurements at more than two energies.

The model in Equation 1.5 assumes a photoelectric absorption devoid of K-edges. If an element with a K-edge in the inspected range is present, as is for example the case in imaging tasks using contrast agents (such as iodine, see Figure 1.5d), then its specific energy-dependent attenuation function can be added as a third basis element.

1

References

[1] T. Alexeev, B. Kavanagh, M. Miften, and C. Altunbas, "Two-dimensional antiscatter grid: A novel scatter rejection device for Cone-beam computed tomography", *Medical Physics*, vol. 45, no. 2, pp. 529–534, 2018. DOI: 10.1002/mp.12724.

[2] J. Allison, K. Amako, J. Apostolakis, *et al.*, "Recent developments in Geant4", *Nuclear Instruments and Methods in Physics Research Section A: Accelerators, Spectrometers, Detectors and Associated Equipment*, vol. 835, pp. 186–225, 2016. DOI: 10.1016/j.nima.2016.06.125.

[3] R. E. Alvarez and A. Macovski, "Energy-selective reconstructions in X-ray computerised tomography", *Physics in Medicine and Biology*, vol. 21, no. 5, pp. 733–744, 1976. DOI: 10.1088/0031-9155/21/5/002.

[4] M. Åslund, B. Cederström, M. Lundqvist, and M. Danielsson, "Physical characterization of a scanning photon counting digital mammography system based on Si-strip detectors", *Medical Physics*, vol. 34, no. 6Part1, pp. 1918–1925, 2007. DOI: 10.1118/1.2731032.

[5] E. Bär, A. Lalonde, G. Royle, H.-M. Lu, and H. Bouchard, "The potential of dual-energy CT to reduce proton beam range uncertainties", *Medical Physics*, vol. 44, no. 6, pp. 2332–2344, 2017. DOI: 10.1002/mp.12215.

[6] R. Behling, "Medical X-ray sources now and for the future", *Nuclear Instruments and Methods in Physics Research Section A: Accelerators, Spectrometers, Detectors and Associated Equipment*, vol. 873, pp. 43–50, 2017. DOI: 10.1016/j.nima.2017.05.038.

[7] A. Bolsi, M. Peroni, D. Amelio, *et al.*, "Practice patterns of image guided particle therapy in Europe: A 2016 survey of the European Particle Therapy Network (EPTN)", *Radiotherapy and Oncology*, vol. 128, no. 1, pp. 4–8, 2018. DOI: 10.1016/j.radonc.2018.03.017.

[8] J. T. Bushberg, J. Anthony Seibert, Edwin M. Leidholdt Jr., and John M. Boone, Eds., *The Essential Physics of Medical Imaging*, 3rd ed. Philadelphia: Wolters Kluwer Health/Lippincott Williams & Wilkins, 2012.

[9] J. Cammin, S. Kappler, T. Weidinger, and K. Taguchi, "Evaluation of models of spectral distortions in photon-counting detectors for computed tomography", *Journal of Medical Imaging*, vol. 3, no. 2, p. 023 503, 2016. DOI: 10.1117/1.JMI.3.2.023503.

[10] *Causes of death, World, 2021*, https://ourworldindata.org/grapher/annual-number-of-deaths-by-cause.

[11] R. A. Chandra, F. K. Keane, F. E. M. Voncken, and C. R. Thomas, "Contemporary radiotherapy: Present and future", *The Lancet*, vol. 398, no. 10295, pp. 171–184, 2021. DOI: 10.1016/S0140-6736(21)00233-6.

[12] L. A. Feldkamp, L. C. Davis, and J. W. Kress, "Practical cone-beam algorithm", *Journal of the Optical Society of America A*, vol. 1, no. 6, p. 612, 1984. DOI: 10.1364/JOSAA.1.000612.

[13] E. Fredenberg, M. Hemmendorff, B. Cederström, M. Åslund, and M. Danielsson, "Contrast-enhanced spectral mammography with a photon-counting detector", *Medical Physics*, vol. 37, no. 5, pp. 2017–2029, 2010. DOI: 10.1118/1.3371689.

[14] S. J. Gardner, W. Mao, C. Liu, *et al.*, "Improvements in CBCT Image Quality Using a Novel Iterative Reconstruction Algorithm: A Clinical Evaluation", *Advances in Radiation Oncology*, vol. 4, no. 2, pp. 390–400, 2019. DOI: 10.1016/j.adro.2018.12.003.

[15] G. Heilemann, M. Buschmann, W. Lechner, *et al.*, "Clinical Implementation and Evaluation of Auto-Segmentation Tools for Multi-Site Contouring in Radiotherapy", *Physics and Imaging in Radiation Oncology*, vol. 28, p. 100 515, 2023. DOI: 10.1016/j.phro.2023.100515.

[16] J. H. Hubbell, "Review of photon interaction cross section data in the medical and biological context", *Physics in Medicine and Biology*, vol. 44, no. 1, R1–R22, 1999. DOI: 10.1088/0031-9155/44/1/001.

[17] E. M. Huijben, M. L. Terpstra, A. J. Galapon, *et al.*, "Generating synthetic computed tomography for radiotherapy: SynthRAD2023 challenge report", *Medical Image Analysis*, vol. 97, p. 103 276, 2024. DOI: 10.1016/j.media.2024.103276.

[18] ICRU, "Report 46", *Journal of the International Commission on Radiation Units and Measurements (ICRU)*, vol. os24, no. 1, 1992. DOI: 10.1093/jicru/os24.1.Report46.

[19] J. Kim, Y. Kang, T. Hwang, M. Park, and W. Chung, "Evaluation of a two-dimensional Moire-free antiscatter grid for cone-beam computed tomography", *Medical Physics*, vol. 50, no. 6, pp. 3435–3444, 2023. DOI: 10.1002/mp.16243.

[20] C. Kurz, F. Kamp, Y.-K. Park, *et al.*, "Investigating deformable image registration and scatter correction for CBCT-based dose calculation in adaptive IMPT", *Medical Physics*, vol. 43, no. 10, pp. 5635–5646, 2016. DOI: 10.1118/1.4962933.

[21] G. Landry and C.-h. Hua, "Current state and future applications of radiological image guidance for particle therapy", *Medical Physics*, vol. 45, no. 11, 2018. DOI: 10.1002/mp.12744.

[22] G. Landry, R. Nijhuis, G. Dedes, *et al.*, "Investigating CT to CBCT image registration for head and neck proton therapy as a tool for daily dose recalculation", *Medical Physics*, vol. 42, no. 3, pp. 1354–1366, 2015. DOI: 10.1118/1.4908223.

[23] M. J. Berger, J.H. Hubbell, S.M. Seltzer, *et al.*, *XCOM-Photon Cross Sections Database, NIST Standard Reference Database 8*, 1987. DOI: 10.18434/T48G6X.

[24] C. H. McCollough, K. Rajendran, S. Leng, *et al.*, "The technical development of photon-counting detector CT", *European Radiology*, vol. 33, no. 8, pp. 5321–5330, 2023. DOI: 10.1007/s00330-023-09545-9.

[25] C. Möhler, T. Russ, P. Wohlfahrt, *et al.*, "Experimental verification of stopping-power prediction from single- and dual-energy computed tomography in biological tissues", *Physics in Medicine & Biology*, vol. 63, no. 2, p. 025 001, 2018. DOI: 10.1088/1361-6560/aaa1c9.

[26] C. Mory, B. Sixou, S. Si-Mohamed, L. Boussel, and S. Rit, "Comparison of five one-step reconstruction algorithms for spectral CT", *Physics in Medicine & Biology*, vol. 63, no. 23, p. 235 001, 2018. DOI: 10.1088/1361-6560/aaeaf2.

[27] V. P. Moskvin, F. Pirlepesov, Y. Yan, *et al.*, "Accuracy of stopping power ratio calculation and experimental validation of proton range with dual-layer computed tomography", *Acta Oncologica*, vol. 61, no. 7, pp. 864–868, 2022. DOI: 10.1080/0284186X.2022.2069477.

[28] M. Naghavi, K. L. Ong, A. Aali, *et al.*, "Global burden of 288 causes of death and life expectancy decomposition in 204 countries and territories and 811 subnational locations, 1990–2021: A systematic analysis for the Global Burden of Disease Study 2021", *The Lancet*, vol. 403, no. 10440, pp. 2100–2132, 2024. DOI: 10.1016/S0140-6736(24)00367-2.

[29] W. D. Newhauser and R. Zhang, "The physics of proton therapy", *Physics in Medicine and Biology*, vol. 60, no. 8, R155–R209, 2015. DOI: 10.1088/0031-9155/60/8/R155.

[30] M. Oud, S. Breedveld, M. Giżyńska, *et al.*, "An online adaptive plan library approach for intensity modulated proton therapy for head and neck cancer", *Radiotherapy and Oncology*, vol. 176, pp. 68–75, 2022. DOI: 10.1016/j.radonc.2022.09.011.

[31] H. Paganetti, Ed., *Proton Therapy Physics*. Taylor & Francis Group, 2012.

[32] H. Paganetti, "Range uncertainties in proton therapy and the role of Monte Carlo simulations", *Physics in Medicine and Biology*, vol. 57, no. 11, R99–R117, 2012. DOI: 10.1088/0031-9155/57/11/R99.

[33] Y. Park, T. Alexeev, B. Miller, M. Miften, and C. Altunbas, "Evaluation of scatter rejection and correction performance of 2D antiscatter grids in cone beam computed tomography", *Medical Physics*, vol. 48, no. 4, pp. 1846–1858, 2021. DOI: 10.1002/mp.14756.

[34] O. Pastor-Serrano and Z. Perkó, "Millisecond speed deep learning based proton dose calculation with Monte Carlo accuracy", *Physics in Medicine & Biology*, vol. 67, no. 10, p. 105 006, 2022. DOI: 10.1088/1361-6560/ac692e.

[35] N. Peters, P. Wohlfahrt, C. Hofmann, *et al.*, "Reduction of clinical safety margins in proton therapy enabled by the clinical implementation of dual-energy CT for direct stopping-power prediction", *Radiotherapy and Oncology*, vol. 166, pp. 71–78, 2022. DOI: 10.1016/j.radonc.2021.11.002.

[36] U. Pyakurel, Y. Zhang, R. Sabounchi, *et al.*, "Investigation of 2D anti-scatter grid implementation in a gantry-mounted cone beam computed tomography system for proton therapy", *Physics and Imaging in Radiation Oncology*, vol. 33, p. 100 730, 2025. DOI: 10.1016/j.phro.2025.100730.

[37] K. Rajendran, M. Petersilka, A. Henning, *et al.*, "First Clinical Photon-counting Detector CT System: Technical Evaluation", *Radiology*, vol. 303, no. 1, pp. 130–138, 2022. DOI: 10.1148/radiol.212579.

[38] B. Rigaud, A. Simon, J. Castelli, *et al.*, "Deformable image registration for radiation therapy: Principle, methods, applications and evaluation", *Acta Oncologica*, vol. 58, no. 9, pp. 1225–1237, 2019. DOI: 10.1080/0284186X.2019.1620331.

[39] R. Sabounchi, U. Pyakurel, F. Bayat, M. Eldib, and C. Altunbas, "Effect of scatter suppression with 2D antiscatter grids in photon counting compact CBCT", in *Medical Imaging 2024: Physics of Medical Imaging*, R. Fahrig, J. M. Sabol, and K. Li, Eds., San Diego, United States: SPIE, 2024, p. 101. DOI: 10.1117/12.3006524.

[40] D. Sarrut, M. Bardiès, N. Boussion, *et al.*, "A review of the use and potential of the GATE Monte Carlo simulation code for radiation therapy and dosimetry applications: GATE for dosimetry", *Medical Physics*, vol. 41, no. 6Part1, p. 064 301, 2014. DOI: 10.1118/1.4871617.

[41] J. Seco and M. F. Spadea, "Imaging in particle therapy: State of the art and future perspective", *Acta Oncologica*, vol. 54, no. 9, pp. 1254–1258, 2015. DOI: 10.3109/0284186X.2015.1075665.

[42] J. A. Seibert and J. M. Boone, "X-Ray Imaging Physics for Nuclear Medicine Technologists. Part 2: X-Ray Interactions and Image Formation", *JOURNAL OF NUCLEAR MEDICINE TECHNOLOGY*, vol. 33, no. 1, p. 16, 2005.

[43] J. H. Siewerdsen, M. J. Daly, B. Bakhtiar, *et al.*, "A simple, direct method for x-ray scatter estimation and correction in digital radiography and cone-beam CT: X-ray scatter correction", *Medical Physics*, vol. 33, no. 1, pp. 187–197, 2005. DOI: 10.1118/1.2148916.

[44] T. P. Szczykutowicz, G. V. Toia, A. Dhanantwari, and B. Nett, "A Review of Deep Learning CT Reconstruction: Concepts, Limitations, and Promise in Clinical Practice", *Current Radiology Reports*, vol. 10, no. 9, pp. 101–115, 2022. DOI: 10.1007/s40134-022-00399-5.

[45] V. T. Taasti, G. J. Michalak, D. C. Hansen, *et al.*, "Validation of proton stopping power ratio estimation based on dual energy CT using fresh tissue samples", *Physics in Medicine & Biology*, vol. 63, no. 1, p. 015 012, 2017. DOI: 10.1088/1361-6560/aa952f.

[46] V. T. Taasti, L. P. Muren, K. Jensen, *et al.*, "Comparison of single and dual energy CT for stopping power determination in proton therapy of head and neck cancer", *Physics and Imaging in Radiation Oncology*, vol. 6, pp. 14–19, 2018. DOI: 10.1016/j.phro.2018.04.002.

[47] K. Taguchi and J. S. Iwanczyk, "Vision 20/20: Single photon counting x-ray detectors in medical imaging: Vision 20/20: Photon counting detectors", *Medical Physics*, vol. 40, no. 10, p. 100 901, 2013. DOI: 10.1118/1.4820371.

[48] A. Thummerer, P. Zaffino, A. Meijers, *et al.*, "Comparison of CBCT based synthetic CT methods suitable for proton dose calculations in adaptive proton therapy", *Physics in Medicine & Biology*, vol. 65, no. 9, p. 095 002, 2020. DOI: 10.1088/1361-6560/ab7d54.

[49] S. J. van der Sar, S. Brunner, and D. Schaart, "X-ray photon-counting using silicon photomultiplier-based scintillation detectors at high x-ray tube currents", in *Medical Imaging 2022: Physics of Medical Imaging*, W. Zhao and L. Yu, Eds., vol. 12031, San Diego, United States: SPIE, 2022, p. 120310I. DOI: 10.1117/12.2611365.

[50] S. J. Van Der Sar, S. E. Brunner, and D. R. Schaart, "Silicon photomultiplier-based scintillation detectors for photon-counting CT: A feasibility study", *Medical Physics*, vol. 48, no. 10, pp. 6324–6338, 2021. DOI: 10.1002/mp.14886.

[51] M. J. Willemink, M. Persson, A. Pourmorteza, N. J. Pelc, and D. Fleischmann, "Photon-counting CT: Technical Principles and Clinical Prospects", *Radiology*, vol. 289, no. 2, pp. 293–312, 2018. DOI: 10.1148/radiol.2018172656.

[52] H. Willers and K. D. Held, "Introduction to Clinical Radiation Biology", *Hematology/Oncology Clinics of North America*, vol. 20, no. 1, pp. 1–24, 2006. DOI: 10.1016/j.hoc.2006.01.007.

[53] R. R. Wilson, "Radiological Use of Fast Protons", *Radiology*, vol. 47, no. 5, pp. 487–491, 1946. DOI: 10.1148/47.5.487.

[54] P. Wohlfahrt, C. Möhler, C. Richter, and S. Greilich, "Evaluation of Stopping-Power Prediction by Dual- and Single-Energy Computed Tomography in an Anthropomorphic Ground-Truth Phantom", *International Journal of Radiation Oncology*Biology*Physics*, vol. 100, no. 1, pp. 244–253, 2018. DOI: 10.1016/j.ijrobp.2017.09.025.

[55] Y. Xie, C. Ainsley, L. Yin, *et al.*, "*Ex vivo* validation of a stoichiometric dual energy CT proton stopping power ratio calibration", *Physics in Medicine & Biology*, vol. 63, no. 5, p. 055 016, 2018. DOI: 10.1088/1361-6560/aaae91.

[56] M. Yang, G. Virshup, J. Clayton, X. R. Zhu, R. Mohan, and L. Dong, "Theoretical variance analysis of single- and dual-energy computed tomography methods for calculating proton stopping power ratios of biological tissues", *Physics in Medicine and Biology*, vol. 55, no. 5, pp. 1343–1362, 2010. DOI: 10.1088/0031-9155/55/5/006.

[57] Z. Yu, Y. Park, and C. Altunbas, "Simultaneous scatter rejection and correction method using 2D antiscatter grids for CBCT", in *Medical Imaging 2020: Physics of Medical Imaging*, H. Bosmans and G.-H. Chen, Eds., Houston, United States: SPIE, 2020, p. 104. DOI: 10.1117/12.2549763.

[58] G. Zentai, "Comparison of CMOS and a-Si flat panel imagers for X-ray imaging", in *2011 IEEE International Conference on Imaging Systems and Techniques*, 2011, pp. 194–200. DOI: 10.1109/IST.2011.5962217.

[59] S. Zhang, D. Han, J. F. Williamson, *et al.*, "Experimental implementation of a joint statistical image reconstruction method for proton stopping power mapping from dual-energy CT data", *Medical Physics*, vol. 46, no. 1, pp. 273–285, 2019. DOI: 10.1002/mp.13287.

Chapter 2

Framework for Evaluating Photon-Counting Detectors Under Pile-up Conditions

Objective: While X-ray photon-counting detectors (PCDs) promise to revolutionise medical imaging, theoretical frameworks to evaluate them are commonly limited to incident fluence rates sufficiently low that the detector response can be considered linear. However, typical clinical operating conditions lead to a significant level of pile-up, invalidating this assumption of a linear response. Here, we present a framework that aims to evaluate PCDs, taking into account their non-linear behaviour.
Methods: We employ small-signal analysis to study the behaviour of PCDs under pile-up conditions. The response is approximated as linear around a given operating point, determined by the incident spectrum and fluence rate. The detector response is subsequently described by the proposed perturbation point spread function (pPSF). We demonstrate this approach using Monte-Carlo simulations of idealised direct- and indirect-conversion PCDs.
Results: The pPSFs of two PCDs are calculated. It is then shown how the pPSF allows to determine the sensitivity of the detector signal to an arbitrary lesion. This example illustrates the detrimental influence of pile-up, which may cause nonintuitive effects such as contrast/contrast-to-noise ratio inversion or cancellation between/within energy bins.
Conclusion: The proposed framework permits quantifying the spectral and spatial performance of PCDs under clinically realistic conditions at a given operating point. The presented example illustrates why PCDs should not be analysed assuming that they are linear systems. The framework can, for example, be used to guide the development of PCDs and PCD-based systems. Furthermore, it can be applied to adapt commonly used measures, such as the modulation transfer function, to non-linear PCDs.

This chapter is based on the following publication: **DL**, S. J. van der Sar, M. C. Goorden, and D. R. Schaart, "Framework for evaluating photon-counting detectors under pile-up conditions", Journal of Medical Imaging 11(S1), S12802 (2024). doi: 10.1117/1.JMI.11.S1.S12802.

2.1 Introduction

Photon-counting detectors (PCDs) herald the next leap in medical X-ray imaging, promising images with increased contrast-to-noise ratios, hence allowing for lower dose, and multi-energy imaging capabilities beyond what can be offered by dual-energy imaging [9, 11, 43], all of which could translate into substantial improvements in patient care. PCDs could therefore supersede the currently dominant energy-integrating detectors (EIDs) in X-ray imaging. Whereas EIDs only measure the total amount of energy deposited by X-rays in each projection, PCDs are capable of counting the number of detector pulses generated by individual X-ray photons and assigning each pulse to one of at least two energy bins. To compare and optimise the performance of different PCDs, suitable detector performance measures are needed. In particular, performance measures that have been devised for EIDs in the past may need to be adapted to the case of PCDs.

A fundamental aspect of any imaging detector is its transfer of the spatial and spectral information contained in the incident beam into its output signal. The corresponding measure is the detector point spread function (PSF), which, in our case, describes the detector's response to irradiating a single pixel homogeneously [5]. For PCDs, the PSF should not only describe the spatial response of the detector (i.e., how the incoming spatial information is distributed over neighbouring pixels), but also the spectral response (i.e., how the incoming spectral information is distributed over energy bins).

An EID has, in very good approximation, a linear response. Hence, the response to an incident beam with an arbitrary spectrum can always be expressed as a linear combination of PSFs of monoenergetic beams. This also applies to a PCD under low fluence rate conditions; however, detectors are exposed to very high fluence rates of up to $3.4 \cdot 10^8$ $\mathrm{mm^{-2}s^{-1}}$ in clinical practice [22]. Under these demanding circumstances, pile-up as well as the specific implementation of pulse processing will influence the transfer of spatial and spectral information and PCDs cease to exhibit a linear response [4, 15, 44]. This warrants research into the characterisation of PCDs under high fluence rates.

The aforementioned effect of *pile-up* is caused by the finite pulse length in any physical detector and refers to the overlap of individual pulses, such that a detector cannot determine the correct underlying number of events and their energies [43]. We refer to the algorithm that is used to process the pulses and to extract the number of counts as well as the corresponding energies as the *counting behaviour*. All in all, the finite pulse length of a detector in response to an incoming photon, the pile-up of pulses, and the subsequent readout via a specific counting behaviour can lead to an incorrectly registered total number of photons, as well as to an incorrectly registered number of photons per energy bin. The extent of these effects is dependent on, first, the fluence rate, because a higher number of photons arriving at the detector per second and per detector pixel increases the pile-up probability, and second, the spectrum, because it determines the probability of an incoming photon of a specific energy to be detected in a certain energy bin after pile-up.

The research on non-linear effects in PCDs has so far focused on developing models to predict the counts registered in a particular energy bin [6, 12, 34, 36, 42] and on calibrating for them [21, 30], but less on the ramifications on commonly used tools to characterise detectors, such as the PSF, modulation transfer function (MTF), noise equivalent quanta (NEQ) and detective quantum efficiency (DQE), all of which are performance metrics based on the assumption of a linear detector response. We argue that a comprehensive characterisation of PCDs must encompass their non-linear behaviour and include the fluence rate into their analysis.

In this study, we explore how to adapt image quality measures to the non-linear response of PCDs. We demonstrate a basic example of calculating the contrast between two projection lines with slightly different line integrals, and show how an adapted formulation of the PSF,

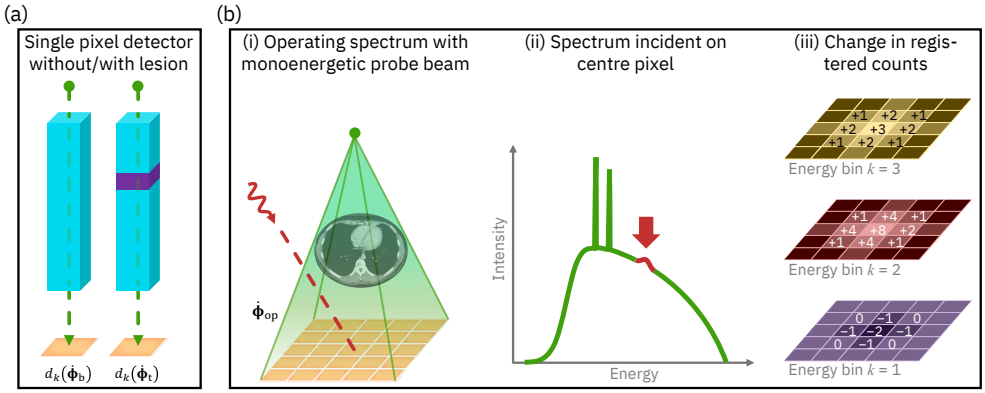

Figure 2.1: (a) A monoenergetic beam travels through an object, resulting in a registered count rate $d_k(\dot{\Phi}_b)$ in energy bin k of a single-pixel PCD. When a lesion is inserted, this results in a count rate $d_k(\dot{\Phi}_t)$. (b) Extension to a detector array and a polychromatic beam: (i) and (ii) A detector array is homogeneously irradiated by an operating spectrum (green) with a given spectral fluence rate $\dot{\Phi}_{op}$. This operating spectrum is perturbed by adding a monoenergetic probe beam (red) incident on the centre pixel of the array. (iii) The change of count rate in the pixels and energy bins k of the PCD due to the addition of the monoenergetic perturbation can be approximated by a linear response.

which we call *perturbation PSF* (pPSF), can be used in the non-linear regime. To illustrate the use of the newly proposed formalism, we show its application to simulated data of two PCDs by performing Monte-Carlo (MC) simulations and investigating the influence of the fluence rate of an X-ray beam with a given spectrum on the adapted detector measures. The focus of this work is on the introduction of a new theoretical framework, rather than on modeling any specific detector as realistically as possible. We therefore apply the framework to idealised versions of direct- and indirect-conversion PCDs, intending to illustrate clearly how differences between detectors translate into differences in the pPSF.

2.2 Theory

2.2.1 Contrast for Single Projection Line

Let us consider a PCD consisting of a single pixel, and a single projection line going through an object of interest (Figure 2.1a). The task is to distinguish between the cases of lesion absent and lesion present. We start with the measure of contrast, which is linked to the measure of detectability via the Rose criterion, which states a minimum required signal-to-noise ratio [27]. Let $\dot{\mathbf{\Phi}} = \left(\dot{\Phi}_{E_1}, ..., \dot{\Phi}_{E_L}\right)$ represent the incident spectral distribution, denoted as the spectral fluence rate, that is, the number of photons per unit area and unit time ($\mathrm{mm}^{-2}\mathrm{s}^{-1}$), where each entry represents the fluence rate at a discrete energy E_l . Here, discretization of the incoming photon energies is done for practical reasons; this facilitates the implementation of studies such as those described in Section 2.3. Let us furthermore denote the total fluence rate, that is, the total number of photons per square millimetre per second, as $\|\dot{\mathbf{\Phi}}\|_1 = \sum_l \dot{\Phi}_{E_l}$.

For the case of a lesion being absent, that is, the baseline, we will denote the spectral fluence rate incident on the pixel by $\dot{\mathbf{\Phi}}_b$, and the detector output, that is, the number of counts registered by the detector in energy bin k per unit time, by $d_k(\dot{\mathbf{\Phi}}_b)$. Now let us insert a lesion, that is, the target, with a size small compared to the dimensions of the whole object, into the path of the projection line, slightly changing the fluence rate exiting the object. The spectral fluence

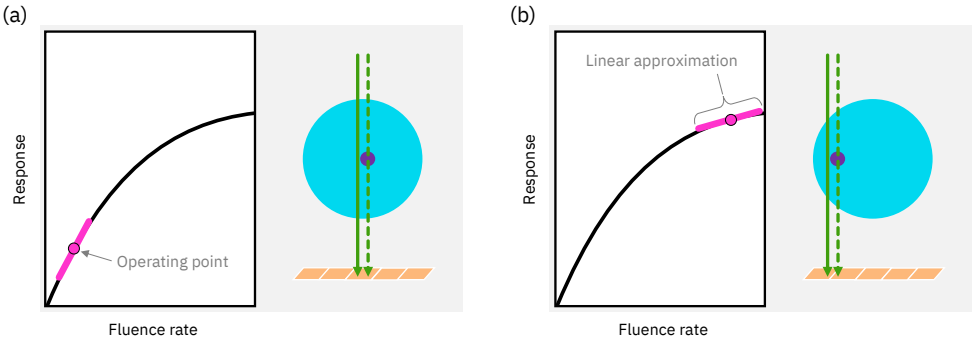

Figure 2.2: Schematic visualisation of the proposed concept. A given fluence rate places the detector at a specific operating point. Around this operating point, the non-linear fluence rate—response curve is approximated as linear.

rate on the detector shall now be denoted by $\dot{\mathbf{\Phi}}_\mathrm{t}$, and the number of registered counts in the pixel per time unit by $d_k(\dot{\mathbf{\Phi}}_\mathrm{t})$. As an indication of how well the detector can distinguish between the two cases of lesion present and lesion absent, let us calculate the contrast C_k between the two detector outputs in each detector energy bin k:

$$C_k = \frac{d_k(\dot{\mathbf{\Phi}}_\mathrm{t}) - d_k(\dot{\mathbf{\Phi}}_\mathrm{b})}{d_k(\dot{\mathbf{\Phi}}_\mathrm{b})} \quad . \tag{2.1}$$

2.2.2 Small-Signal Analysis

To be able to make general statements about a system's ability to preserve contrast, it is desirable to determine $d_k(\dot{\mathbf{\Phi}})$ in Equation 2.1 without having to actually measure it for every possible combination of total incident fluence rate and incident spectral shape. In case of a linear detector, this is straightforward if the detector response is known for every incident energy. To arrive at an expression for d_k for the more challenging case of non-linear systems, we can assume that the spectral fluence rates for the cases with and without lesion only differ by a small amount, i.e., $\dot{\mathbf{\Phi}}_\mathrm{t} = \dot{\mathbf{\Phi}}_\mathrm{b} + \mathbf{\Delta}\dot{\mathbf{\Phi}}$ with $\|\mathbf{\Delta}\dot{\mathbf{\Phi}}\|_1 \ll \|\dot{\mathbf{\Phi}}_\mathrm{b}\|_1$, since we required the lesion to be small compared to the dimensions of the object. In other words, the insertion of the lesion is regarded as a perturbation $\mathbf{\Delta}\dot{\mathbf{\Phi}}$ of the original fluence rate $\dot{\mathbf{\Phi}}_\mathrm{b}$. We can then Taylor-expand the registered count rate $d_k(\dot{\mathbf{\Phi}})$ around the fluence rate $\dot{\mathbf{\Phi}}_\mathrm{b}$ up to and including first order, as follows:

$$\begin{aligned}
d_k(\dot{\mathbf{\Phi}}_\mathrm{t}) &= d_k(\dot{\mathbf{\Phi}}_\mathrm{b} + \mathbf{\Delta}\dot{\mathbf{\Phi}}) \\
&= d_k(\dot{\Phi}_{\mathrm{b},E_1} + \Delta\dot{\Phi}_{E_1}, \ \dots \ , \dot{\Phi}_{\mathrm{b},E_L} + \Delta\dot{\Phi}_{E_L}) \\
&= d_k(\dot{\Phi}_{\mathrm{b},E_1}, \ \dots \ , \dot{\Phi}_{\mathrm{b},E_L}) + \sum_l \frac{\partial d_k(\dot{\mathbf{\Phi}}_\mathrm{b})}{\partial \dot{\Phi}_{E_l}} \Delta\dot{\Phi}_{E_l} + \mathcal{O}(\mathbf{\Delta}\dot{\mathbf{\Phi}}^2) \\
&\approx d_k(\dot{\mathbf{\Phi}}_\mathrm{b}) + \sum_l \frac{\partial d_k(\dot{\mathbf{\Phi}}_\mathrm{b})}{\partial \dot{\Phi}_{E_l}} \Delta\dot{\Phi}_{E_l} \quad ,
\end{aligned} \tag{2.2}$$

where $\dot{\mathbf{\Phi}}_{\text{b/t}} = (\dot{\Phi}_{\text{b/t},E_1}, \dots, \dot{\Phi}_{\text{b/t},E_L})$ and $\mathbf{\Delta\dot{\Phi}} = (\Delta\dot{\Phi}_{E_1}, \dots, \Delta\dot{\Phi}_{E_L})$ are vectors of discrete energies E_l. Inserting Equation 2.2 into Eq. 2.1 then gives the contrast C_k in energy bin k:

$$C_k = \frac{\sum_l \frac{\partial d_k(\dot{\mathbf{\Phi}}_\text{b})}{\partial \dot{\Phi}_{E_l}} \Delta\dot{\Phi}_{E_l}}{d_k(\dot{\mathbf{\Phi}}_\text{b})} \quad . \tag{2.3}$$

This expression describes contrast as the result of a sensitivity analysis, that is, how sensitive the detector is to a (small) change in fluence rate, given the baseline incident spectral fluence rate $\dot{\mathbf{\Phi}}_\text{b}$. In essence, this is equivalent to approximating a non-linear system at a certain *operating point* as a linear system (Figure 2.2). Therefore, we will denote the incident spectral fluence rate at which the detector is approximated by a linear system as the *operating spectrum* $\dot{\mathbf{\Phi}}_\text{op}$, which states the number of incident photons in units of $\text{mm}^{-2}\text{s}^{-1}$. This idea of using small-signal analysis and a Taylor expansion has also been suggested (but not elaborated upon) by Tanguay et al [37], while the terms "operating point"/"operating spectrum" follow the nomenclature commonly used in, e.g., electrical engineering, where one is interested in the behaviour of a system at a specific operating point. The terms also underline the fact that the PCD's response we aim to quantify is determined by the combination of all parameters and circumstances under which a detector is operated. One advantage of approximating a PCD as a linear system around a given operating point is that it enables us to study the change in detector response due to an arbitrary, though small, spectral fluence rate difference $\mathbf{\Delta\dot{\Phi}}$. In the following section, we explore the gradient $\partial d_k(\dot{\mathbf{\Phi}}_\text{b})/\partial\dot{\Phi}_{E_l}$ further.

2.2.3 Extension to Detector Arrays

So far, we have limited the discussion to a detector consisting of a single pixel. Here, we generalise the discussion to an array of pixels. Following the notation introduced by Persson et al [23], let us first introduce a detector PSF $h_k(\boldsymbol{n} - \boldsymbol{n}', E_l)$ which states the probability for photons of energy E_l , incident on the pixel $\boldsymbol{n}'$ with area A, to be registered as a count in pixel $\boldsymbol{n}$ and its energy bin k. To determine the PSF, a single pixel of the detector is illuminated and the response in all other pixels is registered. Under the assumption that the system is linear and shift-invariant, and given an incoming spectral fluence rate distribution $\dot{\mathbf{\Phi}}(\boldsymbol{n})$, we can obtain the count rate d_k in pixel $\boldsymbol{n}$ and energy bin k via [Persson et al [23], p. 4899, Equation (1)]

$$d_k(\boldsymbol{n}, \dot{\mathbf{\Phi}}) = \sum_l \sum_{\boldsymbol{n}'} h_k(\boldsymbol{n} - \boldsymbol{n}', E_l) \cdot \dot{\Phi}_{E_l}(\boldsymbol{n}') \cdot A \quad . \tag{2.4}$$

Equation 2.4 represents a (discrete) convolution of the incoming spectral fluence rate distribution $\dot{\mathbf{\Phi}}(\boldsymbol{n})$ with the PSF h_k . This approach can be used to obtain the detector response of a linear detector to an arbitrary (spectral) fluence rate distribution. It is emphasised that Equation 2.4 is only valid under the condition that the system is linear and shift-invariant, which in the case of PCDs is only fulfilled at low fluence rates.

At high fluence rates where the response of a PCD becomes non-linear a different approach is needed. We will start by assuming that the whole detector array is set at a specific operating point, that is, the detector array is irradiated homogeneously with a certain incident spectral fluence rate $\dot{\mathbf{\Phi}}_\text{op}$ (see Figure 2.1b(i)). This is motivated by the fact that the fluence rate behind an object is approximately constant within a sufficiently small region.
Next, we again approximate the non-linear system as a linear one around the chosen operating point and investigate the effect of a perturbation, which is realised using an additional probe beam of spectral fluence rate $\mathbf{\Delta\dot{\Phi}}^{\boldsymbol{n}_0}$ incident on pixel $\boldsymbol{n}_0$ only (Figures 2.1b(i) and 2.1b(ii)). Since we approximate the non-linear system at the operating point $\dot{\mathbf{\Phi}}_\text{op}$ as a linear one, it is

now possible to express the resulting change in the registered count rate d_k as a convolution between $\boldsymbol{\Delta}\dot{\boldsymbol{\Phi}}^{\boldsymbol{n}_\emptyset}$ and a PSF, similar to Equation 2.4. The important distinction is that, in this case, the PSF must relate a *perturbation* of the incident fluence rate $\boldsymbol{\Delta}\dot{\boldsymbol{\Phi}}^{\boldsymbol{n}_\emptyset}$ to a change in d_k (Figure 2.1b(iii)), and we will therefore denote it as the pPSF $h_k^{\Delta}(\boldsymbol{\Delta n},\, \dot{\boldsymbol{\Phi}}_{\text{op}},\, E_l)$, with $\boldsymbol{\Delta n} = \boldsymbol{n} - \boldsymbol{n}_\emptyset$. It must be stressed that h_k^{Δ} is bound to a specific operating point $\dot{\boldsymbol{\Phi}}_{\text{op}}$, and only applies to a small perturbation thereof.
Using the pPSF, we can express the registered count rate d_k in pixel $\boldsymbol{n}$ as follows:

$$d_k(\boldsymbol{n},\, \dot{\boldsymbol{\Phi}}_{\text{op}} + \boldsymbol{\Delta}\dot{\boldsymbol{\Phi}}^{\boldsymbol{n}_\emptyset}) = d_k(\dot{\boldsymbol{\Phi}}_{\text{op}}) + \sum_l h_k^{\Delta}(\boldsymbol{n} - \boldsymbol{n}_\emptyset,\, \dot{\boldsymbol{\Phi}}_{\text{op}},\, E_l) \cdot \Delta\dot{\Phi}_{E_l}^{\boldsymbol{n}_\emptyset} \cdot A \quad . \tag{2.5}$$

Here we used that, since we assume a shift-invariant system and a constant fluence rate in a sufficiently small region, $d_k(\boldsymbol{n},\, \dot{\boldsymbol{\Phi}}_{\text{op}})$ is the same for all pixels $\boldsymbol{n}$. Comparing Equation 2.2 with Equation 2.5 shows that the gradient $\partial d_k(\dot{\boldsymbol{\Phi}})/\partial\dot{\Phi}_{E_l}$ corresponds to the pPSF.

2.3 Methodology

2.3.1 X-ray Operating Spectrum

The operating spectrum assumed in this work is based on the standardised spectra described in the IEC 61267:2005 standard [8], more specifically, the set of so-called RQA spectra that mimic the X-ray beam behind a patient. The spectra are specified via a source voltage and an added aluminium filtration. Since realistic X-ray sources already exhibit intrinsic filtration, the standard specifies a nominal first half-value layer value to capture the spectrum's shape in a single parameter. We simulated the spectra using SPEKCALC [25] with the source voltage and added filtration as defined in the IEC 61267:2005 standard. The intrinsic filtration was empirically adjusted to yield a very good agreement with the nominal first half-value layer for all spectra, and resulted in 0.8 mm Be and 0.10 mm Cu. In this work, we use the RQA9 spectrum as our operating spectrum, which is based on an X-ray tube voltage of 120 kVp.

2.3.2 Fluence Rates

For the choice of fluence rates relevant to medical imaging we refer to the work by Persson et al [22]. In their study, they investigated the maximum fluence rates encountered in clinical CT protocols, using a CT scanner with tube current modulation and bow-tie filter. The authors concluded that maximum total fluence rates between $3.4 \cdot 10^8$ mm^{-2}s^{-1} (standard head and chest protocol) and $4 \cdot 10^8$ mm^{-2}s^{-1} (ECG gated chest protocol) occur for perfectly centred patients. If the patients are misaligned, then the fluence rate can reach up to $6 \cdot 10^8$ mm^{-2}s^{-1}. For non-standard protocols and maximum available tube currents on modern X-ray tubes, they may even reach up to $1.1 \cdot 10^9$ mm^{-2}s^{-1}. For the present study, we therefore decided to cover a wide range of total fluence rates, from 10^5 up to 10^9 mm^{-2}s^{-1} in increments of factors of 10.

2.3.3 Detector Models

This study considers two hypothetical PCDs, namely an idealised direct-conversion detector based on CdZnTe (CZT), and an idealised indirect-conversion detector based on a $LaBr_3$:Ce scintillation crystal array one-to-one coupled to a silicon photomultiplier array. Indirect-conversion, scintillation-based PCDs may combine cost-effective growth of detector-grade material with efficient X-ray absorption, which is why silicon photomultiplier (SiPM)-based scintillation detectors are under investigation as an alternative to direct-conversion detectors based on, e.g., CdTe or CZT [20, 29, 39, 40].
While we simulate realistic energy resolutions and pulse shapes (see Section 2.3.5), we omit

the inclusion of charge sharing and light leakage for the direct and indirect detector, respectively. As a consequence, the cross-talk between pixels observed in our study is entirely due to X-ray scatter and X-ray fluorescence, which are different for the two detector materials. By limiting the number of physical processes that contribute to cross-talk, we aim to clearly illustrate how differences between detectors correlate with differences in the pPSF.
The thicknesses of the absorbing layers were set to 2 mm for CZT and to 2.8 mm for $LaBr_3$:Ce. The thicknesses were chosen such that, for the incident RQA9 spectrum, the number of photons passing through the detector material without any interaction is the same for both detectors.
The pixel pitch was set to 500 µm for both detectors (both in x- and y-direction); to account for a smaller active pixel size of the indirect-conversion detector due to a reflective layer around the scintillation crystals, a 60 µm thick [13] PTFE (Teflon, $(C_2F_2)_n$) reflector was included, which was wrapped around each pixel and reduces the effective pixel size by 120 µm while keeping the pixel pitch at 500 µm.

2.3.4 Monte-Carlo Simulations of Energy Deposition

A MC simulation was implemented with GATE (version 9.2) [28], which utilises the GEANT4 toolkit [1] (version 11.0.0). It simulates the irradiation of a detector with X-rays of a given spectrum (see Section 2.3.1) and tracks, for each incident photon, in which pixels energy is deposited, as well as the amount of deposited energy. The emission of photons from the source is modelled according to a Poisson process, and the timestamps of their interactions with the detector are stored.
CZT was defined as $Cd_{0.9}Zn_{0.1}Te$ with a density [10] of 5.78 g/cm^3. $LaBr_3$:Ce(5 %) was defined with a 1 : 3 ratio between La and Br, where 5 % of the La ions are replaced [41] by Ce; the density [41] was set to 5.29 g/cm^3.
The physics model used by the MC simulation was based on the *emstandard_opt4* option in GATE. X-ray fluorescence was enabled by setting the production cut to 10 µm for photons and to 1000 µm for electrons. The remaining physics settings were kept at their default values. All events were registered and stored, without rejecting events below a certain energy threshold.

2.3.5 Pulse Train

The simulated events were processed with a pulse train analysis to mimic the readout circuitry of a PCD. For a given set of simulated events of energy E_i with time stamps t_i (sampled with 1 ns resolution), the generated pulse train is a convolution of a series of delta pulses, i.e., $\sum_i E_i \cdot \delta(t - t_i)$, with a pulse shape function $p(t)$. Prior to this convolution, an energy blurring was applied to model the finite energy resolution of the system, which was set to 22.3 % full width at half maximum (FWHM) at 59.5 keV for the scintillation detector based on previously obtained experimental results using a 100 MHz low-pass filter [40], and to 8.0 % FWHM at 59.5 keV for the direct-conversion detector [32]. The energy dependence of the FWHM energy resolution was modelled according to an inverse square law behaviour in both cases. For the CZT detector, a Gaussian pulse shape $p(t)$ with a FWHM of 14 ns was chosen [31]. For the $LaBr_3$:Ce detector, the applied pulse shape $p(t)$ is the convolution of two exponentially decaying functions modelling the scintillation decay (16 ns for $LaBr_3$:Ce [16]) and the recharge time of the SiPM (7 ns) [40].

2.3.6 Counting Behaviour

In this study, we implemented a paralysable-like (P-like) and a non-paralysable-like (NP-like) counting behaviour [38] (see Figure 2.A.1 in the Appendix), both with a peak detection time

τ_{pd} that is started with a positive threshold crossing (P-like counting) or the start of an analysis window τ_{np} (NP-like counting). Within the peak detection time window τ_{pd} the maximum signal height is determined, used as the registered energy, and the counter in the respective energy bin is increased by 1.

The trigger threshold was set to 20 keV; while this value is relatively small in the context of clinical CT, it reveals a lower boundary of the event rate a detector can handle. While realistic PCDs with energy-discriminating capabilities use only a small number of energy bins, we used a near-continuous binning with bin widths of 1 keV to make the effects at play more visible, with the lowest bin centred at 20 keV and the highest at 250 keV; registered counts outside those limits were discarded.

The length of the analysis window τ_{np} (for the NP-like counting only) is chosen such that it is slightly larger than the time over threshold (ToT) of a pulse caused by the photons with the highest energy. This ensures that the counting algorithm outputs a count of exactly 1 for the highest-energy photon in the incident spectrum in case there is no pile-up. The energy of the highest-energy photons is determined by the selected source voltage; since we include a limited energy resolution in our model, we increased this value by the FWHM of the energy resolution at this energy value. With the pulse shapes described in the previous section and for a 120 kVp RQA9 spectrum, this results in an analysis window of length $\tau_{np} = 51$ ns for the $LaBr_3$:Ce-based PCD and of $\tau_{np} = 24$ ns for the CZT-based PCD. These values are very close to those reported by van der Sar et al [40] and Steadman et al [31].

The peak detection time τ_{pd} (for both NP- and P-like counting) is set slightly larger than the time between the trigger threshold crossing and the time where the pulse reaches its maximum. It is again determined for the photons with the highest energy, including an added energy blurring, and for photons of a 120 kVp RQA9 spectrum excluding any pile-up. This results into a peak detection time of $\tau_{np} = 11$ ns for the $LaBr_3$:Ce-based PCD, and of $\tau_{np} = 13$ ns for the CZT-based PCD.

2.3.7 Determination of h_k^{Δ}

Solving Equation 2.5 for h_k^{Δ} yields:

$$h_k^{\Delta}(\boldsymbol{\Delta n}, \dot{\boldsymbol{\Phi}}_{\text{op}}, E_l) = \frac{d_k\left(\boldsymbol{n}, \left(\dot{\Phi}_{\text{op},E_1}, \ldots, \dot{\Phi}_{\text{op},E_l} + \Delta\dot{\Phi}_{E_l}^{\boldsymbol{n}_0}, \ldots, \dot{\Phi}_{\text{op},E_L}\right)\right) - d_k(\boldsymbol{n}, \dot{\boldsymbol{\Phi}}_{\text{op}})}{\Delta\dot{\Phi}_{E_l}^{\boldsymbol{n}_0} \cdot A} \tag{2.6}$$

with A as the pixel area. Here, the perturbation in incident fluence rate is due to an added monoenergetic probe beam with fluence rate $\Delta\dot{\Phi}_{E_l}^{\boldsymbol{n}_0}$ at energy E_l, with a cross section as large as one pixel, exclusively in pixel $\boldsymbol{n}_0$. First, the registered count rate due to the operating spectrum, $d_k(\boldsymbol{n}, \dot{\boldsymbol{\Phi}}_{\text{op}})$ was obtained as described in Sections 2.3.1 – 2.3.6. Since we assume a shift-invariant detector homogeneously irradiated by the operating spectrum, $d_k(\boldsymbol{n}, \dot{\boldsymbol{\Phi}}_{\text{op}})$ is the same for all pixels. Second, we added a monoenergetic probe beam with fluence rate $\Delta\dot{\Phi}_{E_l}^{\boldsymbol{n}_0}$ at energy E_l to pixel $\boldsymbol{n}_0$ and stored the counts caused in all pixels $\boldsymbol{n}$ of the array. Third, h_k^{Δ} was calculated according to Equation 2.6. The energy of the monoenergetic probe beam was swept from 20 to 150 keV in steps of 2 keV. For further details on the implementation of the evaluation of h_k^{Δ} we refer to Section 2.A.1 in the Appendix.

2.3.8 Contrast and Contrast-to-Noise Ratio of Single Projection Line

Section 2.2.1 discusses the scenario of a single pixel detector measuring the spectral fluence rate behind an object with and without the insertion of a lesion. For the case of including a lesion, we attenuate the RQA9 spectrum with an additional object based on the Lambert–Beer law. The added lesion consists of an aqueous iodine solution with a concentra-

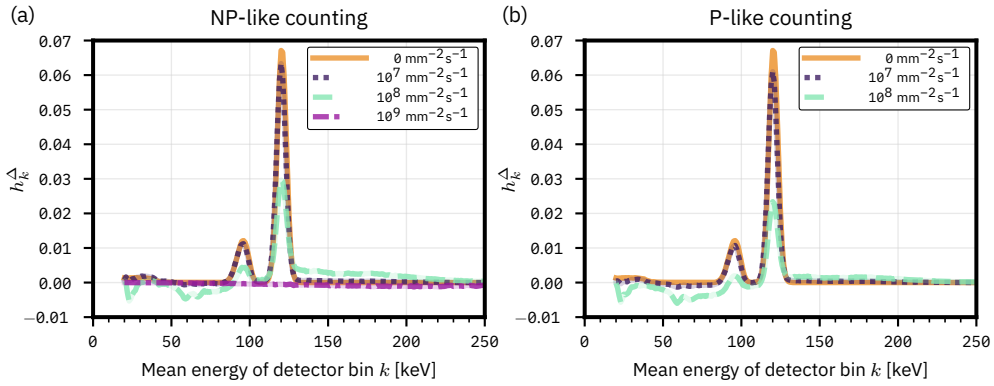

Figure 2.3: $h_k^\Delta(\Delta\boldsymbol{n} = \boldsymbol{0}, \dot{\Phi}_{\text{op}}, E_l = 120\,\text{keV})$, that is, a slice of the pPSF h_k^Δ along all registering energy bins k in the centre pixel $\boldsymbol{n}_0$ of the idealised direct-conversion detector for an incident probe beam energy E_l of 120 keV. The figures show different total fluence rates of the operating spectrum $\dot{\Phi}_{\text{op}}$, including the edge case of no operating spectrum, for (a) non-paralysable and (b) paralysable counting.

tion of 300 g/ml, defined with the following mass fractions: I: 0.2308; O: 0.6832; H: 0.0861; its energy-dependent mass attenuation coefficient $\mu(E)/\rho$ was extracted from the XRAYDB library [18] (version 4.4.7). The change in fluence rate due to the lesion is then calculated via $\Delta\dot{\Phi}_{E_l} = \dot{\Phi}_{\text{op},E_l} \cdot (\exp(-\mu(E_l)/\rho \cdot x\rho) - 1)$. The insertion of the lesion must be small enough that it does not change the (spectral) fluence rate significantly, hence, the thickness x and (homogeneous) mass density ρ of the lesion was selected such that the fluence rate in the energy range under investigation does not change by more than an arbitrary threshold of 1 %. This is fulfilled by setting the product $\rho \cdot x$ to 0.0007 g/cm^2.

The contrast was calculated according to Equation 2.3. For the contrast-to-noise ratio (CNR), the contrast C_k in each energy bin was divided by the square root of the variance $\sigma(C_k)$ of the contrast in that energy bin. The latter was determined via the variance of the number of counts d_k in that energy bin. To obtain $\text{Var}(d_k)$, the pulse train was divided into shorter sections and the result for d_k was saved for each section individually, which allowed to calculate the variance of d_k . The section length was adjusted such that the CNR was evaluated per equal dose for various fluence rates, i.e., for an increase in fluence rate by a factor of 10 the section length was decreased by a factor of 10. For further details on the determination of CNR we refer to Section 2.A.2 in the Appendix.

2.4 Results

2.4.1 Perturbation Point Spread Function

Figures 2.3 and 2.4 show $h_k^\Delta(\Delta\boldsymbol{n} = \boldsymbol{0}, \dot{\Phi}_{\text{op}}, E_l = 120\,\text{keV})$, that is, a slice of the pPSF h_k^Δ for the simulated idealised direct-conversion detector (iDCD) based on CZT and the idealised indirect-conversion detector (iICD) based on $LaBr_3$:Ce, respectively, along all registering energy bins k in the centre pixel $\boldsymbol{n}_0$ (hence, $\Delta\boldsymbol{n} = \boldsymbol{0}$) for an incident probe beam energy E_l of 120 keV. In other words, these graphs give the probability that an additional probe beam photon of energy E_l adds (positive values) or removes (negative values) a count from a certain energy bin k. Note the difference with the PSF of linear systems, which is always positive. While realistic PCDs use only a few energy bins, the near-continuous binning shown here facilitates the understanding of the effects at play.

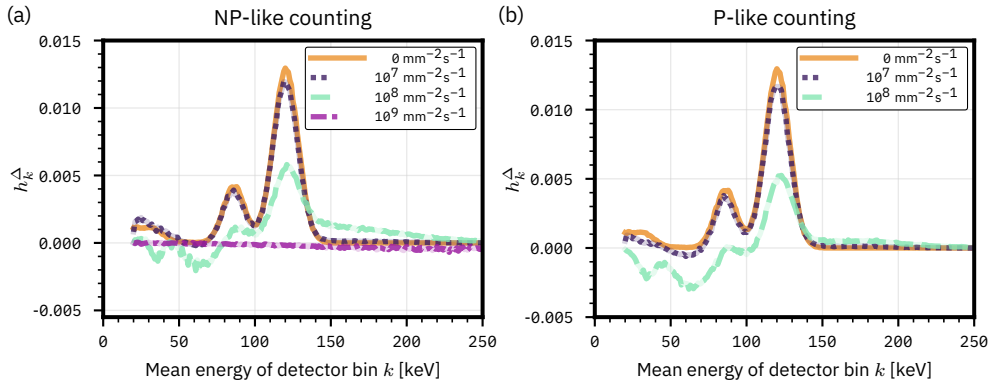

Figure 2.4: $h_k^\Delta(\Delta \boldsymbol{n} = \boldsymbol{0}, \dot{\boldsymbol{\Phi}}_{\text{op}}, E_l = 120\,\text{keV})$, that is, a slice of the pPSF h_k^Δ along all registering energy bins k in the centre pixel $\boldsymbol{n}_{\boldsymbol{0}}$ of the idealised indirect-conversion detector for an incident probe beam energy E_l of 120 keV. The figures show different total fluence rates of the operating spectrum $\dot{\boldsymbol{\Phi}}_{\text{op}}$, including the edge case of no operating spectrum, for (a) non-paralysable and (b) paralysable counting.

Figures 2.3 and 2.4 compare different fluence rates of the operating spectrum $\dot{\boldsymbol{\Phi}}_{\text{op}}$, including the edge case of no operating spectrum, under the assumption of a non-paralysable (a) or a paralysable (b) behaviour, for the iDCD and iICD, respectively. For both the iDCD and iICD detector, the incoming probe beam is most likely registered in the energy bin k of the same energy, barring the limited energy resolution. Furthermore, a K-escape peak is clearly visible, located 23 to 26 keV (Cd)/27 to 31 keV (Te) below the main photopeak in the case of the iDCD, and 33 to 38 keV (La) in the case of the iICD. The iICD also features a higher probability of the incoming beam being registered in the energy bins below 50 keV.
For fluence rates of up to 10^7 mm^{-2}s^{-1}, the detector responses change little compared to the limit of no operating spectrum being present. For higher fluence rates, however, the overall magnitude of h_k^Δ diminishes, which indicates an incipient saturation of the detector. Moreover, the incident probe beam starts to pile-up with the events already present in the operating spectrum, which means that higher energy bins may now register a count, while a count is at the same time removed from the low energy bins. As a consequence of the latter, the pPSF h_k^Δ can assume negative values, which can be prominently seen in case of the iICD detector under a fluence rate of 10^8 mm^{-2}s^{-1}. For very high fluence rates of 10^9 mm^{-2}s^{-1} and a non-paralysable behaviour, both detectors completely saturate. Due to the limitations of our implementation to calculate the pPSF, the data for a fluence rate of 10^9 mm^{-2}s^{-1} and a paralysable behaviour are not shown (see Section 2.A.1 in the Appendix for more information).
For a perfectly linear detector, i.e., a PCD with perfectly linear count rate behaviour, h_k^Δ would have a value of 1 at the photopeak and 0 everywhere else. Since the iICD detector exhibits a smaller geometric efficiency due to a smaller effective pixel size (380 µm) compared to the pixels of the iDCD (500 µm), the absolute values for the probability of adding/removing a count due to an incoming photon of the probe beam (with a cross section of 500 µm × 500 µm) are reduced compared to the iDCD.

While Figures 2.3 and 2.4 show a profile of h_k^Δ for a single incident probe beam energy E_l of 120 keV, Figures 2.5 and 2.6 show $h_k^\Delta(\Delta \boldsymbol{n} = \boldsymbol{0}, \dot{\boldsymbol{\Phi}}_{\text{op}}, E_l)$ for the iDCD and iICD, respectively; that is, h_k^Δ of the centre pixel $\boldsymbol{n}_{\boldsymbol{0}}$ for all tested incoming energies E_l and all registering energy bins k. The total fluence rates $\|\dot{\boldsymbol{\Phi}}_{\text{op}}\|_1$ of the operating spectrum vary from 0 (no operating spectrum

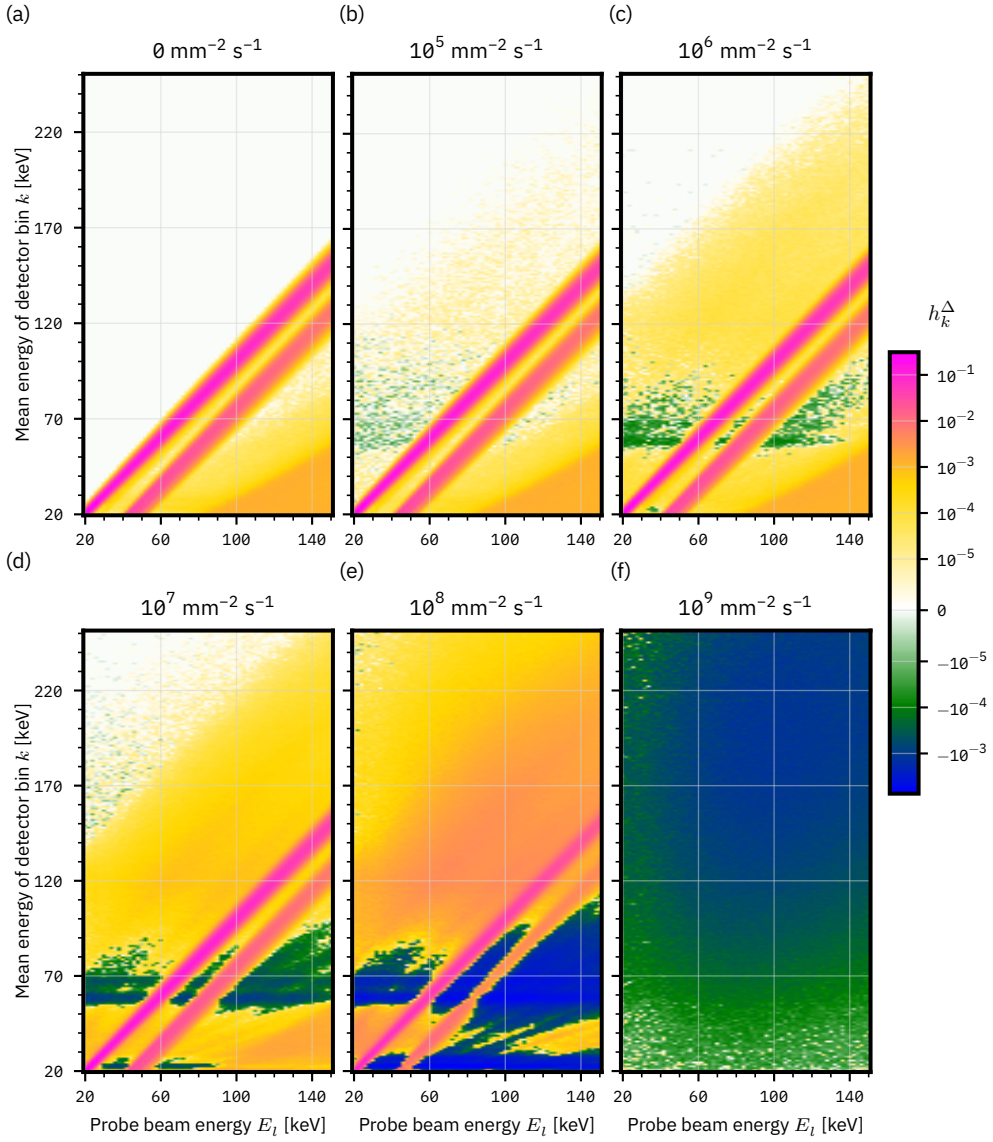

Figure 2.5: $h_k^\Delta(\Delta \boldsymbol{n} = \boldsymbol{0}, \dot{\boldsymbol{\Phi}}_{\text{op}}, E_l)$, that is, the pPSF h_k^Δ for all registering energy bins k and all simulated probe beam energies E_l in the centre pixel $\boldsymbol{n}_{\boldsymbol{0}}$ of the idealised direct-conversion detector. Here, a non-paralysable behaviour is assumed (see Figure 2.B.1 in the Appendix for the paralysable case). (a)–(f) The results for various total fluence rates of the operating spectrum $\dot{\boldsymbol{\Phi}}_{\text{op}}$, starting from the edge case of no operating spectrum up to a fluence rate of 10^9 mm^{-2}s^{-1}. The colour scale is chosen such that it includes the global minimum and maximum values.

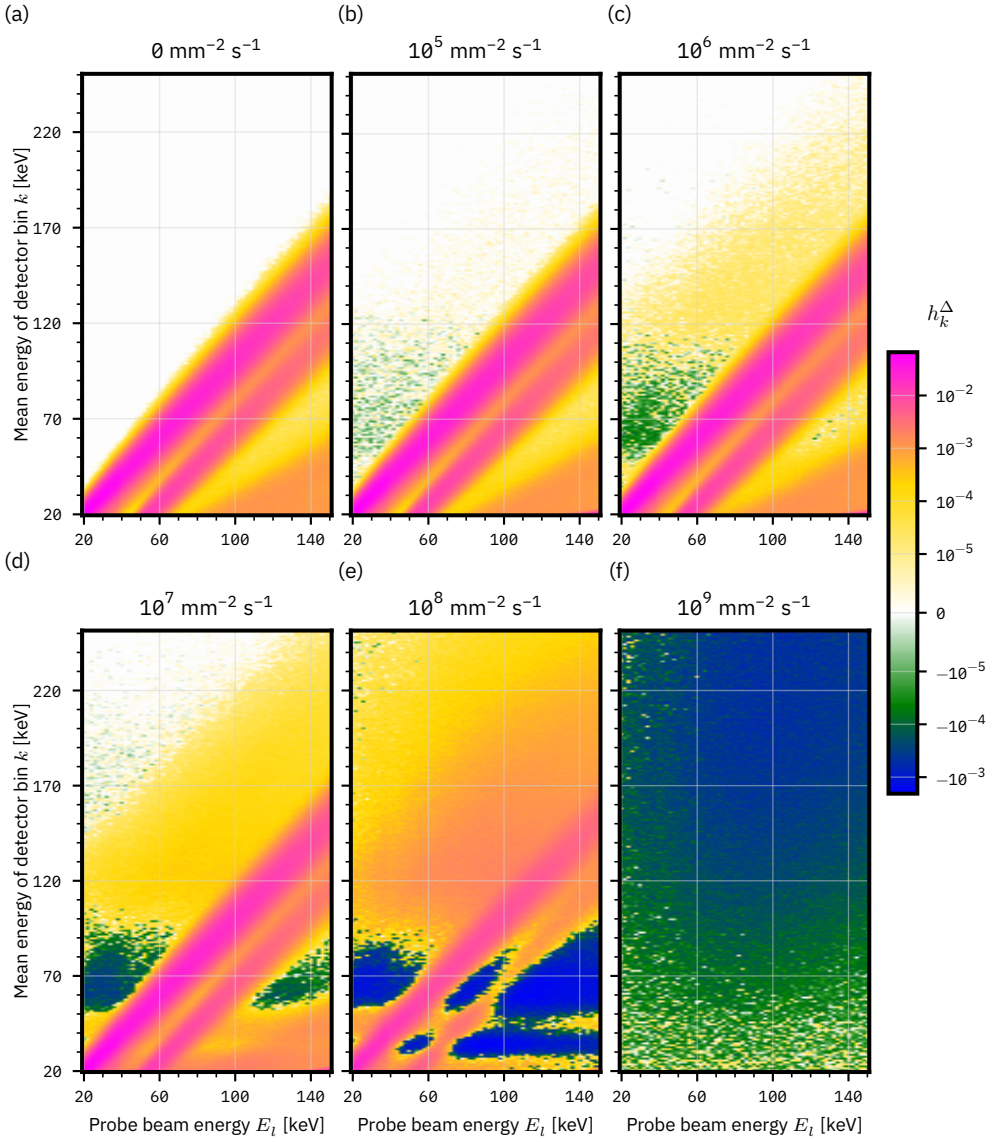

Figure 2.6: $h_k^\Delta(\Delta \boldsymbol{n} = \boldsymbol{0}, \dot{\boldsymbol{\Phi}}_{\text{op}}, E_l)$, that is, the pPSF h_k^Δ for all registering energy bins k and all simulated probe beam energies E_l in the centre pixel $\boldsymbol{n}_0$ of the idealised indirect-conversion detector. Here, a non-paralysable behaviour is assumed (see Figure 2.B.2 for the paralysable case). (a)–(f) The results for various total fluence rates of the operating spectrum $\dot{\boldsymbol{\Phi}}_{\text{op}}$, starting from the edge case of no operating spectrum up to a fluence rate of 10^9 mm^{-2}s^{-1}. The colour scale is chosen such that it includes the global minimum and maximum values.

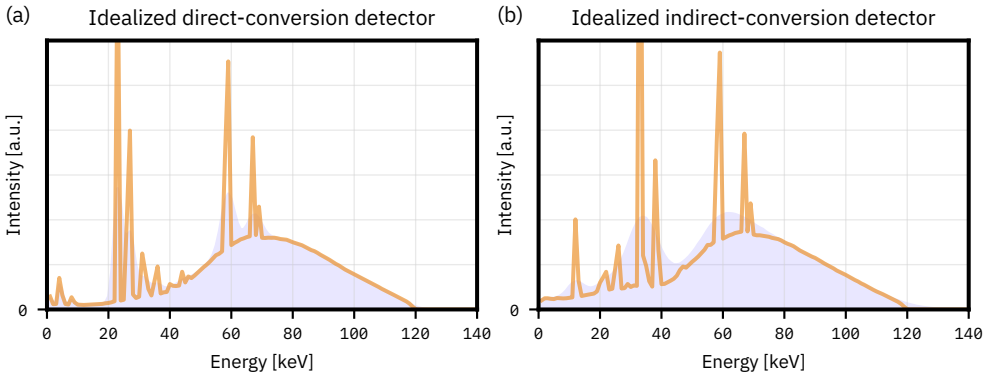

Figure 2.7: Energy spectra of deposited events (solid lines) in the idealised direct- (a) and indirect-conversion (b) detector due to the incident operating spectrum. The filled curves show the spectra of deposited events when taking into account the limited energy resolution of the iDCD (8 % at 59.5 keV) and the iICD (22.3 % at 59.5 keV). The standardised RQA9 spectrum serves as the operating spectrum. Note that the figures show the spectra of deposited events (with and without a given energy resolution), not the spectrum registered by a detector for a given total fluence rate of the operating spectrum.

present, (a)) to 10^9 mm^{-2}s^{-1} (f), assuming a paralysable behaviour. The two (pink) diagonal features in each figure (a)–(e) represent the photopeak and the accompanying K-escape peak, which are both broader in the iICD case due to the worse energy resolution. For fluence rates of the operating spectrum $\|\dot{\mathbf{\Phi}}_{\text{op}}\|_1 > 0$, we can see that the incoming probe beam piles up with events in the operating spectrum and hence causes counts in energy bins above the incoming probe beam energy. For both the iDCD and iICD, horizontal (green/blue) features are present with a high probability of removing counts (see for example Figure 2.5(d)). To understand these, the reader is referred to Figure 2.7, which shows the energy spectra of deposited events in the iDCD (a) and iICD (b), respectively, due to the incident RQA9 operating spectrum. It should be stressed that Figure 2.7 shows the spectra of deposited events with (filled curves) and without (solid lines) a given energy resolution, but not the spectrum registered by a detector for a given total fluence rate of the operating spectrum. A comparison of the spectra of deposited events (Figure 2.7) with the figures for h_k^{Δ} (Figures 2.5 and 2.6) reveals that the minima of h_k^{Δ}, i.e., the highest probability for removing events, are located in those energy bins where the operating spectrum exhibits local maxima, i.e., creates most events, as these are most likely to pile up with probe beam events. For a discussion on the spatial component of h_k^{Δ} along a row of detector pixels we refer to Section 2.B.1 in the Appendix.

2.4.2 Contrast and Contrast-to-Noise Ratio for Single Projection Line

Section 2.2.1 discussed how to obtain the contrast of a non-linear PCD when inserting a lesion with thickness x and mass density ρ along the projection. For comparison, in a perfectly linear PCD, the registered count rate in a certain energy bin is proportional to the total fluence rate $\|\dot{\mathbf{\Phi}}_{\text{op}}\|_1$ of the incoming operating spectrum, i.e., $d_k(\dot{\mathbf{\Phi}}_{\text{op}}) \sim \|\dot{\mathbf{\Phi}}_{\text{op}}\|_1$, and the absolute change of count rate due to an absolute change in the incoming spectrum, $\partial d_k(\dot{\mathbf{\Phi}}_{\text{op}})/\partial\dot{\Phi}_{E_l}$, is constant irrespective of the fluence rate $\|\dot{\mathbf{\Phi}}_{\text{op}}\|_1$. Furthermore, in a perfectly linear PCD each event is registered with its original energy. As a consequence, given our example (Section 2.3.8), the contrast of a perfectly linear PCD is simply proportional to $(\exp(-\mu(E)\cdot x) - 1)$ according to Equation 2.3, that is, the contrast follows the energy dependency of the X-ray attenuation of

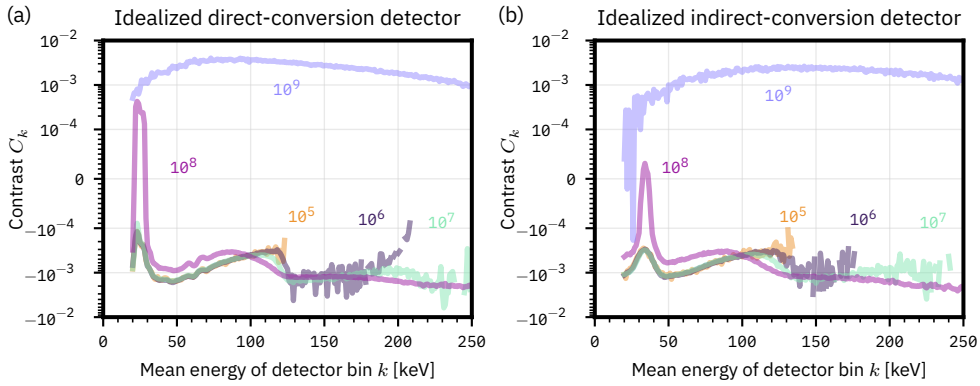

Figure 2.8: Contrast C_k due to the insertion of a small water/iodine lesion, with a product of the lesion's mass density and thickness of $\rho \cdot x = 0.0007$ g/cm^2. The contrast is shown over the registering energy bins k of 1 keV width and for incident total fluence rates of the operating spectrum $\dot{\mathbf{\Phi}}_{\text{op}}$ between 10^5 and 10^9 mm^{-2}s^{-1}; the numbers indicate the total fluence rate corresponding to each curve in mm^{-2}s^{-1}. For both the idealised direct- (a) and indirect-conversion (b) detector a non-paralysable-like behavior was assumed. Missing data points in energy bins above 120 keV are due to division by zero in Equation 2.3.

the lesion.

This result differs considerably from the behaviour of more realistic PCDs shown in Figure 2.8, based on the insertion of a water/iodine lesion as detailed in Section 2.3.8. It shows the contrast C_k calculated according to Equation 2.3, where the derivative $\partial d_k(\dot{\mathbf{\Phi}})/\partial \dot{\Phi}_{E_l}$ in Equation 2.3 corresponds to $h_k^{\Delta}(\boldsymbol{\Delta n},\, \dot{\mathbf{\Phi}}_{\text{op}},\, E_l) \cdot A$. The figure depicts C_k in each detector energy bin k for total fluence rates $\|\dot{\mathbf{\Phi}}_{\text{op}}\|_1$ of the operating spectrum between 10^5 and 10^9 mm^{-2}s^{-1}, assuming a non-paralysable behaviour for both the iDCD (a) and iICD (b) detector (see Figures 2.B.3 and 2.B.4 in the Appendix for the denominator and numerator of Equation 2.3, respectively), and again a near-continuous binning with bin widths of 1 keV.

Several observations can be made in Figure 2.8 for low to moderate total fluence rates of up to 10^7 mm^{-2}s^{-1}. First, the contrast is negative since the fluence rate in the case with inserted lesion is smaller than in the case without lesion (Equation 2.1). Second, the energy bins above the highest incident energy (120 keV in case of the RQA9 spectrum) exhibit on average a higher absolute value of contrast than those below. To understand this, we remind the reader that by definition the absolute value of contrast is highest for those bins in which a change in the incident fluence rate $\boldsymbol{\Delta}\dot{\mathbf{\Phi}}$ leads to the largest change in count rate. In the case of realistic PCDs with a finite pulse length and low to moderate fluence rate, most incoming photons will be registered in a bin of similar energy (deposition via photelectric effect) or smaller energy (K-escape, Compton/Rayleigh scattering); hence, the number of counts in those bins is already large (Figure 2.B.3 in the Appendix) and a change in fluence rate by $\boldsymbol{\Delta}\dot{\mathbf{\Phi}}$ yields only a small relative change in the number of counts in these bins. Due to the low probability of pile-up, however, there is a smaller number of counts in energy bins above the maximum incident energy to begin with; hence, a small absolute change in the number of pile-up events still translates to a large relative change in the number of counts in those bins, which in turn leads to a substantial increase in contrast.

Figure 2.8 furthermore shows that for high fluence rates larger than 10^7 mm^{-2}s^{-1} the contrast starts to switch signs. For example, the contrast at a fluence rate of 10^8 mm^{-2}s^{-1} exhibits both positive and negative values, depending on the energy bin. While Figure 2.8 is based on a hy-

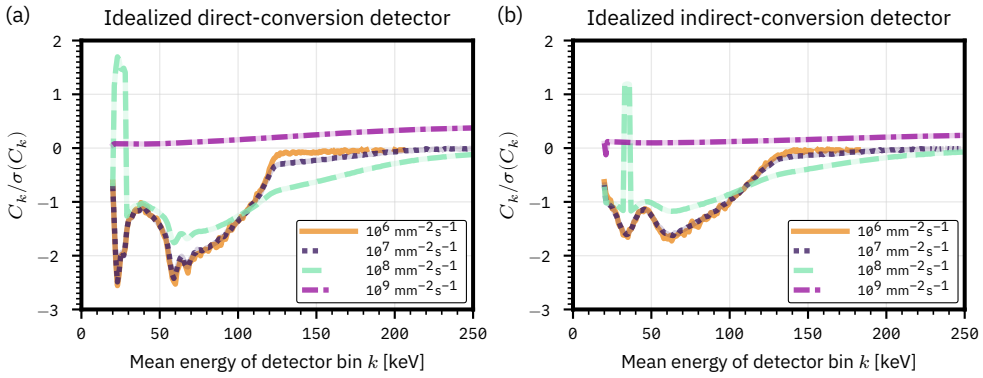

Figure 2.9: Contrast-to-noise ratio $C_k/\sigma(C_k)$ due to the insertion of a small water/iodine lesion, with a product of the lesion's mass density and thickness of $\rho \cdot x = 0.0007$ g/cm^2. The CNR is shown over the registering energy bins k of 1 keV width and for incident total fluence rates of the operating spectrum $\dot{\Phi}_{\text{op}}$ between 10^6 and 10^9 mm^{-2}s^{-1}. For both the idealised direct- (a) and indirect-conversion (b) detector a non-paralysable-like behaviour was assumed. Missing data points in energy bins above 120 keV are due to division by zero in Equation 2.3.

pothetical PCD with bin sizes of 1 keV, a realistic PCD exhibits bin sizes in the order of tens of keV. As a consequence, the resulting contrast in such a realistic macro energy bin might be reduced (contrast cancellation) or even inverted (contrast inversion) compared to the contrast at low fluence rates, where the exact extent of this effect depends on the specific location of the energy bin boundaries.
Finally, for a very high fluence rate of 10^9 mm^{-2}s^{-1} the severe pile-up will cause most events to be registered with an energy above 250 keV and concurrently a significant reduction in the number of counts for energy bins below 250 keV. As a result, the denominator in Equation 2.3 becomes very small, and in turn the absolute value for the contrast becomes very large.

This result may conflict the intuition that a detector should perform worse under conditions of severe pile-up. The cause for this discrepancy is that the above discussion was restricted to contrast only, whereas a clinically more relevant measure would be the CNR, which is shown in Figure 2.9. It shows the CNR $C_k/\sigma(C_k)$ of various fluence rates calculated for equal amounts of dose, as described in Section 2.3.8, for both the iDCD and iICD. The comparison between the iDCD and iICD shows that the maximum CNR achieved by the former is about 50 % higher than the CNR of the latter.
For energy bins below the highest incident energy, the absolute CNR value decreases with increasing fluence rate, whereas for energy bins higher than the highest incident energy the absolute CNR value increases with increasing fluence rate due to an increasing probability of pile-up. Furthermore, while the contrast at a fluence rate of 10^9 mm^{-2}s^{-1} exhibited the maximum absolute values, the CNR of the same fluence rate has now the smallest absolute values compared to all other fluence rates. The previous findings of contrast switching signs and the subsequent contrast reduction or contrast cancellation in realistic detectors with wider energy bins also translate to CNR.

For completion, while Figures 2.8 and 2.9 show contrast and CNR, respectively, assuming near-continuous energy bins with widths of 1 keV, Section 2.B.2 in the Appendix shows results using more realistic energy bin widths.

2.5 Discussion

The performance of the simulated idealised direct- and indirect-conversion detector shows similar trends across the presented results, with the differences mainly due to dissimilarities in energy resolution, pulse duration and geometric efficiency. For example, the CNR achieved by the iDCD in our example is about 50 % higher compared to that of the iICD. In our setup, the iICD compensates its longer intrinsic pulse length with a reduced geometry efficiency due to the reflective septa between pixels; however, this in turn also reduces the dose efficiency.

Figures 2.8 and 2.9 show that, depending on the fluence rate, contrast or CNR cancellation or inversion may occur. For a paralysable detector, this can be expected based on the count rate curve, which exhibits a maximum and therefore a point where its derivative and hence contrast becomes zero. However, Figures 2.8 and 2.9 are for a non-paralysable detector, which makes the explanation less intuitive: While the total count rate curve of a non-paralysable detector is monotonically increasing, this is not necessarily true for the count rate curve of individual energy bins, which may see a decrease in counts at certain fluence rates due to pile-up. Complex behaviour of the measured Hounsfield units over fluence rate has previously been reported by other authors [7, 15] and we hope that our framework may help to shed light on the underlying mechanisms.

Since the focus of this study is on the introduction of a framework to characterise PCD performance in the presence of non-linear effects and not on achieving a high degree of accuracy in the simulation of any specific PCD, we omitted some effects that are important for the full understanding of the operating characteristics of realistic PCDs. For example, we omitted charge sharing and a potential charge summing circuitry in the case of the direct-conversion detector, as well as light leakage due to insufficient optical isolation in case of the indirect-conversion detector, all of which affect pixel cross-talk. Hence, the only causes of cross-talk between pixels observed in our study are X-ray scatter and X-ray fluorescence, which is equivalent to a pixel array with perfect physical isolation of pixels, and hence suppressing any charge or light sharing. While the commonly used CZT/CdTe detectors exhibit a continuous layer of semiconducting material and hence do not physically isolate neighbouring pixels, an indirect-conversion detector array consisting of crystals with sufficiently thick septa, one-to-one coupled to an array of individual SiPMs and with perfect optical isolation, might come close to a detector without light leakage as modelled in our study.
We would like to add that, if charge sharing would be included for the direct-conversion detector, then based on the mean energy of 63 keV of the RQA9 background spectrum, an assumed diameter of the charge cloud of 29 µm (value for CdTe [35]), and our pixel size of 500 µm $\times$ 500 µm, 11 % of incoming events might be subject to charge sharing. This is only slightly less than the value of 18 % obtained for a pixel size of 275 µm $\times$ 322 µm, which is the pixel size used in the currently commercially available PCD CT scanners [17, 19]. While in both cases charge sharing would only affect a minority of events, theoretical studies [24, 26, 33] have shown that the number of events subject to charge sharing does not always correlate linearly with the effects on the estimated quantity of interest. For example, in a study by Taguchi [33] the variance on the estimate of the line integral of water in a water-bone material decomposition task was calculated for a direct-conversion PCD with and without charge sharing. Assuming a charge cloud diameter of 29 µm for the given 140 kVp spectrum, we estimate that in a 450 µm pixel about 12 % of events might be subject to charge sharing, and about 24 % for a 225 µm pixel. Taguchi showed that including the effect of charge sharing increases the variance on the line integral estimate by a factor of about 1.6 for a 450 µm pixel, whereas it increases by a factor of about 2.3 for a 225 µm pixel. For a full assessment of the effects of charge sharing in a specific detector on, e.g., contrast, CNR, or material decomposition, a detailed MC simulation study

would be needed.
While charge sharing is often seen as an essential component for a realistic simulation of direct-conversion detectors, the simulation of light leakage may be considered an equally important component for the realistic simulation of indirect-conversion detectors in cases where the optical isolation between pixels is not perfect. If light leakage occurs, it leads to a different distortion of the registered spectrum compared to charge sharing: common charge sharing models for direct-conversion detectors assume a size of the charge cloud proportional to the incident energy [35], which leads to a larger proportion of high energy events affected by charge sharing. Furthermore, depending on the ratio between the charge cloud size and the pixel size, some events are not subject to charge sharing at all. In indirect-conversion detectors, on the other hand, the scintillation photons are emitted isotropically and the proportion of photons leaking into neighbouring pixels is, at least in first-order approximation, independent of the location and energy of interaction, affecting all events similarly, potentially making this effect easier to correct for.

We would like to note that our framework itself is independent of the (number of) effects influencing detection that are taken into consideration, and it is merely a tool to investigate the results. Any effect influencing the registration of a count in a certain energy bin and pixel can be incorporated, as long as it can be attributed to a photon of an incoming probe beam. Our framework is most relevant, however, for characterising PCDs in the presence of non-linear effects, which, in our study, are caused by pile-up and the specific implementation of the counting algorithm. In PCDs with charge summing circuitry, further non-linear effects can emerge under high fluence rates, as documented by Ji et al [14].

While in this work we only studied the implications of pile-up on the measure of contrast and CNR, it seems feasible to apply the proposed framework of small-signal analysis to other commonly used measures of detector performance that are based on the PSF, such as the MTF or the frequency-dependent expressions for NEQ and DQE [23]. However, it cannot be used to correct count rate curves, since our model is inherently based on a small-signal analysis.
In related research, Alvarez [2, 3] investigated the invertibility and condition number of transforming energy-resolved data into the line integrals of basis set coefficients of an n-material basis. He showed that the transformation may become ill-conditioned for specific line integral values in combination with certain energy spectra [33] or in the presence of high pile-up [2]. In this work, we focus solely on the effect of fluence rate on the detector itself keeping the line integral fixed, without considering the transformation to material basis coefficient line integrals, and show that this can already lead to contrast inversion. This approach may aid in better disentangling the different effects that influence the stability of material decomposition in PCDs.

With this new theoretical framework we aim to contribute to a better insight into the performance of PCDs under clinically relevant operating conditions. It can be used to quantify the detrimental effects of pile-up on spectral and spatial performance of PCDs for a given incident spectrum and fluence rate. Thus, the new framework can be used as a tool in the design, development, and characterisation of PCDs and PCD-based systems.

2.6 Conclusion

In this work, we developed a framework to assess the non-linear spectral and spatial response of photon-counting detectors under pile-up conditions caused by high incident fluence rates. In the proposed framework small-signal analysis is employed, which approximates the non-linear behaviour of PCDs by a linear response around a certain operating point and describes

it by means of a so-called perturbation point spread function, which captures the spectral and spatial response of a PCD around that operating point. The operating point is determined by the spectral shape and the total fluence rate of the spectrum incident on the detector. As an example, we showed how the pPSF can be used to determine the contrast and the contrast-to-noise ratio measured by a PCD for an arbitrary lesion in the projection path. The example illustrates the influence of pile-up on contrast and CNR, which may include non-intuitive effects such as contrast or CNR inversion or cancellation within an energy bin or between energy bins, and which supports the community's efforts to achieve high intrinsic rate capabilities to avoid such effects in clinical images.

Code and Data Availability

The data used in this work, the Python code used for processing and evaluating the data, the code for creating the result plots as well as the plotted data can be found here: https://doi.org/10.4121/8ce1a22f-16a4-450e-b24a-775278cad7a1.

Acknowledgements

The authors would like to acknowledge the high performance computing clusters provided by the ICT department of TU Delft, and thank Ken Taguchi, Casper van Aarle, and Jack Wehr for fruitful discussions. Furthermore, we would like to thank the open source software community for creating GATE, GEANT4, PYTHON, NUMPY, UPROOT, JUPYTER, and all other open-source software that was directly or indirectly used in this work.

References

[1] J. Allison, K. Amako, J. Apostolakis, *et al.*, "Recent developments in Geant4", *Nuclear Instruments and Methods in Physics Research Section A: Accelerators, Spectrometers, Detectors and Associated Equipment*, vol. 835, pp. 186–225, 2016. DOI: 10.1016/j.nima.2016.06.125.

[2] R. Alvarez, "Non-Invertibility of spectral x-ray photon counting data with pileup", *arXiv:1702.04993 [astro-ph, physics:physics]*, 2017, http://arxiv.org/abs/1702.04993. arXiv: 1702.04993 [astro-ph, physics:physics].

[3] R. E. Alvarez, "Invertibility of the dual energy x-ray data transform", *Medical Physics*, vol. 46, no. 1, pp. 93–103, 2019. DOI: 10.1002/mp.13255.

[4] W. C. Barber, E. Nygard, J. S. Iwanczyk, *et al.*, "Characterization of a novel photon counting detector for clinical CT: Count rate, energy resolution, and noise performance", in *SPIE Medical Imaging*, E. Samei and J. Hsieh, Eds., Lake Buena Vista, FL, 2009, p. 725 824. DOI: 10.1117/12.813915.

[5] H. H. Barrett, K. J. Myers, and S. Dhurjaty, "Foundations of image science", *Journal of Electronic Imaging*, vol. 14, no. 2, p. 29 901, 2005.

[6] J. Cammin, J. Xu, W. C. Barber, J. S. Iwanczyk, N. E. Hartsough, and K. Taguchi, "A cascaded model of spectral distortions due to spectral response effects and pulse pileup effects in a photon-counting x-ray detector for CT", *Medical Physics*, vol. 41, no. 4, p. 041 905, 2014. DOI: 10.1118/1.4866890.

[7] J. R. Chen, T. N. Winfree, M. R. Bruesewitz, *et al.*, "Technical Note: Assessment of Pulse Pileup on Single-Energy and Multienergy Images From a Clinical Photon-Counting Detector Computed Tomography", *Journal of Computer Assisted Tomography*, vol. 48, no. 1, pp. 104–109, 2024. DOI: 10.1097/RCT.0000000000001534.

[8] I. E. Commission, *IEC 61267:2005 standard, Medical diagnostic X-ray equipment - Radiation conditions for use in the determination of characteristics*, https://webstore.iec.ch/publication/5079, 2005.

[9] M. Danielsson, M. Persson, and M. Sjölin, "Photon-counting x-ray detectors for CT", *Physics in Medicine & Biology*, vol. 66, no. 3, 03TR01, 2021. DOI: 10.1088/1361-6560/abc5a5.

[10] J. Fink, H. Krüger, P. Lodomez, and N. Wermes, "Characterization of charge collection in CdTe and CZT using the transient current technique", *Nuclear Instruments and Methods in Physics Research Section A: Accelerators, Spectrometers, Detectors and Associated Equipment*, vol. 560, no. 2, pp. 435–443, 2006. DOI: 10.1016/j.nima.2006.01.072.

[11] T. Flohr, M. Petersilka, A. Henning, S. Ulzheimer, J. Ferda, and B. Schmidt, "Photon-counting CT review", *Physica Medica*, vol. 79, pp. 126–136, 2020. DOI: 10.1016/j.ejmp.2020.10.030.

[12] F. Grönberg, M. Danielsson, and M. Sjölin, "Count statistics of nonparalyzable photon-counting detectors with nonzero pulse length", *Medical Physics*, vol. 45, no. 8, pp. 3800–3811, 2018. DOI: 10.1002/mp.13063.

[13] M. Janecek, "Reflectivity Spectra for Commonly Used Reflectors", *IEEE Transactions on Nuclear Science*, vol. 59, no. 3, pp. 490–497, 2012. DOI: 10.1109/TNS.2012.2183385.

[14] X. Ji, K. Treb, and K. Li, "Anomalous edge response of cadmium telluride-based photon counting detectors jointly caused by high-flux radiation and inter-pixel communication", *Physics in Medicine & Biology*, vol. 66, no. 8, p. 085006, 2021. DOI: 10.1088/1361-6560/abf1fe.

[15] S. Kappler, A. Henning, B. Kreisler, F. Schoeck, K. Stierstorfer, and T. Flohr, "Photon counting CT at elevated X-ray tube currents: Contrast stability, image noise and multi-energy performance", in *SPIE Medical Imaging*, B. R. Whiting and C. Hoeschen, Eds., San Diego, California, USA, 2014, p. 90331C. DOI: 10.1117/12.2043511.

[16] P. Lecoq, "Development of new scintillators for medical applications", *Nuclear Instruments and Methods in Physics Research Section A: Accelerators, Spectrometers, Detectors and Associated Equipment*, vol. 809, pp. 130–139, 2016. DOI: 10.1016/j.nima.2015.08.041.

[17] J. F. Marsh, P. D. VanMeter, K. Rajendran, S. Leng, and C. H. McCollough, "Ex vivo coronary calcium volume quantification using a high-spatial-resolution clinical photon-counting-detector computed tomography", *Journal of Medical Imaging*, vol. 10, no. 04, 2023. DOI: 10.1117/1.JMI.10.4.043501.

[18] Matt Newville, *XrayDB*, https://github.com/xraypy/XrayDB/.

[19] C. H. McCollough, K. Rajendran, S. Leng, *et al.*, "The technical development of photon-counting detector CT", *European Radiology*, vol. 33, no. 8, pp. 5321–5330, 2023. DOI: 10.1007/s00330-023-09545-9.

[20] H. Morita, T. Oshima, J. Kataoka, M. Arimoto, and H. Nitta, "Novel photon-counting low-dose computed tomography using a multi-pixel photon counter", *Nuclear Instruments and Methods in Physics Research Section A: Accelerators, Spectrometers, Detectors and Associated Equipment*, vol. 857, pp. 58–65, 2017. DOI: 10.1016/j.nima.2017.02.015.

[21] E. R. Paul, E. Y. Sidky, T. Gilat Schmidt, and X. Pan, "Stability of a spectral calibration model with non-linear intensity correction for photon-counting detectors", in *Medical Imaging 2021: Physics of Medical Imaging*, H. Bosmans, W. Zhao, and L. Yu, Eds., Online Only, United States: SPIE, 2021, p. 68. DOI: 10.1117/12.2581246.

[22] M. Persson, R. Bujila, P. Nowik, *et al.*, "Upper limits of the photon fluence rate on CT detectors: Case study on a commercial scanner", *Medical Physics*, vol. 43, no. 7, pp. 4398–4411, 2016. DOI: 10.1118/1.4954008.

[23] M. Persson, P. L. Rajbhandary, and N. J. Pelc, "A framework for performance characterization of energy-resolving photon-counting detectors", *Medical Physics*, vol. 45, no. 11, pp. 4897–4915, 2018. DOI: 10.1002/mp.13172.

[24] M. Persson, A. Wang, and N. J. Pelc, "Detective quantum efficiency of photon-counting CdTe and Si detectors for computed tomography: A simulation study", *Journal of Medical Imaging*, vol. 7, no. 04, p. 1, 2020. DOI: 10.1117/1.JMI.7.4.043501.

[25] G. Poludniowski, G. Landry, F. DeBlois, P. M. Evans, and F. Verhaegen, "SpekCalc: A program to calculate photon spectra from tungsten anode x-ray tubes", *Physics in Medicine and Biology*, vol. 54, no. 19, N433–N438, 2009. DOI: 10.1088/0031-9155/54/19/n01.

[26] P. L. Rajbhandary, S. S. Hsieh, and N. J. Pelc, "Effect of Spectral Degradation and Spatio-Energy Correlation in X-Ray PCD for Imaging", *IEEE Transactions on Medical Imaging*, vol. 37, no. 8, pp. 1910–1919, 2018. DOI: 10.1109/TMI.2018.2834369.

[27] A. Rose, *Vision: Human and Electronic* (Optical Physics and Engineering). New York: Plenum Press, 1973.

[28] D. Sarrut, M. Bardiès, N. Boussion, *et al.*, "A review of the use and potential of the GATE Monte Carlo simulation code for radiation therapy and dosimetry applications: GATE for dosimetry", *Medical Physics*, vol. 41, no. 6Part1, p. 064 301, 2014. DOI: 10.1118/1.4871617.

[29] D. Sato, M. Arimoto, K. Yoshiura, *et al.*, "Initial results of in vivo CT imaging of contrast agents using MPPC-based photon-counting CT", *Nuclear Instruments and Methods in Physics Research Section A: Accelerators, Spectrometers, Detectors and Associated Equipment*, vol. 1048, p. 167 960, 2023. DOI: 10.1016/j.nima.2022.167960.

[30] E. Y. Sidky, E. R. Paul, T. Gilat-Schmidt, and X. Pan, "Spectral calibration of photon-counting detectors at high photon flux", *Medical Physics*, vol. 49, no. 10, pp. 6368–6383, 2022. DOI: 10.1002/mp.15942.

[31] R. Steadman, C. Herrmann, and A. Livne, "ChromAIX2: A large area, high count-rate energy-resolving photon counting ASIC for a Spectral CT Prototype", *Nuclear Instruments and Methods in Physics Research Section A: Accelerators, Spectrometers, Detectors and Associated Equipment*, vol. 862, pp. 18–24, 2017. DOI: 10.1016/j.nima.2017.05.010.

[32] R. Steadman, C. Herrmann, O. Mülhens, and D. G. Maeding, "ChromAIX: Fast photon-counting ASIC for Spectral Computed Tomography", *Nuclear Instruments and Methods in Physics Research Section A: Accelerators, Spectrometers, Detectors and Associated Equipment*, vol. 648, S211–S215, 2011. DOI: 10.1016/j.nima.2010.11.149.

[33] K. Taguchi, "Assessment of Multienergy Interpixel Coincidence Counters (MEICC) for Charge Sharing Correction or Compensation for Photon Counting Detectors With Boxcar Signals", *IEEE Transactions on Radiation and Plasma Medical Sciences*, vol. 5, no. 4, pp. 465–475, 2021. DOI: 10.1109/TRPMS.2020.3003251.

[34] K. Taguchi, E. C. Frey, X. Wang, J. S. Iwanczyk, and W. C. Barber, "An analytical model of the effects of pulse pileup on the energy spectrum recorded by energy resolved photon counting x-ray detectors", *Medical Physics*, vol. 37, no. 8, pp. 3957–3969, 2010. DOI: 10.1118/1.3429056.

[35] K. Taguchi, C. Polster, O. Lee, K. Stierstorfer, and S. Kappler, "Spatio-energetic cross talk in photon counting detectors: Detector model and correlated Poisson data generator: Spatio-energetic cross talks in photon counting detectors", *Medical Physics*, vol. 43, no. 12, pp. 6386–6404, 2016. DOI: 10.1118/1.4966699.

[36] K. Taguchi, M. Zhang, E. C. Frey, *et al.*, "Modeling the performance of a photon counting x-ray detector for CT: Energy response and pulse pileup effects", *Medical Physics*, vol. 38, no. 2, pp. 1089–1102, 2011. DOI: 10.1118/1.3539602.

[37] J. Tanguay, D. Richtsmeier, C. Dydula, J. A. Day, K. Iniewski, and M. Bazalova-Carter, "A detective quantum efficiency for spectroscopic X-ray imaging detectors", *Medical Physics*, vol. 48, no. 11, pp. 6781–6799, 2021. DOI: 10.1002/mp.15194.

[38] S. J. van der Sar, S. Brunner, and D. Schaart, "X-ray photon-counting using silicon photomultiplier-based scintillation detectors at high x-ray tube currents", in *Medical Imaging 2022: Physics of Medical Imaging*, W. Zhao and L. Yu, Eds., vol. 12031, San Diego, United States: SPIE, 2022, p. 120310I. DOI: 10.1117/12.2611365.

[39] S. J. Van Der Sar, S. E. Brunner, and D. R. Schaart, "Silicon photomultiplier-based scintillation detectors for photon-counting CT: A feasibility study", *Medical Physics*, vol. 48, no. 10, pp. 6324–6338, 2021. DOI: 10.1002/mp.14886.

[40] S. J. Van Der Sar, D. Leibold, S. Brunner, and D. Schaart, "LaBr3:Ce and silicon photomultipliers: Towards the optimal scintillating photon-counting detector", in *7th International Conference on Image Formation in X-Ray Computed Tomography*, J. W. Stayman, Ed., vol. 12304, Baltimore, United States: Proc. SPIE, 2022, 123040A. DOI: 10.1117/12.2646519.

[41] E. V. D. van Loef, P. Dorenbos, C. W. E. van Eijk, K. Krämer, and H. U. Güdel, "High-energy-resolution scintillator: Ce3+ activated LaBr3", *Applied Physics Letters*, vol. 79, no. 10, pp. 1573–1575, 2001. DOI: 10.1063/1.1385342.

[42] L. Wielopolski and R. P. Gardner, "Prediction of the pulse-height spectral distortion caused by the peak pile-up effect", *Nuclear Instruments and Methods*, vol. 133, no. 2, pp. 303–309, 1976. DOI: 10.1016/0029-554X(76)90623-6.

[43] M. J. Willemink, M. Persson, A. Pourmorteza, N. J. Pelc, and D. Fleischmann, "Photon-counting CT: Technical Principles and Clinical Prospects", *Radiology*, vol. 289, no. 2, pp. 293–312, 2018. DOI: 10.1148/radiol.2018172656.

[44] J. Xu, W. Zbijewski, G. Gang, *et al.*, "Cascaded systems analysis of photon counting detectors: Cascaded systems analysis of photon counting detectors", *Medical Physics*, vol. 41, no. 10, p. 101 907, 2014. DOI: 10.1118/1.4894733.

Appendix
2.A Supplementary Methodology

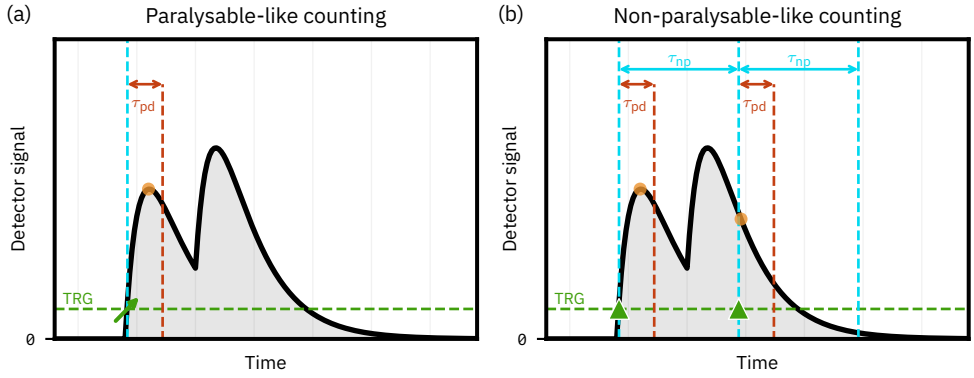

Figure 2.A.1: (a) Paralysable-like behaviour: After every positive trigger threshold crossing (green upward arrow) the maximum pulse height is determined (orange circle) within the peak detection time τ_{pd}. (b) Non-paralysable-like behaviour: If the signal is above the trigger threshold (green upwards triangles), an analysis window of length τ_{np} is started, and the maximum pulse height is determined (orange circles) within the peak detection time τ_{pd}. After the analysis window time elapsed, a new analysis window might start immediately.

2.A.1 Determination of h_k^{Δ}

Section 2.3.7 describes how to determine h_k^{Δ}, which involves irradiating the pixel array with the operating spectrum and registering the count rate $d_k(\boldsymbol{n}, \dot{\boldsymbol{\Phi}}_{\text{op}})$, as well as adding a monoenergetic probe beam to one pixel and registering the resulting count rate $d_k\left(\boldsymbol{n}, \dot{\boldsymbol{\Phi}}_{\text{op}} + \Delta\dot{\boldsymbol{\Phi}}_{E_l}^{\boldsymbol{n}_\emptyset}\right)$ in all other pixels (see Equation 2.6). This section will describe the implementation in more detail.

Fluence rate of the monoenergetic probe beam

The approximation of a non-linear detector response as linear around a certain operating point (such that it can be described via the pPSF h_k^{Δ}) is only valid as long as the perturbation by the probe beam is sufficiently small. For this, the fluence rate of the monoenergetic probe beam $\Delta\dot{\boldsymbol{\Phi}}_{E_l}^{\boldsymbol{n}_\emptyset}$ has to be low enough so that the likelihood of pile-up between events of the probe beam remains negligible, which ensures that each incident probe beam event can unambiguously be matched to a change in count rates. From this condition follows that the pile-up probabilities for $\dot{\boldsymbol{\Phi}}_{\text{op}}$ and $\dot{\boldsymbol{\Phi}}_{\text{op}} + \Delta\dot{\boldsymbol{\Phi}}_{E_l}^{\boldsymbol{n}_\emptyset}$ have to be approximately equal.

Efficient evaluation of h_k^{Δ}

Figure 2.A.2 schematically shows the idea of how to efficiently evaluate h_k^{Δ}. The straight forward approach to evaluate h_k^{Δ} while fulfilling the condition to ensure linearity within the small-signal approach would be to dilate the probe beam pulse train (red) significantly (Figure 2.A.2b, bottom row). However, this would mean that, in order to gain sufficient statistics, the pulse train to be evaluated would be prohibitively long. Since the pulse train of the operating spectrum (blue) is not sufficiently long to cover the dilated probe beam pulse train, the operating spectrum could be repeated (Figure 2.A.2b, top row). For a sufficiently dilated probe beam pulse train, the resulting scenario is equivalent to using the original operating spectrum pulse

2

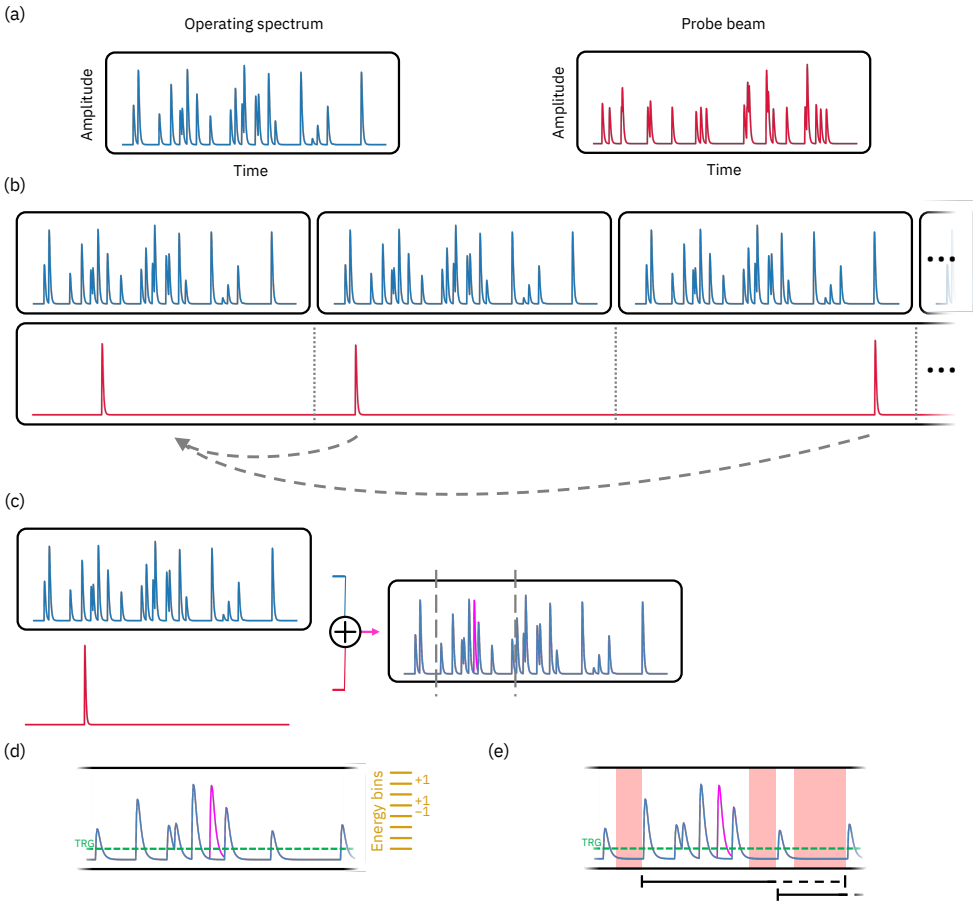

Figure 2.A.2: Schematic overview of the implementation to determine h_k^{Δ}. (a) Operating spectrum pulse train (blue) and probe beam pulse train (red). To ensure linearity within the small-signal approach when adding the probe beam (see text), the time stamps of the probe beam have to be dilated significantly ((b), bottom row). Since the pulse train of the operating spectrum is not sufficiently long to cover the dilated probe beam pulse train, the operating spectrum pulse train is repeated ((b), top row). The resulting scenario is equivalent to using the operating spectrum's original pulse train and adding each of the probe beam events one by one ((c), showing only one probe beam event). (d) First the pulse train of the operating spectrum is evaluated, then the combined pulse train of operating spectrum plus probe beam, and the difference in the counts in energy bins is saved. Since most of the pulse train will stay unaffected by the addition of a single probe beam event, it is sufficient to only evaluate a small region around the probe beam's time stamp. We therefore search for gaps in the pulse train (marked red in (e)) which are large enough to ensure that any change to the pulse train by adding one event within two gaps is unable to change the pulse train after the gaps. See text for further explanations.

train once and adding each of the probe beam events one by one (Figure 2.A.2c left, showing only one probe beam event). Figure 2.A.2d shows a part of the resulting pulse train (pink) around the time stamp of the probe beam event (vertical dashed lines in Figure 2.A.2c, right). In each iteration first the pulse train of the operating spectrum is evaluated with the selected counting behaviour (resulting into $d_k(\boldsymbol{n}, \dot{\boldsymbol{\Phi}}_{\text{op}})$), then the combined pulse train of the operating spectrum plus the pulse train is evaluated (resulting into $d_k\left(\boldsymbol{n}, \dot{\boldsymbol{\Phi}}_{\text{op}} + \Delta\dot{\boldsymbol{\Phi}}_{E_l}^{\boldsymbol{n}_0}\right)$), and the difference in the counts in all energy bins is saved.
However, evaluating the whole pulse train for just one added probe beam event is still computationally very expensive, especially considering the fact that most of the pulse train will stay unaffected by the addition of a single probe beam event. Hence, it is sufficient to only evaluate a small region around the probe beam's time stamp (Figure 2.A.2c right, vertical dashed lines). In our implementation, we search for naturally occurring gaps in the operating spectrum pulse train (marked red in Figure 2.A.2e), dividing the pulse train into smaller clusters. The size of the gaps is equal to the length of a pulse, sufficient that a single additional event added to one cluster is unable to affect the pulse train after two clusters and two gaps. This approach enables us to evaluate pairs of clusters separately, i.e., superimposing the monoenergetic probe beam events one by one and calculating h_k^{Δ} for one cluster for each added event. Two neighbouring clusters (brackets in Figure 2.A.2e) were combined for the evaluation of a single monoenergetic probe beam event. Monoenergetic events were added which occurred during the first cluster including the subsequent gap (solid part of the bracket); the second cluster (dashed part of the bracket) was included since a monoenergetic probe beam event added to the first cluster (plus gap) could change the registered counts up to and including the second cluster, but not beyond the gap after the second cluster. With this approach it is computationally feasible to determine h_k^{Δ} for a large number of monoenergetic probe beams and a large number of pixels. We validated our approach by comparing it to the straight-forward implementation shown in Figure 2.A.2b.
In case the fluence rate of the operating spectrum was so high that no or only few and large clusters were formed, the pulse train was artificially split in order to accelerate the simulation; this was only necessary for a total fluence rate of 10^9 mm^{-2}s^{-1}. However, such artificial splitting introduces additional trigger events in the case of P-like counting, which appeared to be the only source of trigger events at this fluence rate. Hence, the data for P-like counting at a total fluence rate of 10^9 mm^{-2}s^{-1} was not included in the analysis of results.

2.A.2 Variance of Contrast

The variance of the contrast was calculated using error propagation. Starting from the formula for contrast,

$$C_k = \frac{\sum_l h_k^{\Delta}(\boldsymbol{\Delta n} = \boldsymbol{0}, \dot{\boldsymbol{\Phi}}_{\text{op}}, E_l) \cdot \Delta\dot{\Phi}_{E_l} \cdot A}{d_k(\dot{\boldsymbol{\Phi}}_{\text{op}})} \quad , \tag{2.A.1}$$

the variance on C_k caused by the variance on d_k can be calculated as follows:

$$\text{Var}(C_k) = \left(\frac{\partial\, C_k}{\partial\, d_k}\right)^2 \text{Var}(d_k) \quad . \tag{2.A.2}$$

Here, we neglected the influence by the change in fluence rate $\Delta\dot{\boldsymbol{\Phi}}$ on the variance, since, firstly, our investigation showed that this contribution to the variance of C_k is negligible compared to the variance due to d_k , and, secondly, the physical intuition is that, in order to determine the CNR ratio, the variance is measured in a region consisting only of background, and the variance in this region is purely governed by the case that no lesion is present, i.e., $\text{Var}(d_k)$.

Inserting Equation 2.A.1 into Equation 2.A.2 results in:

$$\mathrm{Var}(C_k) = \left(\frac{\sum_l h_k^{\Delta}(\boldsymbol{\Delta n} = \mathbf{0},\, \dot{\boldsymbol{\Phi}}_{\mathrm{op}},\, E_l) \cdot \Delta\dot{\Phi}_{E_l} \cdot A}{d_k^2(\dot{\boldsymbol{\Phi}}_{\mathrm{op}})} \right)^2 \mathrm{Var}(d_k) \quad , \tag{2.A.3}$$

where $\mathrm{Var}(d_k)$ is equal to the mean of d_k . While this assumption holds only for Poisson-distributed data, it was checked that despite the non-linear behaviour of a PCD the variance of d_k in our simulation study is indeed equal to its mean over the whole range of investigated fluence rates.

2.B Supplementary Results and Discussion

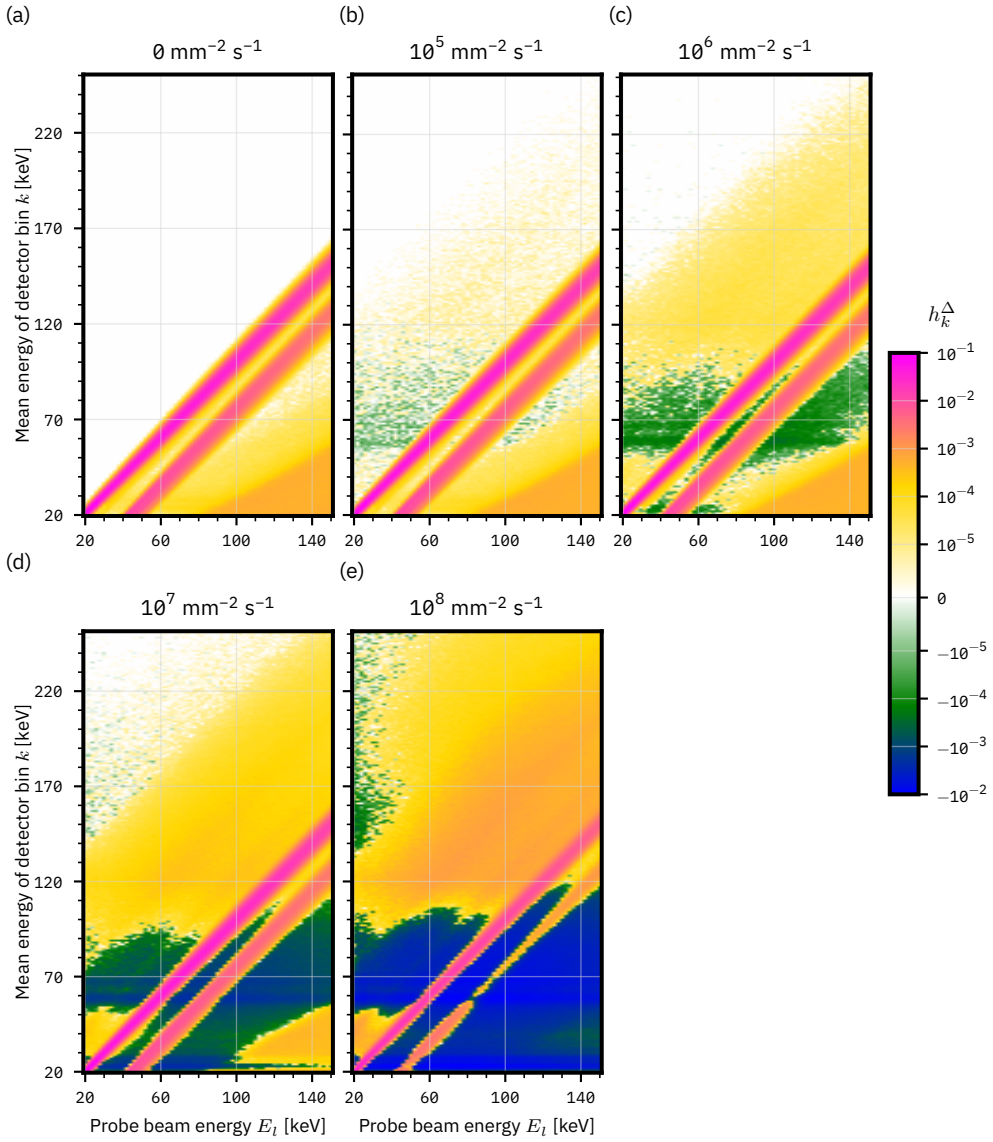

Figure 2.B.1: $h_k^{\Delta}(\boldsymbol{\Delta n} = \mathbf{0}, \dot{\boldsymbol{\Phi}}_{\text{op}}, E_l)$, that is, the pPSF h_k^{Δ} for all registering energy bins k and all simulated probe beam energies E_l in the centre pixel $\boldsymbol{n}_{\mathbf{0}}$ of the idealised direct-conversion detector. Here, a paralysable behaviour is assumed. (a)–(f) The results for various total fluence rates of the operating spectrum $\dot{\boldsymbol{\Phi}}_{\text{op}}$, starting from the edge case of no operating spectrum up to a fluence rate of 10^8 mm^{-2}s^{-1}. The colour scale is chosen such that it includes the global minimum and maximum values.

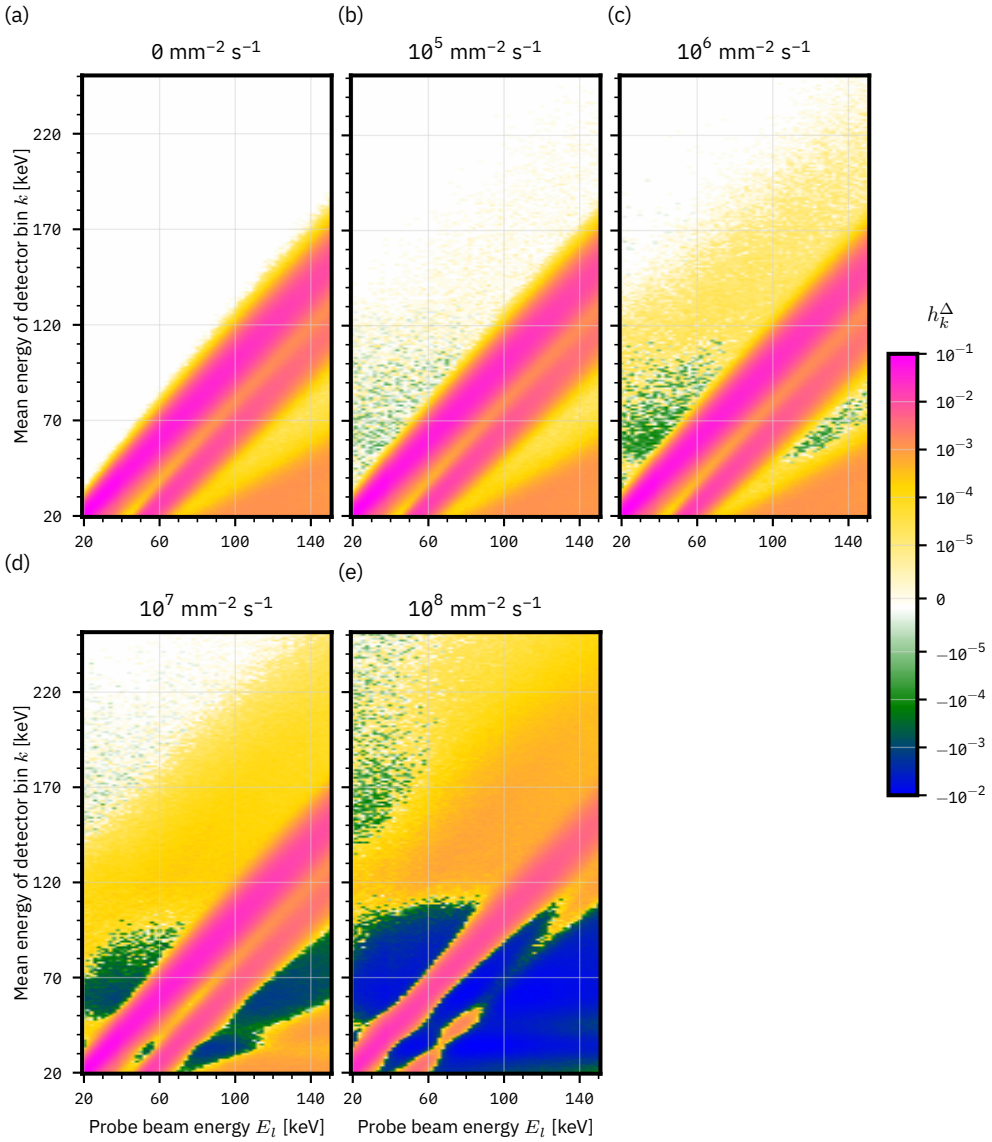

Figure 2.B.2: $h_k^{\Delta}(\boldsymbol{\Delta n} = \boldsymbol{0}, \dot{\boldsymbol{\Phi}}_{\text{op}}, E_l)$, that is, the pPSF h_k^{Δ} for all registering energy bins k and all simulated probe beam energies E_l in the centre pixel $\boldsymbol{n}_0$ of the idealised indirect-conversion detector. Here, a paralysable behaviour is assumed. (a)–(f) The results for various total fluence rates of the operating spectrum $\dot{\boldsymbol{\Phi}}_{\text{op}}$, starting from the edge case of no operating spectrum up to a fluence rate of 10^8 mm^{-2}s^{-1}. The colour scale is chosen such that it includes the global minimum and maximum values.

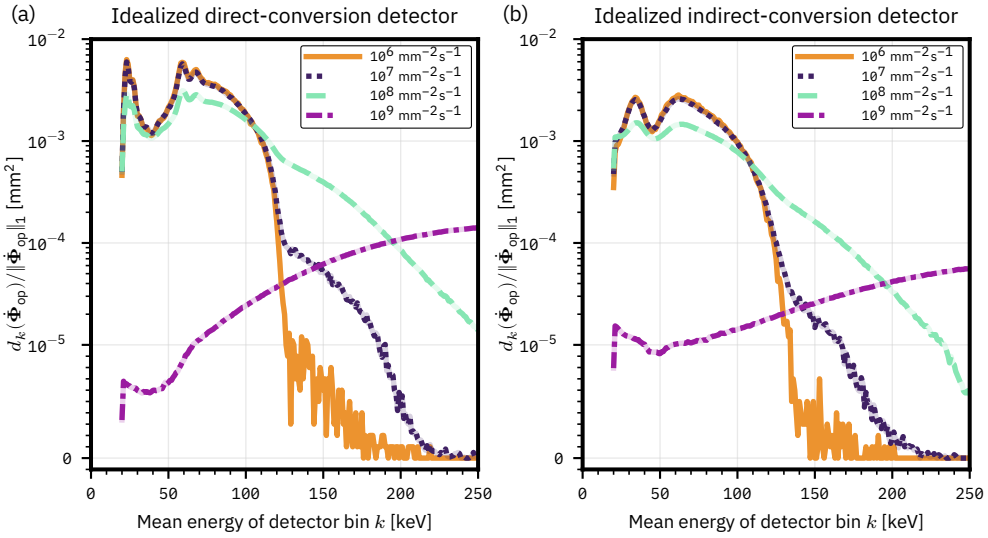

Figure 2.B.3: $d_k(\dot{\Phi}_{\text{op}})/\|\dot{\Phi}_{\text{op}}\|_1$, that is, the count rate in detector bin k of one pixel divided by the total fluence rate, for different fluence rates of the operating spectrum. Result for (a) the idealised direct-conversion detector and (b) for the idealised indirect-conversion detector, both with a non-paralysable counting behaviour.

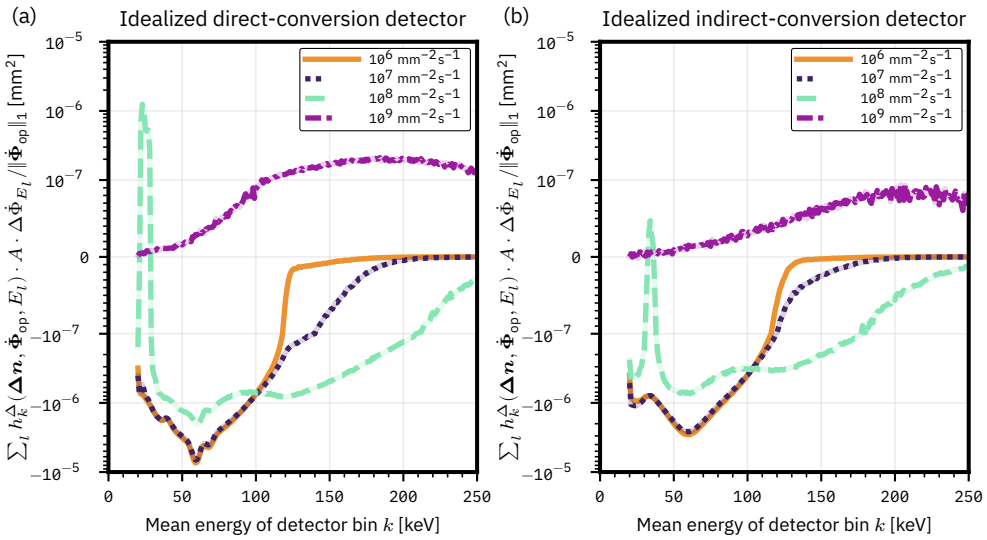

Figure 2.B.4: $\sum_l h_k^{\Delta}(\boldsymbol{\Delta n}, \dot{\Phi}_{\text{op}}, E_l) \cdot A \cdot \Delta\dot{\Phi}_{E_l}/\|\dot{\Phi}_{\text{op}}\|_1$, that is, the numerator of Equation 2.3 divided by the total fluence rate, for different fluence rates of the operating spectrum. Result for (a) the idealised direct-conversion detector and (b) for the idealised indirect-conversion detector, both with a non-paralysable counting behaviour. The water/iodine lesion is assumed to be characterised by $\rho \cdot x = 0.0007$ g/cm^2.

2.B.1 h_k^{Δ} for a Row of Pixels

Figures 2.B.5 and 2.B.6 show how h_k^{Δ} varies for a row of pixels of a detector array, including the centre pixel receiving the probe beam. Figure 2.B.5 (b – e) and Figure 2.B.6 (b – e) show $h_k^{\Delta}(\boldsymbol{\Delta n}, \dot{\boldsymbol{\Phi}}_{\text{op}}, E_l)$, that is, the pPSF h_k^{Δ} for all registering energy bins k and all simulated probe beam energies E_l of the idealised direct-conversion and the idealised indirect-conversion detector, respectively. The schematic in Figure 2.B.5a and 2.B.6a indicates the position of the pixels whose pPSF is shown. A paralysable counting behaviour and a total fluence rate of the operating spectrum $\dot{\boldsymbol{\Phi}}_{\text{op}}$ of 10^6 mm^{-2}s^{-1} is assumed.

For the discussion of the pPSF of the centre pixel we refer to Section 2.4 of the paper. As can be seen in Figures 2.B.5 (c – e) and 2.B.6 (c – e), the probe beam incident on the centre pixel can be registered in the neighbouring pixels via either K-fluorescence events, which explains the features around energy bins at 23 – 31 keV (Cd, Te) in Figure 2.B.5 (c – e) and around 33 – 38 keV (La) in Figure 2.B.6 (c – e), or via Compton/Rayleigh scatter events that preserve most of the initial photon's energy (diagonal features in (c – e)).

Figures 2.B.5f and 2.B.6f show how a probe beam with a white spectrum, i.e., all energies E_l are equally likely, is registered by a row of detector pixels centred around the centre pixel receiving the probe beam, for various fluence rates. The plot then gives the probability that a photon of the incoming probe beam is detected in any energy bin of the respective pixel; this is analogous to summing $h_k^{\Delta}(\boldsymbol{\Delta n}, \dot{\boldsymbol{\Phi}}_{\text{op}}, E_l)$ for each pixel and normalising it by the number of energies in the probe beam. Due to the large pixel size of 500 µm, the probability of registering a count in one of the pixels adjacent to the centre pixel decreases rapidly (please note the log scale of the plot). The probability of detecting a photon from the probe beam in any energy bin of a pixel stays mostly constant for all except the highest fluence rates. This is because for our idealised detectors the spatial distribution of the deposition of energy is governed by X-ray transport only, and although an increase in pile-up due to an increased fluence rate of the operating spectrum changes the registered spectrum, most events are still registered in some energy bin. As a consequence, the probability for detecting a probe beam photon in any energy bin stays mostly constant for all except the highest fluence rates, for which the detector goes into saturation and counts are missed.

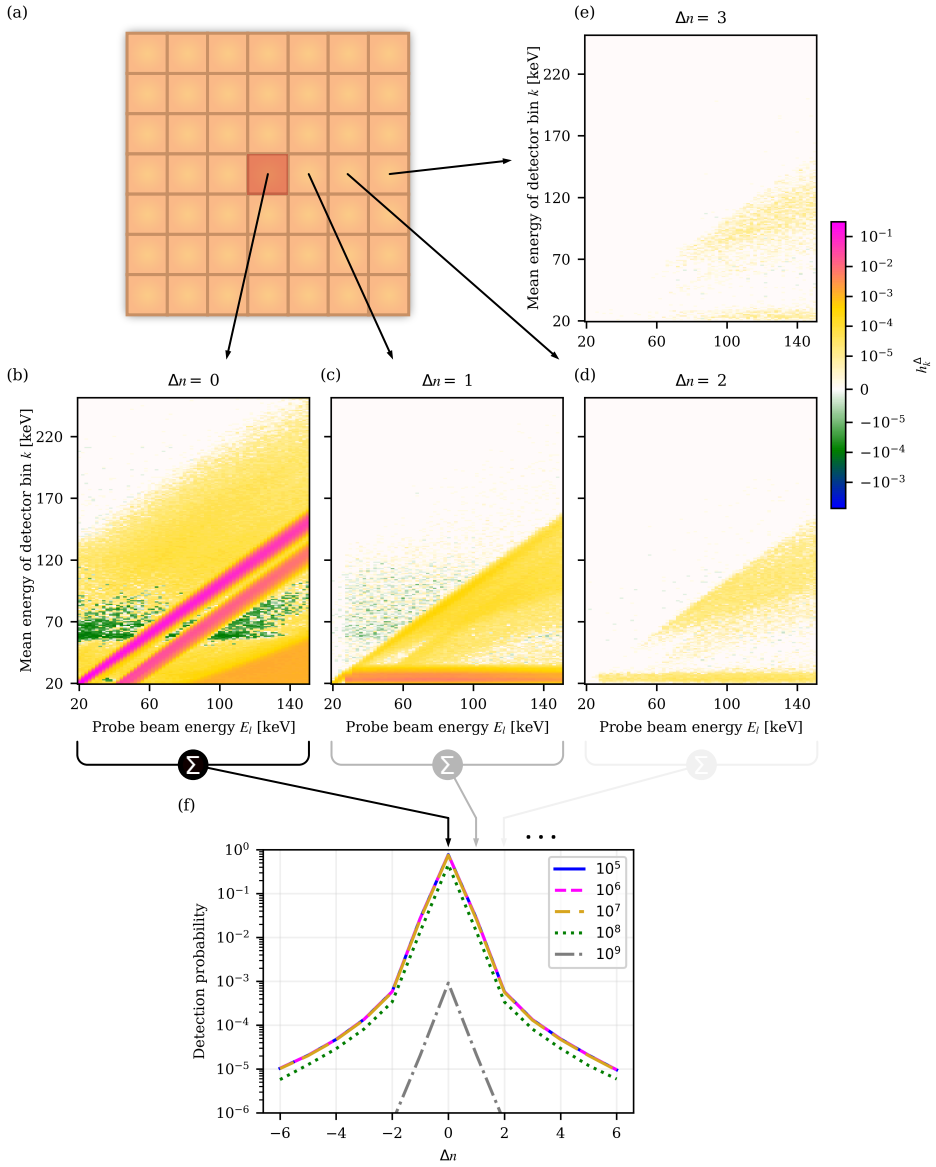

Figure 2.B.5: $h_k^{\Delta}(\boldsymbol{\Delta n}, \dot{\boldsymbol{\Phi}}_{\mathrm{op}}, E_l)$, that is, the pPSF h_k^{Δ} for all registering energy bins k and all simulated probe beam energies E_l of the idealised direct-conversion detector, for the centre pixel ($\Delta \boldsymbol{n} = \boldsymbol{0}$, (b)) and three neighbouring pixels (c – e) as indicated in the schematic (a). Here, a paralysable counting behaviour and a total fluence rate of the operating spectrum $\dot{\boldsymbol{\Phi}}_{\mathrm{op}}$ of 10^6 mm^{-2}s^{-1} is assumed. (e) shows the pPSF for the indicated fluence rates under the assumption that the incident probe beam has a white spectrum, i.e., all energies are equally likely, for a row of pixels (centre pixel as well 6 neighbouring pixels on both sides). (e) then gives the probability that a photon of the incoming probe beam is detected in any energy bin of the neighbouring pixels. This is analogous to summing over $h_k^{\Delta}(\boldsymbol{\Delta n}, \dot{\boldsymbol{\Phi}}_{\mathrm{op}}, E_l)$ for each pixel and normalising by the number of energies in the probe beam spectrum.

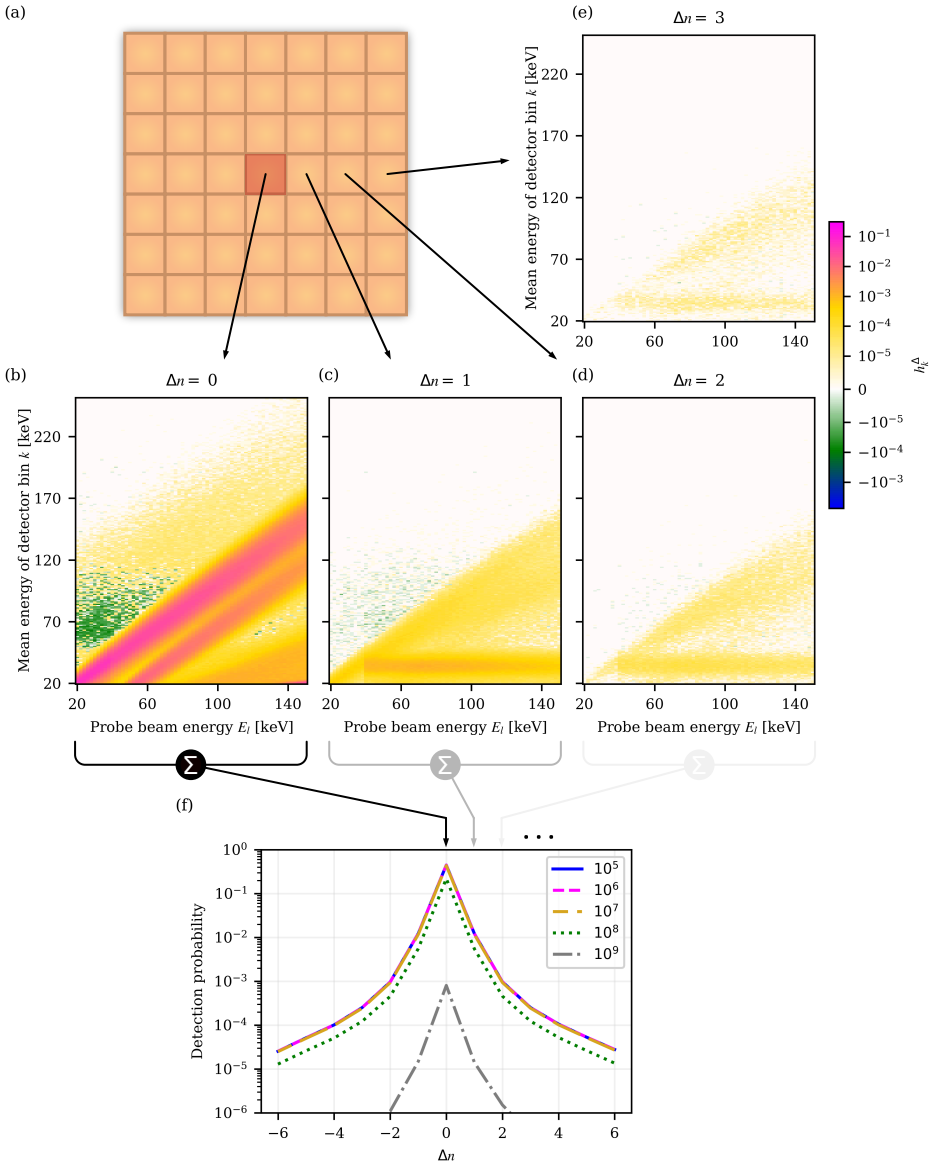

Figure 2.B.6: $h_k^{\Delta}(\boldsymbol{\Delta n},\, \dot{\boldsymbol{\Phi}}_{\mathrm{op}},\, E_l)$, that is, the pPSF h_k^{Δ} for all registering energy bins k and all simulated probe beam energies E_l of the idealised indirect-conversion detector, for the centre pixel ($\Delta \boldsymbol{n} = \boldsymbol{0}$, (b)) and three neighbouring pixels (c – e) as indicated in the schematic (a). Here, a paralysable counting behaviour and a total fluence rate of the operating spectrum $\dot{\boldsymbol{\Phi}}_{\mathrm{op}}$ of 10^6 mm^{-2}s^{-1} is assumed. (e) shows the pPSF for the indicated fluence rates under the assumption that the incident probe beam has a white spectrum, i.e., all energies are equally likely, for a row of pixels (centre pixel as well 6 neighbouring pixels on both sides). (e) then gives the probability that a photon of the incoming probe beam is detected in any energy bin of the neighbouring pixels. This is analogous to summing over $h_k^{\Delta}(\boldsymbol{\Delta n},\, \dot{\boldsymbol{\Phi}}_{\mathrm{op}},\, E_l)$ for each pixel and normalising by the number of energies in the probe beam spectrum.

2.B.2 CNR for Realistic Energy Bin Widths

While Figure 2.8 (Figure 2.9) shows the contrast (CNR) assuming energy bins with widths of 1 keV, Table 2.B.1 (Table 2.B.2) lists the contrast (CNR) obtained when a more realistic energy binning is applied (see Equation 2.3). It compares the results for a low energy bin of [20; 65) keV (including lower boundary, excluding upper boundary), and two high energy bins of either [65; 120) keV, that is, including events up to the highest photon energy emitted by the source, or [65; 250] keV, that is, including also pile-up events.

In the case of contrast, for an energy bin of [20; 65) keV the value of the contrast first drops in magnitude and then switches sign if the fluence rate of the operating spectrum is increased, whereas for energy bins of [65; 120) keV and [65; 250) keV the contrast first increases in magnitude due to the influence of pile-up and then switches sign.

In the case of CNR, for energy bins of [20; 65) keV and [65; 120) keV the value of the CNR first drops in magnitude and then switches sign if the fluence rate of the operating spectrum is increased, whereas for an energy bin of [65; 250) keV the CNR first increases in magnitude due to the influence of pile-up and then switches sign.

Table 2.B.1: Contrast C_k due to the insertion of a small water/iodine lesion for realistic energy bins for both the idealised direct-conversion detector (iDCD) and idealised indirect-conversion detector (iICD). The table shows the results for three realistic energy bins with the given intervals, and for incident total fluence rates of the operating spectrum $\dot{\mathbf{\Phi}}_{\text{op}}$ between $10^6 - 10^9$ mm^{-2}s^{-1}. For both detectors, a non-paralysable-like behaviour was assumed. The lesion is assumed to be characterised by $\rho \cdot x = 0.0007$ g/cm^2.

Fluence rate [mm^{-2}s^{-1}]	Energy bin intervals [keV]					
	iDCD			iICD		
	[20; 65)	[65; 120)	[65; 250)	[20; 65)	[65; 120)	[65; 250)
10^6	−0.050	−0.029	−0.109	−0.039	−0.029	−0.081
10^7	−0.048	−0.031	−0.215	−0.039	−0.030	−0.160
10^8	−0.024	−0.027	−0.227	−0.017	−0.026	−0.240
10^9	0.093	0.198	0.474	0.029	0.108	0.379

Table 2.B.2: Contrast-to-noise ratio $C_k/\sigma(C_k)$ due to the insertion of a small water/iodine lesion for realistic energy bins for both the idealised direct-conversion detector (iDCD) and idealised indirect-conversion detector (iICD). The table shows the results for three realistic energy bins with the given intervals, and for incident total fluence rates of the operating spectrum $\dot{\mathbf{\Phi}}_{\text{op}}$ between $10^6 - 10^9$ mm^{-2}s^{-1}. For both detectors, a non-paralysable-like behaviour was assumed. The lesion is assumed to be characterised by $\rho \cdot x = 0.0007$ g/cm^2.

Fluence rate [mm^{-2}s^{-1}]	Energy bin intervals [keV]					
	iDCD			iICD		
	[20; 65)	[65; 120)	[65; 250)	[20; 65)	[65; 120)	[65; 250)
10^6	−73	−84	−90	−61	−62	−68
10^7	−72	−83	−101	−60	−61	−73
10^8	−35	−74	−128	−39	−51	−85
10^9	3.7	7.8	47	4.4	6.3	31

Chapter 3

Optimising Proton Stopping Power Ratio Prediction with Spectral Cone-Beam CT

Objective: Cone-beam computed tomography (CBCT) is used for patient positioning in proton therapy, but not directly for treatment planning due to its inferior image quality compared to fan-beam CT. One way to improve its value for proton radiotherapy might be to use CBCT setups capable of extracting spectral information, which can be realised through several hardware configurations. Here, we compare different setups with respect to to their capability of predicting proton stopping power ratios (SPRs).
Methods: We investigate six different spectral CBCT realisations in a simulation study, namely a single-source setup with either a dual-layer detector or a photon-counting detector (PCD), a kVp-switching setup with either an energy-integrating detector (EID) or a PCD, and a dual-source setup with either EIDs or PCDs. Our figure of merit is the normalised Cramér-Rao Lower Bound (nCRLB) on SPR variance based on projection data. We take (cross-)scatter into account, and compare ideal and realistic detector models to help guide future detector developments. Each setup is optimised with respect to source spectra, mAs ratios, energy bin settings and layer thicknesses (where applicable).
Results: Assuming a realistic detector response, setups with a kVp-switching source perform best, with the setup paired with an EID slightly outperforming the PCD-based setup (nCRLBs of 2.74 and 2.81, respectively). However, if the mAs ratio of the kVp-switching source is fixed, the performance of the kVp-switching setup with an EID is significantly degraded (nCRLB = 9.46) and outperformed by PCD-based setups, with nCRLBs of 3.27, 3.45 and 3.60 for the dual-source setup with two PCDs, the single-source setup and the kVp-switching setup with one PCD, respectively. Spectra with higher source voltage or wider spectral separation generally yield lower CRLB values, and avoiding the spectral distortion caused by charge sharing in direct-conversion PCDs promises to lower CRLB values by about a third.
Conclusion: We present an extensive comparison of spectral CBCT setups for their application in proton radiotherapy, using a methodology that allows to compare their theoretical limit of performance without being influenced by the choice of reconstruction algorithm or the conversion scheme from Hounsfield units to SPR values.

This chapter is based on the following publication: **DL**, D. R. Schaart and M. C. Goorden, "Optimising proton stopping power ratio prediction with spectral cone-beam CT", Physics in Medicine & Biology 70 (14), 145023 (2025). doi: 10.1088/1361-6560/adebd6

3.1 Introduction

Proton radiotherapy is an alternative to conventional photon radiotherapy [7], offering potentially better tissue sparing due to the finite range of protons and since a significant portion of the dose is deposited in the small volume of the Bragg peak [29]. However, the same characteristics make the deposited dose distribution susceptible to small changes in the patient's anatomy. An accurate knowledge of the proton stopping power ratio (SPR) of the patient's tissues is therefore required.

The standard workflow of proton therapy consists of scanning the patient prior to treatment with an X-ray fan-beam CT scanner [5] in order to perform anatomical delineation and SPR extraction on which subsequent treatment planning is based. At the start of each treatment fraction, in-room imaging modalities such as CT-on-rails, flat-panel X-ray radiography or X-ray cone-beam CT (CBCT) are used to position the patient and check the anatomy of the day against the planning CT [19, 41], but not to update the treatment plan directly.

Since proton dose delivery is particularly sensitive to changes in SPR, the adoption of an adaptive treatment workflow in proton therapy is even more warranted than in the case of photon therapy. A more streamlined workflow could potentially make use of the in-room imaging modality [5] to update the treatment plan via e.g. image registration [14, 17, 18, 20, 35, 54], or ideally even serve directly as the basis for a new treatment plan.

Compared to CT, CBCT offers the advantage of imaging the patient in treatment position, usually without moving the patient table [19]. However, the image quality of CBCT is impacted by increased scatter [43], beam hardening, detector lag [53] and patient movement, making it inferior to fan-beam CT. One way of improving CBCT image quality could be to make use of the spectral information contained in the X-ray beam. In case of fan-beam CT, it has been shown that the accuracy and robustness of SPR extraction can be improved by using dual-energy CT [3, 27, 28, 32, 47, 49, 62, 63, 66] compared to classical single-energy CT. It is therefore reasonable to expect that spectral CBCT can also improve SPR extraction compared to single-energy CBCT.

In single-energy CT, a source operating at a fixed voltage is paired with an energy-integrating detector (EID). The term *spectral CT* as used here refers to any CT implementation in which information contained in the X-ray spectrum is utilised for imaging. Spectral CT can be realised by imprinting spectral information on the source, by extracting it using a suitable detector, or by a combination thereof. Possible implementations are (see Figure 3.1):

- A single X-ray source operating at a fixed voltage with a photon-counting detector (PCD),
- A single source operating at a fixed voltage with a dual-layer detector,
- A rapid voltage-switching source with an EID,
- A rapid voltage-switching source with a PCD,
- Two sources at different fixed voltages coupled with an EID each,
- Two sources at different fixed voltages coupled with a PCD each.

These implementations vary in their complexity and cost. Hence, a comparison of their performance on the task of SPR extraction is warranted to guide further technological developments of spectral CBCT for proton therapy, and will be conducted in this simulation study.

A common approach for comparing different setups with respect to their performance is to acquire either real or simulated scan data, reconstruct Hounsfield unit (HU) maps at different energies, use a conversion scheme from HU to SPR values—either via calibrating a relationship between measured HU values and SPR [31, 40, 48] or via a more physics-based approach [22, 37, 66]—and finally compare the predicted SPR values in image space to the ground truth. However, in case of a discrepancy between ground truth and predicted SPR values, it is not clear whether this is due to limitations in the detection and data acquisition process, the re-

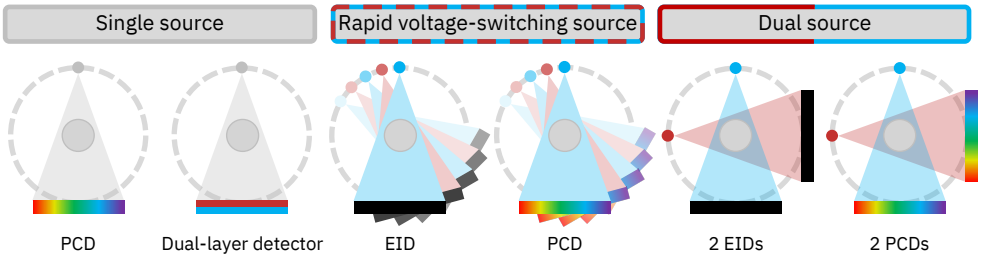

Figure 3.1: Schematic overview of various possible realisations of spectral (CB)CT that are considered in this work. Adapted from Sandvold et al [38] with permission.

construction algorithm, or the conversion scheme from HU to SPR. We therefore opted for a different approach using the Cramér-Rao Lower Bound (CRLB), which, in simple terms, quantifies the information that is available in the acquired sinograms with respect to to the extraction of SPR. The CRLB states the lowest possible variance with which an unbiased estimator can extract SPR information from the acquired sinograms. The advantage of this approach is that it circumvents limitations of reconstruction algorithms or of HU to SPR conversion schemes, and that it does not require knowledge of an explicit analytical expression for the relationship between the acquired sinogram data and SPR. We employ this CRLB-based approach in a simulation study, since comparing and optimising a large number of different spectral CBCT setups with various parameters is feasible in a simulation but not experimentally. Furthermore, determining the CRLB requires taking derivatives of SPR with respect to tissue parameters, a large number of measurement repetitions and an extremely stable source output, which is onerous if not impossible to perform in an experimental setup. In contrast, a study in silico allows to precisely control the acquisition parameters as well as ensure a fair comparison between different spectral CBCT implementations, and it allows to individually probe the influence of various degradation mechanisms on the overall performance.

Our simulation study builds on previously published work in the field, starting with the seminal paper on dual-energy CT by Alvarez and Macovski [2] who used the CRLB to arrive at expressions for the standard deviation on the estimation of material line integrals. The use of the CRLB as a figure of merit has since been adopted for optimising various aspects of X-ray imaging systems, for example for optimising bow-tie filters [11], the processing of PCD signals [12], charge sharing correction algorithms [50] or PCD binning [57, 58]. Our study is most closely related to the work by Roessl and Herrmann [36] who investigated the effect of PCD threshold values on material decomposition as well as the optimum layer thicknesses for dual-layer detectors, and to the work by Cai et al [6] who optimised a dual-layer setup with various filtration materials for use as both a single- and dual-energy modality.

The aforementioned literature focuses on setup optimisation for imaging tasks such as material decomposition and K-edge imaging. In this work, we compare and optimise the possible implementations of spectral CBCT listed above for extraction of SPR. Since scatter significantly degrades CBCT image quality, we also include a realistic scatter component obtained from Monte-Carlo simulations. We first compare highly idealised setups in order to show the theoretical limits of what could be achieved, which might help to guide further developments in detector design by highlighting the areas with the largest potential for performance gains. We then take into account a more realistic detector response in our simulations, which gives an indication of what can be expected based on the currently available detector technology.

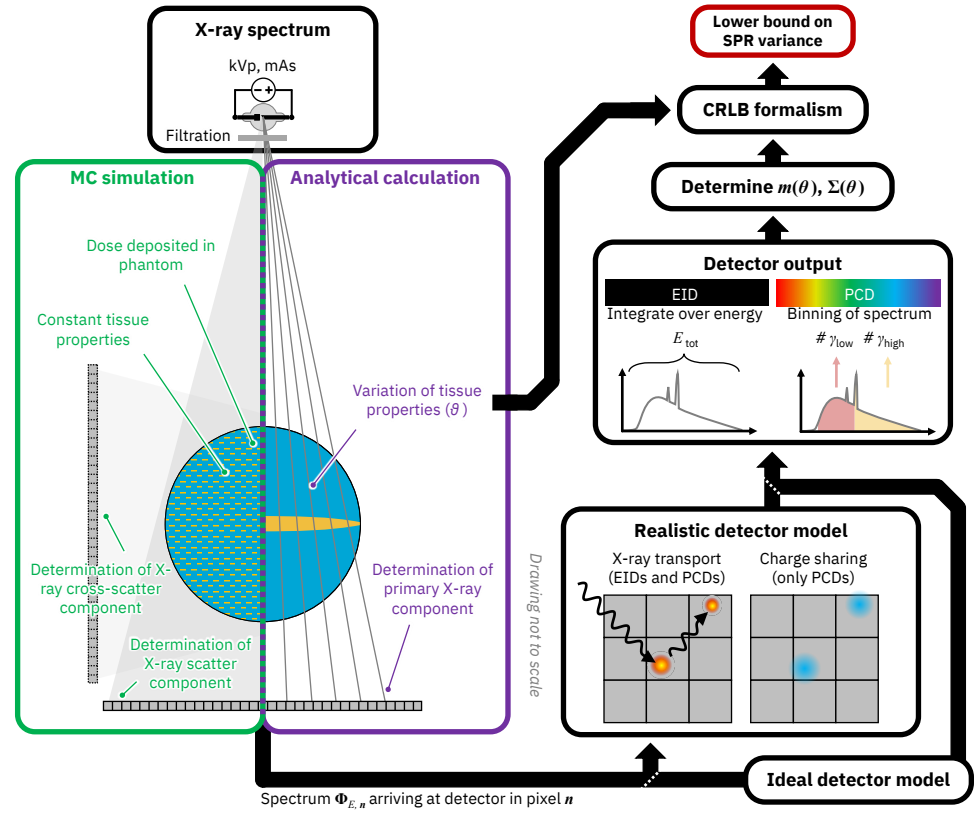

Figure 3.2: Schematic overview of the workflow of our methodology. For explanations we refer to the following sections: Section 3.2.6: X-ray spectra and deposited dose, Section 3.2.7: X-ray scatter originating in the phantom, Section 3.2.8: Detector response function, Section 3.2.4: Cramér-Rao Lower Bound formalism.

3.2 Methodology

3.2.1 Overview

The aim is to compare different implementations of spectral CBCT (Section 3.2.2) with respect to their ability to extract SPR. Our figure of merit is the variance on the estimated SPR values, as given by the CRLB (Section 3.2.4), compared at equal dose (Section 3.2.6). The material properties of the object (Section 3.2.5) determine the spectrum of photons arriving at the detector, comprised of a primary component and a scatter component. For computational speed, we calculate the primary component using the Lambert-Beer law, whereas the scatter component is determined via Monte-Carlo (MC) simulations (Section 3.2.7). To arrive at the detected signal, both an idealised and a realistic detector response are compared (Section 3.2.8). Figure 3.2 gives an overview of the workflow of our methodology.

3.2.2 Spectral CBCT Setups

Section 3.1 and Figure 3.1 list the investigated spectral CBCT setups, which are described in more detail in the following. Each setup uses one of the following types of detector:

- **Photon-counting detector:** A PCD outputs the number of events that are registered in each of a given number of energy bins during the exposure time. In case of an ideal detector response, the incoming spectrum is perfectly registered and separated into the desired number of energy bins. In case of a realistic detector response, the detector material is set to cadmium telluride (CdTe; mass fractions: $f_{\mathrm{Cd}} = 0.4684$; $f_{\mathrm{Te}} = 0.5316$; mass density: $\rho_{\mathrm{mass,\ CdTe}} = 5.85\,\mathrm{g\,cm^{-3}}$) of 1.6 mm thickness. See Section 3.2.8 for more information on the modelling of detector responses.
- **Energy-integrating detector:** An EID outputs the total deposited energy during the exposure time, that is, the sum over the number of deposited events, each multiplied by their energy. In case of an ideal detector response, the incoming spectrum is fully deposited. In case of a realistic detector response, the detector material is set to caesium iodide (CsI; mass fractions: $f_{\mathrm{Cs}} = 0.5115$; $f_{\mathrm{I}} = 0.4885$; mass density: $\rho_{\mathrm{mass,\ CsI}} = 4.51\,\mathrm{g\,cm^{-3}}$; its scintillation-inducing dopant (e.g., Tl) is neglected) of 1.9 mm thickness (equivalent to 1.6 mm CdTe based on equal deposited energy by an incoming RQA9 spectrum [8]).
- **Dual-layer detector:** The dual-layer detector consists of two detector layers with a filtration layer sandwiched in between them; each detector layer acts as an EID.
  An ideal dual-layer detector is considered to be capable of perfectly separating the spectrum into a low and high energy region, and it is modelled based on three energy bins: The lowest and highest energy bin represent the top and bottom layer, respectively, each being read out in the fashion of an EID. The third energy bin, located between the low and high energy bin, acts as an ideal filtration layer; all photons registered in this bin are discarded.
  In case of a realistic detector response we assume that the dual-layer detector consists of two CsI detector layers and, if applicable, a copper filtration layer; other layers such as silicon-based photodetection layers are neglected.
  Please note that "top layer" refers to the layer of the detector that faces the source.

For the X-ray source we assume ideal behaviour, in that it can supply any desired voltage and any desired product of current and exposure time (commonly referred to as mAs), and in that it can be considered a point source. Furthermore, it is assumed that the X-ray source can switch between any two mAs and/or voltage levels instantaneously. The investigated source voltages range from 80 to 140 kVp in steps of 20 kVp. Optional source filtration based on tin (Sn) with thicknesses between 0.2 to 0.8 mm covers the range used in commercial CT scanners.

In case of dual-source setups, cross-scatter between source-detector pairs is included and filtration can be adjusted individually for each source, unlike in a kVp-switching setup where no cross-scatter is present and filtration affects both the low and high energy phase of the source simultaneously.

Table 3.1 outlines the parameters that are optimised for each setup. Figure 3.3 illustrates the optimised parameters using two setups as representative examples; for all other setups, the optimised operating parameters are a subset of the ones shown in Figure 3.3. The optimisation is performed by conducting a grid search exploring all possible combinations of all parameters of a setup, which is feasible since the computation time of our CRLB implementation takes a few seconds per parameter and detector pixel. The only exception is the parameter of source

Table 3.1: List of the investigated spectral CBCT setups and respective optimised parameters. LE: low energy; HE: high energy.

Spectral CBCT setup	Optimised parameters
Single-source setup with PCD	• Source voltage • Source filtration for the best performing source voltage • Thresholds of energy bins
Single-source setup with dual-layer detector	• Source voltage • Source filtration for the best performing source voltage • In case of ideal detectors: thresholds of energy bins (including the bin acting as a filtration layer). In case of realistic detectors: thicknesses of top, bottom and filtration layer.
kVp-switching setup with EID	• Combination of source voltages • Source filtration for the best performing source voltage pair (filtration affects both the LE and HE spectra simultaneously) • Ratio $mAs_{LE} : mAs_{HE}$
Dual-source setup with EIDs	• Combination of source voltages • Source filtration for the best performing source voltage pairs (filtration for each source is independent) • Ratio $mAs_{LE} : mAs_{HE}$
kVp-switching setup with PCD	• Combination of source voltages • Source filtration for the best performing source voltage pair (filtration affects both the LE and HE spectra simultaneously) • Ratio $mAs_{LE} : mAs_{HE}$ • Thresholds of energy bins
Dual-source setup with PCDs	• Combination of source voltages • Source filtration for the best performing source voltage pair (filtration for each source is independent) • Ratio $mAs_{LE} : mAs_{HE}$ • Thresholds of energy bins

filtration, which is only optimised for the best performing source voltage (pair). In the following, a more detailed account is given:

- **Single source operating at a constant voltage and single PCD:** We compare PCDs with two, three and four energy bins, corresponding to three, four and five thresholds with the bottom threshold of the lowest energy bin always fixed at 20 keV, and the upper threshold of the highest energy bin fixed at the energy corresponding to the source voltage (this also applies to all other setups using PCDs with a similar configuration). The positions of all non-fixed thresholds are optimised using step sizes of 2 (5) keV for the PCDs with two and three (four) energy bins, taking into account all possible combinations of threshold values.
  Furthermore, we investigate PCDs with near-continuous binning, using bins with 1 keV width, as a reference, since they should be able to utilise the spectral information to its fullest.
  Additional Sn source filtration is investigated for the best performing 140 kVp source spectrum.
- **Single source operating at a constant voltage and dual-layer detector:** When assuming an ideal detector, the bottom threshold of the low energy (LE) bin is fixed at 20 keV,

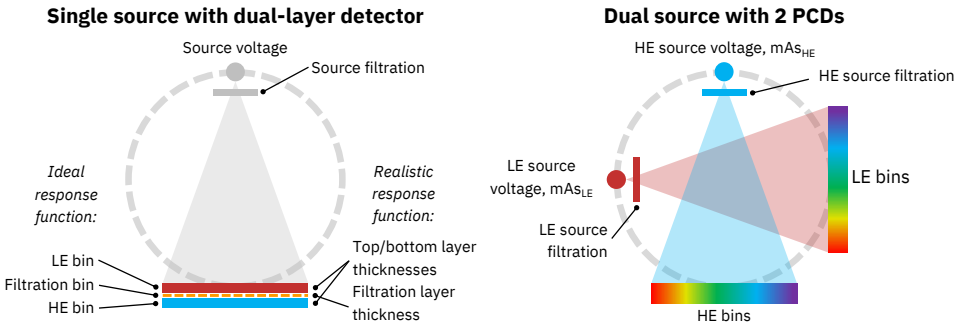

Figure 3.3: Representative examples of optimised parameters in case of a single source combined with a dual-layer detector (left) and a dual-source setup combined with two PCDs (right). The optimised parameters for the dual-layer detector differ between the case of assuming an ideal or realistic detector response function (see explanations in the text). The optimised operating parameters for all other setups are a subset of the parameters shown here. LE: low energy; HE: high energy. Adapted from Sandvold et al [38] with permission.

and the upper threshold of the high energy (HE) bin is fixed at the energy corresponding to the source voltage. The upper threshold of the LE bin and the bottom threshold of the HE bin are optimised using a step size of 2 keV, taking into account all possible combinations of threshold values, which includes the width of the third interjacent bin representing the filtration layer.
For a realistic detector, the combined thickness of the top and bottom layer is kept fixed at 1.9 mm CsI. For the top (bottom) layer, thicknesses from 0.05 to 0.8 mm (1.85 to 1.1 mm) are investigated in step sizes of 0.05 mm. The thickness of an additional copper filtration layer is varied from 0.2 to 4.25 mm.
Additional Sn source filtration is investigated for the best performing 140 kVp source spectrum.

- **Single rapid voltage-switching source and single EID:** We investigate all possible pairs of source voltages between 80 kVp and 140 kVp. For the best performing voltage pair of 80 kVp/140 kVp we investigate additional Sn source filtration.
  The investigated range of $mAs_{LE} : mAs_{HE}$, that is, the ratio of the product of source current and exposure time for the LE phase (mAs_{LE}) and for the HE phase (mAs_{HE}) of the source, is set individually for each spectrum combination such that the optimum falls within the covered range, with a lower limit for the ratio of 1 : 2 and an upper limit of 30 : 1.

- **Two sources at different fixed voltages coupled with an EID each:** The optimisation of operating parameters for this setup differs from the previous one only in that the filtration for the low and high energy source spectrum are adjusted independently. Additional filtration is investigated for both the 80 kVp/140 kVp and 100 kVp/140 kVp voltage pair. The investigated range of the ratio $mAs_{LE} : mAs_{HE}$ is set individually for each spectrum, with a lower limit of 1 : 4 and an upper limit of 60 : 1.

- **Single rapid voltage-switching source and single PCD:** We investigate all possible pairs of source voltages between 80 kVp and 140 kVp. For the best performing voltage pair of 80 kVp/140 kVp we investigate additional Sn source filtration.
  The investigated range of the ratio $mAs_{LE} : mAs_{HE}$ ranges from 1 : 100 000 to 10 000 : 1,

that is, in between the limits that only the HE or only the LE source is active.
A PCD with two energy bins is investigated, and its non-fixed threshold is set individually for the duration of the LE and HE phase of the source and optimised using a step size of 5 keV, taking into account all possible combinations of LE and HE bin threshold values.

- **Two sources at different fixed voltages coupled with a PCD each:** The optimisation of operating parameters for this setup differs from the previous one only in that the filtration for the low and high energy source spectrum is adjusted independently. As before, PCDs with two energy bins are assumed, and their thresholds are optimised independently using a step size of 5 keV.

3.2.3 Calculation of Stopping Power Ratios

According to the Bethe equation [30] the SPR, that is, the proton stopping power of a material relative to water, can be calculated as

$$\mathrm{SPR} = \frac{\rho_{\mathrm{elec,\,mat}}}{\rho_{\mathrm{elec,\,water}}} \cdot \frac{\ln\left(\frac{2m_e c^2\beta^2}{I_{\mathrm{mat}}\cdot(1-\beta^2)}\right) - \beta^2}{\ln\left(\frac{2m_e c^2\beta^2}{I_{\mathrm{water}}\cdot(1-\beta^2)}\right) - \beta^2} \quad , \tag{3.1}$$

with $\rho_{\mathrm{elec},\,m}$ and I_m as the electron density and the mean ionisation energy, respectively, with m as the index for the material under investigation or water, β as the proton velocity relative to the speed of light c, m_e as the electron mass, and ignoring density and shell corrections. We assume a proton energy of 200 MeV, noting that the energy dependency of the SPR value is very small in this energy range (in the order of 0.3 % between 10 and 250 MeV).

The mean ionisation energy I of a compound is determined by combining the ionisation energies of the its elemental constituents using Bragg's additivity rule, neglecting the influence of chemical binding energies:

$$\ln(I) = \left(\sum_p \frac{w_p Z_p}{A_p}\ln(I_p)\right)\left(\sum_p \frac{w_p Z_p}{A_p}\right)^{-1} \quad , \tag{3.2}$$

with the weight fraction w_p , atomic number Z_p , atomic weight A_p and the ionisation energy I_p of element p. Values for the elemental ionisation energies are taken from ICRU report 49 [15], applying the rule by Seltzer and Berger [42] which is to use I-values that are 13 % larger than the I-values for elemental substances in the condensed phase (except for the elements H, C, N, F and Cl; see also Section 3.A.2 in the Appendix).

3.2.4 Cramér-Rao Lower Bound Formalism

For a comprehensive description of the CRLB formalism we refer to the book by Steven M. Kay [45]; here, we summarise the aspects relevant to this work, following mostly the notation therein.
We assume that the k measurements $\mathbf{x}$—which denote either the deposited energy in the detector (for setups using EIDs) or the number of photons in different energy bins (for setups using PCDs)—follow a k-dimensional multi-variate normal probability density function (PDF), i.e.,

$$f(\mathbf{x}|\boldsymbol{\theta}) = (2\pi)^{-k/2}\det[\boldsymbol{\Sigma}(\boldsymbol{\theta})]^{-1/2}\exp\left(-\frac{1}{2}(\mathbf{x}-\mathbf{m}(\boldsymbol{\theta}))^{\mathsf{T}}\boldsymbol{\Sigma}(\boldsymbol{\theta})^{-1}(\mathbf{x}-\mathbf{m}(\boldsymbol{\theta}))\right) \quad . \tag{3.3}$$

Here, $\boldsymbol{\theta} = [\rho_{\mathrm{elec},\,m} \;\; I_m]^{\mathsf{T}}$ denotes the underlying material properties on which X-ray transmission depends, while $\mathbf{m}(\boldsymbol{\theta})$ and $\boldsymbol{\Sigma}(\boldsymbol{\theta})$ are the mean and covariance matrix of the measurements,

respectively. From these measurements, we wish to estimate SPR($\boldsymbol{\theta}$). The CRLB provides the lower bound on the variance of any unbiased estimator of SPR of material m for the given object geometry:

$$\mathrm{Var}(\mathrm{SPR}) \geq \left(\frac{\partial \mathrm{SPR}(\boldsymbol{\theta})}{\partial \rho_{\mathrm{elec},\,m}}\right)^2 \left[\mathbf{F}^{-1}(\boldsymbol{\theta})\right]_{00} + \left(\frac{\partial \mathrm{SPR}(\boldsymbol{\theta})}{\partial I_m}\right)^2 \left[\mathbf{F}^{-1}(\boldsymbol{\theta})\right]_{11} + \left(\frac{\partial \mathrm{SPR}(\boldsymbol{\theta})}{\partial \rho_{\mathrm{elec},\,m}} \cdot \frac{\partial \mathrm{SPR}(\boldsymbol{\theta})}{\partial I_m}\right) \cdot \left(\left[\mathbf{F}^{-1}(\boldsymbol{\theta})\right]_{01} + \left[\mathbf{F}^{-1}(\boldsymbol{\theta})\right]_{10}\right) \quad . \tag{3.4}$$

In the following, we denote the lower bound on Var(SPR), as given by the CRLB formalism, simply as CRLB.
The derivatives of SPR with respect to $\rho_{\mathrm{elec},\,m}$ and I_m can be calculated analytically using Equation 3.1. The elements of the Fisher information matrix $\mathbf{F}(\boldsymbol{\theta})$ can be calculated according to (Kay [45], Equation 3.31):

$$\left[\mathbf{F}(\boldsymbol{\theta})\right]_{ij} = \left[\frac{\partial \mathbf{m}(\boldsymbol{\theta})}{\partial \theta_i}\right]^{\mathsf{T}} \boldsymbol{\Sigma}^{-1}(\boldsymbol{\theta}) \left[\frac{\partial \mathbf{m}(\boldsymbol{\theta})}{\partial \theta_j}\right] + \frac{1}{2}\mathrm{tr}\left[\boldsymbol{\Sigma}^{-1}(\boldsymbol{\theta}) \frac{\partial \boldsymbol{\Sigma}(\boldsymbol{\theta})}{\partial \theta_i} \boldsymbol{\Sigma}^{-1}(\boldsymbol{\theta}) \frac{\partial \boldsymbol{\Sigma}(\boldsymbol{\theta})}{\partial \theta_j}\right] \quad . \tag{3.5}$$

The partial derivatives $\partial \mathbf{m}(\boldsymbol{\theta})/\partial \theta_i$ and $\partial \boldsymbol{\Sigma}(\boldsymbol{\theta})/\partial \theta_i$ are obtained by varying the electron density or ionisation energy of the material (Section 3.2.5). For the resulting object composition, we calculate the expected number of primary photons arriving at the detector analytically based on the Lambert-Beer law, adding a (cross-)scatter component obtained from MC simulations (Section 3.2.7, Figure 3.2). After the application of a detector response function (Section 3.2.8), the spectrum is then either binned (in case of PCDs) or the deposited energy is calculated (in case of EIDs), and the mean and variance of the resulting quantities are calculated. Finally, the derivative of the mean and variance are calculated with respect to $\boldsymbol{\theta}$. To reduce the computational burden, we calculate the CRLB for a selected subset of lines only (as indicated in Figure 3.2, box "Analytical calculation"), combining the CRLB values of this subset of lines. An illustration of the workflow is shown in Figure 3.2; for details on this and the implementation of the CRLB calculation we refer to Section 3.A.1 in the Appendix.
Please note that the CRLB methodology only provides a lower bound on the variance with which SPR can be estimated, but it neither yields SPR values, neither does it provide an estimator that can reach the theoretical CRLB limit, nor does it make a statement if such an estimator even exists.

3.2.5 Object and Material Definitions, Setup Geometry

In case of MC simulations of scatter or deposited dose, we define the phantom as a homogeneous object with a composition approximating the average composition of humans (Figure 3.2, box "MC simulation").

For the analytical calculation of primary X-rays arriving at the detector, we use a two-compartment model consisting of soft tissue and bone, whose combined composition equals the homogeneous composition used for MC simulations. As a consequence of this choice, the two-compartment model uses a constant ratio of the ray length through soft tissue to the ray length through bone for every ray crossing the phantom (Figure 3.2, box "Analytical calculation"). A two-compartment model allows us to apply the CRLB to SPR extraction of either soft tissue or bone by varying the material parameters of either of them. In order to estimate $\partial \mathbf{m}(\boldsymbol{\theta})/\partial \rho_{\mathrm{elec},\,m}$ and $\partial \boldsymbol{\Sigma}(\boldsymbol{\theta})/\partial \rho_{\mathrm{elec},\,m}$ the mass density of either soft tissue or bone is varied in steps of 1 %, and in order to estimate $\partial \mathbf{m}(\boldsymbol{\theta})/\partial I_m$ and $\partial \boldsymbol{\Sigma}(\boldsymbol{\theta})/\partial I_m$ the composition of either soft tissue or bone

is changed such that the ionisation energy varies in steps of (1.0000 ± 0.0001) eV. For further details on elemental compositions, mass densities and weight fractions of the simulated materials as well as their variation we refer to Section 3.A.2 in the Appendix.

As shown in Section 3.B.1 of the Appendix, the optimisation of setup parameters depends on whether one optimises for the extraction of SPR of bone or of soft tissue. However, the best performing settings for the two tissues differ by such a small margin (e.g., less than 1 keV in case of a single-source setup with a PCD with 2 bins) that in this work we focus on the extraction of SPR of soft tissue only.

The simulated CBCT geometry (Figure 3.A.2 in the Appendix) mimics a typical CBCT setup integrated into a proton radiotherapy gantry with a source-isocenter distance of 2300 mm and an isocenter-detector distance of 900 mm. The phantom is simulated as a cylinder with a diameter and height of both 330 mm. The size of the phantom is based on standard image quality phantom sizes, which in turn are based on average patient sizes.

3.2.6 X-ray Spectra and Deposited Dose

We obtain X-ray spectra from SPEKCALC [33] for a tungsten target and an anode angle of 7° with energy steps of 1 keV (see Figures 3.A.4 to 3.A.7 in the Appendix). The intrinsic source filtration is assumed to be 0.8 mm Be and 0.89 mm Ti. For further beam hardening, 0.2, 0.4, 0.6 and 0.8 mm of tin are investigated.

For a fair comparison between all setups and acquisition settings, we keep the cumulative dose deposited in the phantom constant at an arbitrary value of $(1.244\,26 \pm 0.000\,46) \cdot 10^{16}$ MeV. As discussed in the Appendix, Section 3.B.1, the chosen value of the cumulative reference dose does not have any influence on the optimisation result. The deposited dose per number of emitted photons from the source is determined using MC simulations as described in Section 3.2.7.

3.2.7 X-ray Scatter Originating in the Phantom

We use MC simulations using $3.6 \cdot 10^{10}$ primaries to obtain the X-ray scatter caused by the phantom for a given source voltage and filtration, based on the setup described in Section 3.2.5. The MC simulations are implemented using GATE (version 9.2) [39] which is based on the GEANT4 toolkit (version 11.0.0) [1].
In order to obtain the scatter component, the photons intersecting the detector plane are split into scattered and non-scattered photons based on their trajectory. For registration of cross-scatter between two orthogonal source-detector pairs, a second detector plane is placed at the same isocenter-detector distance as the first detector plane, but perpendicular to the axis between source and first detector plane (see Figure 3.2, box "MC simulation").
The MC data of primary photons and (cross-)scatter contributions are stored as histograms of the number of photons per energy bin, using energy bins of 1 keV width. The data are then smoothed using a two-dimensional Gaussian kernel in the spatial domain. The (cross-)scatter data is finally normalised to the number of primary photons.
Our algorithm for determining the CRLB calculates the primary component analytically in steps of 1 keV and subsequently adds the MC-based scatter as well as, if applicable, cross-scatter components, yielding the total expected number of photons arriving at the detector in steps of 1 keV. It is assumed that the volume spanned by the source and a given detector pixel is negligibly small compared to the irradiated volume of the phantom. As a result, when the number of primaries changes due to a variation of the line integral between the source and that pixel, either due to a variation in electron density or composition to calculate the derivatives in Equa-

tion 3.5, then the number of scattered and cross-scattered photons stays constant.
The variance of the smoothed (cross-)scatter component and its influence on the resulting CRLB values is negligible with relative standard deviations ≤ 0.2 %; as a consequence, we do not report the standard deviation on obtained CRLB values. For more information see Section 3.B.2 in the Appendix.

3.2.8 Detector Response Functions

When modelling ideal detectors in our simulation study, it is assumed that the detection efficiency is 100 %, that inter-pixel cross-talk, electronic noise and pile-up are all absent, and, as a result, that the spectrum of registered events equals the spectrum of incoming photons.
When modelling realistic detectors in our simulation study, the spectrum of deposited events is determined based on X-ray transport detector response functions. These X-ray transport detector response functions, specific for the layer compositions and layer thicknesses stated above, are obtained using MC simulations in GATE (see Section 3.2.7) by irradiating the centre pixel of a grid of pixels (without dead-space between the pixels) with monoenergetic beams and registering the spectrum of events deposited in the centre pixel, the spectrum of events deposited in all surrounding pixels, and the spectrum of events leaving the detector downstream from the source.
For realistic EIDs it is then assumed that the spectrum of registered events equals the spectrum of deposited events. For realistic PCDs, however, the spectrum of deposited events obtained from the X-ray transport simulations is used as input for a charge sharing model unless explicitly stated otherwise, based on an isotropic 3D-Gaussian distribution [52] with a charge cloud size of $\sigma = 30\,\mu$m, independent of deposited energy [46]. The output of the charge sharing model is subsequently used as the spectrum of registered events. The pixel size for both simulation of X-ray cross-talk and charge sharing is $300 \times 300\,\mu\text{m}^2$ for both EIDs and PCDs, which is similar to the pixel cross-section of commercially available PCD CT scanners [24, 26, 34].
It is noted that our model of realistic detectors does not include effects degrading the energy resolution apart from those described above. For example, neither electronic noise nor pulse pile-up are included.
For more details we refer to Section 3.A.3 in the Appendix.

3.3 Results

3.3.1 Optimisation of Setups Based on an Ideal Detector Response Function

In the following, we present the results for the optimisation of spectral CBCT implementations assuming an ideal detector response function, with the lowest possible variance on SPR as given by the CRLB as our figure of merit (lower is better); for a summary see Table 3.2 and Figure 3.4. Note that X-ray scatter originating from the phantom and, if applicable, cross-scatter between two source-detector pairs is included.

Single-source setup with ideal PCD

Higher source voltages prove to be beneficial for this setup. A source voltage of 140 kVp without additional source filtration yields the best results regardless of the number of energy bins used by the PCD. In the limit of a near-continuous binning with bins of 1 keV width (Table 3.B.5), the lowest (i.e., best) CRLB value across all setups, source voltages and filtrations is achieved and hence used as a reference value. All CRLB values in this work are reported as normalised CRLB values (nCRLB) relative to this reference value, regardless of whether an ideal or realistic detector model is considered.
Using a limited number of two (Table 3.B.2 and Figure 3.4a), three or four (Table 3.B.3 and 3.B.4) bins only, nCRLB values of 1.31, 1.16 and 1.11 are reached (Table 3.2).

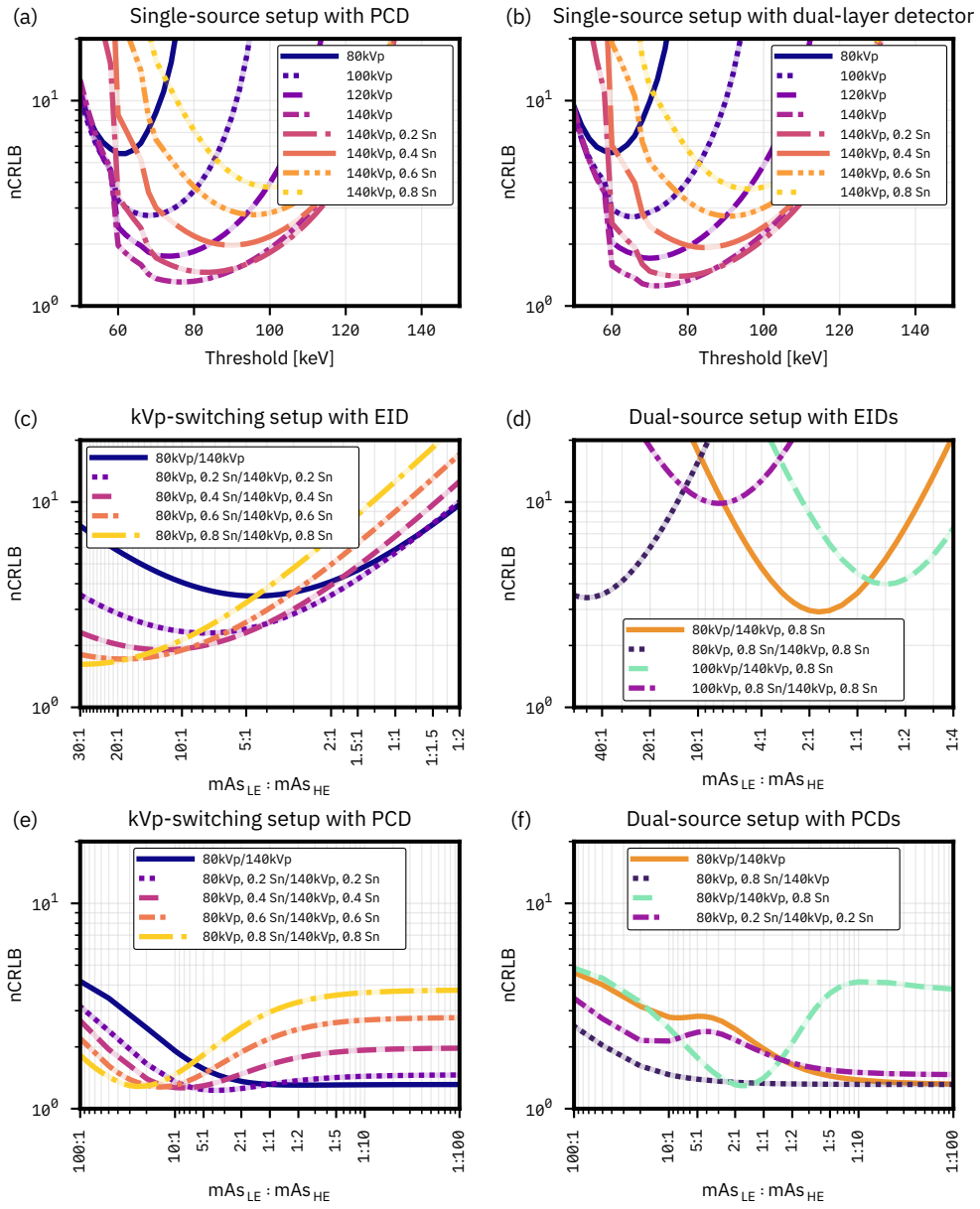

Figure 3.4: Examples of optimisation of spectral CBCT setups with respect to the extraction of SPR, assuming an ideal detector response function. Single-source setup with (a) a PCD with two energy bins and (b) a dual-layer detector without filtration bin, optimising the threshold between the low and high energy bins. (c) kVp-switching setup with one EID and (d) dual-source setup with two EIDs, optimising the ratio $mAs_{LE} : mAs_{HE}$ between the LE and HE spectra. (e) kVp-switching setup with one PCD and (f) dual-source setup with two PCDs; for each mAs ratio, the minimum nCRLB of all tested threshold combinations is plotted. All values are reported as normalised CRLB values as stated in the text with the same nCRLB value range for all figures; source filtration is specified in millimetres of tin.

Table 3.2: Results for the optimisation of various spectral CBCT setups with respect to the extraction of SPR, assuming an ideal detector response function. The table lists the settings yielding the lowest nCRLB for each setup as well as additional entries of interest.

Setup	**Spectrum (combination)**	**Parameters (bins, $mAs_{LE} : mAs_{HE}$)**	**min. nCRLB**
Single-source setup with PCD	140 kVp	[20, 76, 140] keV	1.31
	140 kVp	[20, 70, 94, 140] keV	1.16
	140 kVp	[20, 60, 75, 95, 140] keV	1.11
	140 kVp	Continuous binning	1.00
Single source with dual-layer detector	140 kVp	[20, 72, 140] keV	1.25
	140 kVp	[20, 68, 84, 140] keV	1.16
kVp-switching setup with EID	80 kVp, 0.2 mm Sn/ 140 kVp, 0.2 mm Sn	1 : 1	5.65
	80 kVp, 0.8 mm Sn/ 140 kVp, 0.8 mm Sn	29 : 1	1.62
Dual-source setup with EIDs	80 kVp/ 140 kVp, 0.8 mm Sn	1.75 : 1	2.92
kVp-switching setup with PCD	80 kVp/140 kVp	1:1; LE bins: [20, 60, 80] keV, HE bins: [20, 75, 140] keV.	1.31
	80 kVp, 0.2 mm Sn/ 140 kVp, 0.2 mm Sn	3.5 : 1; LE bins: [20, 65, 80] keV, HE bins: [20, 85, 140] keV.	1.23
Dual-source setup with PCDs	80 kVp/140 kVp	HE only; HE bins: [20, 75, 140] keV.	1.31
	80 kVp/ 140 kVp, 0.8 mm Sn	1.75 : 1; LE bins: [20, 60, 80] keV, HE bins: [20, 90, 140] keV.	1.30

Single-source setup with ideal dual-layer detector

Across all source voltages, all Sn source filtration thicknesses for 140 kVp, and without an additional filtration layer bin, the lowest nCRLB value of 1.25 is achieved for 140 kVp without additional source filtration (Figure 3.4b and Table 3.B.6). Adding a filtration layer bin with a width of 16 keV lowers the nCRLB further by 8 % to a value of 1.16 (Figure 3.B.6).

Single rapid voltage-switching source with ideal EID

For all possible source voltage combinations between 80 kVp and 140 kVp without additional source filtration, the 80/140 kVp voltage pair performs best (Table 3.B.7 and Figure 3.B.7). Additional Sn source filtration applied to the 80/140 kVp voltage pair affects both the LE and HE spectrum simultaneously (Figure 3.4c). The lowest nCRLB value of 1.62 is achieved for a filtration of 0.8 mm Sn, however, this optimum is achieved for a very high mAs ratio of $mAs_{LE} : mAs_{HE}$ = 29 : 1. Examining the results not as a function of mAs ratio but as a function of the ratio between the number of photons emitted (incl. source filtration) during the LE or HE phase (Figure 3.B.22a) shows that the minimum nCRLB value is always reached in the vicinity of a photon number ratio of 1 : 1, i.e., equal number of photons emitted during the LE and HE phase. The high value of 29 : 1 for the optimum mAs ratio for an 80/140 kVp spectrum combination filtered by 0.8 mm of tin hence counteracts the influence of stronger filtration on the LE spectrum.

In case we assume that the rapid switching source can only switch between voltages, but not between mAs levels (i.e., $mAs_{LE} : mAs_{HE} = 1:1$), the lowest nCRLB of 5.65 is achieved using a 0.2 mm Sn filtration (Table 3.2). This result is more than three times worse than that obtained with the optimised mAs ratio, emphasizing the importance of optimising both voltages and mAs levels. Moreover, depending on the mAs ratios achievable with a realistic switching source, a different filtration might perform best.

Dual-source setup with two ideal EIDs

Comparing different voltage pairs, the 100/140 kVp voltage pair performs best for a mAs ratio of $mAs_{LE} : mAs_{HE} \leq 2.5:1$, whereas the 80/140 kVp voltage pair achieves the lowest nCRLB values for larger mAs ratios (Figure 3.B.9).
We observe the same trends regarding filtration for both the 80/140 kVp and the 100/140 kVp voltage pair: adding Sn filtration to only the LE spectrum does not lower the nCRLB compared to the unfiltered spectra (Figure 3.B.10 and 3.B.13). Adding Sn filtration to only the HE spectrum lowers the nCRLB significantly, with stronger filtration yielding lower nCRLB values (Figure 3.B.11 and 3.B.14) while shifting the minimum towards lower values of $mAs_{LE} : mAs_{HE}$. Adding the same thickness of Sn filtration to both the LE and HE spectra decreases the nCRLB values as well, but shifts the minimum to larger mAs ratios (Figure 3.B.12 and 3.B.15) and is still outperformed by applying filtration to the HE spectrum only.
The lowest nCRLB value of 2.92 is reached by an 80/140 kVp voltage pair with 0.8 mm Sn filtration added to the 140 kVp spectrum only, and a mAs ratio of $mAs_{LE} : mAs_{HE} = 1.75:1$ (Figure 3.4d and Table 3.B.8). Similarly to the kVp-switching setup, we observe that, while the optimum mAs ratios for the various filtration settings differ considerably, their corresponding ratios between the number of photons emitted by the LE and HE source are between 1 : 1 and 5 : 1 (Figure 3.B.22b). Hence, large mAs ratios counteract the stronger effect of filtration on the LE spectrum also in this setup.

Single rapid voltage-switching source with ideal PCD

Comparing all possible source voltage combinations between 80 and 140 kVp without additional source filtration (Figure 3.B.16), we see that while the mean nCRLB value of the 120/140 kVp voltage pair, averaged over the whole investigated mAs ratio range, is lowest, it is always outperformed by the 80/140 kVp voltage pair for $mAs_{LE} : mAs_{HE} \leq 5:1$. The lowest nCRLB is achieved in the limit of very low mAs ratios for all source voltage combinations, that is, in the limit that only the HE phase of the source is used (Table 3.B.9).
As soon as filtration is added to the 80/140 kVp spectrum combination, affecting both the LE and HE spectrum simultaneously, the minimum CRLB is found in the regime of mAs ratios where both the LE and HE phase of the source are used. The lowest nCRLB value of 1.23 is achieved for a filtration of 0.2 mm Sn at a mAs ratio of $mAs_{LE} : mAs_{HE} = 3.5:1$. If the mAs ratio is fixed at $mAs_{LE} : mAs_{HE} = 1:1$, the nCRLB value increases to 1.31 using no additional source filtration. Hence, depending on the mAs ratios achievable with a realistic source, a different filtration might perform best (Figure 3.4e).

Dual-source setup with two ideal PCDs

The investigation of different voltage pairs shows the same behaviour as for the kVp-switching counterpart, with the only difference that the 80/140 kVp voltage pair outperforms the 120/140 kVp voltage pair for a mAs ratio of $mAs_{LE} : mAs_{HE} \leq 3.5:1$.
For the 80/140 kVp voltage pair, adding filtration to only the LE spectrum lowers the nCRLB in the regime of mAs ratios where both sources are active, but the lowest nCRLB values are still achieved in the limit that only the HE source is active (Figure 3.B.19).

In the case that only the HE spectrum is filtered, the simultaneous utilisation of both sources yields nCRLB values that are lower than those obtained with only the HE source, provided that stronger filtration is used. For the combination of 80 kVp/140 kVp with a strong HE filtration of 0.8 mm Sn, the lowest overall nCRLB value for this setup of 1.30 is achieved using a mAs ratio of $mAs_{LE} : mAs_{HE} = 1.75 : 1$ (Figure 3.B.21).
The best performing settings for each of the different filtration cases (no filtration, only LE filtration, only HE filtration, and both LE and HE filtration) are compared in Figure 3.4f (see also Table 3.B.11).

Setups based on ideal detector response function: Summary
Comparing all spectral CBCT implementations based on an ideal detector response function (Table 3.2), excluding the reference PCD with near-continuous binning, the setup using a single source and a PCD with four energy bins performs best (nCRLB = 1.11), closely followed by a single-source setup using an ideal dual-layer detector and three effective bins (nCRLB = 1.16) and a single-source setup using a PCD with three energy bins (nCRLB = 1.16), with an increase in nCRLB by 4.5 %. A dual-source setup with two PCDs with two energy bins each (nCRLB = 1.30) performs only slightly better than a single-source setup with a PCD with two energy bins (nCRLB = 1.31), but worse than a kVp-switching setup with a PCD with two energy bins for each phase (nCRLB = 1.23), which in turn performs worse than a single source setup with a PCD with four energy bins. The performance of setups using EIDs is worse compared to setups using any other type of detector: the kVp-switching setup with one EID reaches a nCRLB value of 1.62, whereas the dual-source setup with two EIDs is additionally affected by cross-scatter and reaches a nCRLB value of 2.92.
Under the assumption that the rapid switching source can only switch between voltages but not mAs levels, the kVp-switching setup with a PCD performs slightly worse (nCRLB = 1.31) than a dual-source setup with two PCDs (nCRLB = 1.30). For the kVp-switching setup using an EID, however, the deterioration is much more pronounced, leading to a nCRLB of 5.65, which is the worst out of all spectral CBCT configurations with ideal detectors.

3.3.2 Optimisation of Setups Based on a Realistic Detector Response Function

The optimisation of setups using a realistic detector response function is performed analogously to the optimisation of setups using an ideal detector response function; a summary thereof can be found in Table 3.3. We observe that for each individual spectral CBCT setup, the trends in performance with respect to the optimised parameters are similar for both an ideal and realistic detector response function. Due to this similarity, here we only summarise the results and refer the interested reader to the Appendix, Section 3.B.4, for details on the results for the optimisation of setups using a realistic detector response function.

Setups based on realistic detector response function: Summary
Comparing all spectral CBCT implementations based on a realistic detector response function (Table 3.3), excluding the PCD with near-continuous binning, the single-source setup with a dual-layer detector performs worst out of all setups (nCRLB = 7.78, with filtration layer), unless the source of the kVp-switching setup with one EID is limited to a mAs ratio of 1 : 1 in which case this setup has worst performance (nCRLB = 9.46). In contrast, if the kVp-switching setup with one EID uses a source that can reach any mAs ratio, it performs best out of all setups (nCRLB = 2.74), closely followed by a kVp-switching source combined with a PCD (nCRLB = 2.81). Similarly, limiting the kVp-switching setup with one PCD to a mAs ratio of 1 : 1 causes it

Table 3.3: Results for the optimisation of various spectral CBCT setups with respect to the extraction of SPR, assuming a realistic detector response function. The table lists the settings yielding the lowest nCRLB for each setup as well as additional entries of interest.

Setup	**Spectrum (combination)**	**Parameters (bins, mAs_{LE} : mAs_{HE}, layer thicknesses)**	**min. nCRLB**
Single-source setup with PCD	140 kVp	[20, 70, 140] keV	3.96
	140 kVp	[20, 68, 88, 140] keV	3.62
	140 kVp	[20, 60, 70, 90, 140] keV	3.45
	140 kVp	Continuous binning	3.14
Single source with dual-layer detector	140 kVp	Top layer: 0.45 mm CsI, bottom layer: 1.45 mm CsI.	11.6
	140 kVp	Top layer: 0.2 mm CsI, filtration layer: 1.8 mm Cu, bottom layer: 1.7 mm CsI.	7.78
kVp-switching setup with EID	80 kVp, 0.2 mm Sn/ 140 kVp, 0.2 mm Sn	1 : 1	9.46
	80 kVp, 0.8 mm Sn/ 140 kVp, 0.8 mm Sn	26 : 1	2.74
Dual-source setup with EIDs	80 kVp/ 140 kVp, 0.8 mm Sn	1.5 : 1	4.97
kVp-switching setup with PCD	80 kVp/140 kVp	1:1; LE bins: [20, 65, 80] keV, HE bins: [20, 70, 140] keV.	3.60
	80 kVp, 0.8 mm Sn/ 140 kVp, 0.8 mm Sn	20 : 1; LE bins: [20, 30, 80] keV, HE bins: [20, 80, 140] keV.	2.81
Dual-source setup with PCDs	80 kVp/140 kVp	HE only; HE bins: [20, 70, 140] keV.	3.96
	80 kVp/ 140 kVp, 0.8 mm Sn	1.5 : 1; LE bins: [20, 65, 80] keV, HE bins: [20, 70, 140] keV.	3.27

to perform worse (nCRLB = 3.60) than the dual-source setup with PCDs (nCRLB = 3.27). The dual-source setup with two PCDs (nCRLB = 3.27) now performs better than a single-source setup with a PCD with either two, three or even four energy bins (nCRLB of 3.96, 3.62 and 3.45, respectively). In comparison to the kVp-switching setups capable of any mAs ratio, the dual-source setups again perform worse (nCRLB = 4.97 using EIDs, nCRLB = 3.27 using PCDs) due to the influence of cross-scatter.

3.3.3 Comparison of Setups Using either an Ideal or Realistic Detector Response Function

Figure 3.5 compares the performance of spectral CBCT setups using either an ideal or realistic detector response function. As mentioned before, the trends are largely the same with respect to the optimised parameters for individual setups, with the assumption of a realistic detector response function yielding consistently worse results.

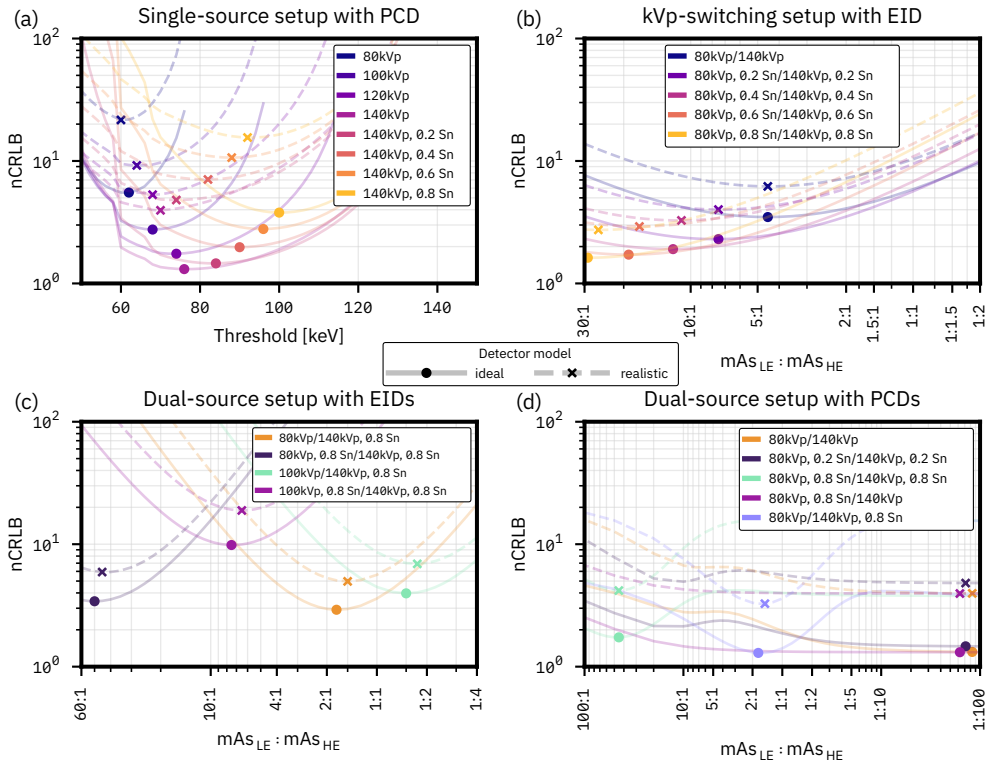

Figure 3.5: Comparison of spectral CBCT setups optimised with respect to the extraction of SPR, assuming either an ideal or a realistic detector response function. Markers indicate the position of optima. (a) Single-source setup with one PCD using two energy bins, optimising the threshold between the low and high energy bin. (b) kVp-switching setup with EID and (c) dual-source setup with two EIDs, optimising the ratio $\mathrm{mAs}_{\mathrm{LE}} : \mathrm{mAs}_{\mathrm{HE}}$ between the LE and HE spectra. (d) Dual-source setup with PCDs; for each mAs ratio, the minimum nCRLB of all tested threshold combinations is plotted; markers at a mAs ratio of $1:100$ indicate that the best performance is reached in the limit of using the HE source only; overlapping markers are slightly offset for better readability. All values are reported as normalised CRLB values as stated in the text; source filtration is specified in millimetres of tin.

Comparing the difference in optimum performance assuming either ideal or realistic detectors, the nCRLB of a single-source setup with a realistic PCD is about a factor of 3.0 to 3.1 larger than in the ideal case, about a factor of 2.3 for a kVp-switching setup with one PCD, and about a factor of 2.5 for a dual-source setup with PCDs. For the setups based on one or two EIDs, the performance of realistic setups deteriorates by a smaller factor of about 1.7 compared to ideal setups. For a single-source setup with a dual-layer detector, the ideal and realistic setup differ in performance by a factor of 9.2 without and a factor of 6.7 with filtration between the detector layers/bins.

3.4 Discussion

3.4.1 Comparison of Setups

When assuming a realistic detector response function, we observe that the optimal threshold settings are shifted towards lower energies compared to their ideal detector counterparts for the case of a single-source setup with a PCD with either two (Figure 3.5a), three or four bins (Table 3.2 and 3.3). This could be due to the shift of the spectrum of registered events to lower energies in the case of a realistic detector response function (Figure 3.6a), which is a consequence of X-ray cross-talk and charge sharing.
For the kVp-switching setup combined with an EID as well as for the dual-source setup with EIDs, we observe that the optimum current ratio is shifted towards the high energy source spectrum when assuming a realistic detector response function, compared to their ideal counterparts (Figure 3.5b and c). A possible contribution to this behaviour could be that, when changing from an ideal to a realistic detector response function, the deposited energy during the LE phase is reduced by −6.6 % in the example shown in Figure 3.6c and d (values for centre pixel of detector only), whereas the deposited energy during the HE phase is reduced by −25 %. An increase of the HE source current for the realistic setups would counteract the change in the ratio of deposited energy to some extent.

Comparing ideal and realistic setups, the degradation in performance is largest for the dual-layer setup. The good performance of an ideal dual-layer detector is due to its perfect separation of the registered spectrum into two energy bins (three with filtration) combined with a readout in the fashion of an EID; however, for the realistic dual-layer detector the spectral separation between the spectra registered by the top and bottom layer is relatively poor (see Figure 3.6b).

Generally, we observe that a higher source voltage or a larger spectral separation between the source spectra leads to better SPR extraction. For example, when comparing all possible voltage pairs between 80 kVp and 140 kVp, the 80/140 kVp voltage pair usually performs best. Another example illustrating this point particularly well is the comparison between an ideal PCD with two energy bins and an ideal dual-layer detector with two effective energy bins, both paired with a single source: The dual-layer detector assigns a stronger weight to high energy photons and achieves a better performance. Both setups show equal performance when using three instead of two bins, even despite the dual-layer detector's third filtration bin discarding all photons falling into this bin (140 kVp, 2 bins: nCRLB = 1.25 for dual-layer detector, nCRLB = 1.31 for PCD; 140 kVp, 3 bins: nCRLB = 1.16 for both dual-layer detector and PCD).

A comparison between kVp-switching and dual-source setups shows that the kVp-switching setups perform better; this holds true for both the case of an ideal and realistic detector response function, and for both the case of using EIDs or PCDs as detectors. Given the same source spectra and source filtration, cross-scatter is the only difference between kVp-switching and dual-source setups in our model and therefore the reason for their difference in performance. For example, if we compare the kVp-switching setup with one EID to the dual-source setup with two EIDs for the same operating conditions of an unfiltered spectrum combination of 80/140 kVp, a mAs ratio of $\mathrm{mAs}_{\mathrm{LE}} : \mathrm{mAs}_{\mathrm{HE}} = 6.5 : 1$ and an ideal detector response, then the addition of cross-scatter causes a 2.6 fold increase in the CRLB values for the dual-source setup compared to the kVp-switching setup (see also Figure 3.B.42 and 3.B.43 for a comparison between kVp-switching and dual-source setups based on EIDs). The absence of cross-scatter is hence the reason for the better performance of the kVp-switching setups, despite their limitations when it comes to the choice of source filtrations. It should be noted, however, that kVp-switching setups only outperform their dual-source counterparts as long as an ideal

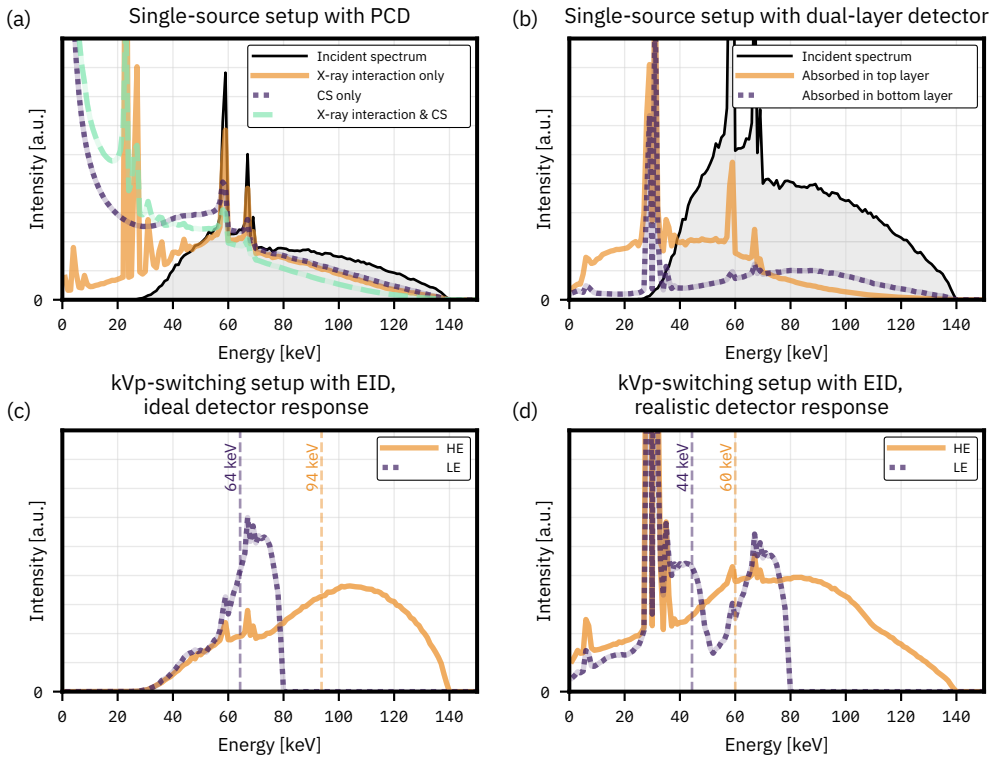

Figure 3.6: (a) Spectrum incident on a PCD as well as the spectrum of events created in a pixel taking into account only X-ray interaction, only charge sharing (CS), or both X-ray interaction and charge sharing (centre pixel of detector, 140 kVp source spectrum). (b) Spectrum incident on a dual-layer detector as well as the spectra of events absorbed in the top and bottom layer (centre pixel of detector, 140 kVp source spectrum, 0.2 mm CsI top layer, 1.8 mm Cu filtration layer, 1.7 mm CsI bottom layer). (c), (d) Spectra of events created in the detector in case of a kVp-switching source combined with an ideal (c) and a realistic (d) EID, during either the low or high energy phase (centre pixel of detector, 80 kVp, 0.8 mm Sn/140 kVp, 0.8 mm Sn spectrum combination, $\mathrm{mAs}_{\mathrm{LE}} : \mathrm{mAs}_{\mathrm{HE}} = 27.5 : 1$). The horizontal lines mark the mean energy of each spectrum. The value range of the y-axes is set individually for each figure to show relevant features more clearly.

source capable of reaching any mAs ratio is assumed; we refer to the discussion in Section 3.4.3 for more on this.

Comparing the difference in performance between setups based on either ideal or realistic PCDs, the nCRLB for the kVp-switching and the dual-source setup degrades less (by a factor of 2.3 and 2.5, respectively) compared to a single-source setup (by a factor between 3.0 to 3.1, depending on the number of bins), since the use of two distinct source spectra can counteract the deterioration of spectral response in the detector. In contrast to this, a realistic detector response function degrades the nCRLB of setups based on EIDs by a factor of only 1.7; hence, the degradation is more severe for PCDs, and consequently there are greater gains possible by improving the performance of (realistic) PCDs. We attribute the more severe deterioration in the case of PCDs to the additional cross-talk caused by charge sharing, which degrades their

spectral performance. If charge sharing is neglected and only X-ray transport is included in the detector response function, then in case of a single-source setup with a PCD the nCRLB is only increased by a factor of about 2.0 to 2.1 relative to the results based on an ideal detector response function (see Appendix, Figure 3.B.47 and Tables 3.B.22 to 3.B.25), compared to a factor of 3.0 to 3.1 if charge sharing is included on top of X-ray transport. This translates to an improvement of CRLB values by 32 to 35 % when charge sharing is neglected, compared to the case of including both X-ray transport and charge sharing. These results are in line with a work published by Taguchi and us, indicating that indirect-conversion PCDs, which do not suffer from charge sharing, may offer better performance than PCDs based on CdTe or CZT in spectral imaging tasks such as water-bone decomposition or K-edge imaging [51]. Similarly, indirect-conversion PCDs may be better suited for the task of SPR determination investigated here.

For a single-source setup paired with a PCD we observe that the nCRLB is lower the higher the number of energy bins; this holds true for the case of both an ideal and realistic response function. This is in line with results previously published by Taguchi for ideal PCDs [16] (even when including electronic noise).

Concerning the future development of spectral CBCT for adaptive proton therapy, we would like to note that dual-source setups with EIDs are already available in some proton gantries, while the installation of rapid switching X-ray sources seems feasible. While our results based on an ideal detector response function suggest that both these setups are outperformed by a single-source setup with a PCD (Table 3.2), our results based on a realistic detector response function (Table 3.3) show that a kVp-switching setup with an EID and an ideal source outperforms a dual-source setup with EIDs by a factor of 1.8, and a single-source setup with a PCD with four bins by a factor of 1.3. If the detector response function of PCDs is assumed to be based solely on X-ray transport, then a PCD with 4 bins (Table 3.B.24) outperforms the kVp-switching setup with an EID by a factor of 0.82. Hence, taking into account the currently available technology, a rapid switching source with an EID seems preferable. For future developments, we encourage the investigation of concepts for PCDs free of charge sharing, such as PCDs based on ultrafast scintillators [55].

While we only focus on optimising and comparing spectral CBCT setups with respect to their performance for SPR extraction, the decision to implement one of the discussed variants should also take into account its performance with respect to soft tissue contrast, its sensitivity to patient motion, as well as its cost and feasibility. Dual-source setups will be more expensive than single-source setups, and setups based on an EID are likely to be cheaper than those including a PCD, with dual-layer detectors probably lying somewhere in between.

3.4.2 Limitations of the Applied Methodology

Photon-counting detector model

We do not include the effect of pulse pile-up on PCD performance. Addressing this concern, we would like to note that pile-up is most prominent for pixels for which the projection lines pass just below the surface of the object under investigation, and therefore exhibit the least attenuation. In our case, the photon flux for pixels in the centre is about 130 times lower, which decreases the probability of pile-up while it simultaneously causes an increase of CRLB values. Furthermore, we find that these pixels in the centre dominate the overall behaviour of the CRLB in our case. We therefore expect that pile-up does not significantly affect the trends we observe. Last but not least, we have estimated the fluence rate at the position of the detector to be one order of magnitude lower for CBCT compared to fan-beam CT [56].

Energy-integrating detector model

Our model only accounts for inter-pixel cross-talk via X-ray interactions, but we do not include a statistical model that accounts for their conversion to optical photons and the subsequent detection in indirect-conversion EIDs, and neither do we include a model for cross-talk due to optical photons.

Dual-layer detector model

Our model of a realistic dual-layer detector has several limitations, among which are the following:
(1) We keep the combined thickness of the top and bottom layer detection layers fixed at a thickness of 1.9 mm, corresponding to 1.6 mm CsI, merely to reduce the search space used for optimisation. This condition could be relaxed in future work.
(2) We only investigate CsI as a material for the detection layers and only copper for the filtration layer. However, as shown by Cai et al [6], an iodine solution-based filtration layer worked best for the imaging tasks investigated in their work.
(3) Our X-ray transport model does not take into account the spreading of the X-ray beam after leaving the top layer or, if applicable, filtration layer due to scattering. If we consider two pixels of interest $\boldsymbol{n}'_{\text{top}}$ and $\boldsymbol{n}'_{\text{bottom}}$ in the top and bottom layer lying directly on top of each other, then the inter-pixel cross-scatter from pixels $\boldsymbol{n}_{\text{top}} \neq \boldsymbol{n}'_{\text{top}}$ into $\boldsymbol{n}'_{\text{bottom}}$ is neglected in our model. Taking this effect into account would further degrade the performance of the dual-layer detector.

kVp-switching setup with one PCD

We assume that the thresholds can be set individually for the duration of the LE and HE phase of the source, believing that it is feasible to do so (Table 3.B.9 and 3.B.19). Tables 3.B.10 and 3.B.20 show the results if the thresholds are kept the same for both the LE and HE phase of the source, leading to an increase in CRLB by up to 17 % and 5.4 % assuming an ideal and realistic detector response, respectively.

CRLB formalism

While the CRLB gives the theoretical limit of performance, it does not state which estimator can reach this limit and if such an estimator exists. Moreover, the approach of comparing different spectral CBCT setups based on their CRLB can unfortunately not be extended to single-energy SPR estimation since SPR depends on the two variables ρ_{elec} and I, hence, there exists no unbiased estimator for extracting SPR via ρ_{elec} and I from a single-energy measurement. While in principle it is possible to calculate the CRLB on extracting SPR using a single-energy measurement under the assumption that the SPR only depends on ρ_{elec} and under the assumption of a fixed excitation energy, the expression for SPR would then be biased and the variance introduced by the dependency on I would be neglected. Consequently, our methodology cannot be used to compare the results based on spectral CBCT presented here to single-energy CBCT. Furthermore, we cannot compare the CRLB values on SPR extraction we obtain with values reported in literature, since the CRLB values depend linearly on the number of photons emitted by the source. Without knowing this number precisely, a comparison to experimental values of variance on SPR cannot be drawn. Moreover, values reported in literature are mostly obtained using image-based methods and hence influenced by both the choice of reconstruction algorithm and the conversion scheme from HU to SPR values. Similarly, we cannot quantify the range uncertainty achievable with the setups investigated in this study. We therefore plan a follow-up simulation study to compare our CRLB approach to image-based methods.

3.4.3 Closing Remarks

One main difference between cone-beam CT and fan-beam CT is the increased scatter in CBCT. To give an intuition for how this affects performance, a selection of results without any (cross-) scatter can be found in Section 3.B.8 of the Appendix. While removing scatter approximately halves the resulting CRLB values, we note that this is better than what even a fan-beam CT could achieve.

Since the location of the optimum parameters weakly depends on the length of the ray traversing the object (see Figure 3.B.1 in the Appendix), the threshold of PCDs should ideally be set on a per-pixel basis, or even dynamically. However, this obviously necessitates more elaborate reconstruction algorithms and calibration procedures.

We observe that the performance of the source ultimately determines whether a kVp-switching or a dual-source setup performs better. In our simulation we assume an ideal kVp-switching source capable of instant and perfect transitions between source voltages and mAs levels, which in reality is not the case. However, we note that, first, we focus on gantry-mounted CBCT with rotation times in the order of 60 s, which therefore provides more time for switching voltages and currents. Current ratios of $4:1$, and therefore mAs ratios, for a rapid switching source with a cycle frequency of 7.5 Hz were reported [9]. Second, a limited current-switching capability of a source can be mitigated by using different duty cycles for the low and high energy levels, assuming that the acquisition time of the detector can be adjusted accordingly. Using this technique, mAs ratios between $5.7:1$ to $1:5.7$ were reported for a clinical-grade fan-beam CT switching source [38]. Third, novel X-ray sources, such as those based on carbon nanotubes, could offer an alternative approach that also addresses the imperfect separation of voltage levels, moreover, they might offer greater flexibility in designing the source by being able to incorporate multiple focal spots into a compact housing with optional individual filtration [23, 64, 65]. This also offers the possibility of using an array of source focal spots to realise a more fan-beam-like geometry, reducing scatter and limiting reconstruction artefacts due to insufficient data [13, 44].

3.5 Conclusion

In this work, we compared different realisations of simulated spectral cone-beam CT with respect to their suitability for extracting proton stopping power ratios. The investigated setups were as follows:

- A single X-ray source operating at a fixed voltage with a PCD,
- A single source operating at a fixed voltage with a dual-layer detector,
- A rapid voltage-switching source with an EID,
- A rapid voltage-switching source with a PCD,
- Two sources at different fixed voltages coupled with an EID each,
- Two sources at different fixed voltages coupled with a PCD each.

All setups were optimised with respect to their main operating parameters to allow for a fair comparison between them. The figure of merit was the lowest possible variance on SPR as given by the CRLB. We found that setups based on a single source benefit from the absence of cross-scatter, that a higher source voltage or a larger energy separation appear beneficial for the extraction of SPR, and that the effect of charge sharing in direct-conversion PCDs strongly degrades the accuracy of SPR estimation. Assuming an ideal source and a realistic detector response, a kVp-switching setup coupled with an EID performs best, and a single-source setup based on a dual-layer detector performs worst.

Code and Data Availability

The code and data used in this work can be found here: https://doi.org/10.4121/bd754669-5af8-4e2d-9a70-37ac56bd6674.

Acknowledgements

The authors would like to acknowledge the high-performance computing clusters provided by the ICT department of TU Delft. We would also like to thank Rolf Behling for fruitful discussions. DL would like to thank Dan Wang for help with the Cramér-Rao Lower Bound formalism. Furthermore, we would like to thank the open source software community for creating GATE, GEANT4, JUPYTER, NUMPY, PYTHON, UPROOT and all other open source software that was directly or indirectly used in this work.

References

[1] J. Allison, K. Amako, J. Apostolakis, *et al.*, "Recent developments in Geant4", *Nuclear Instruments and Methods in Physics Research Section A: Accelerators, Spectrometers, Detectors and Associated Equipment*, vol. 835, pp. 186–225, 2016. DOI: 10.1016/j.nima.2016.06.125.

[2] R. E. Alvarez and A. Macovski, "Energy-selective reconstructions in X-ray computerised tomography", *Physics in Medicine and Biology*, vol. 21, no. 5, pp. 733–744, 1976. DOI: 10.1088/0031-9155/21/5/002.

[3] E. Bär, A. Lalonde, G. Royle, H.-M. Lu, and H. Bouchard, "The potential of dual-energy CT to reduce proton beam range uncertainties", *Medical Physics*, vol. 44, no. 6, pp. 2332–2344, 2017. DOI: 10.1002/mp.12215.

[5] A. Bolsi, M. Peroni, D. Amelio, *et al.*, "Practice patterns of image guided particle therapy in Europe: A 2016 survey of the European Particle Therapy Network (EPTN)", *Radiotherapy and Oncology*, vol. 128, no. 1, pp. 4–8, 2018. DOI: 10.1016/j.radonc.2018.03.017.

[6] E. Y. Cai, C. De Caro, K. Treb, and K. Li, "Benefits of using removable filters in dual-layer flat panel detectors", *Physics in Medicine & Biology*, vol. 68, no. 8, p. 085 013, 2023. DOI: 10.1088/1361-6560/acc77d.

[7] Z. Chen, M. M. Dominello, M. C. Joiner, and J. W. Burmeister, "Proton versus photon radiation therapy: A clinical review", *Frontiers in Oncology*, vol. 13, p. 1 133 909, 2023. DOI: 10.3389/fonc.2023.1133909.

[8] I. E. Commission, *IEC 61267:2005 standard, Medical diagnostic X-ray equipment - Radiation conditions for use in the determination of characteristics*, https://webstore.iec.ch/publication/5079, 2005.

[9] M. Haytmyradov, H. Mostafavi, A. Wang, *et al.*, "Markerless tumor tracking using fast-kV switching dual-energy fluoroscopy on a benchtop system", *Medical Physics*, vol. 46, no. 7, pp. 3235–3244, 2019. DOI: 10.1002/mp.13573.

[11] S. S. Hsieh and N. J. Pelc, "A Dynamic Attenuator Improves Spectral Imaging With Energy-Discriminating, Photon Counting Detectors", *IEEE Transactions on Medical Imaging*, vol. 34, no. 3, pp. 729–739, 2015. DOI: 10.1109/TMI.2014.2360381.

[12] S. S. Hsieh and N. J. Pelc, "Improving pulse detection in multibin photon-counting detectors", *Journal of Medical Imaging*, vol. 3, no. 2, p. 023 505, 2016. DOI: 10.1117/1.JMI.3.2.023505.

[13] Y. Hu, S. Xu, B. Li, *et al.*, "Improving the accuracy of bone mineral density using a multi-source CBCT", *Scientific Reports*, vol. 14, no. 1, p. 3887, 2024. DOI: 10.1038/s41598-024-54529-4.

[14] E. M. Huijben, M. L. Terpstra, A. J. Galapon, *et al.*, "Generating synthetic computed tomography for radiotherapy: SynthRAD2023 challenge report", *Medical Image Analysis*, vol. 97, p. 103 276, 2024. DOI: 10.1016/j.media.2024.103276.

[15] International Commission on Radiation Units and Measurements, Ed., *ICRU Report 49: Stopping Powers and Ranges for Protons and Alpha Particles* (ICRU Report 49). Bethesda, MD: International Commission on Radiation Units and Measurements, 1993.

[16] Katsuyuki Taguchi, "The Number of Energy Windows for Photon Counting Detectors: Is More Actually More?", *Proceedings of CT meeting 2020*, pp. 422–425, 2020.

[17] C. Kurz, F. Kamp, Y.-K. Park, *et al.*, "Investigating deformable image registration and scatter correction for CBCT-based dose calculation in adaptive IMPT", *Medical Physics*, vol. 43, no. 10, pp. 5635–5646, 2016. DOI: 10.1118/1.4962933.

[18] G. Landry, G. Dedes, C. Zöllner, *et al.*, "Phantom based evaluation of CT to CBCT image registration for proton therapy dose recalculation", *Physics in Medicine and Biology*, vol. 60, no. 2, pp. 595–613, 2015. DOI: 10.1088/0031-9155/60/2/595.

[19] G. Landry and C.-h. Hua, "Current state and future applications of radiological image guidance for particle therapy", *Medical Physics*, vol. 45, no. 11, 2018. DOI: 10.1002/mp.12744.

[20] G. Landry, R. Nijhuis, G. Dedes, *et al.*, "Investigating CT to CBCT image registration for head and neck proton therapy as a tool for daily dose recalculation", *Medical Physics*, vol. 42, no. 3, pp. 1354–1366, 2015. DOI: 10.1118/1.4908223.

[22] B. Li, H. C. Lee, X. Duan, *et al.*, "Comprehensive analysis of proton range uncertainties related to stopping-power-ratio estimation using dual-energy CT imaging", *Physics in Medicine & Biology*, vol. 62, no. 17, pp. 7056–7074, 2017. DOI: 10.1088/1361-6560/aa7dc9.

[23] B. Li, Y. Hu, S. Xu, *et al.*, "Low-cost dual-energy CBCT by spectral filtration of a dual focal spot X-ray source", *Scientific Reports*, vol. 14, no. 1, p. 9886, 2024. DOI: 10.1038/s41598-024-60774-4.

[24] J. F. Marsh, P. D. VanMeter, K. Rajendran, S. Leng, and C. H. McCollough, "Ex vivo coronary calcium volume quantification using a high-spatial-resolution clinical photon-counting-detector computed tomography", *Journal of Medical Imaging*, vol. 10, no. 04, 2023. DOI: 10.1117/1.JMI.10.4.043501.

[26] C. H. McCollough, K. Rajendran, S. Leng, *et al.*, "The technical development of photon-counting detector CT", *European Radiology*, vol. 33, no. 8, pp. 5321–5330, 2023. DOI: 10.1007/s00330-023-09545-9.

[27] C. Möhler, T. Russ, P. Wohlfahrt, *et al.*, "Experimental verification of stopping-power prediction from single- and dual-energy computed tomography in biological tissues", *Physics in Medicine & Biology*, vol. 63, no. 2, p. 025 001, 2018. DOI: 10.1088/1361-6560/aaa1c9.

[28] V. P. Moskvin, F. Pirlepesov, Y. Yan, *et al.*, "Accuracy of stopping power ratio calculation and experimental validation of proton range with dual-layer computed tomography", *Acta Oncologica*, vol. 61, no. 7, pp. 864–868, 2022. DOI: 10.1080/0284186X.2022.2069477.

[29] W. D. Newhauser and R. Zhang, "The physics of proton therapy", *Physics in Medicine and Biology*, vol. 60, no. 8, R155–R209, 2015. DOI: 10.1088/0031-9155/60/8/R155.

[30] J. Ödén, J. Zimmerman, R. Bujila, P. Nowik, and G. Poludniowski, "Technical Note: On the calculation of stopping-power ratio for stoichiometric calibration in proton therapy", *Medical Physics*, vol. 42, no. 9, pp. 5252–5257, 2015. DOI: 10.1118/1.4928399.

[31] N. Peters, V. Trier Taasti, B. Ackermann, *et al.*, "Consensus guide on CT-based prediction of stopping-power ratio using a Hounsfield look-up table for proton therapy", *Radiotherapy and Oncology*, vol. 184, p. 109 675, 2023. DOI: 10.1016/j.radonc.2023.109675.

[32] N. Peters, P. Wohlfahrt, C. Hofmann, *et al.*, "Reduction of clinical safety margins in proton therapy enabled by the clinical implementation of dual-energy CT for direct stopping-power prediction", *Radiotherapy and Oncology*, vol. 166, pp. 71–78, 2022. DOI: 10.1016/j.radonc.2021.11.002.

[33] G. Poludniowski, G. Landry, F. DeBlois, P. M. Evans, and F. Verhaegen, "SpekCalc: A program to calculate photon spectra from tungsten anode x-ray tubes", *Physics in Medicine and Biology*, vol. 54, no. 19, N433–N438, 2009. DOI: 10.1088/0031-9155/54/19/n01.

[34] K. Rajendran, M. Petersilka, A. Henning, *et al.*, "First Clinical Photon-counting Detector CT System: Technical Evaluation", *Radiology*, vol. 303, no. 1, pp. 130–138, 2022. DOI: 10.1148/radiol.212579.

[35] B. Rigaud, A. Simon, J. Castelli, *et al.*, "Deformable image registration for radiation therapy: Principle, methods, applications and evaluation", *Acta Oncologica*, vol. 58, no. 9, pp. 1225–1237, 2019. DOI: 10.1080/0284186X.2019.1620331.

[36] E. Roessl and C. Herrmann, "Cramér–Rao lower bound of basis image noise in multiple-energy x-ray imaging", *Physics in Medicine and Biology*, vol. 54, no. 5, pp. 1307–1318, 2009. DOI: 10.1088/0031-9155/54/5/014.

[37] M. Saito, "Potential of dual-energy subtraction for converting CT numbers to electron density based on a single linear relationship: Conversion of energy-subtracted CT number to electron density", *Medical Physics*, vol. 39, no. 4, pp. 2021–2030, 2012. DOI: 10.1118/1.3694111.

[38] O. F. Sandvold, R. Proksa, H. Daerr, *et al.*, "Hybrid spectral CT system with clinical rapid kVp-switching x-ray tube and dual-layer detector for improved iodine quantification", in *Medical Imaging 2024: Physics of Medical Imaging*, R. Fahrig, J. M. Sabol, and K. Li, Eds., San Diego, United States: SPIE, 2024, p. 51. DOI: 10.1117/12.3006451.

[39] D. Sarrut, M. Bardiès, N. Boussion, *et al.*, "A review of the use and potential of the GATE Monte Carlo simulation code for radiation therapy and dosimetry applications: GATE for dosimetry", *Medical Physics*, vol. 41, no. 6Part1, p. 064 301, 2014. DOI: 10.1118/1.4871617.

[40] U. Schneider, E. Pedroni, and A. Lomax, "The calibration of CT Hounsfield units for radiotherapy treatment planning", *Physics in Medicine and Biology*, vol. 41, no. 1, pp. 111–124, 1996. DOI: 10.1088/0031-9155/41/1/009.

[41] J. Seco and M. F. Spadea, "Imaging in particle therapy: State of the art and future perspective", *Acta Oncologica*, vol. 54, no. 9, pp. 1254–1258, 2015. DOI: 10.3109/0284186X.2015.1075665.

[42] S. M. Seltzer and M. J. Berger, "Evaluation of the collision stopping power of elements and compounds for electrons and positrons", *The International Journal of Applied Radiation and Isotopes*, vol. 33, no. 11, pp. 1189–1218, 1982. DOI: 10.1016/0020-708X(82)90244-7.

[43] J. H. Siewerdsen, M. J. Daly, B. Bakhtiar, *et al.*, "A simple, direct method for x-ray scatter estimation and correction in digital radiography and cone-beam CT: X-ray scatter correction", *Medical Physics*, vol. 33, no. 1, pp. 187–197, 2005. DOI: 10.1118/1.2148916.

[44] D. Spronk, Y. Luo, C. R. Inscoe, Y. Z. Lee, J. Lu, and O. Zhou, "Evaluation of carbon nanotube x-ray source array for stationary head computed tomography", *Medical Physics*, vol. 48, no. 3, pp. 1089–1099, 2021. DOI: 10.1002/mp.14696.

[45] Steven M Kay, *Fundamentals of Statistical Signal Processing: Estimation Theory*. Prentice-Hall, Inc., 1993, vol. 1.

[46] K. Stierstorfer, "Modeling the frequency-dependent detective quantum efficiency of photon-counting x-ray detectors", *Medical Physics*, vol. 45, no. 1, pp. 156–166, 2018. DOI: 10.1002/mp.12667.

[47] V. T. Taasti, G. J. Michalak, D. C. Hansen, *et al.*, "Validation of proton stopping power ratio estimation based on dual energy CT using fresh tissue samples", *Physics in Medicine & Biology*, vol. 63, no. 1, p. 015 012, 2017. DOI: 10.1088/1361-6560/aa952f.

[48] V. T. Taasti, J. B. B. Petersen, L. P. Muren, J. Thygesen, and D. C. Hansen, "A robust empirical parametrization of proton stopping power using dual energy CT", *Medical Physics*, vol. 43, no. 10, pp. 5547–5560, 2016. DOI: 10.1118/1.4962934.

[49] V. T. Taasti, L. P. Muren, K. Jensen, *et al.*, "Comparison of single and dual energy CT for stopping power determination in proton therapy of head and neck cancer", *Physics and Imaging in Radiation Oncology*, vol. 6, pp. 14–19, 2018. DOI: 10.1016/j.phro.2018.04.002.

[50] K. Taguchi, "Assessment of Multienergy Interpixel Coincidence Counters (MEICC) for Charge Sharing Correction or Compensation for Photon Counting Detectors With Boxcar Signals", *IEEE Transactions on Radiation and Plasma Medical Sciences*, vol. 5, no. 4, pp. 465–475, 2021. DOI: 10.1109/TRPMS.2020.3003251.

[51] K. Taguchi, D. R. Schaart, M. C. Goorden, and S. S. Hsieh, "Imaging performance of a $LaBr_3$:Ce scintillation detector for photon counting x-ray computed tomography: Simulation study", *Medical Physics*, vol. 52, no. 1, pp. 158–170, 2025. DOI: 10.1002/mp.17436.

[52] K. Taguchi, K. Stierstorfer, C. Polster, O. Lee, and S. Kappler, "Spatio-energetic cross-talk in photon counting detectors: Numerical detector model (PcTK) and workflow for CT image quality assessment", *Medical Physics*, vol. 45, no. 5, pp. 1985–1998, 2018. DOI: 10.1002/mp.12863.

[53] R. Tanaka, K. Ichikawa, S. Mori, *et al.*, "Investigation on Effect of Image Lag in Fluoroscopic Images Obtained with a Dynamic Flat-panel Detector (FPD) on Accuracy of Target Tracking in Radiotherapy", *Journal of Radiation Research*, vol. 51, no. 6, pp. 723–731, 2010. DOI: 10.1269/jrr.10059.

[54] A. Thummerer, P. Zaffino, A. Meijers, *et al.*, "Comparison of CBCT based synthetic CT methods suitable for proton dose calculations in adaptive proton therapy", *Physics in Medicine & Biology*, vol. 65, no. 9, p. 095 002, 2020. DOI: 10.1088/1361-6560/ab7d54.

[55] S. J. Van Der Sar, S. E. Brunner, and D. R. Schaart, "Silicon photomultiplier-based scintillation detectors for photon-counting CT: A feasibility study", *Medical Physics*, vol. 48, no. 10, pp. 6324–6338, 2021. DOI: 10.1002/mp.14886.

[56] S. J. Van Der Sar and D. R. Schaart, "Performance of X-ray Photon-Counting Scintillation Detectors Under Pile-up Conditions at 60 keV", *IEEE Transactions on Radiation and Plasma Medical Sciences*, pp. 1–1, 2025. DOI: 10.1109/TRPMS.2025.3532592.

[57] A. S. Wang and N. J. Pelc, "Sufficient Statistics as a Generalization of Binning in Spectral X-ray Imaging", *IEEE Transactions on Medical Imaging*, vol. 30, no. 1, pp. 84–93, 2011. DOI: 10.1109/TMI.2010.2061862.

[58] A. S. Wang, D. Harrison, V. Lobastov, and J. E. Tkaczyk, "Pulse pileup statistics for energy discriminating photon counting x-ray detectors: Pulse pileup statistics for photon counting detectors", *Medical Physics*, vol. 38, no. 7, pp. 4265–4275, 2011. DOI: 10.1118/1.3592932.

[62] P. Wohlfahrt, C. Möhler, C. Richter, and S. Greilich, "Evaluation of Stopping-Power Prediction by Dual- and Single-Energy Computed Tomography in an Anthropomorphic Ground-Truth Phantom", *International Journal of Radiation Oncology*Biology*Physics*, vol. 100, no. 1, pp. 244–253, 2018. DOI: 10.1016/j.ijrobp.2017.09.025.

[63] Y. Xie, C. Ainsley, L. Yin, *et al.*, "*Ex vivo* validation of a stoichiometric dual energy CT proton stopping power ratio calibration", *Physics in Medicine & Biology*, vol. 63, no. 5, p. 055 016, 2018. DOI: 10.1088/1361-6560/aaae91.

[64] S. Xu, Y. Hu, B. Li, *et al.*, "Volumetric computed tomography with carbon nanotube X-ray source array for improved image quality and accuracy", *Communications Engineering*, vol. 2, no. 1, p. 71, 2023. DOI: 10.1038/s44172-023-00123-x.

[65] S. Xu, B. Li, C. R. Inscoe, *et al.*, "Evaluation of the feasibility of a multisource CBCT for maxillofacial imaging", *Physics in Medicine & Biology*, vol. 68, no. 17, p. 175 012, 2023. DOI: 10.1088/1361-6560/acea17.

[66] M. Yang, G. Virshup, J. Clayton, X. R. Zhu, R. Mohan, and L. Dong, "Theoretical variance analysis of single- and dual-energy computed tomography methods for calculating proton stopping power ratios of biological tissues", *Physics in Medicine and Biology*, vol. 55, no. 5, pp. 1343–1362, 2010. DOI: 10.1088/0031-9155/55/5/006.

Appendix

3.A Supplementary Methodology

3.A.1 Details on CRLB Implementation

The partial derivatives $\partial\mathbf{m}(\boldsymbol{\theta})/\partial\theta_i$ and $\partial\boldsymbol{\Sigma}(\boldsymbol{\theta})/\partial\theta_i$ in Equation 3.5 are obtained by calculating $\mathbf{m}$ and $\boldsymbol{\Sigma}$ for θ_i, $\theta_i \pm \Delta\theta_i$ and $\theta_i \pm 2\Delta\theta_i$, changing one component at a time (electron density or ionisation energy) while keeping the other fixed, and using the five-point method for calculating the first derivative: Let h be a function of θ_i, then

$$h'(\theta_i) = \left(-h(\theta_i + 2\Delta\theta_i) + 8h(\theta_i + \Delta\theta_i) - 8h(\theta_i - \Delta\theta_i) + h(\theta_i - 2\Delta\theta_i)\right) / \left(12 \cdot \Delta\theta_i\right)$$

The variation of electron density and ionisation energy is described in detail in section 3.A.2.

For the given object composition, we first calculate the expected number of primary photons arriving at the detector analytically based on the Lambert-Beer law, with attenuation coefficients extracted from the XRAYDB library [25] (version 4.4.7) on an energy grid with spacing of 1 keV. A (cross-)scatter component is then added as described in Section 3.2.7, resulting into the spectrum $\boldsymbol{\Phi}_E$ of photons arriving at the detector. Applying a detector response function as described in Section 3.2.8 and 3.A.3 yields the spectrum $\boldsymbol{\varphi}_{E',\boldsymbol{n}'}$ of events in a given pixel $\boldsymbol{n}'$.

With that, the mean $\mathbf{m}(\boldsymbol{\theta})$ and the variance $\boldsymbol{\Sigma}(\boldsymbol{\theta})$in case of a PCD can be calculated as follows:

$$\mathbf{m}_k = \sum_{E_{k,1} \leq E' < E_{k,2}} \boldsymbol{\varphi}^{\text{reg}}_{E',\boldsymbol{n}'} \tag{3.A.1}$$

$$\boldsymbol{\Sigma}_k = \mathbf{m}_k \tag{3.A.2}$$

where k indicates the energy bin ranging from energy $E_{k,1}$ up to $E_{k,2}$.

The expressions for the mean and variance in case of an energy-integrating detector are (see Whiting et al [61] and Lasio et al [21]):

$$\mathbf{m}_k = \sum_{E'} E' \cdot \boldsymbol{\varphi}^{\text{depos},\,k}_{E',\boldsymbol{n}'} \tag{3.A.3}$$

$$\boldsymbol{\Sigma}_k = \sum_{E'} E'^2 \cdot \boldsymbol{\varphi}^{\text{depos},\,k}_{E',\boldsymbol{n}'} \tag{3.A.4}$$

where k indicates either the spectrum (setup with multiple X-ray spectra) or the layer (dual-layer detector setup).

In our case, the covariance is always zero. This also applies to the dual-layer detector: The absorption of photons in a layer constitutes a binomial selection, which, however, does not introduce a statistical dependence between the number of photons deposited in the top and bottom layer. Hence, the covariance between the measurements in the top and bottom layer is zero; see Section 11.1.3 in the book by Barrett and Myers [4].

As shown in this Appendix, Section 3.B.1, the optimum parameters resulting in the lowest CRLB for a single ray depend on the length of the ray within the phantom. Hence, in order to optimise the acquisition parameters for a specific object, ideally a combined CRLB should be calculated using every pixel of the detector and for every projection angle. Since we use a rotationally symmetric phantom (see Section 3.2.5), it is sufficient to optimise the CRLB for one projection angle. Furthermore, due to the high computational cost of calculating the CRLB for every detector pixel, we use a small subset of detector pixels. Due to the geometry of our setup with

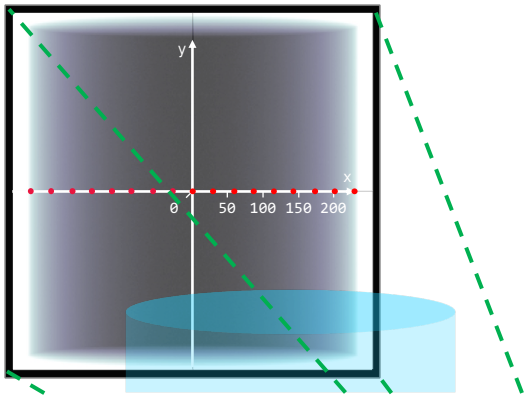

Figure 3.A.1: The figure indicates the sampled detector coordinates (red dots) used for the CRLB calculation in millimetres, with the centre of the detector as the origin of the coordinate system. The axes of the coordinate system coincide with the symmetry axes of the phantom's X-ray shadow on the detector.

its large source-to-detector distance (see Section 3.2.5), the length of the ray that lies within the phantom barely changes along the y-direction of the detector; as a result, it is sufficient to sample the detector coordinates only along the x-axis (see Figure 3.A.1). We choose a subsets of coordinates on the detector along the x-axis such that the mean distance travelled by the rays through the phantom and reaching this subset of coordinates is the same as the mean for all detector pixels, within a margin of 5 %. The following x-coordinates are selected: [0, ±29, ±59, ±87, ±115, ±143, ±173, ±201, ±229] mm; we exploit mirror symmetry whenever possible.

To arrive at the final CRLB value, we sum the CRLB values obtained for each individual pixel.

3.A.2 Details on Object and Material Definitions, Setup Geometry

The mass fractions of soft tissue mass and bone mass relative to the total body mass of humans are taken from White et al [60]. For both the male and female specimen (total weights of 70 kg and 58 kg, respectively) investigated by White et al, we add the weight of miscellaneous soft tissues and body fluids (1013 g and 186 g, respectively) to the weight of soft tissues (62 658 g and 52 590 g, respectively). The mass fraction of soft tissue mass to total body mass is then (averaged over both male and female specimen) 0.9098.

The elemental composition and mass density of soft tissue are set to the tissue definition of 'Group 1 (all soft tissues)' in Table III by White et al, averaged for both the female and male specimen (see Table 3.A.1).

The remaining tissue is defined as cortical bone (see Table 3.A.1), with properties similar to the tissue 'Skeleton cortical bone' in Table 4.4 of the ICRU report 44 [59]. Deviating from the ICRU publication, chlorine and potassium are omitted, and its mass density is set to 1.232 g/cm^3 in order to yield a mass density of 1.041 g/cm^3 for the whole body; the latter value is calculated based on the data presented by Heymsfield et al [10] assuming an equal ratio between the number of male and female specimen.

In case of the MC simulation, the object is defined as a volume filled homogeneously with the combined soft tissue/bone composition (lower half of Figure 3.A.2). For the calculation of line

Table 3.A.1: Elemental compositions, mass densities and mass fractions of the tissues used in this work, along with the mean ionisation energies calculated based on Equation 3.2. f_p is the mass fraction of element p for a given tissue, Δf_p is the change in mass fraction in order to calculate the partial derivative with respect to the ionisation energy (for details see text).

	Soft tissue		Bone		Combined
	f_i	Δf_p	f_p	Δf_p	f_p
Composition [%]:					
Calcium	0.00	0.0	22.50	0.092	2.03
Carbon	28.55	0.2855	15.50	−0.106	27.37
Chlorine	0.15	0.0015	0.00	0.0	0.14
Hydrogen	10.55	−0.006 398	3.40	−0.029	9.90
Magnesium	0.00	0.0	0.20	0.0	0.02
Nitrogen	2.55	0.0255	4.20	0.003	2.70
Oxygen	57.45	−0.313 602	43.50	−0.001	56.19
Phosphor	0.20	0.002	10.30	0.042	1.11
Potassium	0.20	0.002	0.00	0.0	0.18
Sodium	0.10	0.001	0.10	−0.001	0.10
Sulfur	0.25	0.002	0.30	0.0	0.25
Mass density ρ_{mass} [g/cm^3]	1.025		1.232		1.041
Mass fraction r	0.9098		0.0902		1
Ionisation energy I [eV]	71.43		112.0		74.21

integrals as part of the CRLB formalism, the volume is defined using two separate compartments of soft tissue and bone (upper half of Figure 3.A.2). Based on the mass fractions r_1 and r_2 of soft tissue and bone to total body mass, as well as the mass densities $\rho_{\text{mass, 1}}$ and $\rho_{\text{mass, 2}}$ of these tissues, the ratio of the ray length through soft tissue to the ray length through bone is then equal to $r_1/\rho_{\text{mass, 1}} \cdot \rho_{\text{mass, 2}}/r_2$.

To calculate the partial derivatives $\partial\mathbf{m}(\boldsymbol{\theta})/\partial\theta_i$ and $\partial\boldsymbol{\Sigma}(\boldsymbol{\theta})/\partial\theta_i$ with respect to electron density and ionisation energy, one of the parameters needs to be changed while keeping the other parameter fixed. The electron density is changed in steps of 1 % by changing the mass density. The ionisation energy is changed in steps of (1.0000 ± 0.0001) eV by changing the composition of the tissues: Let f_p be the mass fraction of element p for a given tissue and let Δf_p be its change in mass fraction, then the mass fractions of the altered tissue composition can be calculated according to $\tilde{f}_p = f_p - \alpha\Delta f_p$, with $\alpha \in$ [0.51917, 0.26096, 0, -0.263787, -0.530467] for the change in soft tissue composition and $\alpha \in$ [-0.0836295, -0.042051, 0, 0.042532, 0.0855569] for the change in bone composition; Table 3.A.1 lists Δf_p for both soft tissue and bone.

The elemental ionisation energies we use are as follows: Ca: 215.8 eV, C: 81.00 eV, Cl: 180.0 eV, H: 19.20 eV, Mg: 176.3 eV, N: 82.00 eV, O: 106.0 eV, P: 195.5 eV, K: 214.7 eV, Na: 168.4 eV, S: 203.4 eV. For water, this results in a mean ionisation energy of 75.32 eV.

For the dimensions of the setup, we refer to Figure 3.A.2.

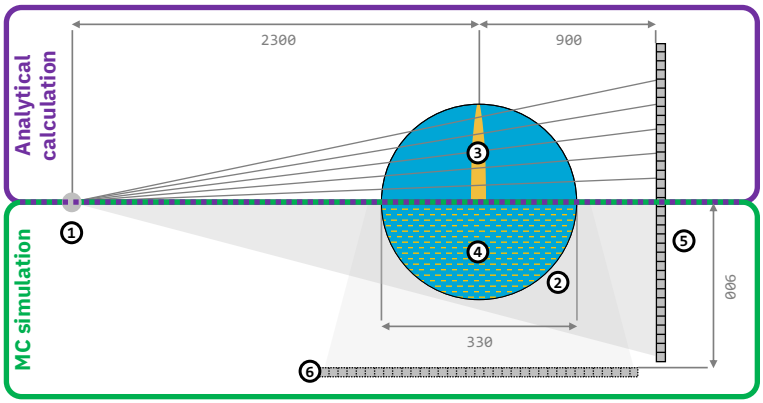

Figure 3.A.2: Schematic of the spectral CBCT simulation, consisting of an X-ray source (**1**), a cylindrical phantom (**2**) and a detector (**5**). For the analytical calculation of primary X-rays arriving at the detector (top half, **A**), the phantom is assumed to consist of a mixture of soft tissue (blue) and bone (yellow) with a fixed ratio of ray length through the two tissues (**3**). For the Monte-Carlo simulation of scatter and deposited dose (bottom half, **B**), the phantom is defined as a homogeneous mixture of soft tissue and bone (**4**). (**6**) indicates the position of a second detector in case a dual-source setup is simulated (second source and X-ray beam not shown). Dimensions are given in millimetres; the drawing is not to scale.

3.A.3 Details on Detector Response Functions

X-ray transport

This section applies to both EIDs (including realistic dual-layer detectors) and PCDs.

In order to mimic a realistic detector, we calculate the spectrum $\varphi^{\text{depos}}_{E',\boldsymbol{n}'}$ of deposited events of energy E' in a pixel of interest $\boldsymbol{n}'$ assuming an incoming spectrum of photons $\boldsymbol{\Phi}_{E,\boldsymbol{n}}$ arriving at the detector in pixel $\boldsymbol{n}$.

We employ a simplified approach that assumes that the spectrum of photons is constant for a small region $\mathcal{N}$ around a given pixel $\boldsymbol{n}'$, that is, $\boldsymbol{\Phi}_{E,\boldsymbol{n}} = \text{const.}\ \forall\ \boldsymbol{n} \neq \boldsymbol{n}', \boldsymbol{n} \in \mathcal{N}$, which is probably a good approximation in the case of our homogeneous cylindrical phantom. Furthermore, we assume that a variation of the line integral between source and pixel $\boldsymbol{n}'$, either due to a variation in electron density or composition to calculate the derivatives in Equation 3.5, only influences $\boldsymbol{\Phi}_{E,\boldsymbol{n}'}$ but not $\boldsymbol{\Phi}_{E,\boldsymbol{n}\neq\boldsymbol{n}'}$, and that without a variation $\boldsymbol{\Phi}_{E,\boldsymbol{n}'}$ equals $\boldsymbol{\Phi}_{E,\boldsymbol{n}\neq\boldsymbol{n}'}$. Hence, we set $\boldsymbol{\Phi}_{E,\boldsymbol{n}'}(\boldsymbol{\theta}) = \boldsymbol{\Phi}_{E,\boldsymbol{n}\neq\boldsymbol{n}'}(\boldsymbol{\theta}) = \boldsymbol{\Phi}_{E,\boldsymbol{n}\neq\boldsymbol{n}'}(\boldsymbol{\theta} \pm \boldsymbol{\Delta\theta}) = \boldsymbol{\Phi}_{E,\boldsymbol{n}\neq\boldsymbol{n}'}(\boldsymbol{\theta} \pm 2\boldsymbol{\Delta\theta})$ for a given tissue parameter $\boldsymbol{\theta}$ for which the CRLB is determined, whereas $\boldsymbol{\Phi}_{E,\boldsymbol{n}'}(\boldsymbol{\theta}) \neq \boldsymbol{\Phi}_{E,\boldsymbol{n}'}(\boldsymbol{\theta} \pm \boldsymbol{\Delta\theta}) \neq \boldsymbol{\Phi}_{E,\boldsymbol{n}'}(\boldsymbol{\theta} \pm 2\boldsymbol{\Delta\theta})$.

Let us now denote $\mathbf{P}^{\text{pixel}}_{E,E'}$ as the probability that a photon of energy E incident on a specific pixel deposits a total energy E' in that same pixel, and let us furthermore denote $\mathbf{P}^{\text{neighb}}_{E,E'}$ as the average number of events with total deposited energy E' in a given pixel caused by a photon of energy E incident on any pixel in the neighbourhood of that given pixel.

Given $\boldsymbol{\Phi}_{E,\boldsymbol{n}}$, we can then calculate the spectrum of deposited events and the spectrum of transmitted events (the latter only being relevant in case of dual-layer detectors) in the pixel

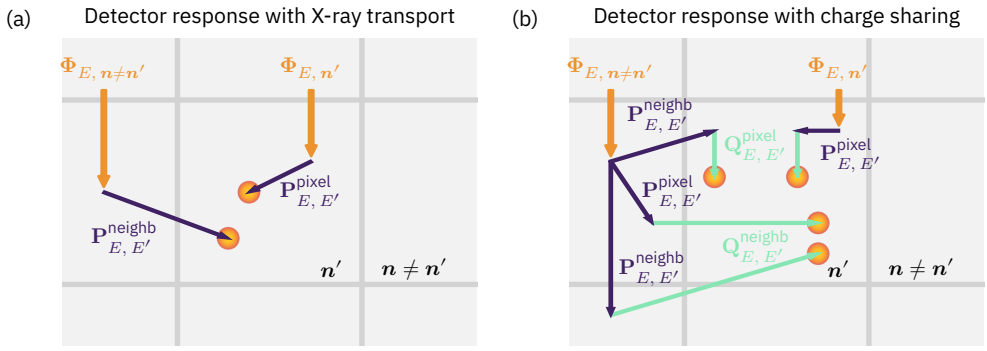

Figure 3.A.3: Schematic illustration of the detector response function modelling, using (a) only X-ray transport functions in the case of EIDs, or using (b) both X-ray transport and charge sharing transport functions in the case of PCDs. The orange dots indicate the location where events are registered.

of interest n':

$$\varphi^{\text{depos}}_{E',\, n'} = \sum_E \left(\mathbf{\Phi}_{E,\, n'} \cdot \mathbf{P}^{\text{pixel}}_{E,\, E'} + \mathbf{\Phi}_{E,\, n\neq n'} \cdot \mathbf{P}^{\text{neighb}}_{E,\, E'} \right) \quad ,$$

$$\varphi^{\text{transm}}_{E',\, n'} = \sum_E \mathbf{\Phi}_{E,\, n'} \cdot \mathbf{P}^{\text{transm}}_{E,\, E'} \quad . \tag{3.A.5}$$

(See Figure 3.A.3a for illustration.)

Considering the transmitted spectrum, please note that we do not take into account a widening of the transmitted beam due to scatter.

Charge sharing

This section on charge sharing only applies to PCDs.

In order to obtain the spectrum of registered events due to charge sharing, we need to consider events deposited in the pixel of interest n' with only part of their energy registered in n' due to charge sharing, photons incident on n' but scattering into adjacent pixels causing charge sharing events in n', and all other events deposited in pixels directly adjacent to n' and causing charge sharing events in n'.

The spectrum of deposited events $\varphi^{\text{depos}}_{E',\, n'}$ in the pixel of interest n' due to X-ray transport is determined as described in the previous section.

The spectrum of deposited events $\varphi^{\text{depos}}_{E',\, n\neq n'}$ in pixels $n \neq n'$ directly adjacent to the pixel of interest n' is determined by the spectrum $\mathbf{\Phi}_{E,\, n\neq n'}$ incident on $n \neq n'$ and the probability that a photon deposits its energy in $n \neq n'$, as well as photons scattering into $n \neq n'$. The photons scattering into $n \neq n'$ directly adjacent to n' originate from both n' as well as all other neighbouring pixels; since it is more likely that they originate from pixels $n \neq n'$ than from n', we assume for simplicity that all photons scattering into the pixels $n \neq n'$ directly adjacent to n' originate from neighbouring pixels with spectrum $\mathbf{\Phi}_{E,\, n\neq n'}$.

Let us now denote the charge sharing response function by $\mathbf{Q}$, where $\mathbf{Q}^{\text{pixel}}_{E,\, E'}$ specifies the probability that an energy deposition of energy E leads to an accumulation of a charge corresponding to an energy E' in in the same pixel. $\mathbf{Q}^{\text{neighb}}_{E,\, E'}$ specifies the average number of charge sharing

events with an energy E' in a given pixel caused by an energy deposition of energy E in any pixel in the neighbourhood of that given pixel.

Combining X-ray transport and charge sharing leads to the following spectrum of registered events in the pixel of interest $\boldsymbol{n}'$:

$$\varphi^{\text{reg}}_{E',\boldsymbol{n}'} = \sum_{E} \Big(\boldsymbol{\Phi}_{E,\boldsymbol{n}'} \cdot \mathbf{P}^{\text{pixel}}_{E,E'} \cdot \mathbf{Q}^{\text{pixel}}_{E,E'} + \boldsymbol{\Phi}_{E,\boldsymbol{n}\neq\boldsymbol{n}'} \cdot \left(\mathbf{P}^{\text{pixel}}_{E,E'} \cdot \mathbf{Q}^{\text{neighb}}_{E,E'} + \mathbf{P}^{\text{neighb}}_{E,E'} \cdot \mathbf{Q}^{\text{pixel}}_{E,E'} + \mathbf{P}^{\text{neighb}}_{E,E'} \cdot \mathbf{Q}^{\text{neighb}}_{E,E'} \right) \Big) \quad (3.A.6)$$

(See Figure 3.A.3b for illustration.)

3.A.4 X-ray Source Spectra

Figures 3.A.4 to 3.A.7 show the spectra emitted by the X-ray source employed in this work. X-ray spectra are obtained from SPEKCALC [33] for a tungsten target and an anode angle of 7° with energy steps of 1 keV. The intrinsic source filtration is assumed to be 0.8 mm Be and 0.89 mm Ti. For further beam hardening, 0.2, 0.4, 0.6 and 0.8 mm of tin are investigated.

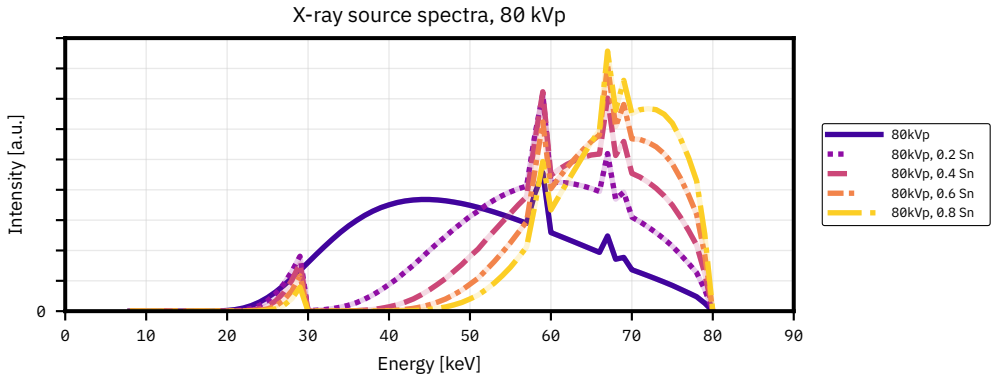

Figure 3.A.4: X-ray source spectra for a source voltage of 80 kVp and optional source filtration using tin, with thicknesses ranging between 0.2 and 0.8 mm tin.

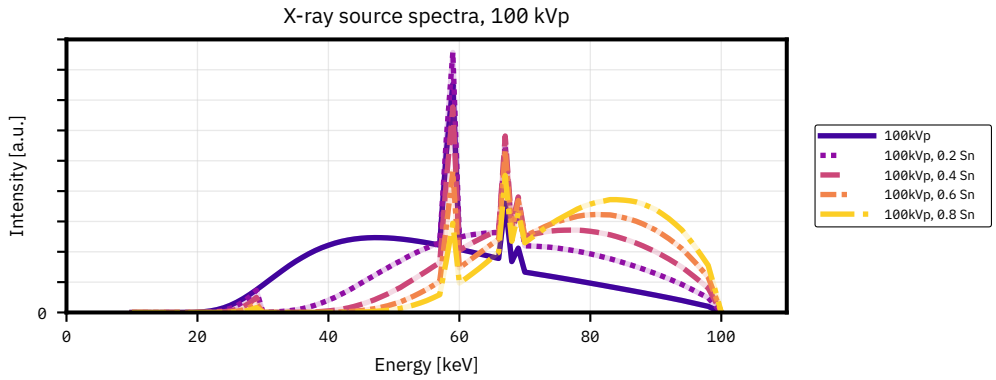

Figure 3.A.5: X-ray source spectra for a source voltage of 100 kVp and optional source filtration using tin, with thicknesses ranging between 0.2 and 0.8 mm tin.

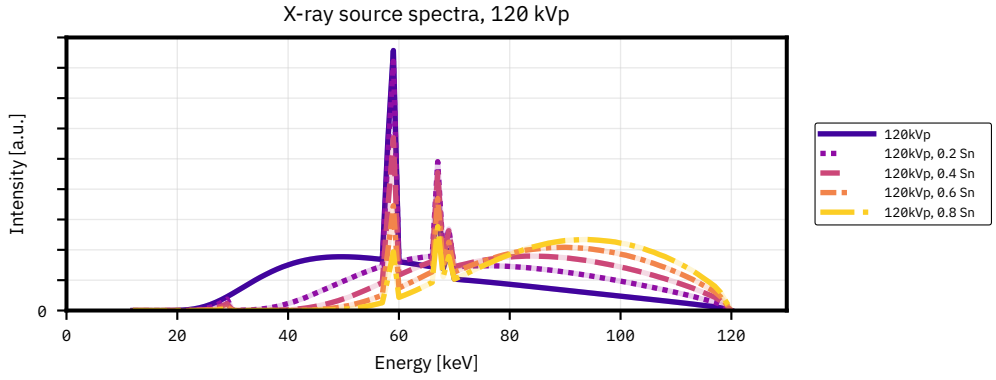

Figure 3.A.6: X-ray source spectra for a source voltage of 120 kVp and optional source filtration using tin, with thicknesses ranging between 0.2 and 0.8 mm tin.

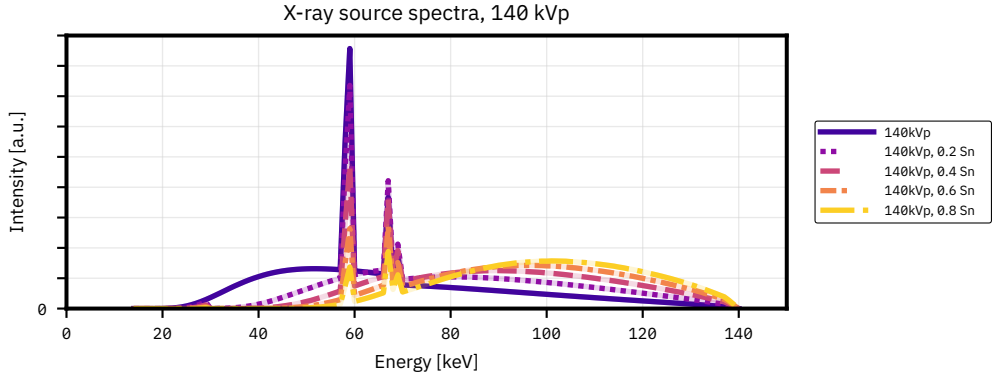

Figure 3.A.7: X-ray source spectra for a source voltage of 140 kVp and optional source filtration using tin, with thicknesses ranging between 0.2 and 0.8 mm tin.

3.B Supplementary Results

3.B.1 Dependence of Optimisation on Line Integral, on Number of Photons and on Tissue

Here we show that the optimum parameters resulting in the minimum CRLB depend on the length of the ray traversing the object (with fixed composition), as well as on whether one optimises parameters to extract the SPR of either soft tissue or bone. However, it does not depend on the number of photons used and hence not on the cumulative reference dose deposited in the phantom.

Please note that the lines in the figures in this section are normalised by their minima in order to allow for a convenient comparison.

Figure 3.B.1 shows normalised CRLB values for a kVp-switching setup coupled with an EID (80/140 kVp spectrum combination, (a)) and a single source coupled with a PCD (140 kVp, 2 bins, (b)) for different distances that the ray traverses the phantom. The ratio of the line integral over soft tissue to the line integral over bone is the same for all distances. As can be seen, the optimum parameters to achieve the minimum variance depend on the length of the ray within the phantom due to the change in the spectrum incident on the detector, caused by beam hardening.

Figure 3.B.2 shows normalised CRLB values for extracting SPR of either soft tissue or bone for the same setups and operating conditions as before, except that only the centre coordinate of the detector is used. The kVp-switching setup with an EID achieves the minimum CRLB value at a mAs ratio of $\mathrm{mAs}_{\mathrm{LE}} : \mathrm{mAs}_{\mathrm{HE}} = 4:1$ if optimising for the SPR extraction of bone, and at a mAs ratio of 5 : 1 if optimising for the SPR extraction of soft tissue. In case of the single-source setup with a PCD, the minimum CRLB for SPR extraction is found at a threshold value of 79 keV for the threshold between the LE and HE bin for both soft tissue and bone; however, the optimisation of the bin threshold was performed using a step size of 1 keV, and the data indicates that the minima are indeed distinct from each other with a difference smaller than 1 keV. Since the difference in the optimum parameters to achieve the minimum CRLB for either soft tissue and bone is so small, we restrict ourselves in this work to the extraction of SPR of soft tissue only.

Figure 3.B.3 shows normalised CRLB values for a single-source setup using a PCD with two bins and using different numbers of photons emitted by the source. The normalised CRLB values for different numbers of photons lie perfectly on top of each other, which indicates that the number of photons emitted by the source, and hence the arbitrarily chosen cumulative reference dose in the phantom, does not have an influence on the position of the minimum. For our simulations, the reference dose and hence the number of emitted photons is chosen such that the approximation of Poisson statistics by a normal distribution always holds.

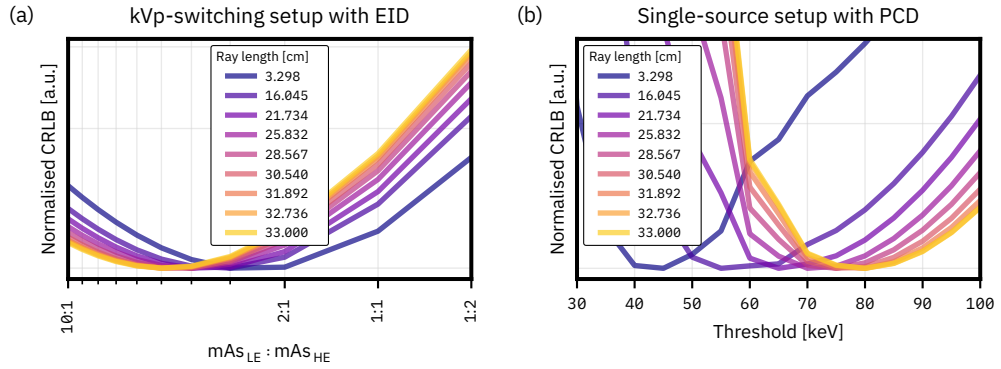

Figure 3.B.1: Normalised CRLB values for estimating SPR as achieved by the (a) kVp-switching setup with an EID for different ratios between the mAs_{LE} of the low energy phase at 80 kVp and the mAs_{HE} of the high energy phase at 140 kVp, and as achieved by the (b) single-source setup with a PCD with two bins for different locations of the threshold between the low and high energy bin and a 140 kVp spectrum. The CRLB values are calculated for different lengths of the line segment of the ray within the phantom (see legend). All lines are normalised by their minimum CRLB value to allow for a convenient comparison of the position of their minima.

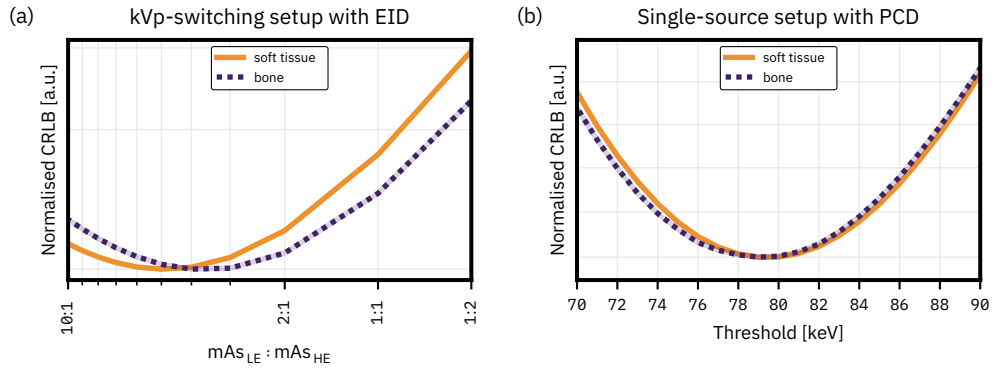

Figure 3.B.2: Normalised CRLB values for estimating SPR as achieved by the (a) kVp-switching setup with an EID for different ratios between the mAs_{LE} of the low energy phase at 80 kVp and the mAs_{HE} of the high energy phase at 140 kVp, and as achieved by the (b) single-source setup with a PCD with two bins for different locations of the threshold between the low and high energy bin and a 140 kVp spectrum. The CRLB values are for extracting SPR of either soft tissue or bone. All lines are normalised by their minimum CRLB value to allow for a convenient comparison of the position of their minima.

3

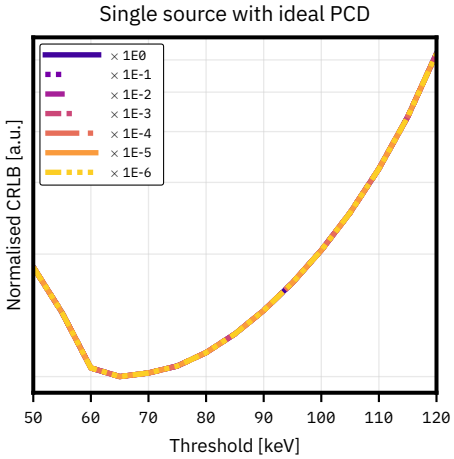

Figure 3.B.3: Normalised CRLB values for estimating SPR as achieved by the single-source setup with a PCD using two bins, for different locations of the threshold between the low and high energy bin, a 140 kVp spectrum and a single pixel only. The CRLB values are based on different numbers of emitted photons due to a reduction factor (see legend) applied to them. All lines are normalised by their minimum CRLB value to allow for a convenient comparison of the position of their minima.

3.B.2 Variance on MC-Generated Data, Influence on Reported CRLB Values

The number of primaries that is used in the MC simulations to obtain the (cross-)scatter components in one quadrant of the setup is $3.6 \cdot 10^{10}$. The (cross-)scatter data is then mirrored to the remaining three quadrants, utilising the symmetry of the setup.

The variance of the (cross-)scatter component is the only source of statistical error on the CRLB. We investigate the variance of the (cross-)scatter component and its influence on the CRLB results by repeating the MC simulation of a 140 kVp spectrum three times. Note that the smoothing of the (cross-)scatter component reduces the resulting variance in each pixel compared to that of the raw data.

We find that the maximum value for the relative standard deviation (standard deviation divided by mean) on the (cross-)scattered number of photons in a pixel after applying Gaussian smoothing is 0.38 % for the scatter component and 0.30 % for the cross-scatter component.

Furthermore, we check the influence of the variance of the smoothed (cross-)scatter component on the CRLB results for two cases, namely the single-source setup paired with an ideal dual-layer detector and the single-source setup paired with an ideal PCD detector. Table 3.B.1 reports the relative standard deviation of the CRLB values (σ(CRLB)/$\overline{\text{CRLB}}$) for these setups. It shows that the variance on the resulting CRLB values due to the variance on the (cross-)scatter component is negligibly small. Due to this, we do not investigate the variance on CRLB values further, and we do not report the variance on obtained CRLB values.

Table 3.B.1: Variance of CRLB results for a single source paired with either an ideal dual-layer detector or an ideal PCD, reported as relative standard deviations (σ(CRLB)/$\overline{\text{CRLB}}$) based on three different realisations of MC-generated (cross-)scatter data.

Setup	Operating parameters	σ(CRLB)/$\overline{\text{CRLB}}$ [%]
Single source with ideal dual-layer detector		
	140kVp, 16 keV filtration layer, bin edges = [20, 68, 84, 140] keV	0.16
Single source with ideal PCD		
PCD with 2 bins	140kVp, bin edges = [20, 76, 140] keV	0.19
PCD with 3 bins	140kVp, bin edges = [20, 70, 94, 140] keV	0.17
PCD with 4 bins	140kVp, bin edges = [20, 60, 75, 95, 140] keV	0.20
PCD with bins of 1 keV width	140kVp, bin edges = [20, 23, 24, ⋯, 139, 140] keV	0.14

3.B.3 Supplementary Results for Setup Optimisations Based on Ideal Detector Response Functions

Single source with PCD

Table 3.B.2: Results for the optimisation of the setup based on a single source with an ideal PCD using two energy bins. The table states the minimum nCRLB values that are achieved and their respective parameters.

Spectrum	Optimum thresholds [keV]	min. nCRLB
80 kVp	[20, 62, 80]	5.522
100 kVp	[20, 68, 100]	2.755
120 kVp	[20, 74, 120]	1.748
140 kVp	[20, 76, 140]	1.309
140 kVp, 0.2 mm Sn	[20, 84, 140]	1.458
140 kVp, 0.4 mm Sn	[20, 90, 140]	1.976
140 kVp, 0.6 mm Sn	[20, 96, 140]	2.782
140 kVp, 0.8 mm Sn	[20, 100, 140]	3.787

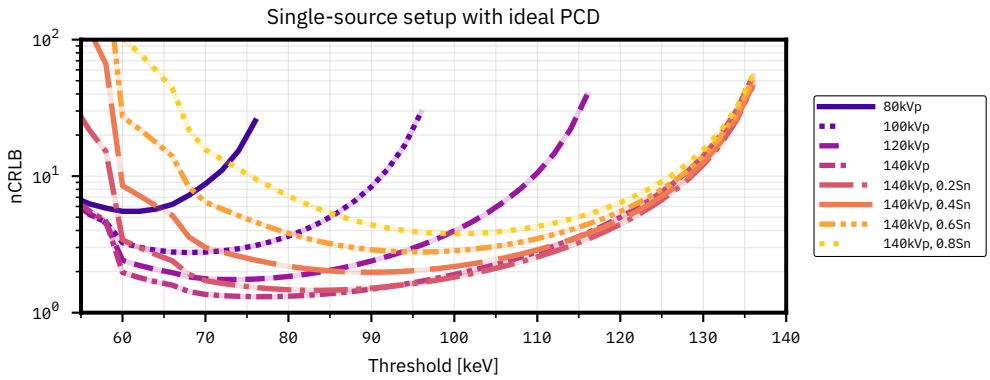

Figure 3.B.4: nCRLB values for estimating SPR as achieved by a single-source setup using an ideal PCD with two bins, for different locations of the threshold between the low and high energy bin and for different spectra.

Table 3.B.3: Results for the optimisation of the setup based on a single source with an ideal PCD using three energy bins. The table states the minimum nCRLB values that are achieved and their respective parameters.

Spectrum	Optimum thresholds [keV]	min. nCRLB
80 kVp	[20, 56, 66, 80]	4.671
100 kVp	[20, 62, 76, 100]	2.338
120 kVp	[20, 64, 82, 120]	1.536
140 kVp	[20, 70, 94, 140]	1.158
140 kVp, 0.2 mm Sn	[20, 74, 98, 140]	1.274
140 kVp, 0.4 mm Sn	[20, 82, 104, 140]	1.717
140 kVp, 0.6 mm Sn	[20, 88, 108, 140]	2.417
140 kVp, 0.8 mm Sn	[20, 94, 112, 140]	3.296

Table 3.B.4: Results for the optimisation of the setup based on a single source with an ideal PCD using four energy bins. The table states the minimum nCRLB values that are achieved and their respective parameters.

Spectrum	Optimum thresholds [keV]	min. nCRLB
80 kVp	[20, 55, 60, 70, 80]	4.497
100 kVp	[20, 60, 70, 80, 100]	2.246
120 kVp	[20, 60, 75, 90, 120]	1.465
140 kVp	[20, 60, 75, 95, 140]	1.111
140 kVp, 0.2 mm Sn	[20, 55, 70, 95, 140]	1.197
140 kVp, 0.4 mm Sn	[20, 55, 75, 100, 140]	1.559
140 kVp, 0.6 mm Sn	[20, 55, 85, 105, 140]	2.168
140 kVp, 0.8 mm Sn	[20, 55, 90, 110, 140]	2.965

Table 3.B.5: Results for the setup based on a single source with an ideal PCD using near-continuous energy binning. The first bin is between 3 to 5 keV wide to prevent photon starvation, whereas all subsequent bins have a width of 1 keV. The table states the resulting nCRLB values and their respective parameters. Please note that the nCRLB value for 140 kVp and 0.2 mm Sn filtration equals one by definition.

Spectrum	Thresholds [keV]	min. nCRLB
80 kVp	[20, 23, 24, ..., 79, 80]	4.092
100 kVp	[20, 23, 24, ..., 99, 100]	2.068
120 kVp	[20, 23, 24, ..., 119, 120]	1.341
140 kVp	[20, 23, 24, ..., 139, 140]	1.000
140 kVp, 0.2 mm Sn	[20, 25, 26, ..., 139, 140]	1.009
140 kVp, 0.4 mm Sn	[20, 25, 26, ..., 139, 140]	1.265
140 kVp, 0.6 mm Sn	[20, 25, 26, ..., 139, 140]	1.751
140 kVp, 0.8 mm Sn	[20, 25, 26, ..., 139, 140]	2.427

Single source with dual-layer detector

Table 3.B.6: Results for the optimisation of the setup based on a single source with an ideal dual-layer detector, for configurations with 2 bins (no filtration layer bin included) and three bins (filtration layer bin included). The table states the minimum nCRLB values that are achieved and their respective parameters.

Spectrum	Optimum thresholds without a filtration layer bin [keV]	Optimum thresholds with a filtration layer bin [keV]	min. nCRLB
80 kVp	[20, 60, 80]	—	5.580
	—	[20, 56, 66, 80]	4.738
100 kVp	[20, 66, 100]	—	2.716
	—	[20, 60, 74, 100]	2.367
120 kVp	[20, 70, 120]	—	1.707
	—	[20, 64, 80, 120]	1.528
140 kVp	[20, 72, 140]	—	1.254
	—	[20, 68, 84, 140]	1.158
140 kVp, 0.2 mm Sn	[20, 78, 140]	—	1.395
	—	[20, 72, 94, 140]	1.245
140 kVp, 0.4 mm Sn	[20, 84, 140]	—	1.924
	—	[20, 80, 102, 140]	1.692
140 kVp, 0.6 mm Sn	[20, 90, 140]	—	2.738
	—	[20, 86, 106, 140]	2.386
140 kVp, 0.8 mm Sn	[20, 96, 140]	—	3.712
	—	[20, 92, 110, 140]	3.228

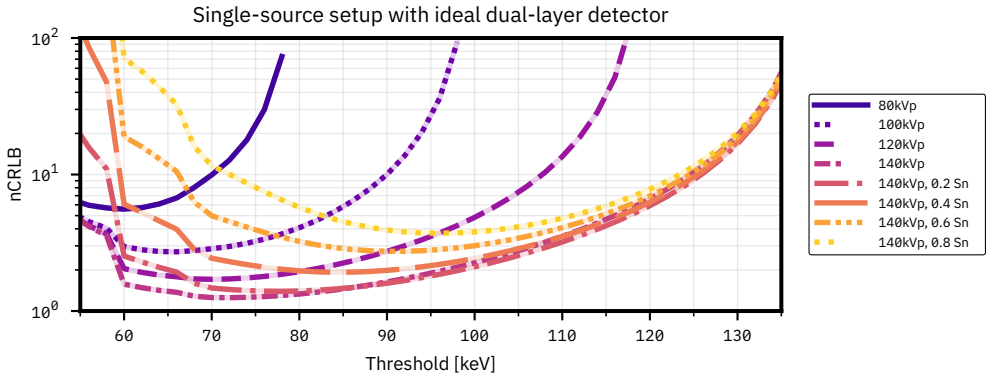

Figure 3.B.5: nCRLB values for estimating SPR as achieved by the ideal dual-layer detector for different locations of the threshold between the low and high energy bin, that is, without using a filtration layer bin, and spectra up to 140 kVp, with additional source filtration for the 140 kVp spectra. The filtration is specified in millimetres of tin.

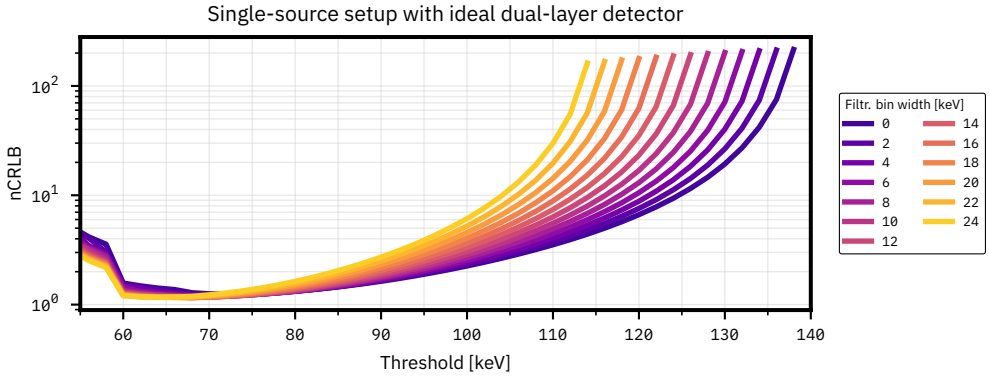

Figure 3.B.6: nCRLB values for estimating SPR as achieved by the ideal dual-layer detector with a spectrum of 140 kVp and no additional source filtration. The horizontal axis denotes the upper threshold of the LE bin. Each line corresponds to a different width of the filtration layer bin.

Single rapid voltage-switching source with EID

Table 3.B.7: Results for the optimisation of the kVp-switching setup using an ideal EID, optimising the ratio $mAs_{LE} : mAs_{HE}$ between the LE and HE phase. The table states the minimum nCRLB values that are achieved and their respective parameters.

Spectrum combination	mAs ratio $mAs_{LE} : mAs_{HE}$	min. nCRLB
80 kVp/100 kVp	2 : 1	20.88
80 kVp/120 kVp	3 : 1	6.487
80 kVp/140 kVp	4.5 : 1	3.484
LE & HE filtration		
80 kVp, 0.2 mm Sn/140 kVp, 0.2 mm Sn	7.5 : 1	2.301
80 kVp, 0.4 mm Sn/140 kVp, 0.4 mm Sn	12 : 1	1.907
80 kVp, 0.6 mm Sn/140 kVp, 0.6 mm Sn	19 : 1	1.718
80 kVp, 0.8 mm Sn/140 kVp, 0.8 mm Sn	29 : 1	1.621
100 kVp/120 kVp	1.5 : 1	31.27
100 kVp/140 kVp	2.25 : 1	9.328
120 kVp/140 kVp	1.5 : 1	44.53

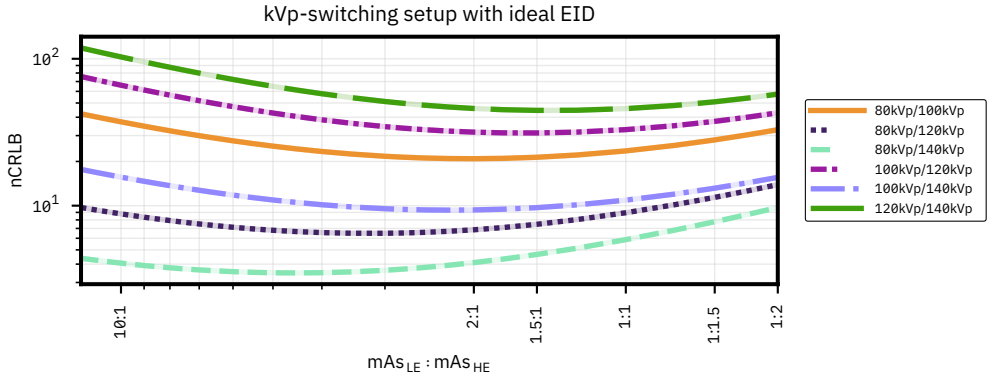

Figure 3.B.7: nCRLB values for estimating SPR as achieved by a kVp-switching setup using an ideal EID for different ratios $mAs_{LE} : mAs_{HE}$ between the LE and HE phase, and different spectrum combinations between 80 kVp and 140 kVp without additional source filtration.

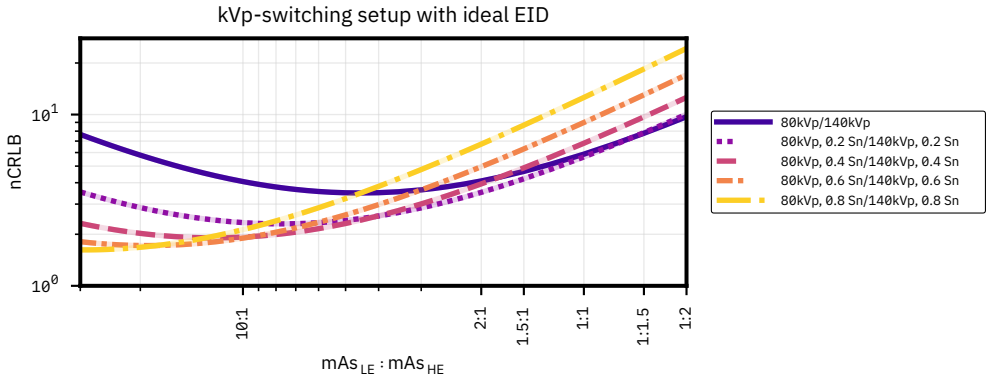

Figure 3.B.8: nCRLB values for estimating SPR as achieved by a kVp-switching setup using an ideal EID for different ratios $mAs_{LE} : mAs_{HE}$ between the LE and HE phase, using an 80/140 kVp spectrum combination and applying filtration to both the LE and HE spectrum. The filtration is specified in millimetres of tin.

Dual-source setup with two EIDs

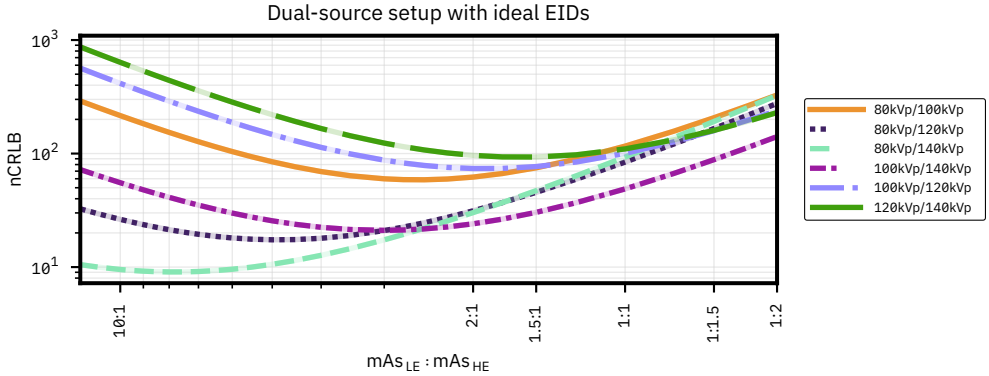

Figure 3.B.9: nCRLB values for estimating SPR as achieved by a dual-source setup using ideal EIDs for different ratios $mAs_{LE} : mAs_{HE}$ between the LE and HE spectrum, and different spectrum combinations without additional source filtration.

Table 3.B.8: Results for the optimisation of the dual-source setup using two ideal EIDs, optimising the ratio $mAs_{LE} : mAs_{HE}$ between the LE and HE spectrum. The table states the minimum nCRLB values that are achieved and their respective parameters.

Spectrum combination	mAs ratio $mAs_{LE} : mAs_{HE}$	min. nCRLB
80 kVp/100 kVp	2.5 : 1	58.75
80 kVp/120 kVp	5 : 1	17.40
80 kVp/140 kVp	8 : 1	9.063
LE filtration only		
80 kVp, 0.2 mm Sn/140 kVp	22.5 : 1	11.06
80 kVp, 0.4 mm Sn/140 kVp	50 : 1	45.10
HE filtration only		
80 kVp/140 kVp, 0.2 mm Sn	4.5 : 1	5.137
80 kVp/140 kVp, 0.4 mm Sn	3 : 1	3.857
80 kVp/140 kVp, 0.6 mm Sn	2.25 : 1	3.254
80 kVp/140 kVp, 0.8 mm Sn	1.75 : 1	2.915
LE & HE filtration		
80 kVp, 0.2 mm Sn/140 kVp, 0.2 mm Sn	13 : 1	5.352
80 kVp, 0.4 mm Sn/140 kVp, 0.4 mm Sn	20 : 1	4.229
80 kVp, 0.6 mm Sn/140 kVp, 0.6 mm Sn	30 : 1	3.717
80 kVp, 0.8 mm Sn/140 kVp, 0.8 mm Sn	50 : 1	3.420
100 kVp/120 kVp	2 : 1	73.84
100 kVp/140 kVp	3 : 1	21.08
LE filtration only		
100 kVp, 0.2 mm Sn/140 kVp	6.5 : 1	52.04
100 kVp, 0.4 mm Sn/140 kVp	12 : 1	192.1
100 kVp, 0.6 mm Sn/140 kVp	20 : 1	$3.785 \cdot 10^5$
100 kVp, 0.8 mm Sn/140 kVp	35 : 1	$2.343 \cdot 10^4$
HE filtration only		
100 kVp/140 kVp, 0.2 mm Sn	1.75 : 1	8.788
100 kVp/140 kVp, 0.4 mm Sn	1.25 : 1	5.827
100 kVp/140 kVp, 0.6 mm Sn	1 : 1.25	4.637
100 kVp/140 kVp, 0.8 mm Sn	1 : 1.5	3.968
LE & HE filtration		
100 kVp, 0.2 mm Sn/140 kVp, 0.2 mm Sn	4 : 1	13.52
100 kVp, 0.4 mm Sn/140 kVp, 0.4 mm Sn	5 : 1	11.22
100 kVp, 0.6 mm Sn/140 kVp, 0.6 mm Sn	6 : 1	10.25
100 kVp, 0.8 mm Sn/140 kVp, 0.8 mm Sn	7.5 : 1	9.846
120 kVp/140 kVp	1.5 : 1	93.24

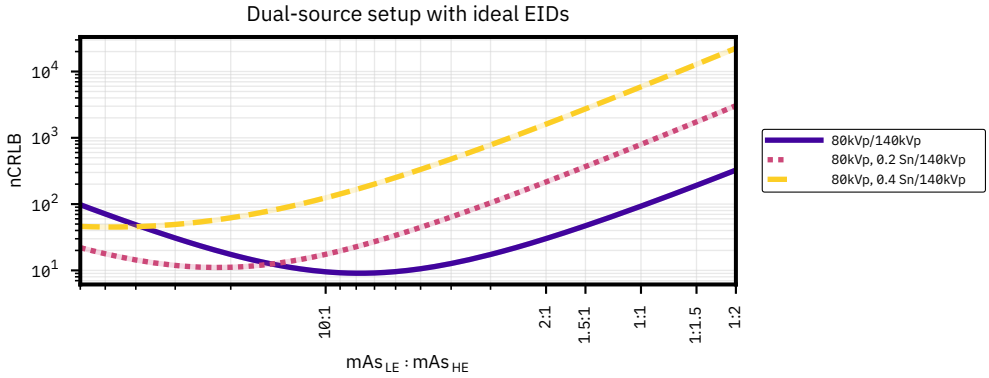

Figure 3.B.10: nCRLB values for estimating SPR as achieved by a dual-source setup using ideal EIDs for different ratios $mAs_{LE} : mAs_{HE}$ between the LE and HE spectrum, using an 80/140 kVp spectrum combination and applying filtration to the LE spectrum only. The filtration is specified in millimetres of tin.

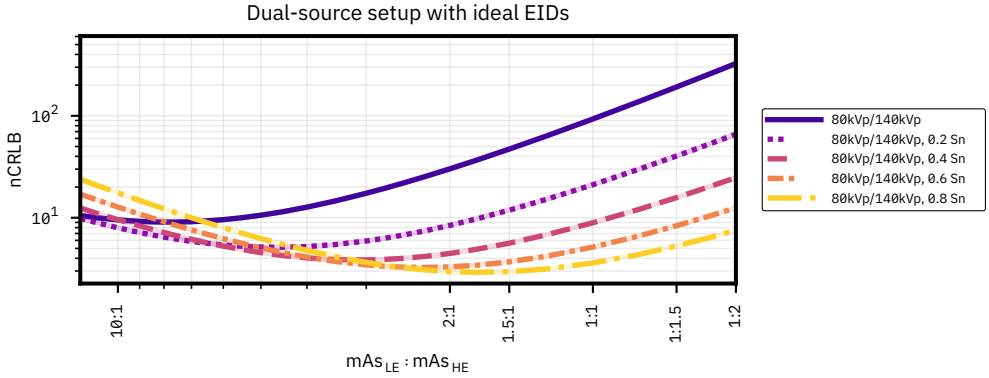

Figure 3.B.11: nCRLB values for estimating SPR as achieved by a dual-source setup using ideal EIDs for different ratios $mAs_{LE} : mAs_{HE}$ between the LE and HE spectrum, using an 80/140 kVp spectrum combination and applying filtration to the HE spectrum only. The filtration is specified in millimetres of tin.

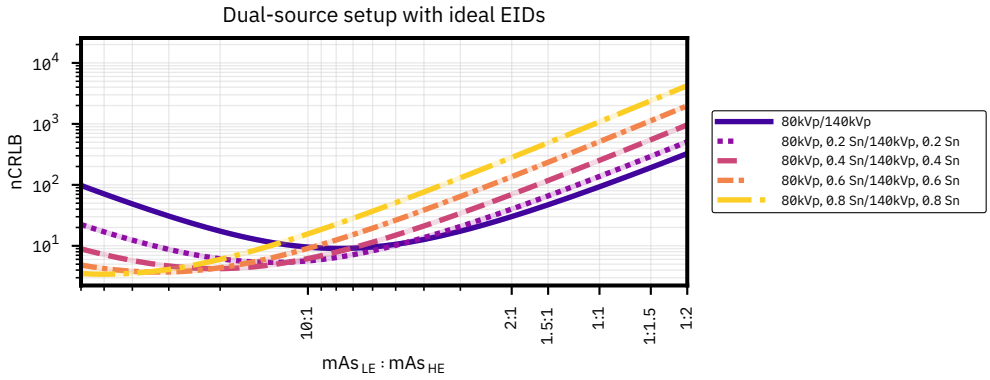

Figure 3.B.12: nCRLB values for estimating SPR as achieved by a dual-source setup using ideal EIDs for different ratios $mAs_{LE} : mAs_{HE}$ between the LE and HE spectrum, using an 80/140 kVp spectrum combination and applying filtration to both the LE and HE spectrum. The filtration is specified in millimetres of tin.

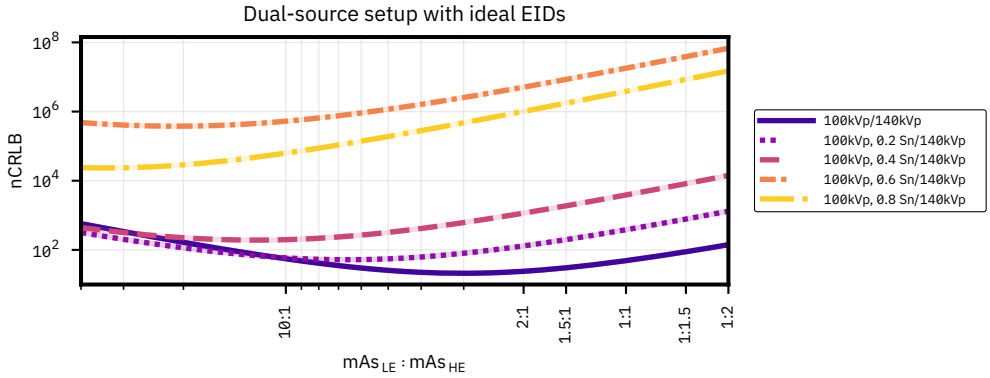

Figure 3.B.13: nCRLB values for estimating SPR as achieved by a dual-source setup using ideal EIDs for different ratios $mAs_{LE} : mAs_{HE}$ between the LE and HE spectrum, using a 100/140 kVp spectrum combination and applying filtration to the LE spectrum only. The filtration is specified in millimetres of tin.

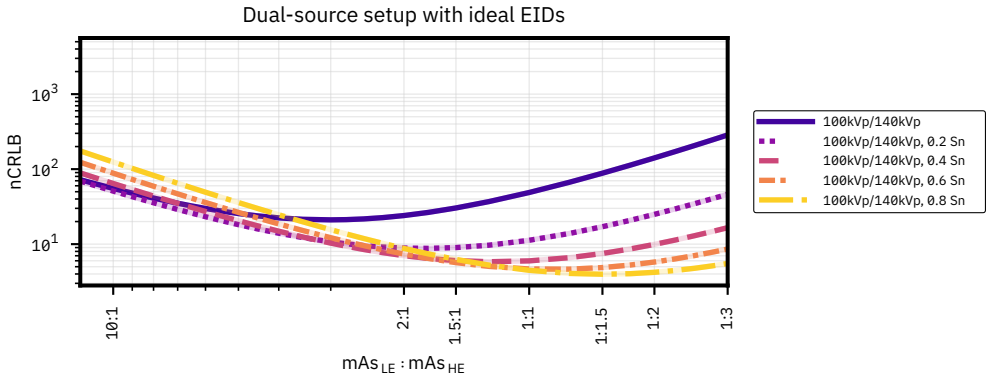

Figure 3.B.14: nCRLB values for estimating SPR as achieved by a dual-source setup using ideal EIDs for different ratios $mAs_{LE} : mAs_{HE}$ between the LE and HE spectrum, using a 100/140 kVp spectrum combination and applying filtration to the HE spectrum only. The filtration is specified in millimetres of tin.

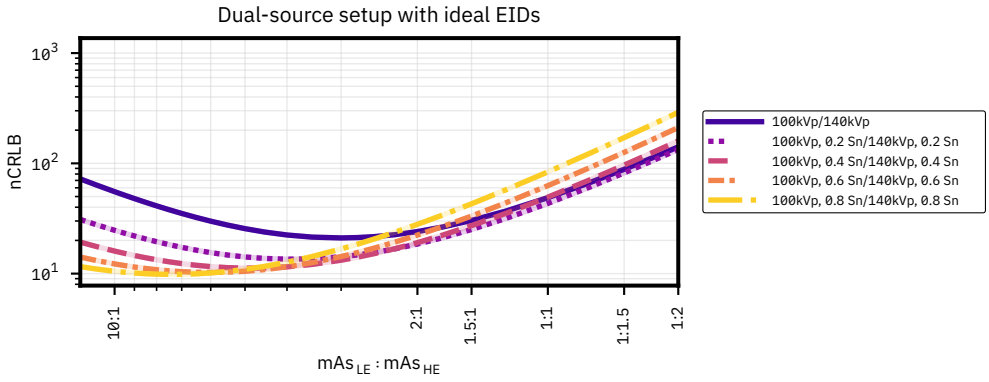

Figure 3.B.15: nCRLB values for estimating SPR as achieved by a dual-source setup using ideal EIDs for different ratios $mAs_{LE} : mAs_{HE}$ between the LE and HE spectrum, using a 100/140 kVp spectrum combination and applying filtration to both the LE and HE spectrum. The filtration is specified in millimetres of tin.

Single rapid voltage-switching source with PCD

Table 3.B.9: Results for the optimisation of the kVp-switching setup using an ideal PCD, optimising the ratio $mAs_{LE} : mAs_{HE}$ between the LE and HE phase, as well as optimising the thresholds of the PCD for both the LE and HE phase independently (see Table 3.B.10 for the results when using the same thresholds for the LE and HE phase). The table states the minimum nCRLB values that are achieved and their respective parameters. The nCRLB in the limit of only using the HE phase deviates slightly from the results for a single source with one PCD shown earlier due to the larger step size of bins used here (5 keV vs. 2 keV).

Spectrum combination	mAs ratio $mAs_{LE} : mAs_{HE}$	Optimum thresholds LE phase [keV]	Optimum thresholds HE phase [keV]	min. nCRLB
80 kVp/100 kVp	1 : 100000	[20, 60, 80]	[20, 70, 100]	2.781
80 kVp/120 kVp	1 : 200	[20, 60, 80]	[20, 75, 120]	1.753
80 kVp/140 kVp	1 : 2	[20, 60, 80]	[20, 75, 140]	1.303
LE & HE filtration				
80 kVp, 0.2 mm Sn/ 140 kVp, 0.2 mm Sn	3.5 : 1	[20, 65, 80]	[20, 85, 140]	1.228
80 kVp, 0.4 mm Sn/ 140 kVp, 0.4 mm Sn	8.75 : 1	[20, 70, 80]	[20, 85, 140]	1.263
80 kVp, 0.6 mm Sn/ 140 kVp, 0.6 mm Sn	14 : 1	[20, 50, 80]	[20, 90, 140]	1.275
80 kVp, 0.8 mm Sn/ 140 kVp, 0.8 mm Sn	25 : 1	[20, 50, 80]	[20, 95, 140]	1.283
100 kVp/120 kVp	1 : 100000	[20, 70, 100]	[20, 75, 120]	1.753
100 kVp/140 kVp	1 : 100000	[20, 70, 100]	[20, 75, 140]	1.312
120 kVp/140 kVp	1 : 100000	[20, 75, 120]	[20, 75, 140]	1.312

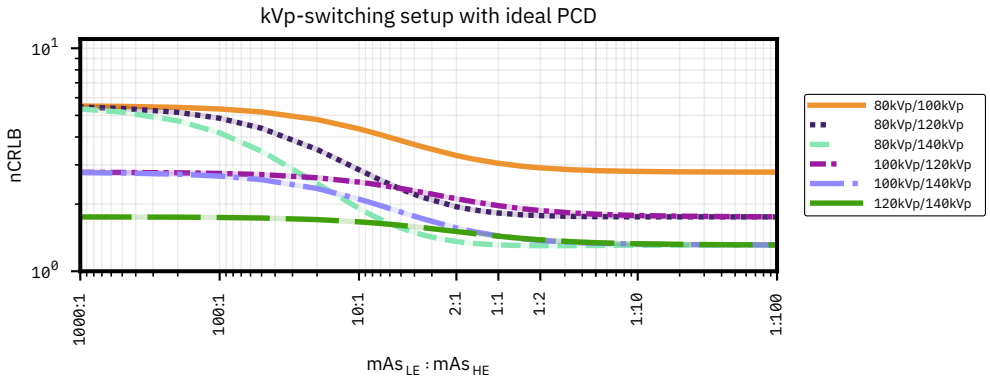

Figure 3.B.16: nCRLB values for estimating SPR as achieved by a kVp-switching setup using an ideal PCD for different ratios $mAs_{LE} : mAs_{HE}$ between the LE and HE phase, optimising the thresholds of the PCD for both the LE and HE phase independently, and different spectrum combinations without additional source filtration. For each mAs ratio, the minimum nCRLB of all tested threshold combinations is plotted.

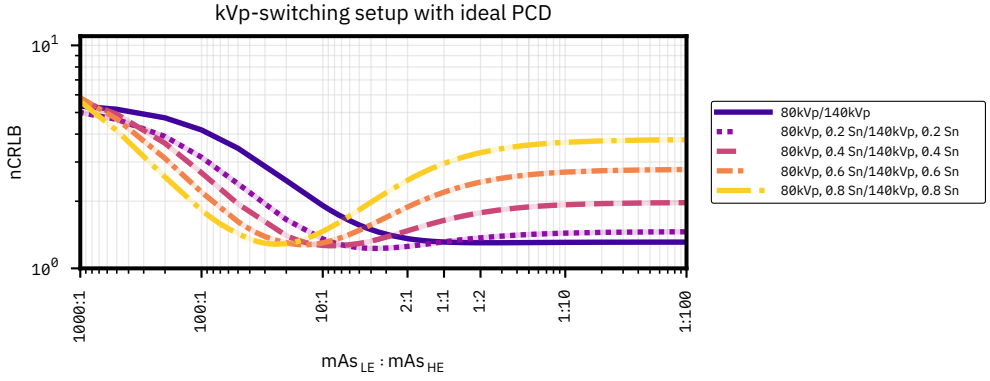

Figure 3.B.17: nCRLB values for estimating SPR as achieved by a kVp-switching setup using an ideal PCD for different ratios $mAs_{LE} : mAs_{HE}$ between the LE and HE phase, optimising the thresholds of the PCD for both the LE and HE phase independently, using an 80/140 kVp spectrum combination and applying filtration to both the LE and HE spectrum. The filtration is specified in millimetres of tin. For each mAs ratio, the minimum nCRLB of all tested threshold combinations is plotted.

3

Table 3.B.10: Results for the optimisation of the kVp-switching setup using an ideal PCD, optimising the ratio $mAs_{LE} : mAs_{HE}$ between the LE and HE phase. In contrast to the results shown in Table 3.B.9, the threshold settings for the LE and HE phase are kept the same here. The table states the minimum nCRLB values that are achieved and their respective parameters. The nCRLB in the limit of only using the HE phase deviates slightly from the results for a single source with one PCD shown earlier due to the larger step size of bins used here (5 keV vs. 2 keV).

Spectrum combination	mAs ratio $mAs_{LE} : mAs_{HE}$	Optimum thresholds LE phase [keV]	Optimum thresholds HE phase [keV]	min. nCRLB
80 kVp/100 kVp	1 : 100000	[20, 70, 100]	[20, 70, 100]	2.781
80 kVp/120 kVp	1 : 100000	[20, 75, 120]	[20, 75, 120]	1.753
80 kVp/140 kVp	1 : 50	[20, 75, 140]	[20, 75, 140]	1.312
LE & HE filtration				
80 kVp, 0.2 mm Sn/ 140 kVp, 0.2 mm Sn	3.5 : 1	[20, 75, 140]	[20, 75, 140]	1.298
80 kVp, 0.4 mm Sn/ 140 kVp, 0.4 mm Sn	8.75 : 1	[20, 75, 140]	[20, 75, 140]	1.371
80 kVp, 0.6 mm Sn/ 140 kVp, 0.6 mm Sn	18 : 1	[20, 75, 140]	[20, 75, 140]	1.442
80 kVp, 0.8 mm Sn/ 140 kVp, 0.8 mm Sn	30 : 1	[20, 75, 140]	[20, 75, 140]	1.495
100 kVp/120 kVp	1 : 100000	[20, 75, 120]	[20, 75, 120]	1.753
100 kVp/140 kVp	1 : 100000	[20, 75, 140]	[20, 75, 140]	1.312
120 kVp/140 kVp	1 : 100000	[20, 75, 140]	[20, 75, 140]	1.312

Dual-source setup with two PCDs

We would like to note that the investigated range of $mAs_{LE} : mAs_{HE}$ goes by default down to 1 : 100 000, however, due to photon starvation sometimes the investigated range has to be reduced.

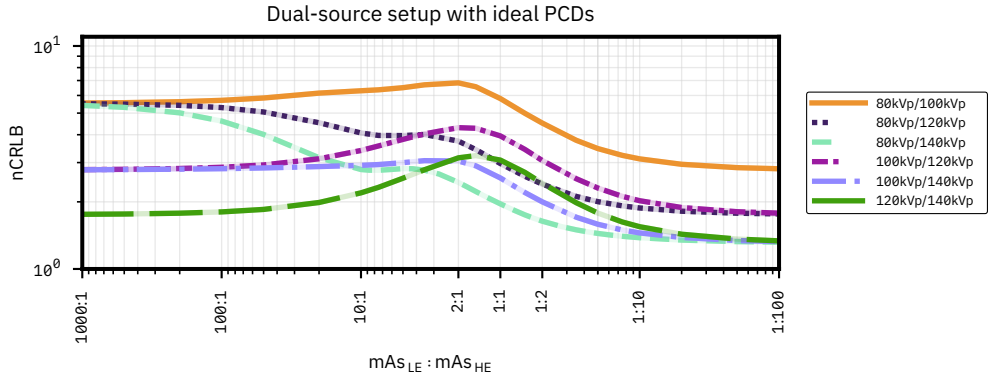

Figure 3.B.18: nCRLB values for estimating SPR as achieved by a dual-source setup using ideal PCDs for different ratios $mAs_{LE} : mAs_{HE}$ between the LE and HE spectrum, and different spectrum combinations without additional source filtration. For each mAs ratio, the minimum nCRLB of all tested threshold combinations is plotted.

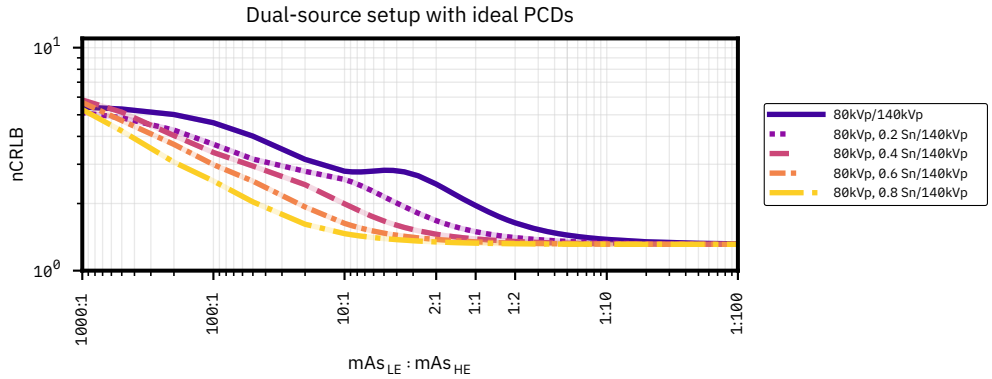

Figure 3.B.19: nCRLB values for estimating SPR as achieved by a dual-source setup using ideal PCDs for different ratios $mAs_{LE} : mAs_{HE}$ between the LE and HE spectrum, using an 80/140 kVp spectrum combination and applying filtration to the LE spectrum only. The filtration is specified in millimetres of tin. For each mAs ratio, the minimum nCRLB of all tested threshold combinations is plotted.

Table 3.B.11: Results for the optimisation of the dual-source setup with two ideal PCDs, optimising the ratio $mAs_{LE} : mAs_{HE}$ between the LE and HE spectrum, as well as optimising the thresholds of both the PCD facing the LE source and the PCD facing the HE source simultaneously and independently. The table states the minimum nCRLB values that are achieved and their respective parameters. The nCRLB in the limit of only using the HE source deviates slightly from the results for a single source with one PCD shown earlier due to the larger step size of bins used here (5 keV vs. 2 keV).

Spectrum combination	mAs ratio $mAs_{LE} : mAs_{HE}$	Optimum thresholds LE PCD [keV]	Optimum thresholds HE PCD [keV]	min. nCRLB
80 kVp/100 kVp	1 : 100000	[20, 25, 80]	[20, 70, 100]	2.781
80 kVp/120 kVp	1 : 100000	[20, 25, 80]	[20, 75, 120]	1.753
80 kVp/140 kVp	1 : 100000	[20, 25, 80]	[20, 75, 140]	1.312
LE filtration only				
80 kVp, 0.2 mm Sn/ 140 kVp	1 : 100000	[20, 25, 80]	[20, 75, 140]	1.312
80 kVp, 0.4 mm Sn/ 140 kVp	1 : 100000	[20, 25, 80]	[20, 75, 140]	1.312
80 kVp, 0.6 mm Sn/ 140 kVp	1 : 100000	[20, 25, 80]	[20, 75, 140]	1.312
80 kVp, 0.8 mm Sn/ 140 kVp	1 : 100000	[20, 25, 80]	[20, 75, 140]	1.312
HE filtration only				
80 kVp/ 140 kVp, 0.2 mm Sn	1 : 100000	[20, 35, 80]	[20, 85, 140]	1.462
80 kVp/ 140 kVp, 0.4 mm Sn	3.5 : 1	[20, 60, 80]	[20, 90, 140]	1.638
80 kVp/ 140 kVp, 0.6 mm Sn	2 : 1	[20, 60, 80]	[20, 95, 140]	1.435
80 kVp/ 140 kVp, 0.8 mm Sn	1.75 : 1	[20, 60, 80]	[20, 90, 140]	1.295
LE & HE filtration				
80 kVp, 0.2 mm Sn/ 140 kVp, 0.2 mm Sn	1 : 100000	[20, 25, 80]	[20, 85, 140]	1.462
80 kVp, 0.4 mm Sn/ 140 kVp, 0.4 mm Sn	20 : 1	[20, 50, 80]	[20, 90, 140]	1.904
80 kVp, 0.6 mm Sn/ 140 kVp, 0.6 mm Sn	30 : 1	[20, 55, 80]	[20, 95, 140]	1.797
80 kVp, 0.8 mm Sn/ 140 kVp, 0.8 mm Sn	45 : 1	[20, 55, 80]	[20, 95, 140]	1.735
100 kVp/120 kVp	1 : 100000	[20, 25, 100]	[20, 75, 120]	1.753
100 kVp/140 kVp	1 : 100000	[20, 25, 100]	[20, 75, 140]	1.312
120 kVp/140 kVp	1 : 100000	[20, 25, 120]	[20, 75, 140]	1.312

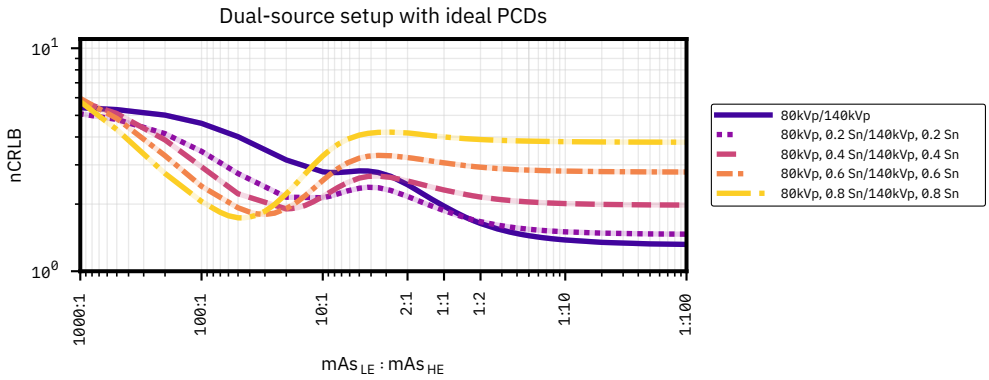

Figure 3.B.20: nCRLB values for estimating SPR as achieved by a dual-source setup using ideal PCDs for different ratios $mAs_{LE} : mAs_{HE}$ between the LE and HE spectrum, using an 80/140 kVp spectrum combination and applying filtration to both the LE and HE spectrum. The filtration is specified in millimetres of tin. For each mAs ratio, the minimum nCRLB of all tested threshold combinations is plotted.

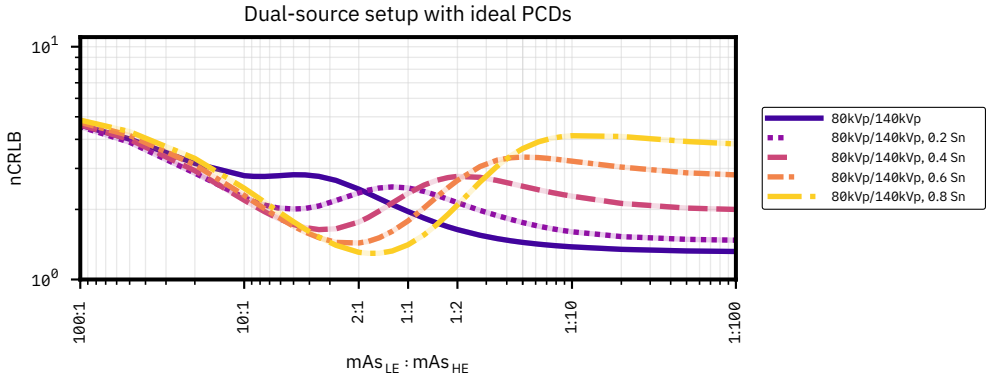

Figure 3.B.21: nCRLB values for estimating SPR as achieved by a dual-source setup using ideal PCDs for different ratios $mAs_{LE} : mAs_{HE}$ between the LE and HE spectrum, using an 80/140 kVp spectrum combination and applying filtration to the HE spectrum only. The filtration is specified in millimetres of tin. For each mAs ratio, the minimum nCRLB of all tested threshold combinations is plotted.

Results as a function of photon number ratio

Here, selected results for setups using two distinct source spectra (i.e., kVp-switching and dual-source setups) are plotted over the ratio of photon numbers n_γ instead of over the mAs ratio. The photon number ratio $n_{\gamma,\mathrm{LE}} : n_{\gamma,\mathrm{HE}}$ specifies the ratio between the number of photons leaving the source, including source filtration, when using the low energy ($n_{\gamma,\mathrm{LE}}$) and high energy ($n_{\gamma,\mathrm{HE}}$) phase/source.

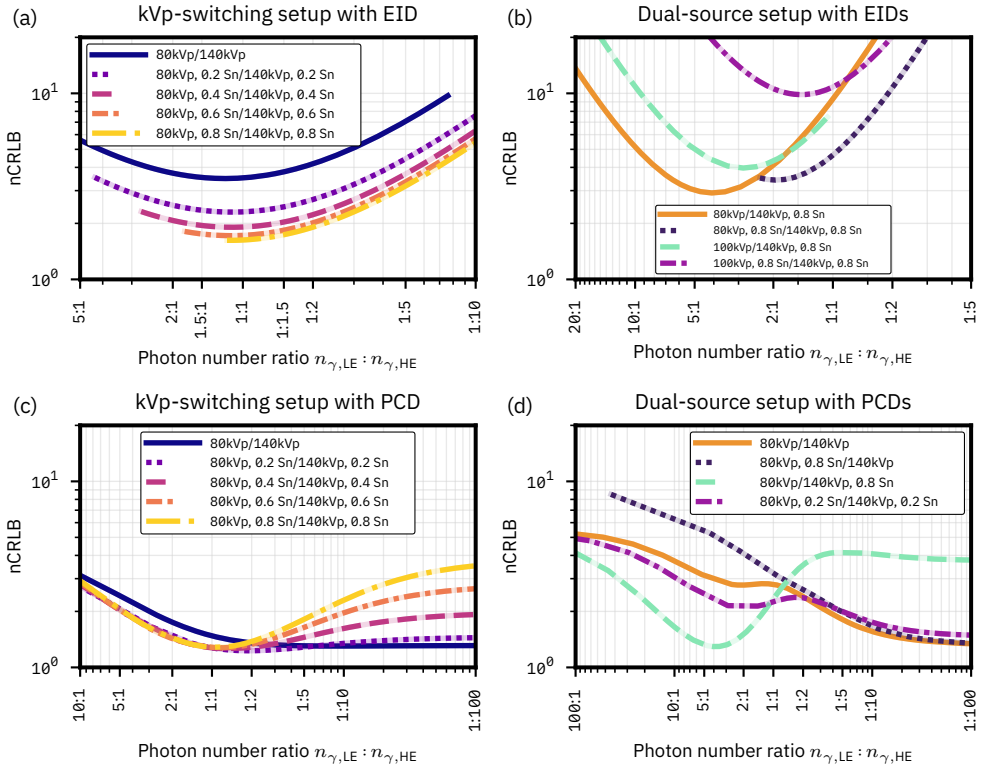

Figure 3.B.22: This figure is identical to Figure 3.4 except that the results are plotted over the photon number ratio $n_{\gamma,\mathrm{LE}} : n_{\gamma,\mathrm{HE}}$ instead of over the mAs ratio.
This figure shows examples of the optimisation of spectral CBCT setups with respect to the extraction of SPR, assuming an ideal detector response function. (a) kVp-switching setup with one EID and (b) dual-source setup with two EIDs, optimising the ratio $n_{\gamma,\mathrm{LE}} : n_{\gamma,\mathrm{HE}}$ between the LE and HE spectra. (c) kVp-switching setup with one PCD and (d) dual-source setup with two PCDs; for each $n_{\gamma,\mathrm{LE}} : n_{\gamma,\mathrm{HE}}$ ratio, the minimum nCRLB of all tested threshold combinations is plotted. All values are reported as normalised CRLB values as stated in the text with the same nCRLB value range for all figures; source filtration is specified in millimetres of tin.

3.B.4 Supplementary Results for Setup Optimisations Based on Realistic Detector Response Functions

Single source with PCD

Table 3.B.12: Results for the optimisation of the setup based on a single source with a realistic PCD using two energy bins. The table states the minimum nCRLB values that are achieved and their respective parameters.

Spectrum	Optimum thresholds [keV]	min. nCRLB
80 kVp	[20, 60, 80]	21.63
100 kVp	[20, 64, 100]	9.202
120 kVp	[20, 68, 120]	5.303
140 kVp	[20, 70, 140]	3.955
140 kVp, 0.2 mm Sn	[20, 74, 140]	4.800
140 kVp, 0.4 mm Sn	[20, 82, 140]	7.062
140 kVp, 0.6 mm Sn	[20, 88, 140]	10.65
140 kVp, 0.8 mm Sn	[20, 92, 140]	15.54

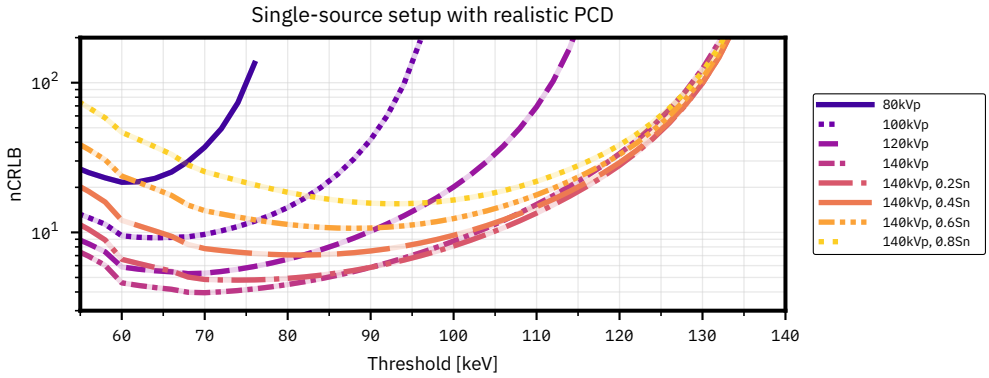

Figure 3.B.23: nCRLB values for estimating SPR as achieved by a single-source setup using a realistic PCD with two bins, for different locations of the threshold between the low and high energy bin, and different spectra.

Table 3.B.13: Results for the optimisation of the setup based on a single source with a realistic PCD using three energy bins. The table states the minimum nCRLB values that are achieved and their respective parameters.

Spectrum	Optimum thresholds [keV]	min. nCRLB
80 kVp	[20, 58, 66, 80]	19.37
100 kVp	[20, 60, 74, 100]	7.910
120 kVp	[20, 60, 76, 120]	4.744
140 kVp	[20, 68, 88, 140]	3.616
140 kVp, 0.2 mm Sn	[20, 70, 92, 140]	4.238
140 kVp, 0.4 mm Sn	[20, 72, 94, 140]	6.207
140 kVp, 0.6 mm Sn	[20, 80, 100, 140]	9.433
140 kVp, 0.8 mm Sn	[20, 86, 106, 140]	13.80

Table 3.B.14: Results for the optimisation of the setup based on a single source with a realistic PCD using four energy bins. The table states the minimum nCRLB values that are achieved and their respective parameters.

Spectrum	Optimum thresholds [keV]	min. nCRLB
80 kVp	[20, 55, 60, 70, 80]	18.67
100 kVp	[20, 60, 70, 80, 100]	7.634
120 kVp	[20, 60, 70, 85, 120]	4.546
140 kVp	[20, 60, 70, 90, 140]	3.447
140 kVp, 0.2 mm Sn	[20, 70, 85, 105, 140]	4.134
140 kVp, 0.4 mm Sn	[20, 70, 85, 105, 140]	5.973
140 kVp, 0.6 mm Sn	[20, 75, 90, 105, 140]	9.100
140 kVp, 0.8 mm Sn	[20, 30, 80, 100, 140]	12.40

Table 3.B.15: Results for the setup based on a single source with a realistic PCD using near-continuous energy binning. The first bin is between 3 to 5 keV wide to prevent photon starvation, whereas all subsequent bins have a width of 1 keV. The table states the resulting nCRLB values and their respective parameters.

Spectrum	Thresholds [keV]	min. nCRLB
80 kVp	[20, 23, 24, ..., 79, 80]	17.46
100 kVp	[20, 23, 24, ..., 99, 100]	7.189
120 kVp	[20, 23, 24, ..., 119, 120]	4.218
140 kVp	[20, 23, 24, ..., 139, 140]	3.136
140 kVp, 0.2 mm Sn	[20, 25, 26, ..., 139, 140]	3.571
140 kVp, 0.4 mm Sn	[20, 25, 26, ..., 139, 140]	5.019
140 kVp, 0.6 mm Sn	[20, 25, 26, ..., 139, 140]	7.480
140 kVp, 0.8 mm Sn	[20, 25, 26, ..., 139, 140]	10.90

Single source with dual-layer detector

Table 3.B.16: Results for the optimisation of the setup based on a single source with a realistic dual-layer detector with and without a copper filtration layer, and with top and bottom layers consisting of CsI. The table states the minimum nCRLB values that are achieved and their respective parameters.

Spectrum	Optimum top layer thickness [mm]	Optimum bottom layer thickness [mm]	Optimum filtration layer thickness (if applicable) [mm]	min. nCRLB
80 kVp	0.35	1.55	–	72.84
	0.15	1.75	0.8	48.24
100 kVp	0.45	1.45	–	26.31
	0.2	1.7	1.0	18.20
120 kVp	0.45	1.45	–	15.34
	0.2	1.7	1.4	10.48
140 kVp	0.45	1.45	–	11.58
	0.2	1.7	1.8	7.783
140 kVp, 0.2 mm Sn	0.5	1.4	–	16.45
	0.25	1.65	2.0	10.62
140 kVp, 0.4 mm Sn	0.55	1.35	–	27.76
	0.25	1.65	2.6	17.06
140 kVp, 0.6 mm Sn	0.55	1.35	–	48.90
	0.3	1.6	3.0	28.19
140 kVp, 0.8 mm Sn	0.6	1.3	–	84.12
	0.3	1.6	3.5	45.15

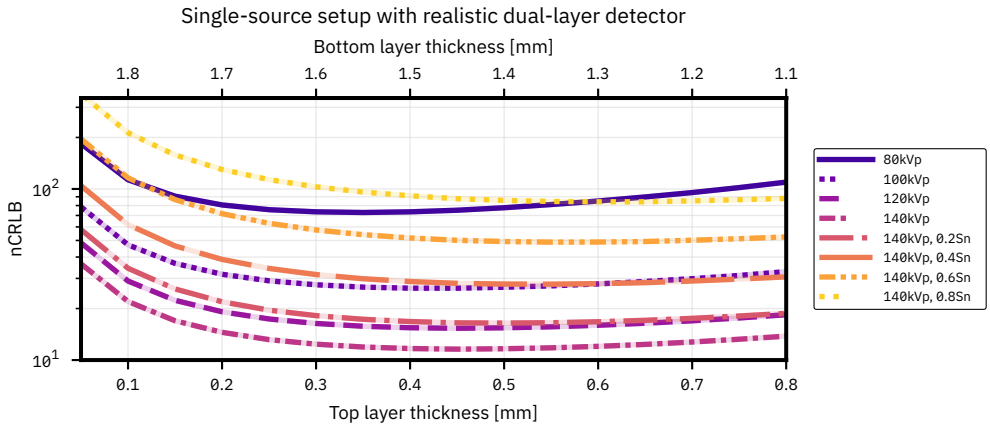

Figure 3.B.24: nCRLB values for estimating SPR as achieved by a realistic dual-layer detector for different thicknesses of the CsI top and bottom detection layers, without using a copper filtration layer in between the detection layers, and for spectra up to 140 kVp, with additional source filtration for the 140 kVp spectra. The filtration is specified in millimetres of tin.

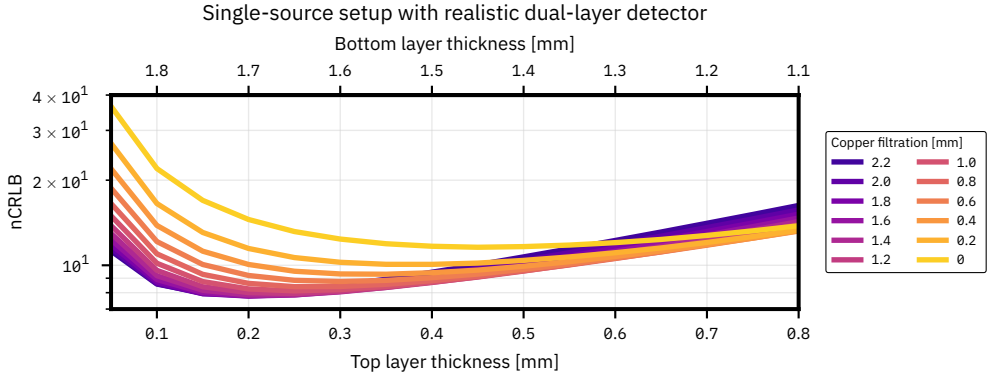

Figure 3.B.25: nCRLB values for estimating SPR as achieved by a realistic dual-layer detector for different thicknesses of the CsI top and bottom detection layers with a spectrum of 140 kVp and different thicknesses of the copper filtration layer in between the top and bottom detection layers.

Single rapid voltage-switching source with EID

Table 3.B.17: Results for the optimisation of the kVp-switching setup using a realistic EID, optimising the ratio $mAs_{LE} : mAs_{HE}$ between the LE and HE phase. The table states the minimum nCRLB values that are achieved and their respective parameters.

Spectrum combination	mAs ratio $mAs_{LE} : mAs_{HE}$	min. nCRLB
80 kVp/100 kVp	2 : 1	30.29
80 kVp/120 kVp	3 : 1	10.38
80 kVp/140 kVp	4.5 : 1	6.202
LE & HE filtration		
80 kVp, 0.2 mm Sn/140 kVp, 0.2 mm Sn	7.5 : 1	4.012
80 kVp, 0.4 mm Sn/140 kVp, 0.4 mm Sn	11 : 1	3.271
80 kVp, 0.6 mm Sn/140 kVp, 0.6 mm Sn	17 : 1	2.918
80 kVp, 0.8 mm Sn/140 kVp, 0.8 mm Sn	26 : 1	2.737
100 kVp/120 kVp	1.5 : 1	55.92
100 kVp/140 kVp	2.25 : 1	18.87
120 kVp/140 kVp	1.5 : 1	104.0

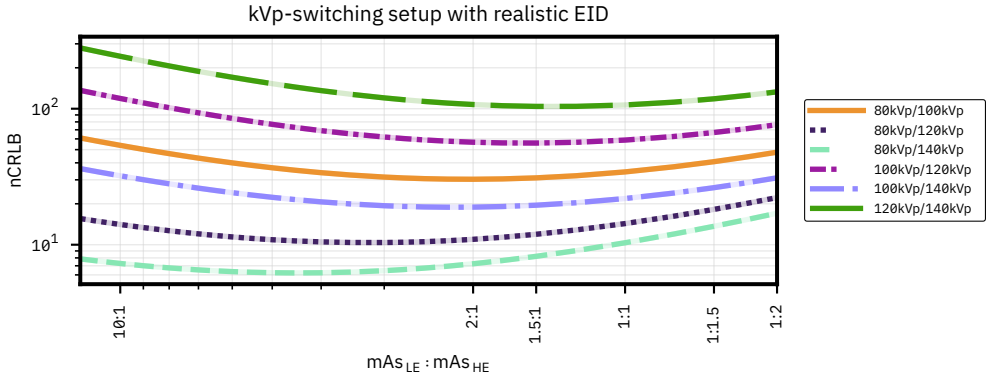

Figure 3.B.26: nCRLB values for estimating SPR as achieved by a kVp-switching setup using a realistic EID for different ratios $mAs_{LE} : mAs_{HE}$ between the LE and HE phase, and different spectrum combinations between 80 kVp and 140 kVp without additional source filtration.

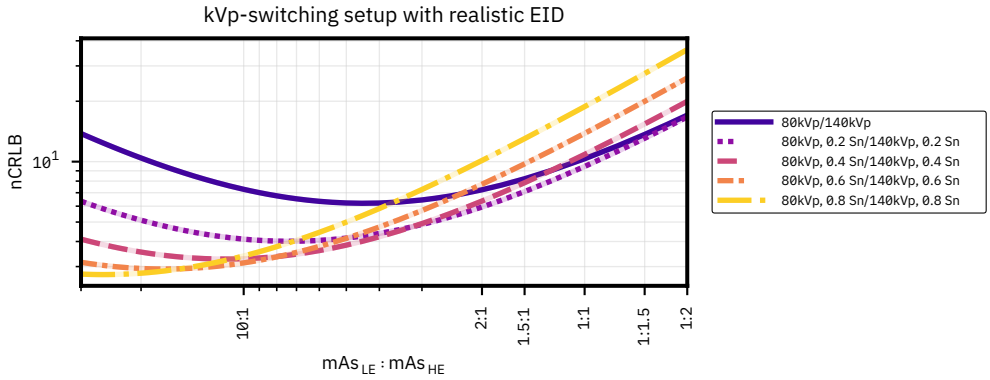

Figure 3.B.27: nCRLB values for estimating SPR as achieved by a kVp-switching setup using a realistic EID for different ratios $mAs_{LE} : mAs_{HE}$ between the LE and HE phase, using an 80/140 kVp spectrum combination and applying filtration to both the LE and HE spectrum. The filtration is specified in millimetres of tin.

Dual-source setup with two EIDs

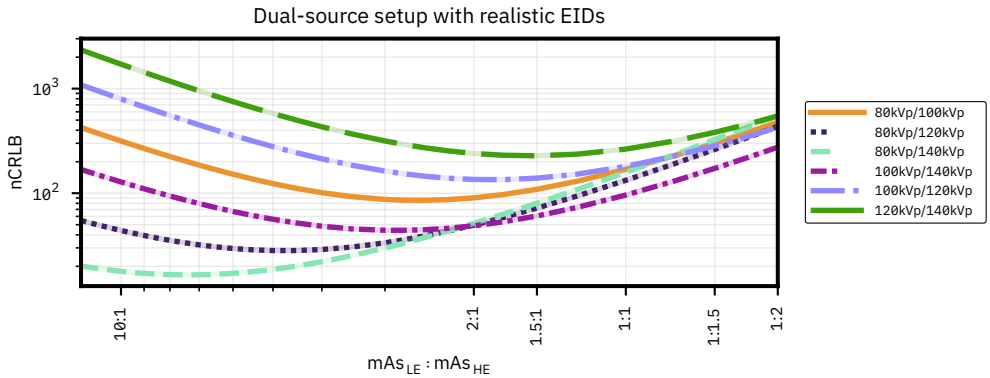

Figure 3.B.28: nCRLB values for estimating SPR as achieved by a dual-source setup using realistic EIDs for different ratios $mAs_{LE} : mAs_{HE}$ between the LE and HE spectrum, and different spectrum combinations without additional source filtration.

Table 3.B.18: Results for the optimisation of the dual-source setup using two realistic EIDs, optimising the ratio $mAs_{LE} : mAs_{HE}$ between the LE and HE spectrum. The table states the minimum nCRLB values that are achieved and their respective parameters.

Spectrum combination	mAs ratio $mAs_{LE} : mAs_{HE}$	min. nCRLB
80 kVp/100 kVp	2.5 : 1	85.51
80 kVp/120 kVp	5 : 1	28.29
80 kVp/140 kVp	7.5 : 1	16.57
LE filtration only		
80 kVp, 0.2 mm Sn/140 kVp	20 : 1	20.96
80 kVp, 0.4 mm Sn/140 kVp	45 : 1	644.6
HE filtration only		
80 kVp/140 kVp, 0.2 mm Sn	4.5 : 1	9.085
80 kVp/140 kVp, 0.4 mm Sn	2.75 : 1	6.675
80 kVp/140 kVp, 0.6 mm Sn	2 : 1	5.580
80 kVp/140 kVp, 0.8 mm Sn	1.5 : 1	4.971
LE & HE filtration		
80 kVp, 0.2 mm Sn/140 kVp, 0.2 mm Sn	12 : 1	9.562
80 kVp, 0.4 mm Sn/140 kVp, 0.4 mm Sn	18 : 1	7.427
80 kVp, 0.6 mm Sn/140 kVp, 0.6 mm Sn	27.5 : 1	6.437
80 kVp, 0.8 mm Sn/140 kVp, 0.8 mm Sn	45 : 1	5.924
100 kVp/120 kVp	1.75 : 1	134.8
100 kVp/140 kVp	2.75 : 1	44.16
LE filtration only		
100 kVp, 0.2 mm Sn/140 kVp	6 : 1	138.1
100 kVp, 0.4 mm Sn/140 kVp	12 : 1	$1.094 \cdot 10^3$
HE filtration only		
100 kVp/140 kVp, 0.2 mm Sn	1.75 : 1	16.61
100 kVp/140 kVp, 0.4 mm Sn	1 : 1	10.56
100 kVp/140 kVp, 0.6 mm Sn	1 : 1.25	8.127
100 kVp/140 kVp, 0.8 mm Sn	1 : 1.75	6.908
LE & HE filtration		
100 kVp, 0.2 mm Sn/140 kVp, 0.2 mm Sn	3.5 : 1	27.37
100 kVp, 0.4 mm Sn/140 kVp, 0.4 mm Sn	4.5 : 1	22.10
100 kVp, 0.6 mm Sn/140 kVp, 0.6 mm Sn	5.5 : 1	19.85
100 kVp, 0.8 mm Sn/140 kVp, 0.8 mm Sn	6.5 : 1	18.86
120 kVp/140 kVp	1.5 : 1	228.0

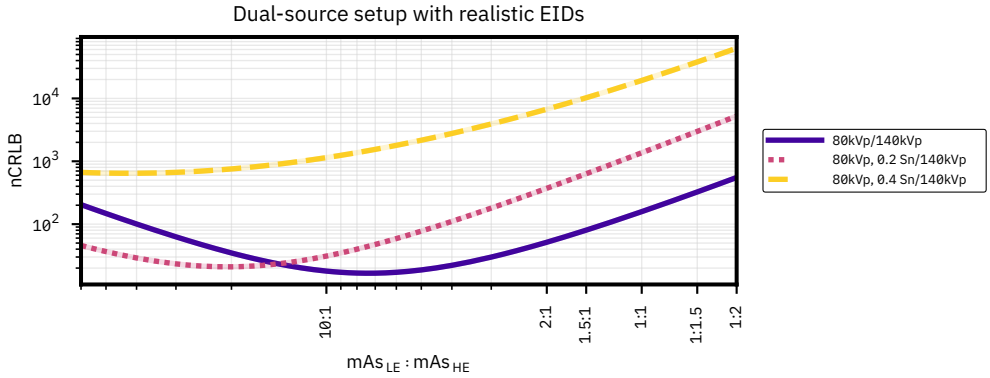

Figure 3.B.29: nCRLB values for estimating SPR as achieved by a dual-source setup using realistic EIDs for different ratios $mAs_{LE} : mAs_{HE}$ between the LE and HE spectrum, using an 80/140 kVp spectrum combination and applying filtration to the LE spectrum only. The filtration is specified in millimetres of tin.

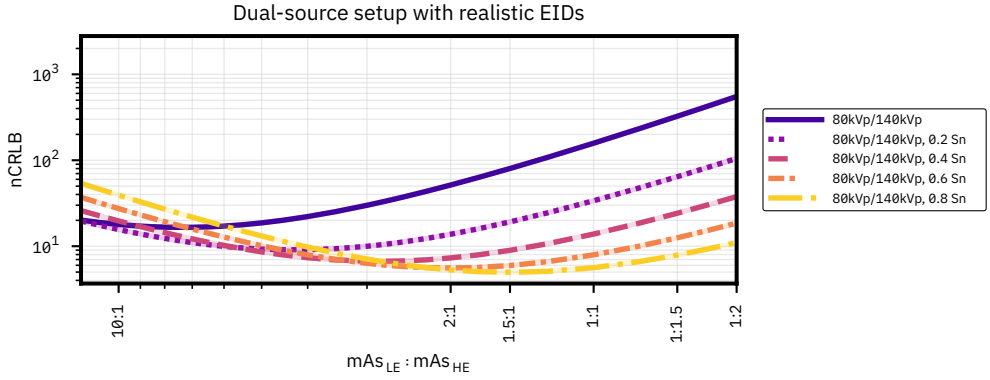

Figure 3.B.30: nCRLB values for estimating SPR as achieved by a dual-source setup using realistic EIDs for different ratios $mAs_{LE} : mAs_{HE}$ between the LE and HE spectrum, using an 80/140 kVp spectrum combination and applying filtration to the HE spectrum only. The filtration is specified in millimetres of tin.

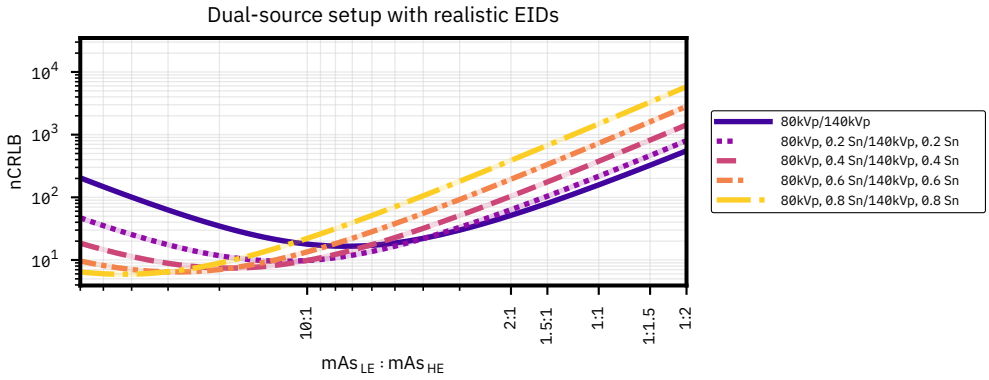

Figure 3.B.31: nCRLB values for estimating SPR as achieved by a dual-source setup using realistic EIDs for different ratios $mAs_{LE} : mAs_{HE}$ between the LE and HE spectrum, using an 80/140 kVp spectrum combination and applying filtration to both the LE and HE spectrum. The filtration is specified in millimetres of tin.

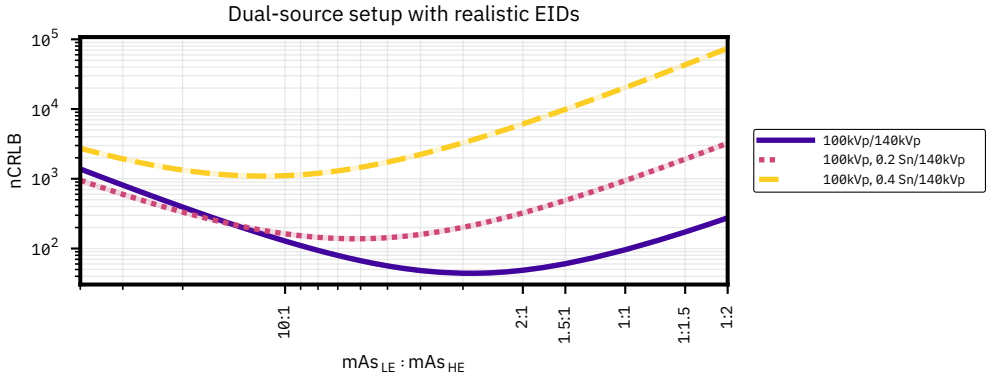

Figure 3.B.32: nCRLB values for estimating SPR as achieved by a dual-source setup using realistic EIDs for different ratios $mAs_{LE} : mAs_{HE}$ between the LE and HE spectrum, using a 100/140 kVp spectrum combination and applying filtration to the LE spectrum only. The filtration is specified in millimetres of tin.

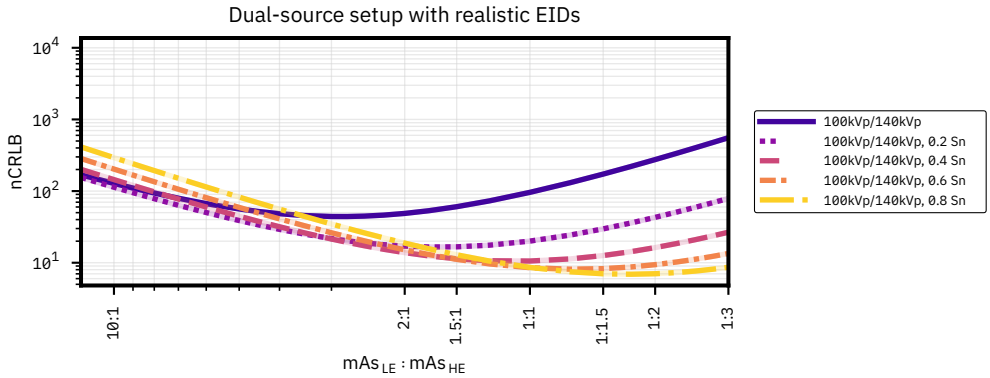

Figure 3.B.33: nCRLB values for estimating SPR as achieved by a dual-source setup using realistic EIDs for different ratios $mAs_{LE} : mAs_{HE}$ between the LE and HE spectrum, using a 100/140 kVp spectrum combination and applying filtration to the HE spectrum only. The filtration is specified in millimetres of tin.

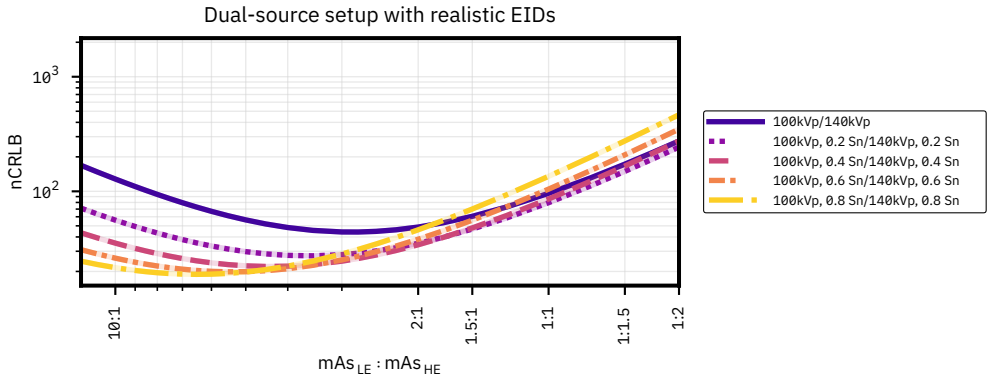

Figure 3.B.34: nCRLB values for estimating SPR as achieved by a dual-source setup using realistic EIDs for different ratios $mAs_{LE} : mAs_{HE}$ between the LE and HE spectrum, using a 100/140 kVp spectrum combination and applying filtration to both the LE and HE spectrum. The filtration is specified in millimetres of tin.

Single rapid voltage-switching source with PCD

Table 3.B.19: Results for the optimisation of the kVp-switching setup using a realistic PCD, optimising the ratio $mAs_{LE} : mAs_{HE}$ between the LE and HE phase, as well as optimising the thresholds of the PCD for both the LE and HE phase independently (see Table 3.B.20 for the results when using the same thresholds for the LE and HE phase). The table states the minimum nCRLB values that are achieved and their respective parameters. The nCRLB in the limit of only using the HE phase deviates slightly from the results for a single source with one PCD shown earlier due to the larger step size of bins used here (5 keV vs. 2 keV).

Spectrum combination	mAs ratio $mAs_{LE} : mAs_{HE}$	Optimum thresholds LE phase [keV]	Optimum thresholds HE phase [keV]	min. nCRLB
80 kVp/100 kVp	1 : 2	[20, 60, 80]	[20, 65, 100]	9.021
80 kVp/120 kVp	1 : 1	[20, 60, 80]	[20, 70, 120]	5.015
80 kVp/140 kVp	1.5 : 1	[20, 65, 80]	[20, 70, 140]	3.577
LE & HE filtration				
80 kVp, 0.2 mm Sn/ 140 kVp, 0.2 mm Sn	4.25 : 1	[20, 30, 80]	[20, 70, 140]	3.068
80 kVp, 0.4 mm Sn/ 140 kVp, 0.4 mm Sn	8.75 : 1	[20, 30, 80]	[20, 70, 140]	2.921
80 kVp, 0.6 mm Sn/ 140 kVp, 0.6 mm Sn	14 : 1	[20, 30, 80]	[20, 75, 140]	2.840
80 kVp, 0.8 mm Sn/ 140 kVp, 0.8 mm Sn	20 : 1	[20, 30, 80]	[20, 80, 140]	2.808
100 kVp/120 kVp	1 : 100000	[20, 65, 100]	[20, 70, 120]	5.339
100 kVp/140 kVp	1 : 100000	[20, 70, 100]	[20, 70, 140]	3.955
120 kVp/140 kVp	1 : 100000	[20, 70, 120]	[20, 70, 140]	3.955

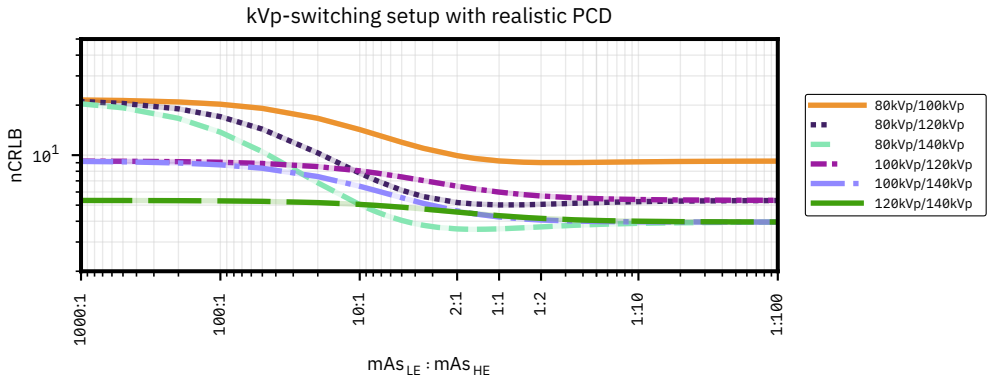

Figure 3.B.35: nCRLB values for estimating SPR as achieved by a kVp-switching setup using a realistic PCD for different ratios $mAs_{LE} : mAs_{HE}$ between the LE and HE phase, optimising the thresholds of the PCD for both the LE and HE phase independently, and different spectrum combinations without additional source filtration. For each mAs ratio, the minimum nCRLB of all tested threshold combinations is plotted.

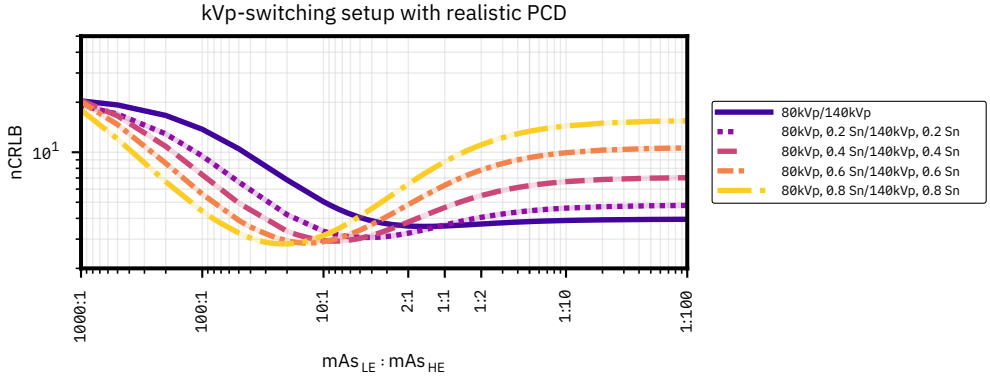

Figure 3.B.36: nCRLB values for estimating SPR as achieved by a kVp-switching setup using a realistic PCD for different ratios $mAs_{LE} : mAs_{HE}$ between the LE and HE phase, optimising the thresholds of the PCD for both the LE and HE phase independently, using an 80/140 kVp spectrum combination and applying filtration to both the LE and HE spectrum. The filtration is specified in millimetres of tin. For each mAs ratio, the minimum nCRLB of all tested threshold combinations is plotted.

Table 3.B.20: Results for the optimisation of the kVp-switching setup using a realistic PCD, optimising the ratio $mAs_{LE} : mAs_{HE}$ between the LE and HE phase. In contrast to the results shown in Table 3.B.19, the threshold settings for the LE and HE phase are kept the same here. The table states the minimum nCRLB values that are achieved and their respective parameters. The nCRLB in the limit of only using the HE phase deviates slightly from the results for a single source with one PCD shown earlier due to the larger step size of bins used here (5 keV vs. 2 keV).

Spectrum combination	mAs ratio $mAs_{LE} : mAs_{HE}$	Optimum thresholds LE phase [keV]	Optimum thresholds HE phase [keV]	min. nCRLB
80 kVp/100 kVp	1 : 3.5	[20, 65, 100]	[20, 65, 100]	9.033
80 kVp/120 kVp	1 : 1	[20, 65, 120]	[20, 65, 120]	5.048
80 kVp/140 kVp	1.5 : 1	[20, 70, 140]	[20, 70, 140]	3.602
LE & HE filtration				
80 kVp, 0.2 mm Sn/ 140 kVp, 0.2 mm Sn	4.25 : 1	[20, 70, 140]	[20, 70, 140]	3.084
80 kVp, 0.4 mm Sn/ 140 kVp, 0.4 mm Sn	8.75 : 1	[20, 70, 140]	[20, 70, 140]	2.987
80 kVp, 0.6 mm Sn/ 140 kVp, 0.6 mm Sn	14 : 1	[20, 75, 140]	[20, 75, 140]	2.966
80 kVp, 0.8 mm Sn/ 140 kVp, 0.8 mm Sn	25 : 1	[20, 75, 140]	[20, 75, 140]	2.959
100 kVp/120 kVp	1 : 100000	[20, 70, 120]	[20, 70, 120]	5.339
100 kVp/140 kVp	1 : 100000	[20, 70, 140]	[20, 70, 140]	3.955
120 kVp/140 kVp	1 : 100000	[20, 70, 140]	[20, 70, 140]	3.955

Dual-source setup with two PCDs

We would like to note that the investigated range of $mAs_{LE} : mAs_{HE}$ goes by default down to 1 : 10 000, however, due to photon starvation sometimes the investigated range has to be reduced.

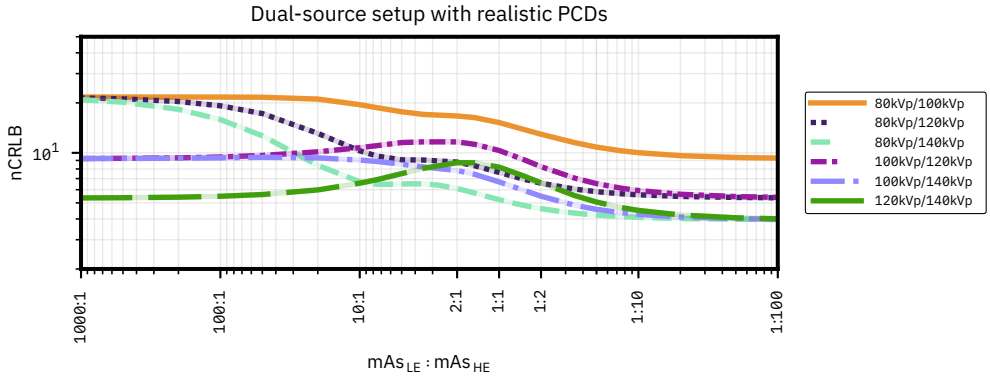

Figure 3.B.37: nCRLB values for estimating SPR as achieved by a dual-source setup using realistic PCDs for different ratios $mAs_{LE} : mAs_{HE}$ between the LE and HE spectrum, and different spectrum combinations without additional source filtration. For each mAs ratio, the minimum nCRLB of all tested threshold combinations is plotted.

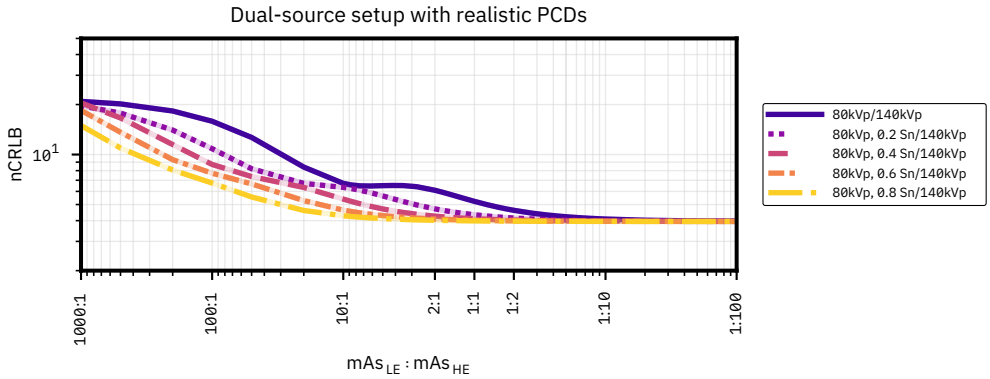

Figure 3.B.38: nCRLB values for estimating SPR as achieved by a dual-source setup using realistic PCDs for different ratios $mAs_{LE} : mAs_{HE}$ between the LE and HE spectrum, using an 80/140 kVp spectrum combination and applying filtration to the LE spectrum only. The filtration is specified in millimetres of tin. For each mAs ratio, the minimum nCRLB of all tested threshold combinations is plotted.

Table 3.B.21: Results for the optimisation of the dual-source setup with two realistic PCDs, optimising the ratio $mAs_{LE} : mAs_{HE}$ between the LE and HE spectrum, as well as optimising the thresholds of both the PCD facing the LE source and the PCD facing the HE source simultaneously and independently. The table states the minimum nCRLB values that are achieved and their respective parameters. The nCRLB in the limit of only using the HE source deviates slightly from the results for a single source with one PCD shown earlier due to the larger step size of bins used here (5 keV vs. 2 keV).

Spectrum combination	mAs ratio $mAs_{LE} : mAs_{HE}$	Optimum thresholds LE PCD [keV]	Optimum thresholds HE PCD [keV]	min. nCRLB
80 kVp/100 kVp	1 : 100000	[20, 25, 80]	[20, 65, 100]	9.218
80 kVp/120 kVp	1 : 100000	[20, 25, 80]	[20, 70, 120]	5.339
80 kVp/140 kVp	1 : 100000	[20, 25, 80]	[20, 70, 140]	3.955
LE filtration only				
80 kVp, 0.2 mm Sn/ 140 kVp	1 : 100000	[20, 25, 80]	[20, 70, 140]	3.955
80 kVp, 0.4 mm Sn/ 140 kVp	1 : 50000	[20, 25, 80]	[20, 70, 140]	3.955
80 kVp, 0.6 mm Sn/ 140 kVp	1 : 20000	[20, 25, 80]	[20, 70, 140]	3.955
80 kVp, 0.8 mm Sn/ 140 kVp	1 : 10000	[20, 25, 80]	[20, 70, 140]	3.955
HE filtration only				
80 kVp/ 140 kVp, 0.2 mm Sn	1 : 100000	[20, 25, 80]	[20, 75, 140]	4.805
80 kVp/ 140 kVp, 0.4 mm Sn	2.75 : 1	[20, 65, 80]	[20, 70, 140]	4.030
80 kVp/ 140 kVp, 0.6 mm Sn	2 : 1	[20, 65, 80]	[20, 70, 140]	3.567
80 kVp/ 140 kVp, 0.8 mm Sn	1.5 : 1	[20, 65, 80]	[20, 70, 140]	3.267
LE & HE filtration				
80 kVp, 0.2 mm Sn/ 140 kVp, 0.2 mm Sn	1 : 100000	[20, 25, 80]	[20, 75, 140]	4.805
80 kVp, 0.4 mm Sn/ 140 kVp, 0.4 mm Sn	18 : 1	[20, 30, 80]	[20, 75, 140]	4.462
80 kVp, 0.6 mm Sn/ 140 kVp, 0.6 mm Sn	30 : 1	[20, 30, 80]	[20, 75, 140]	4.271
80 kVp, 0.8 mm Sn/ 140 kVp, 0.8 mm Sn	45 : 1	[20, 30, 80]	[20, 75, 140]	4.181
100 kVp/120 kVp	1 : 100000	[20, 25, 100]	[20, 70, 120]	5.339
100 kVp/140 kVp	1 : 100000	[20, 25, 100]	[20, 70, 140]	3.955
120 kVp/140 kVp	1 : 100000	[20, 25, 120]	[20, 70, 140]	3.956

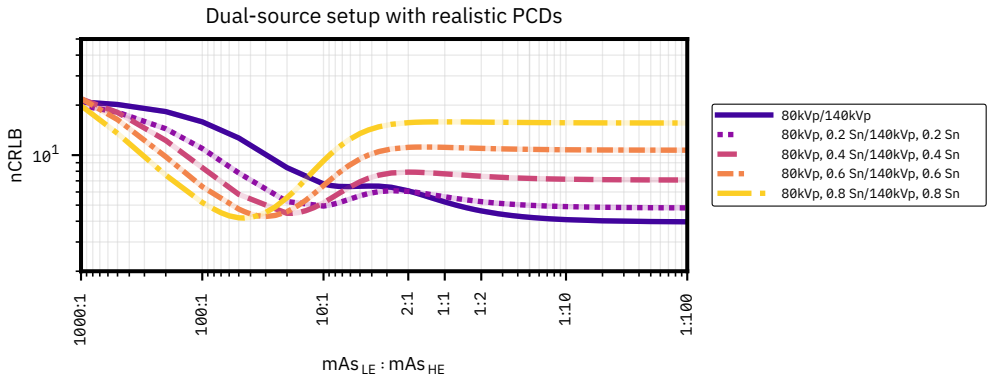

Figure 3.B.39: nCRLB values for estimating SPR as achieved by a dual-source setup using realistic PCDs for different ratios $mAs_{LE} : mAs_{HE}$ between the LE and HE spectrum, using an 80/140 kVp spectrum combination and applying filtration to both the LE and HE spectrum. The filtration is specified in millimetres of tin. For each mAs ratio, the minimum nCRLB of all tested threshold combinations is plotted.

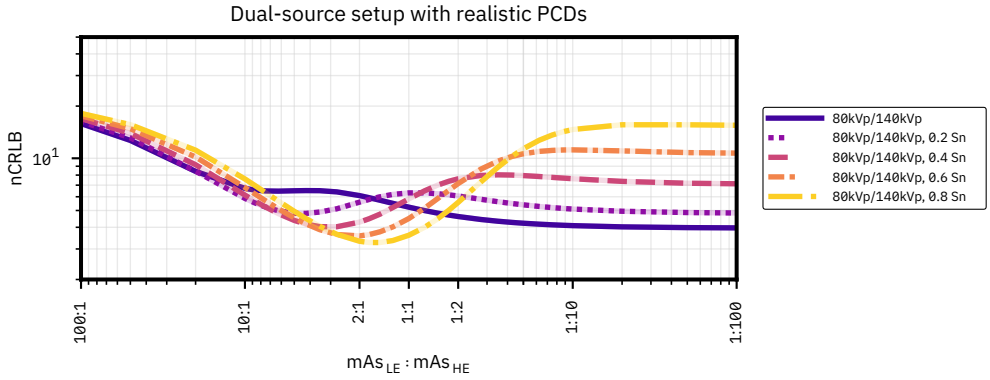

Figure 3.B.40: nCRLB values for estimating SPR as achieved by a dual-source setup using realistic PCDs for different ratios $mAs_{LE} : mAs_{HE}$ between the LE and HE spectrum, using an 80/140 kVp spectrum combination and applying filtration to the HE spectrum only. The filtration is specified in millimetres of tin. For each mAs ratio, the minimum nCRLB of all tested threshold combinations is plotted.

Results as a function of photon number ratio

Here, selected results for setups using two distinct source spectra (i.e., kVp-switching and dual-source setups) are plotted over the ratio of photon numbers n_γ instead of over the mAs ratio. The photon number ratio $n_{\gamma,\mathrm{LE}} : n_{\gamma,\mathrm{HE}}$ specifies the ratio between the number of photons leaving the source, including source filtration, when using the low energy ($n_{\gamma,\mathrm{LE}}$) and high energy ($n_{\gamma,\mathrm{HE}}$) phase/source.

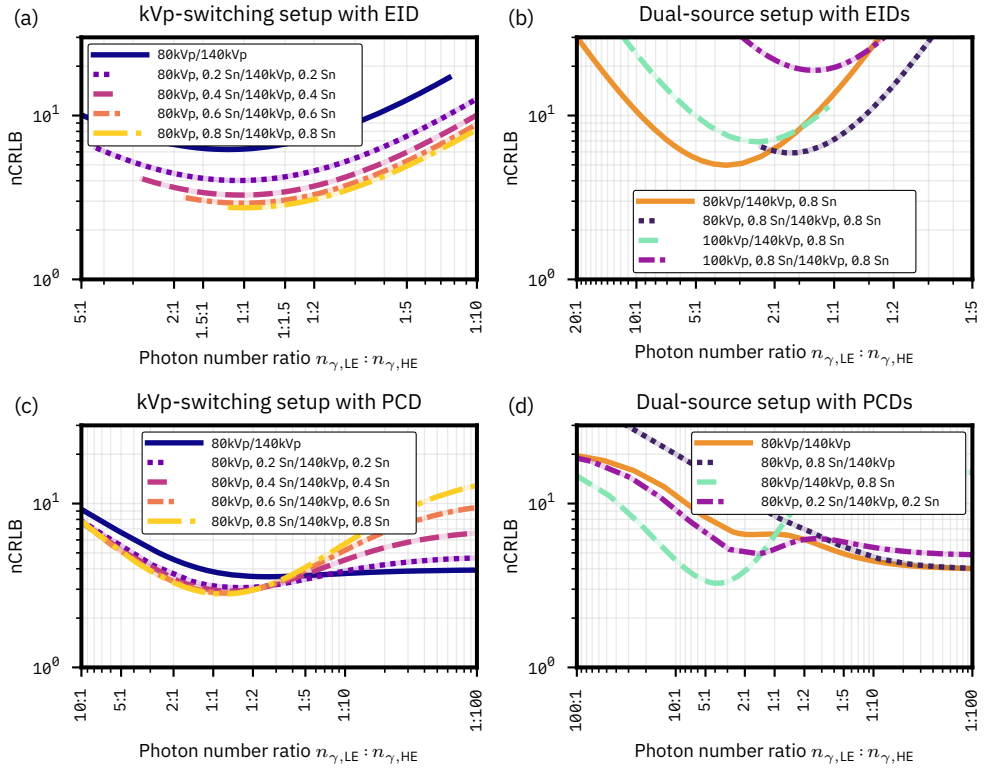

Figure 3.B.41: This figure is identical to Figure 3.4 except that the results are plotted over the photon number ratio $n_{\gamma,\mathrm{LE}} : n_{\gamma,\mathrm{HE}}$ instead of over the mAs ratio and except that a realistic detector response function is assumed.
This figure shows the optimisation of spectral CBCT setups with respect to the extraction of SPR, assuming a realistic detector response function. (a) kVp-switching setup with one EID and (b) dual-source setup with two EIDs, optimising the ratio $n_{\gamma,\mathrm{LE}} : n_{\gamma,\mathrm{HE}}$ between the LE and HE spectra. (c) kVp-switching setup with one PCD and (d) dual-source setup with two PCDs; for each $n_{\gamma,\mathrm{LE}} : n_{\gamma,\mathrm{HE}}$ ratio, the minimum nCRLB of all tested threshold combinations is plotted. All values are reported as normalised CRLB values as stated in the text, with the same nCRLB value range for all figures; source filtration is specified in millimetres of tin.

3.B.5 Supplementary Results for Comparison of kVp-Switching and Dual-Source Setups

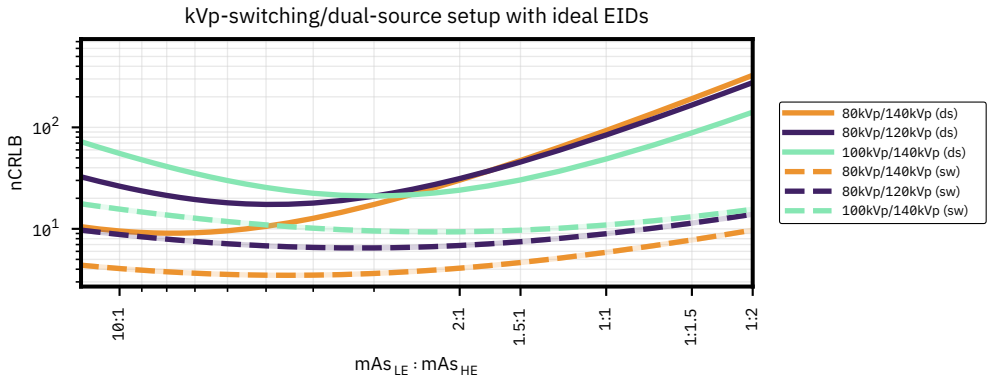

Figure 3.B.42: nCRLB values for estimating SPR as achieved by a dual-source setup using ideal EIDs (ds) or a kVp-switching setup using one ideal EID (sw), for different ratios $mAs_{LE} : mAs_{HE}$ between the LE and HE spectrum/phase.

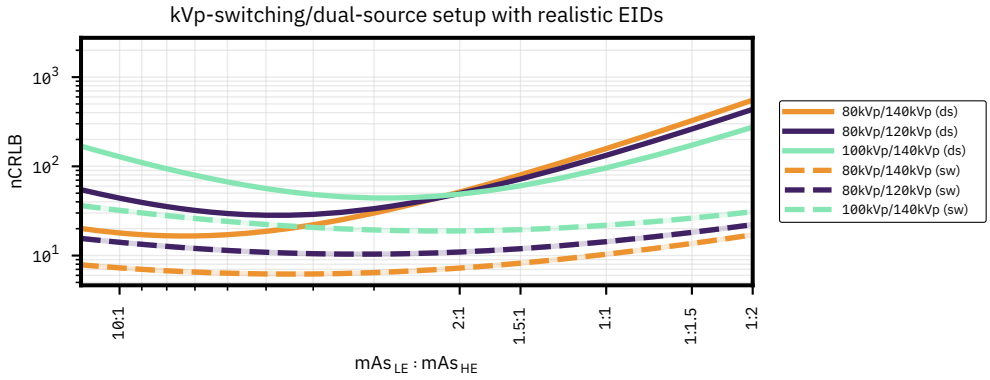

Figure 3.B.43: nCRLB values for estimating SPR as achieved by a dual-source setup using realistic EIDs (ds) or a kVp-switching setup using one realistic EID (sw), for different ratios $mAs_{LE} : mAs_{HE}$ between the LE and HE spectrum/phase.

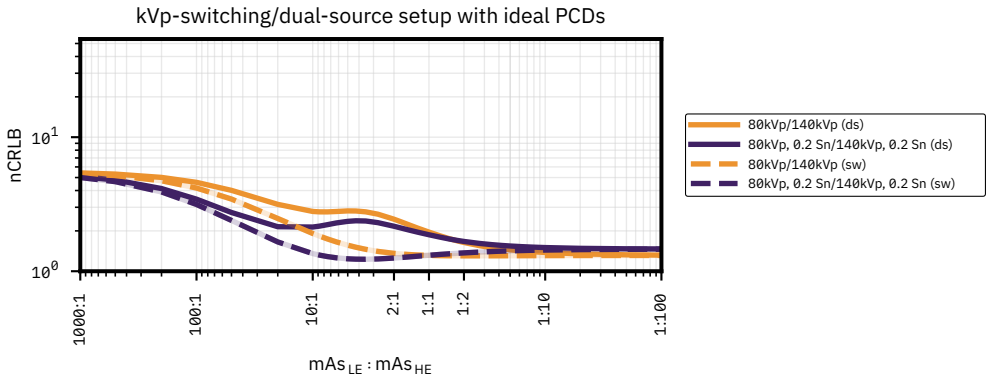

Figure 3.B.44: nCRLB values for estimating SPR as achieved by a dual-source setup using ideal PCDs (ds) or a kVp-switching setup using one ideal PCD (sw), for different ratios $mAs_{LE} : mAs_{HE}$ between the LE and HE spectrum/phase. For each mAs ratio, the minimum nCRLB of all tested threshold combinations is plotted. In case of the kVp-switching setup, the thresholds are adjusted independently for each phase.

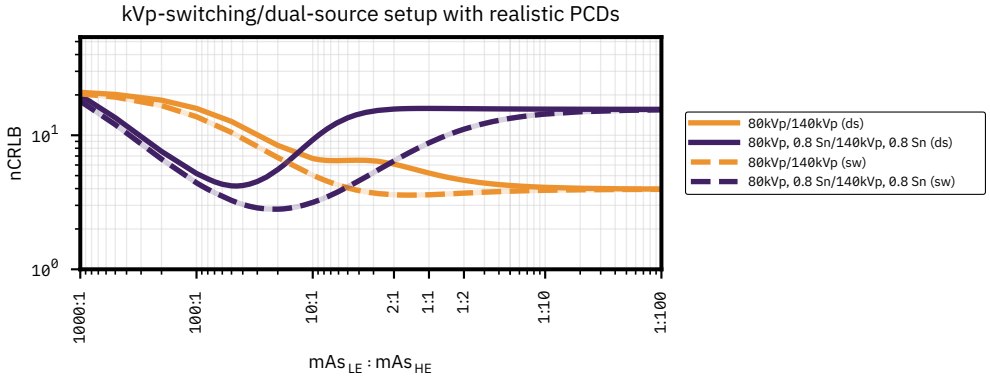

Figure 3.B.45: nCRLB values for estimating SPR as achieved by a dual-source setup using realistic PCDs (ds) or a kVp-switching setup using one realistic PCD (sw), for different ratios $mAs_{LE} : mAs_{HE}$ between the LE and HE spectrum/phase. For each mAs ratio, the minimum nCRLB of all tested threshold combinations is plotted. In case of the kVp-switching setup, the thresholds are adjusted independently for each phase.

3.B.6 Supplementary Results for Comparison of Detector Response Functions

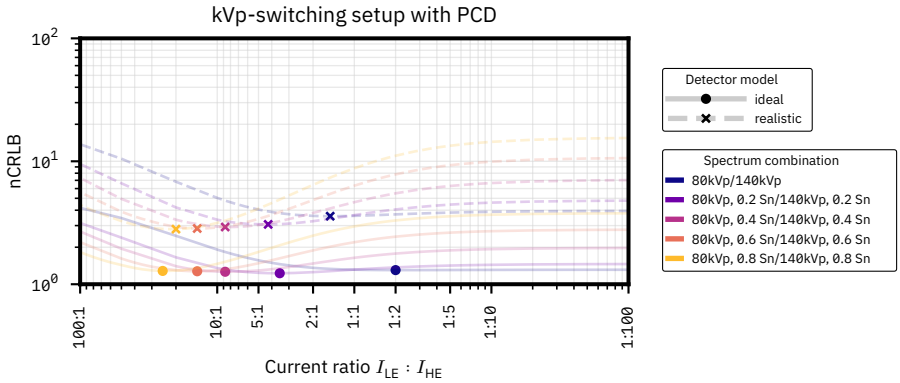

Figure 3.B.46: kVp-switching setup using one PCD with two bins optimised with respect to the extraction of SPR, comparing ideal and realistic detector response functions. For each mAs ratio, the minimum nCRLB of all tested threshold combinations is plotted (thresholds are adjusted independently for each phase); source filtration is specified in millimetres of tin.

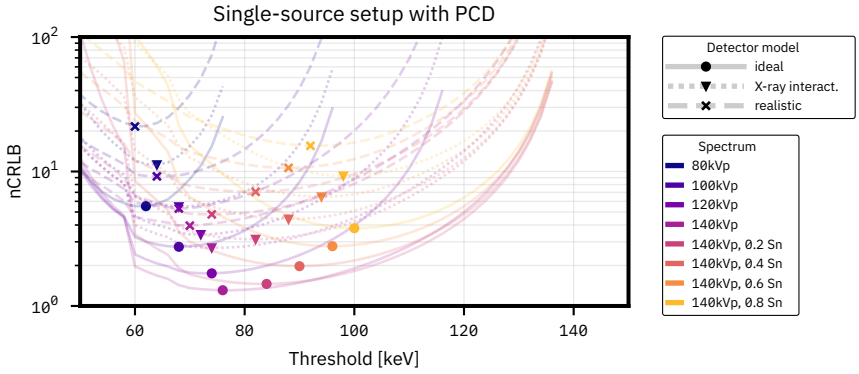

Figure 3.B.47: Single-source setup using one PCD with two bins optimised with respect to the extraction of SPR by optimising the threshold between the low and high energy bin. The figure compares an ideal detector response function, a detector response function based solely on X-ray transport, and a realistic detector response function comprised of both X-ray transport and charge sharing. Markers indicate the position of optima; source filtration is specified in millimetres of tin.

3.B.7 Supplementary Results for Different Detector Response Functions Applied to PCDs

This section presents the results for the optimisation of a single-source setup using one PCD, with a detector response function that only incorporates X-ray transport while neglecting charge sharing. For the results assuming an ideal detector response function or a realistic detector response function (incorporating both X-ray transport and charge sharing) see Section 3.B.3 and 3.B.4, respectively.

Table 3.B.22: Results for the optimisation of the setup based on a single source with a PCD using two energy bins. The detector response function only incorporates X-ray transport, but not charge sharing. The table states the minimum nCRLB values that are achieved and their respective parameters.

Spectrum	Optimum thresholds [keV]	min. nCRLB
80 kVp	[20, 64, 80]	11.23
100 kVp	[20, 68, 100]	5.470
120 kVp	[20, 72, 120]	3.400
140 kVp	[20, 74, 140]	2.707
140 kVp, 0.2 mm Sn	[20, 82, 140]	3.135
140 kVp, 0.4 mm Sn	[20, 88, 140]	4.424
140 kVp, 0.6 mm Sn	[20, 94, 140]	6.488
140 kVp, 0.8 mm Sn	[20, 98, 140]	9.259

Table 3.B.23: Results for the optimisation of the setup based on a single source with a PCD using three energy bins. The detector response function only incorporates X-ray transport, but not charge sharing. The table states the minimum nCRLB values that are achieved and their respective parameters.

Spectrum	Optimum thresholds [keV]	min. nCRLB
80 kVp	[20, 60, 68, 80]	10.06
100 kVp	[20, 64, 78, 100]	4.743
120 kVp	[20, 68, 84, 120]	3.053
140 kVp	[20, 70, 92, 140]	2.416
140 kVp, 0.2 mm Sn	[20, 74, 96, 140]	2.783
140 kVp, 0.4 mm Sn	[20, 82, 102, 140]	3.932
140 kVp, 0.6 mm Sn	[20, 88, 106, 140]	5.781
140 kVp, 0.8 mm Sn	[20, 32, 94, 140]	7.749

Table 3.B.24: Results for the optimisation of the setup based on a single source with a PCD using four energy bins. The detector response function only incorporates X-ray transport, but not charge sharing. The table states the minimum nCRLB values that are achieved and their respective parameters.

Spectrum	Optimum thresholds [keV]	min. nCRLB
80 kVp	[20, 60, 65, 70, 80]	9.723
100 kVp	[20, 60, 70, 80, 100]	4.565
120 kVp	[20, 65, 75, 90, 120]	2.956
140 kVp	[20, 30, 70, 90, 140]	2.243
140 kVp, 0.2 mm Sn	[20, 30, 70, 95, 140]	2.397
140 kVp, 0.4 mm Sn	[20, 55, 70, 95, 140]	3.398
140 kVp, 0.6 mm Sn	[20, 55, 80, 100, 140]	4.980
140 kVp, 0.8 mm Sn	[20, 55, 85, 105, 140]	7.008

Table 3.B.25: Results for the setup based on a single source with a PCD using near-continuous energy binning. The first bin is between 3 to 5 keV wide to prevent photon starvation, whereas all subsequent bins have a width of 1 keV. The detector response function only incorporates X-ray transport, but not charge sharing. The table states the resulting nCRLB values and their respective parameters.

Spectrum	Thresholds [keV]	min. nCRLB
80 kVp	[20, 23, 24, ..., 79, 80]	8.232
100 kVp	[20, 23, 24, ..., 99, 100]	3.913
120 kVp	[20, 23, 24, ..., 119, 120]	2.458
140 kVp	[20, 23, 24, ..., 139, 140]	1.911
140 kVp, 0.2 mm Sn	[20, 25, 26, ..., 139, 140]	1.952
140 kVp, 0.4 mm Sn	[20, 25, 26, ..., 139, 140]	2.543
140 kVp, 0.6 mm Sn	[20, 25, 26, ..., 139, 140]	3.707
140 kVp, 0.8 mm Sn	[20, 25, 26, ..., 139, 140]	5.433

3.B.8 Supplementary Results Excluding (Cross-)Scatter

This section presents results when excluding scatter in the case of single-source setups (with either a source of fixed voltage or a kVp-switching source) and when excluding both scatter and cross-scatter in the case of dual-source setups. Please note that no optimisation is performed, instead, the optimum operating parameters obtained for the case including (cross-)scatter are used, as reported in Table 3.2 (ideal detector response) and Table 3.3 (realistic detector response).

The results presented here are not equivalent to the performance that could be achieved by a fan-beam CT. Firstly, (cross-)scatter is the main, but not the only difference between fan- and cone-beam CT. Secondly, while fan-beam CT is less susceptible to (cross-)scatter than CBCT, (cross-)scatter is not completely eliminated. Omitting (cross-)scatter entirely therefore yields a performance that is even better than what is achievable using fan-beam CT, which is especially true for modern fan-beam CT scanners featuring a larger detector coverage along the z-axis (cranial-caudal direction of patients).

3

Table 3.B.26: Results for the various spectral CBCT setups with respect to the extraction of SPR, assuming an ideal detector response function but excluding (cross-)scatter. The operating parameters were kept the same as in the case of included (cross-)scatter (see Table 3.2), without any further optimisation. Note that the nCRLB value of the single-source setup with one PCD deviates slightly from the dual-source setup with two PCDs, operated in the limit of using only the HE source-detector pair, due to the different step sizes chosen for the optimisation of bins.

Setup	**Spectrum (combination)**	**Parameters (bins, $mAs_{LE} : mAs_{HE}$)**	**min. nCRLB**
Single-source setup with PCD	140 kVp	[20, 76, 140] keV	0.552
	140 kVp	[20, 70, 94, 140] keV	0.498
	140 kVp	[20, 60, 75, 95, 140] keV	0.431
	140 kVp	Continuous binning	(0.341)[a]
Single source with dual-layer detector	140 kVp	[20, 72, 140] keV	0.551
	140 kVp	[20, 68, 84, 140] keV	0.533
kVp-switching setup with EID	80 kVp, 0.2 mm Sn/ 140 kVp, 0.2 mm Sn	1 : 1	2.39
	80 kVp, 0.8 mm Sn/ 140 kVp, 0.8 mm Sn	29 : 1	0.826
Dual-source setup with EIDs	80 kVp/ 140 kVp, 0.8 mm Sn	1.75 : 1	0.654
kVp-switching setup with PCD	80 kVp/140 kVp	1:1; LE bins: [20, 60, 80] keV, HE bins: [20, 75, 140] keV.	0.541
	80 kVp, 0.2 mm Sn/ 140 kVp, 0.2 mm Sn	3.5 : 1; LE bins: [20, 65, 80] keV, HE bins: [20, 85, 140] keV.	0.540
Dual-source setup with PCDs	80 kVp/140 kVp	HE only; HE bins: [20, 75, 140] keV.	0.545
	80 kVp/ 140 kVp, 0.8 mm Sn	1.75 : 1; LE bins: [20, 60, 80] keV, HE bins: [20, 90, 140] keV.	0.417

[a] The number of photons received by some bins was too low to allow for an approximation of the Poisson distribution by a normal distribution.

Table 3.B.27: Results for the various spectral CBCT setups with respect to the extraction of SPR, assuming a realistic detector response function but excluding (cross-)scatter. The operating parameters were kept the same as in the case of included (cross-)scatter (see Table 3.3), without any further optimisation.

Setup	**Spectrum (combination)**	**Parameters (bins, $mAs_{LE} : mAs_{HE}$, layer thicknesses)**	**min. nCRLB**
Single-source setup with PCD	140 kVp	[20, 70, 140] keV	1.92
	140 kVp	[20, 68, 88, 140] keV	1.81
	140 kVp	[20, 60, 70, 90, 140] keV	1.66
	140 kVp	Continuous binning	1.55
Single source with dual-layer detector	140 kVp	Top layer: 0.45 mm CsI, bottom layer: 1.45 mm CsI.	5.62
	140 kVp	Top layer: 0.2 mm CsI, filtration layer: 1.8 mm Cu, bottom layer: 1.7 mm CsI.	3.94
kVp-switching setup with EID	80 kVp, 0.2 mm Sn/ 140 kVp, 0.2 mm Sn	1 : 1	4.00
	80 kVp, 0.8 mm Sn/ 140 kVp, 0.8 mm Sn	26 : 1	1.37
Dual-source setup with EIDs	80 kVp/ 140 kVp, 0.8 mm Sn	1.5 : 1	1.03
kVp-switching setup with PCD	80 kVp/140 kVp	1:1; LE bins: [20, 65, 80] keV, HE bins: [20, 70, 140] keV.	1.70
	80 kVp, 0.8 mm Sn/ 140 kVp, 0.8 mm Sn	20 : 1; LE bins: [20, 30, 80] keV, HE bins: [20, 80, 140] keV.	1.44
Dual-source setup with PCDs	80 kVp/140 kVp	HE only; HE bins: [20, 70, 140] keV.	1.92
	80 kVp/ 140 kVp, 0.8 mm Sn	1.5 : 1; LE bins: [20, 65, 80] keV, HE bins: [20, 70, 140] keV.	1.01

References

[4] H. H. Barrett and K. J. Myers, *Foundations of Image Science* (Wiley Series in Pure and Applied Optics). Hoboken, NJ: Wiley-Interscience, 2004.

[10] S. B. Heymsfield, J. Wang, J. Kehayias, S. Heshka, S. Lichtman, and R. N. Pierson, "Chemical determination of human body density in vivo: Relevance to hydrodensitometry", *The American Journal of Clinical Nutrition*, vol. 50, no. 6, pp. 1282–1289, 1989. DOI: 10.1093/ajcn/50.6.1282.

[21] G. M. Lasio, B. R. Whiting, and J. F. Williamson, "Statistical reconstruction for x-ray computed tomography using energy-integrating detectors", *Physics in Medicine and Biology*, vol. 52, no. 8, pp. 2247–2266, 2007. DOI: 10.1088/0031-9155/52/8/014.

[25] Matt Newville, *XrayDB*, https://github.com/xraypy/XrayDB/.

[59] D. R. White, J. Booz, R. V. Griffith, J. J. Spokas, and I. J. Wilson, "Report 44", *Journal of the International Commission on Radiation Units and Measurements (ICRU)*, vol. os23, no. 1, NP–NP, 1989. DOI: 10.1093/jicru/os23.1.Report44.

[60] D. R. White, H. Q. Woodard, and S. M. Hammond, "Average soft-tissue and bone models for use in radiation dosimetry", *The British Journal of Radiology*, vol. 60, no. 717, pp. 907–913, 1987. DOI: 10.1259/0007-1285-60-717-907.

[61] B. R. Whiting, "Signal statistics in x-ray computed tomography", in *Medical Imaging 2002: Physics of Medical Imaging*, L. E. Antonuk and M. J. Yaffe, Eds., vol. 4682, San Diego, CA: SPIE, 2002, pp. 53–60. DOI: 10.1117/12.465601.

Chapter 4

Experimental Study on Clinical Dual-Energy Cone-Beam CT for Proton Therapy Planning

Objective: To test the ability of dual-energy CBCT to extract proton stopping power ratio (SPR) values for proton radiotherapy planning and to compare its performance to single-energy CBCT, while optimising the operating parameters of both single- and dual-energy CBCT for SPR extraction.
Methods: We scanned three phantoms with a clinical CBCT system installed in the gantry of a proton therapy facility with a selection of different source voltage and current settings. Dual-energy CBCT was emulated by combining scans from different kVps. A fair comparison between single- and dual-energy CBCT scans was ensured by using the same CT dose index. We employed the Hünemohr-Saito method to predict SPR values for dual-energy CBCT scans, whereas we used a Hounsfield look-up table for predicting SPR values based on single-energy CT scans. As a measure of the system's ability to differentiate between tissues, we calculated the overlap of CT number distributions of inserts mimicking adipose and soft tissues.
Results: For single-energy CBCT scans, 125 kVp was determined to be the optimum voltage, yielding a relative mean error (RME), a relative mean absolute error (RMAE) and a relative root mean square error (RRMSE) value of (1.5 ± 3.3) %, (3.4 ± 2.7) % and (7.1 ± 6.9) %, respectively. The optimum operating parameters for dual-energy CBCT scans were an 80/125 kVp combination with a low/high kVp dose ratio of 75/25. This resulted in a RME, RMAE and RRMSE value of (0.1 ± 1.2) %, (2.23 ± 0.87) % and (2.53 ± 0.73) %, respectively. Furthermore, we found that inserts could be differentiated better by dual-energy CBCT than by single-energy CBCT.
Conclusion: Although limited in scope and in need of further experiments, this study indicates that dual-energy CBCT might perform better for SPR extraction than single-energy CBCT.

Parts of this chapter were submitted for presentation at the SPIE Medical Imaging conference 2026.

4.1 Introduction

Proton radiotherapy is being investigated as a promising form of radiotherapy [3] in addition to conventional X-ray photon radiotherapy. Its main appeal is the deposition of the highest dose per traversed length at the end of a finite proton range [16]. At the same time, the susceptibility of the proton range to changes in tissue density and composition makes it imperative to extract proton stopping power ratio (SPR) values of the volume to be treated as precisely as possible in order to ensure a dose delivery distributed as requested by the clinicians. The state-of-the-art imaging modality for extracting SPR values for proton radiotherapy treatment planning is fan-beam CT [2], since it achieves a contrast sufficiently high for anatomical delineation of soft tissues, and since a relation between SPR and X-ray attenuation can be drawn. In contrast to fan-beam CT, cone-beam CT (CBCT) is not used for treatment planning directly, but mostly used as an in-room modality for patient positioning [11, 23] since its image quality is inferior to that of fan-beam CT. This is mainly due to the influence of more pronounced scatter (flat-panel instead of line detector, see Figure 1.2) [25] and increased patient motion (longer rotation times). In contrast to fan-beam CT, however, CBCT offers the advantage of integrating the imaging modality isocentrically with the proton beam.

A possible route to enable direct utilisation of CBCT images in treatment planning could be to enhance CBCT setups in such a way that they can extract spectral information from X-rays instead of just measuring their intensity, which is the current standard. This hypothesis is based on previous studies that have shown that a better accuracy and robustness can be achieved when using spectral fan-beam CT instead of single-energy (SE) fan-beam CT [1, 13, 15, 19, 26, 27, 30, 32, 33].

The aim of this study was to compare the accuracy and robustness of SPR extraction from (emulated) dual-energy (DE) CBCT scans and SE CBCT scans, acquired with a clinical CBCT system. We emulated DE CBCT scans by scanning three different phantoms subsequently at different source voltages, and tested different combinations of low and high energy source voltages as well as different ratios of dose assigned to the low and high energy scans. Similarly, we tested different source voltages for SE CBCT. The total dose was kept the same for all DE and SE scans. We applied the Hünemohr-Saito (HS) method [12] and a Hounsfield look-up table (HLUT) [18] for predicting SPRs based on DE and SE scans, respectively. Furthermore, we investigated the ability of SE and DE CBCT systems to differentiate between adipose- and soft tissue-like inserts with very similar CT numbers.

4.2 Methodology

4.2.1 Phantoms

We scanned a Catphan 700 phantom (diameter of 200 mm; THE PHANTOM LABORATORY), a CIRS 062 Electron Density Phantom body (diameter of 180 mm; SUN NUCLEAR CORP.) with a custom selection of inserts, and a Gammex 467 phantom (diameter of 330 mm; the outer ring of inserts is arranged along a circle with 220 mm diameter; SUN NUCLEAR CORP.). Table 4.1 lists the ground truth values for the relative electron density $\rho_{\text{elec}}^{\text{rel}}$, effective atomic number Z_{eff}, ionisation energy I and SPR values for the phantom inserts used in this study, based on elemental composition and mass density data, and calculated based on Equations 4.1 to 4.4; for more information we refer to Section 4.2.4 and Section 4.A.3 in the Appendix. For the elemental composition and physical mass density nominal values provided by the manufacturers are used, with the exception of inserts of the Gammex and CIRS phantom for which specific physical mass density values are provided by the manufacturers.

The phantom inserts are classified for the HLUT calibration as either *soft tissue*-like, *bone tissue*-like, *adipose tissue*-like, *lung tissue*-like or *others*. The classification of CIRS and Gammex

Table 4.1: Overview of the phantoms and their inserts used in this study. The table states the inserts' names, their position as indicated in Figure 4.2, as well as their ground truth values for the relative electron density $\rho_{\text{elec}}^{\text{rel}}$, effective atomic number Z_{eff}, ionisation energy I and SPR (calculated based on Equation 4.1, 4.2, 4.3 and 4.4, respectively), using the data on elemental composition and mass density provided by the manufacturers. Inserts are color-coded depending on whether they try to mimic **adipose tissue**, **bone tissue**, **lung tissue**, **soft tissue** or **others**.

Phantom	Insert	Position	$\rho_{\text{elec}}^{\text{rel}}$	Z_{eff}	I [eV]	SPR
Catphan	Acrylic	1	1.15	6.50	71	1.15
	Air	0	—	—	—	—
	20 % bone	4	1.08	9.28	80	1.08
	50 % bone	2	1.31	11.7	94	1.28
	Delrin	7	1.36	6.98	77	1.36
	LDPE	3	0.945	5.47	57	0.977
	Lung foam	8	0.179	6.66	77	0.178
	PMP	9	0.853	5.47	57	0.882
	Polystyrene	6	0.998	5.71	66	1.01
	Teflon	5	1.87	8.45	103	1.80
	Vial (empty)	10	—	—	—	—
CIRS	70 % cort./30 % trab. bone	1	1.52	12.5	98	1.47
	30 % gland/70 % adipose	6	0.960	6.58	66	0.975
	70 % gland/30 % adipose	0	0.997	6.94	67	1.01
	Kidney	4	1.04	7.46	71	1.05
	Lung (inhale)	2	0.201	7.33	69	0.203
	Prostate	7	1.04	7.32	75	1.04
	Spinal cord	5	1.03	7.40	73	1.03
	Spinal disk	3	1.08	7.92	81	1.07
Gammex	Adipose	2	0.933	6.12	66	0.948
	Brain	1	1.04	6.12	65	1.05
	Breast	7	0.963	6.75	67	0.976
	B200 bone mineral	13	1.11	9.97	80	1.10
	CB2-30 % $CaCO_3$ bone	5	1.27	10.6	84	1.25
	CB2-50 % $CaCO_3$ bone	3	1.46	12.2	96	1.42
	Cortical bone	0	1.68	13.4	108	1.61
	Inner bone	10	1.10	9.97	80	1.09
	Liver	12	1.06	7.49	69	1.07
	LN300 lung	8	0.270	7.56	76	0.270
	LN450 lung	14	0.444	7.53	76	0.443
	Solid water (1–4)	4, 9, 11, 15	0.989	7.49	69	0.999
	Water	6	1.000	7.45	75	1.000

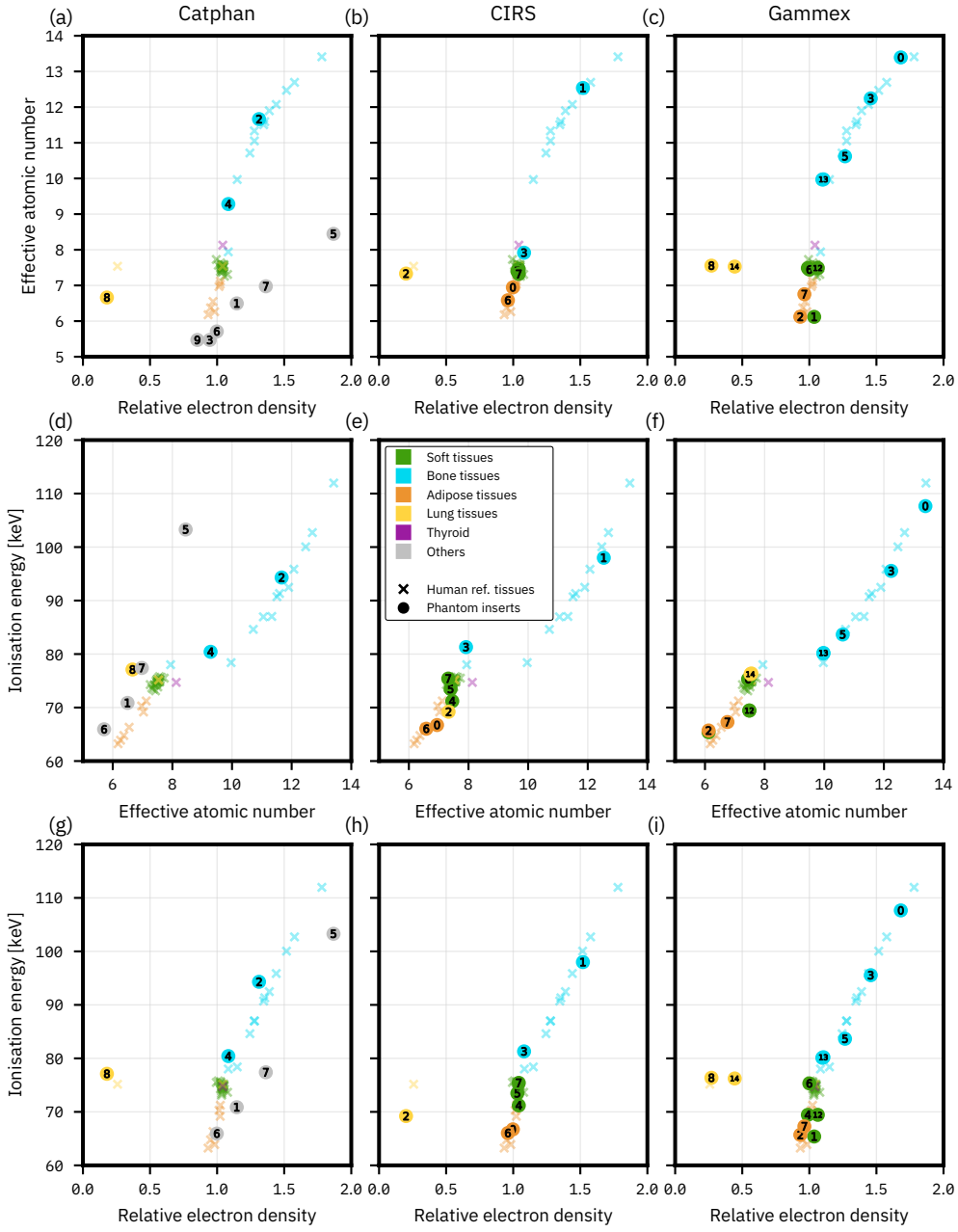

Figure 4.1: Testing equivalency between phantom inserts and tabulated human tissues based on their relative electron density, effective atomic number and ionisation energy. See Table 4.1 for the phantom inserts' position number as indicated in the figure, their assignment to tissue classes, as well as the values for $\rho_{\text{elec}}^{\text{rel}}$, Z_{eff} and I. Left column: Catphan phantom; centre column: CIRS phantom; right column: Gammex phantom. First row: Z_{eff} vs. $\rho_{\text{elec}}^{\text{rel}}$; second row: I vs. Z_{eff}; third row: I vs. $\rho_{\text{elec}}^{\text{rel}}$. Markers can overlap.

inserts follows the classification in Table S1.3 in the consensus guide by Peters, Taasti et al [18] (see Supplementary Material therein) where possible. For all other inserts as well as for the Catphan phantom, we follow the *Evaluation box 2* in the aforementioned consensus guide (Supplementary Material, p. 3) and compare the phantom inserts to tabulated human tissues with respect to effective atomic number, relative electron density and ionisation energy. The comparison is shown in Figure 4.1, with both human tissues as well as phantom tissues divided into their corresponding tissue classes. The resulting classification of phantom inserts can be found in Table 4.1.

For the tabulated human tissues used in this comparison, we use data on tabulated human tissues listed in Peters, Taasti et al [18], which in turn is taken from Woodard and White [31]. Additionally, we show tissues tabulated in the ICRU report 44 [28] and in White et al [29], as compiled by Yang et al [33]. For the HLUT calibration (see Section 4.2.5) Peters, Taasti et al excluded small volume tissues from their selection of tabulated human tissues and only included the base tissues of the bone tissue class, since, as they point out, additional bone tissues listed in White et al [29] are simply a mixture of a limited number of base tissues. We follow Peters, Taasti et al. in their selection of tissues for the HLUT calibration, however, for the comparison of phantom inserts to human tissues we use the extended selection, which allows to better assess the spread of each class of human tissues.

We would like to note that Peters, Taasti et al classified the Gammex inserts 'HE Brain', 'HE Liver' and 'HE CT Solid Water' as soft tissues. We follow their classification for our corresponding Gammex inserts, although our inserts differ in both mass density and elemental composition. When comparing the physical quantities of our Gammex inserts to tabulated human tissues, our Gammex insert 'Brain' is more similar to adipose tissue than to soft tissue, and the Gammex inserts 'Liver' and 'Solid water (1–4)' are somewhere between soft and adipose tissue.

4.2.2 Acquisition and Reconstruction of CBCT Scans

All CBCT scans in this study were acquired in a proton therapy treatment gantry (VARIAN PROBEAM SYSTEM®, VARIAN MEDICAL SYSTEMS, Inc., Palo Alto, CA) of the Holland Proton Therapy Center (HOLLANDPTC, Delft, The Netherlands), which features two orthogonal CBCT systems per gantry. All scans evaluated in this study were acquired on the same CBCT system.

The phantoms were scanned with the three available X-ray source voltages of 80, 100 and 125 kVp. For a fair comparison between different combinations of scans from different voltages, we adjusted the source current for each source voltage such that the maximum radiation output by the system, as specified by the system through the so-called *CT dose index* (CTDI) value, is the same for each given source voltage ($CTDI_{vol,\ 16cm}$ = 4.6 mGy). In addition to that, scans with 75 %, 50 % and 25 % of the maximum radiation output (100 %) were acquired. This allows us to compare SE scans acquired with 100 % dose to DE scans composed of scans at different kVps with the same total dose; for example, one can combine a low and a high voltage scan by assigning 25 % and 75 % , 50 % and 50 %, or 75 % and 25 % radiation output to the low and high voltage scan, respectively.

All scans were reconstructed with the default reconstruction software available on the clinical system, which performs a reconstruction based on the Feldkamp-Davis-Kress (FDK) algorithm, and which includes beam hardening correction as well as a kernel-based scatter correction algorithm. The reconstructed volumes consist of 106 slices (stacked along the rotational axis of the gantry) with a slice thickness of 1.99 mm; each slice consists of 512 × 512 pixels (dimensions orthogonal to the rotational axis); the voxel size is 0.5655 × 0.5655 × 1.99 mm^3.

On our clinical system, scans at all three desired source voltages are only available in combina-

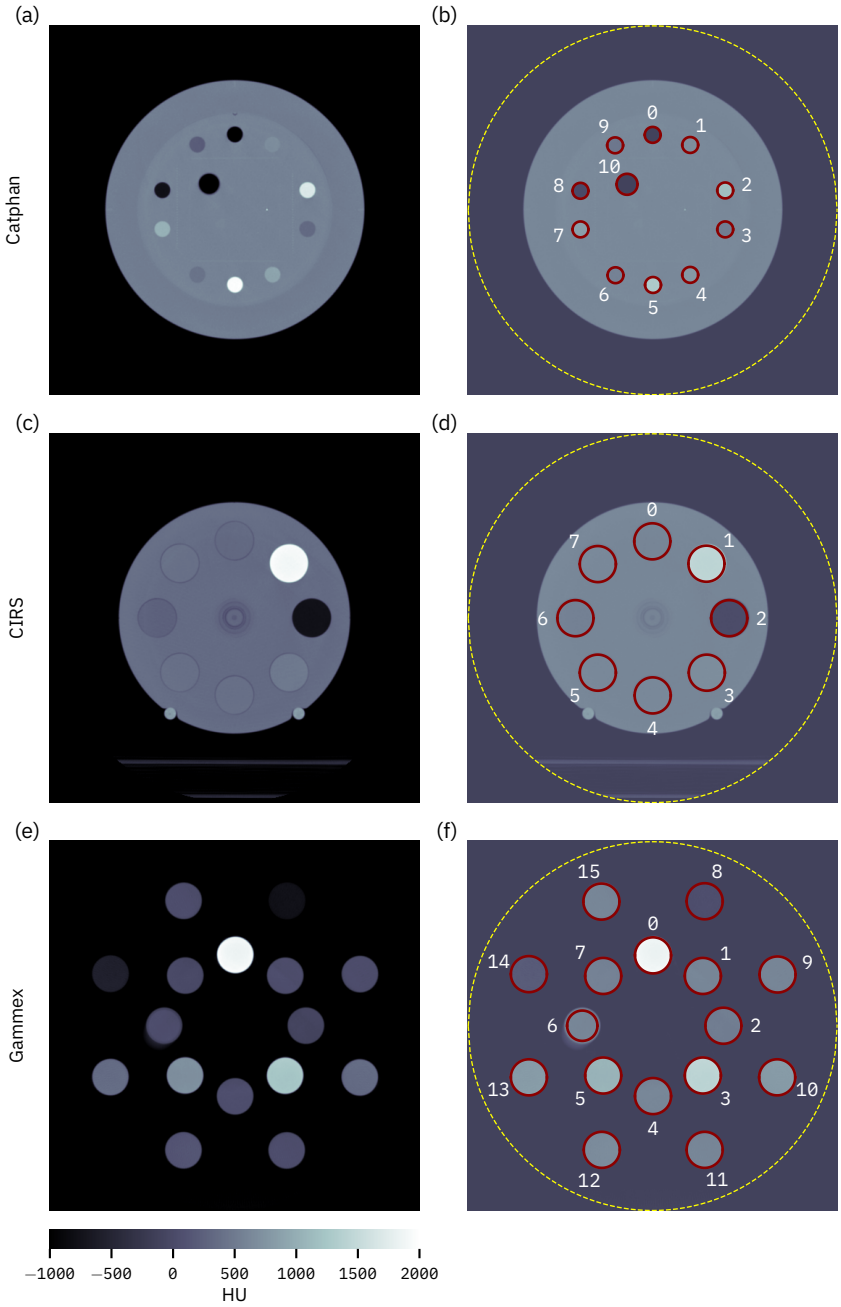

Figure 4.2: Left column: mean images of the evaluated reconstructed slices. Right column: Insert locations, see Table 4.1 for insert names. First row: Catphan phantom. Second row: CIRS phantom. Third row: Gammex phantom (only slices that excluded the phantom body were used). All reconstructed slices are 512 × 512 pixels (289.5 × 289.5 mm). Field-of-view is indicated via a yellow, dashed line.

tion with a mode that is intended for head scans, featuring a limited field-of-view[1] (FOV) with a diameter of 289.5 mm. The Gammex phantom's body is wider than this FOV, which in principle gives rise to severe reconstruction artefacts. However, its inserts protrude from the phantom body and still fit inside the FOV. For evaluation pertaining to the Gammex phantom, we therefore used reconstructed slices devoid of the Gammex phantom body and only containing the protruding inserts. Since the reconstruction software applies a beam hardening correction, though, this means that the reconstructed attenuation values for the inserts will be off when there is no water-like object present in the beam with a diameter similar to what was used to calibrate the beam-hardening correction algorithm.

Figure 4.2 shows mean images of the reconstructed slices for the three phantoms, averaged over all slices included in the CT number evaluation; please note that the averaging greatly reduces the noise in these images.

4.2.3 Placement of ROIs

A cylindrical region-of-interest (ROI) is placed manually in each insert, with a diameter that corresponds to 80 % of an insert's diameter. Along the axial direction we include as many slices as possible, while excluding as many slices as necessary in order to reduce the effect of edge artefacts at the end of inserts or phantoms. Table 4.A.1 in the Appendix lists the number of slices evaluated for each phantom and the number of voxels included in the ROI of each insert. Tables 4.B.1 to 4.B.3 in the Appendix list the extracted Hounsfield unit values for each insert and phantom.

The central insert of the CIRS phantom is a partially empty container, which is hence excluded in the following. In case of the Catphan phantom, the insert containing only air (position 0) and the empty vial (position 10) are also excluded.

4.2.4 Calculation of Material Properties

The absolute electron density ρ_{elec} (number of electrons per unit volume) of a compound is calculated according to

$$\rho_{\text{elec}} = \rho_{\text{mass}} \frac{1}{m_{\text{u}}} \sum_p \frac{w_p \cdot Z_p}{A_p} \quad , \tag{4.1}$$

with ρ_{mass} as the compound's mass density, m_{u} as the unified atomic mass unit, w_p as the mass fraction, A_p as the atomic mass number and Z_p as the atomic number of element p in the compound. The relative electron density of a compound (mat) is defined as its electron density relative to water, i.e., $\rho_{\text{elec}}^{\text{rel}} = \rho_{\text{elec, mat}} / \rho_{\text{elec, water}}$.

The effective atomic number Z_{eff} of a compound is calculated according to

$$Z_{\text{eff},\, n} = \left(\frac{\sum_p \frac{w_p}{A_p} Z_p^{n+1}}{\sum_p \frac{w_p}{A_p} Z_p} \right)^{1/n} \quad , \tag{4.2}$$

with the exponent n having a value around 3. Since we do not have information about the effective spectrum for a given source voltage, we cannot calculate n directly. As part of the procedure to determine the free parameters of the HS method (see Section 4.2.6) we investigated the quality of fits with respect to n as well as the error on predicted values of $Z_{\text{eff},\, n}$ with

[1] The mode with limited field-of-view is called the *full-fan beam mode* configuration, where the centre of the detector lies on a line through the isocentre and the source. In contrast to this, the *half-fan beam mode* uses a configuration where the detector is shifted such that the edge of the detector lies on a line through the isocentre and the source.

respect to n, however, the results were inconclusive. We therefore chose $n = 3.1$, following other authors [7]. In the following, we omit the subscript n in $Z_{\text{eff},\,n}$ whenever $n \equiv 3.1$.

The mean ionisation energy I of a compound is calculated based on the ionisation energies of its elemental constituents using Bragg's additivity rule, neglecting the influence of chemical binding energies:

$$\ln(I) = \left(\sum_p \frac{w_p Z_p}{A_p} \ln(I_p)\right) \left(\sum_p \frac{w_p Z_p}{A_p}\right)^{-1} \quad , \tag{4.3}$$

with I_p as the ionisation energy of element p. Values for the elemental ionisation energies are taken from ICRU report 49 [10], while applying the rule by Seltzer and Berger[24] which is to increase ionisation values by 13 % for elemental substances in the condensed phase (except for the elements H, C, N, F and Cl). See Table 4.A.2 for the elemental values of Z_p, A_p and I_p used in this study.

According to the Bethe equation [17], the SPR relative to water can be determined as follows:

$$\text{SPR} = \frac{\rho_{\text{elec, mat}}}{\rho_{\text{elec, water}}} \cdot \frac{\ln\left(\frac{2m_e c^2 \beta^2}{I_{\text{mat}} \cdot (1-\beta^2)}\right) - \beta^2}{\ln\left(\frac{2m_e c^2 \beta^2}{I_{\text{water}} \cdot (1-\beta^2)}\right) - \beta^2} \quad , \tag{4.4}$$

with $\rho_{\text{elec},\,m}$ and I_m as the electron density and the mean excitation energy, respectively, with m as the index for the material under investigation (mat) or water, β as the proton velocity relative to the speed of light in vacuum (not to be confused with the fitting parameter β in Equation 4.9), m_e as the electron mass ($m_e c^2 = 510\,999$ eV), and ignoring density and shell corrections. We use 100 MeV as the proton energy in SPR calculations, following other authors and the recommendations by Inaniwa et al [9].

4.2.5 Hounsfield Look-Up Table

We follow the conventional approach of using a HLUT to predict SPR values from SE CBCT scans. A HLUT is a look-up table from CT numbers to SPR values, specified as a piecewise linear, continuous, monotonically increasing function. The CT number range commonly encountered in medical imaging is divided into four different intervals corresponding to lung tissues, adipose tissues, soft tissues and bone tissues, for each of which a linear function is defined. The CT number intervals of the four tissue classes need not be directly adjacent; in that case, the end points of the linear functions for the four tissue classes are connected via linear functions as well.

The phantom inserts mimicking human tissues are classified according to the four aforementioned tissue classes (based on Figure 4.1) and used to determine the regression line for each corresponding CT number region based on the measured CT value and SPR of each insert, where the latter is in our case calculated from the elemental composition (Equation 4.4). Usually, though, the available number of tissue-mimicking inserts in a phantom is limited. As a remedy, Schneider et al [22] included tabulated human tissues in order to increase the robustness of the fit, which, however, requires to calculate the theoretical CT number of tabulated human tissues for the given scan protocol. To achieve this, Schneider et al introduced the following parametrisation of the linear attenuation coefficient of a material with known composition [20, 22]:

$$\mu = \rho_{\text{mass}} \cdot N_A \cdot \sum_p \frac{w_p \cdot Z_p}{A_p} \cdot \left(K^{\text{ph}} \cdot (Z_{\text{eff, 3.62}})^{3.62} + K^{\text{coh}} \cdot (Z_{\text{eff, 1.86}})^{1.86} + K^{\text{KN}}\right) \quad , \tag{4.5}$$

with N_A as the Avogadro number. By determining the coefficients K^{ph}, K^{coh} and K^{KN} through regression based on the available phantom inserts, the attenuation, and hence CT number, of any material with known composition can be calculated; this is called the *stoichiometric calibration*.
For details on the process of specifying a HLUT we refer the reader to the consensus guide by Peters, Taasti et al [18], which provides reference implementations as well as a suggested selection of tabulated human tissues to incorporate in the HLUT generation, based on a collection by Woodard and White [31]. Both are used in this study, and we follow their instructions on choosing CT number intervals for the HLUT generation. However, due to the limited scope of this study we did not follow all of the recommendations of the consensus guide. For example, we did not acquire individual CT scans for each bone insert in the centre of the phantom while filling all other insert positions with materials similar to water. Furthermore, we used 80 % of the inserts' diameter for the definition of ROIs to maximise the volume unaffected by density gradients, whereas the consensus guide advises 70 %.

We would like to note that in case of the Catphan phantom, we include all inserts for the stoichiometric calibration (Equation 4.5), however, for the specification of the HLUT, which by its very definition revolves around the four main human tissue classes, only the human tissue-mimicking inserts '20 % bone', '50 % bone' and 'Lung foam' are used. As is evident from Figure 4.1, the Catphan inserts classified in Table 4.1 as 'others' do not resemble any human tissues and are hence excluded from the HLUT specification.
In order to make the HS and the HLUT method as comparable as possible, the same inserts that were excluded from evaluation by the HS method were also excluded from evaluation by the HLUT approach:

- Catphan phantom: 'Lung foam' and 'polystyrene',
- CIRS phantom: 'Lung (inhale)',
- Gammex phantom: 'LN300 lung'.

4.2.6 Hünemohr-Saito Method

We implemented the HS method introduced by Li et al [12] to predict SPR values from DE CBCT scans, which combines the methods introduced by Hünemohr et al [7] and Saito et al [21]. It assumes that there is a linear relationship between the relative electron density ρ_{elec}^{rel} and the so-called *subtracted CT number*, which is a linear combination of the Hounsfield (HU) values obtained at low and high energy:

$$\rho_{elec}^{rel} = a \cdot \frac{\Delta_\alpha \mathrm{HU}}{1000} + b \quad , \tag{4.6}$$

with the subtracted CT number Δ_αHU

$$\Delta_\alpha \mathrm{HU} = (1+\alpha) \cdot \mathrm{HU_H} - \alpha \cdot \mathrm{HU_L} \quad , \tag{4.7}$$

and with $\mathrm{HU_L}$ and $\mathrm{HU_H}$ being the HU values obtained at low and high energy, respectively, and with α, a and b as free parameters.
Analogously, it is assumed that the product $\rho_{elec}^{rel} \cdot Z_{eff}^{n}$, with Z_{eff} being the effective atomic number and $n = 3.1$ (see Section 4.2.4), behaves linearly with respect to a (dedicated) subtracted CT number, that is,

$$\rho_{elec}^{rel} \cdot Z_{eff}^{n} = c \cdot \frac{\Delta_\beta \mathrm{HU}}{1000} + d \quad , \tag{4.8}$$

with the subtracted CT number Δ_βHU

$$\Delta_\beta \mathrm{HU} = (1+\beta) \cdot \mathrm{HU_H} - \beta \cdot \mathrm{HU_L} \quad , \tag{4.9}$$

and with β, c and d as free parameters.
The free parameters are determined by fitting Equation 4.6 (Equation 4.8) to measured HU values of materials with known electron density (and effective atomic number) over a range of values for α (β), while maximising the coefficient of determination R^2 resulting from the fit.
Furthermore, in order to convert the effective atomic number obtained via Equation 4.8 to an ionisation energy, we apply the approach by Yang et al [33] which assumes a linear relation between Z_{eff} and the logarithm of the ionisation energy, $\ln(I)$. A distinction is made between soft and bone tissues based on their effective atomic number:

$$\ln(I) = \begin{cases} c_1 \cdot Z_{\text{eff}} + c_2 & \text{for } Z_{\text{eff}} < 8.5 \quad , \\ c_3 \cdot Z_{\text{eff}} + c_4 & \text{for } Z_{\text{eff}} \geq 8.5 \quad . \end{cases} \tag{4.10}$$

The scanner- and protocol-independent parameters c_1 to c_4 (listed Table 4.A.6) are determined based on 34 tabulated human tissues, whose compositions are taken from the ICRU report 44 [28] and from the work by White et al [29], as listed in Table 1 in Yang et al [33]. Following Yang et al [33], thyroid was not included in the data used for regression.

For the calibration of the HS method, that is, finding its free parameters in Equations 4.6 to 4.9, all inserts of all phantoms were used (including all four solid water inserts of the Gammex phantom) regardless of their tissue class.
When applying the HS method to obtain predicted SPR values, it is possible that a negative value for $\rho_{\text{elec}} \cdot Z_{\text{eff}}^n$ is predicted, in which case taking the n^{th} root to obtain Z_{eff} yields a non-physical complex value. This occurred for the following inserts for at least one set of parameters:

- Catphan phantom: 'Lung foam' and 'polystyrene',
- CIRS phantom: 'Lung (inhale)',
- Gammex phantom: 'LN300 lung'.

These four inserts are hence excluded from evaluation when comparing the results for different source voltage combinations and dose ratios.

4.2.7 Error Metrics

In the following, we describe the error metrics used in this work to evaluate SPR values in the case of using a single calibration phantom.

The relative mean error (RME) quantifies the bias and is defined as

$$\text{RME} = \frac{1}{N} \sum_i \frac{\Delta x_i}{x_{\text{gt},\,i}} = \frac{1}{N} \sum_i \frac{x_{\text{gt},\,i} - x_{\text{p},\,i}}{x_{\text{gt},\,i}} \quad , \tag{4.11}$$

with $x_{\text{gt},\,i}$ as the ground truth value of insert i, $x_{\text{p},\,i}$ as the predicted value of insert i, and Δx_i as the difference between these two values. Note that for ground truth values on SPR, $x_{\text{gt}} > 0$ always holds, with $x_{\text{gt}} \in [0.178, 1.80]$.
The standard deviation on RME is

$$\sigma\,(\text{RME}) = \sqrt{\frac{1}{N-1} \sum_i \left(\frac{\Delta x_i}{x_{\text{gt},\,i}} - \text{RME} \right)^2} \quad . \tag{4.12}$$

The relative mean absolute error (RMAE) quantifies the mean deviation between predicted and ground truth values, and is defined as

$$\text{RMAE} = \frac{1}{N} \sum_i \left| \frac{\Delta x_i}{x_{\text{gt},\,i}} \right| = \frac{1}{N} \sum_i \left| \frac{x_{\text{gt},\,i} - x_{\text{p},\,i}}{x_{\text{gt},\,i}} \right| \quad , \tag{4.13}$$

the standard deviation on which is

$$\sigma\left(\mathrm{RMAE}\right) = \sqrt{\frac{1}{N-1}\sum_i \left(\left|\frac{\Delta x_i}{x_{\mathrm{gt},\,i}}\right| - \mathrm{RMAE}\right)^2} \quad . \tag{4.14}$$

The relative root mean square error (RRMSE) is defined as

$$\mathrm{RRMSE} = \frac{\sqrt{\frac{1}{N}\sum_i (x_{\mathrm{gt},\,i} - x_{\mathrm{p},\,i})^2}}{\frac{1}{N}\sum_i x_{\mathrm{gt},\,i}} \quad , \tag{4.15}$$

the standard deviation on which is

$$\sigma(\mathrm{RRMSE}) = \frac{\sqrt{\frac{1}{N-1}\sum_i \left((x_{\mathrm{gt},\,i} - x_{\mathrm{p},\,i})^2 - \frac{1}{N}\sum_i (x_{\mathrm{gt},\,i} - x_{\mathrm{p},\,i})^2\right)^2}}{\frac{2}{N}\sum_i x_{\mathrm{gt},\,i} \cdot \sqrt{\frac{1}{N}\sum_i (x_{\mathrm{gt},\,i} - x_{\mathrm{p},\,i})^2}} \quad . \tag{4.16}$$

When we combine the results for several calibration phantoms, the reported RME, RMAE and RRMSE values are the mean of the RME, RMAE and RRMSE values for the individual calibration phantoms; the 1σ standard deviation reported on the mean is then calculated via uncertainty propagation of the standard deviations on the results for the individual calibration phantoms.

4.2.8 Insert Differentiation Feasibility

As a measure for how well two inserts can be distinguished from each other, we calculate the Bhattacharyya coefficient (BC) between their CT number probability distributions. The BC quantifies the overlap between two probability distributions P and Q, with $\mathrm{BC}(P, Q) = 0$ indicating no overlap and $\mathrm{BC}(P, Q) = 1$ indicating perfect overlap. For two probability distributions P and Q of discrete CT numbers in the ROIs of two inserts, $\mathrm{BC}(P, Q)$ is calculated according to

$$\mathrm{BC}(P, Q) = \sum_{x \in \mathcal{H}} \sqrt{P(x) \cdot Q(x)} \quad , \tag{4.17}$$

where $\mathcal{H}$ is the set of CT numbers of a single voltage in the case of a SE CBCT scan, or a set of tuples of CT numbers in the case of DE CBCT scans.

For creating CT number probability distributions, we used a bin size of 4 HU as a compromise between reducing statistical noise and using the smallest possible bin size. We only included inserts mimicking soft tissue or adipose tissue (CIRS and Gammex phantom only), since the CT values of these inserts lie close together.

4.3 Results

4.3.1 Stopping Power Ratio Prediction

For both the HS and the HLUT method we use three different scenarios to evaluate SPR prediction performance: We use one phantom for calibration, while for evaluation we use either (1) the same phantom, or (2) all phantoms but the calibration phantom, or (3) all three phantoms (including the calibration phantom).

We would like to point out that scenario (2), evaluated for all choices of calibration phantoms, results in a leave-one-out cross validation, which makes it the scenario that is the most indicative of how well the applied SPR extraction method is able to generalise, under the constraints of using a similar phantom diameter, similar insert compositions and same scan settings. For this reason, while we will also show results on scenarios (1) and (3) in the referenced figures and tables, we will focus mainly on scenario (2).

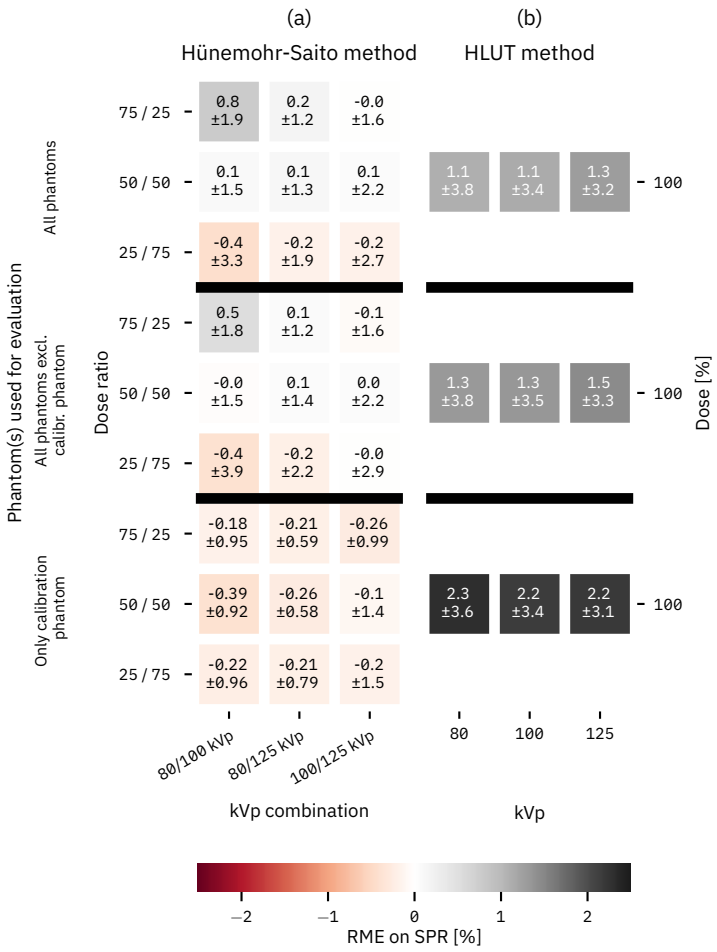

Figure 4.3: RME on SPR incl. 1σ standard deviation for (a) dual-energy CBCT and (b) single-energy CBCT. The results are grouped according to the scenario used for evaluation: evaluation using the same phantom that was used for calibration (bottom row), evaluation using all phantoms except the calibration phantom (centre row), and evaluation using all phantoms (top row). The dose ratio is given as the ratio between the dose given to the low and high energy scan.

Results for the HLUT method

For the HLUT method applied to SE CBCT scans, we show results for each choice of kVp; the dose is always kept at 100 % to enable a fair comparison with DE scans. Figures 4.3b to 4.5b show RME, RMAE and RRMSE for the three scenarios used for evaluation (only calibration phantom, all phantoms except calibration phantom, and all phantoms), averaged over all three possible calibration phantoms. For results for each calibration phantom separately we refer to Section 4.B.2 in the Appendix.

The evaluation of scenario (2) (all phantoms used for evaluating SPR prediction bias except the calibration phantom itself), depicted in the centre row of Figure 4.3b, shows that the low-

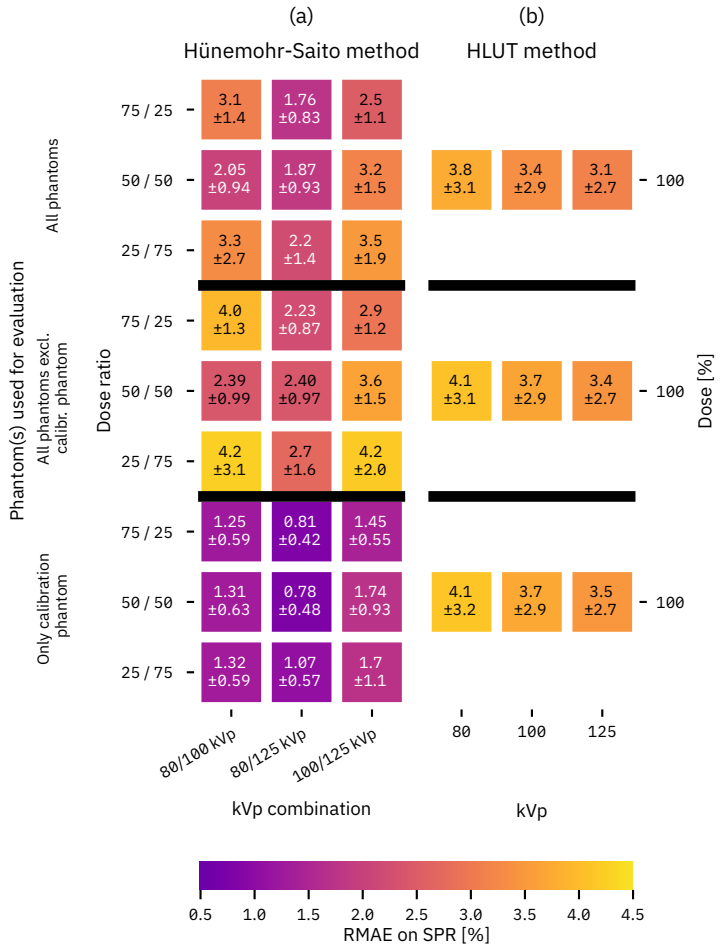

Figure 4.4: RMAE on SPR incl. 1σ standard deviation for (a) dual-energy CBCT and (b) single-energy CBCT. The results are grouped according to the scenario used for evaluation: evaluation using the same phantom that was used for calibration (bottom row), evaluation using all phantoms except the calibration phantom (centre row), and evaluation using all phantoms (top row). The dose ratio is given as the ratio between the dose given to the low and high energy scan.

est RME value of 1.3 % is achieved for a source voltage of both 80 kVp (± 3.8 %) and 100 kVp (± 3.5 %). The difference in RME for the a 125 kVp voltage, however, is small (a factor of 1.2). Examining the results in terms of RMAE (Figure 4.4b) and RRMSE (Figure 4.5b), we find that both these metrics are lowest for a 125 kVp source voltage, with a RMAE of (3.4 ± 2.7) % and a RRMSE of (7.1 ± 6.9) %. For this optimum voltage of 125 kVp, the bias, that is, the RME, is still low compared to 80 and 100 kVp, with a value of RME = (1.5 ± 3.3) %. The minimum and maximum values achieved for different choices of the source voltage differ by a factor of 1.2 for both RMAE and RRMSE (see Appendix Section 4.A.4 for the best performing set of calibration parameters for the HLUT method).

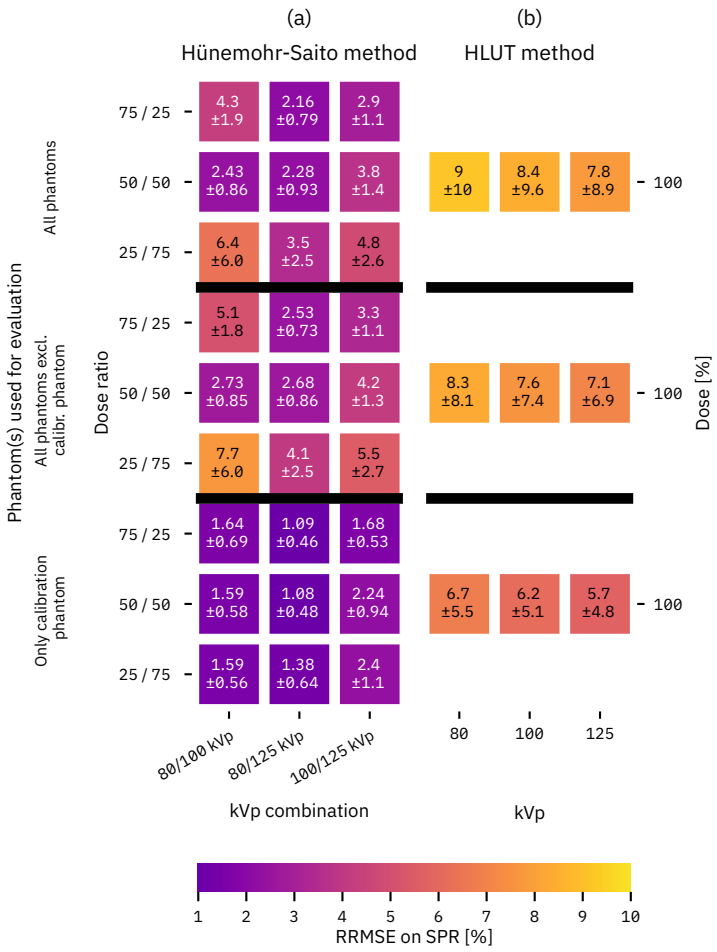

Figure 4.5: RRMSE on SPR incl. 1σ standard deviation for (a) dual-energy CBCT and (b) single-energy CBCT. The results are grouped according to the scenario used for evaluation: evaluation using the same phantom that was used for calibration (bottom row), evaluation using all phantoms except the calibration phantom (centre row), and evaluation using all phantoms (top row). The dose ratio is given as the ratio between the dose given to the low and high energy scan.

Results for the Hünemohr-Saito Method

For the HS method applied to DE CBCT scans, we show results for each chosen kVp combination as well as for each dose ratio. Figures 4.3a to 4.5a show RME, RMAE and RRMSE for the three scenarios used for evaluation (only calibration phantom, all phantoms except calibration phantom, and all phantoms), averaged over all three possible calibration phantoms. For results for each calibration phantom separately we refer to Section 4.B.3 in the Appendix.

The evaluation of scenario (2) (all phantoms used for evaluating SPR prediction bias except the calibration phantom itself), depicted in the centre row of Figure 4.3a, shows that the lowest RME value, i.e., the smallest bias, is achieved in several instances: a 100/125 kVp voltage

combination and either a 25/75 dose ratio (25 % of the dose assigned to the low energy scan, 75 % to the high energy scan) or a 50/50 dose ratio, and an 80/100 kVp voltage combination and a 50/50 dose ratio, all resulting in a RME of 0.0 (within the given number of significant digits).
Examining the results achieved by the HS method in terms of RMAE (Figure 4.4a) and RRMSE (Figure 4.5a), we find that both these metrics are lowest for an 80/125 kVp combination and a 75/25 dose ratio, with a RMAE of (2.23 ± 0.87) % and a RRMSE of (2.53 ± 0.73) %. For this set of optimum parameters, the bias, that is, the RME, is still low compared to other choices of operating parameters, with a value of RME = (0.1 ± 1.2) %. The minimum and maximum values achieved for different choices of operating parameters differ by a factor of 1.9 and 3.0 for the error metric of RMAE and RRMSE, respectively (see Appendix Section 4.A.5 for the best performing set of calibration parameters for the HS method).

4.3.2 Insert Differentiation Results

Figure 4.6 depicts the distribution of SE CT numbers of inserts mimicking adipose and soft tissues, either approximated as normal distributions or plotting the CT number of a limited number of voxels. Analogously, Figures 4.7 and 4.8 show the same for DE CT numbers.

The results for the calculated overlap, based on the Bhattacharyya coefficient, are shown in Table 4.2 and 4.3 as the mean value over all pairs of adipose- and soft tissue-mimicking inserts for SE and DE CBCT, respectively.
In the SE case, the lowest overlap between tissues is achieved for a 125 kVp voltage, reaching a BC of 0.220. In the DE case, the lowest overlap is reached for an 80/125 kVp voltage combination and a 25/75 dose ratio (BC = 0.193), which is lower than in the SE case.

Table 4.2: Mean BC values over all pairs of adipose- and soft tissue-mimicking inserts (lower is better), calculated for the case of SE CBCT for different source voltages, always using the full dose.

kVp	**Mean BC value**
80	0.315
100	0.354
125	0.220

Table 4.3: Mean BC values over all pairs of adipose- and soft tissue-mimicking inserts (lower is better), calculated for the case of DE CBCT for different combinations of the low (kVp_L) and high (kVp_H) source voltage, and for different ratios of dose assigned to the low and high source voltage.

kVp_L	kVp_H	**Dose ratio**	**Mean BC value**
80	100	25/75	0.285
		50/50	0.276
		75/25	0.271
80	125	25/75	0.193
		50/50	0.212
		75/25	0.233
100	125	25/75	0.196
		50/50	0.223
		75/25	0.255

4.4 Discussion

4.4.1 SPR Prediction Methods

Comparing the performance of SPR extraction based on DE CBCT scans with the HS method to that based on SE CBCT scans applying a HLUT, we find that in terms of bias, the HS method achieves a minimum RME of (0.0 ± 2.9) %, whereas the HLUT achieves a best value of (1.3 ± 3.8) %. In terms of RMAE, the HS and HLUT methods achieve a lowest value of (2.23 ±

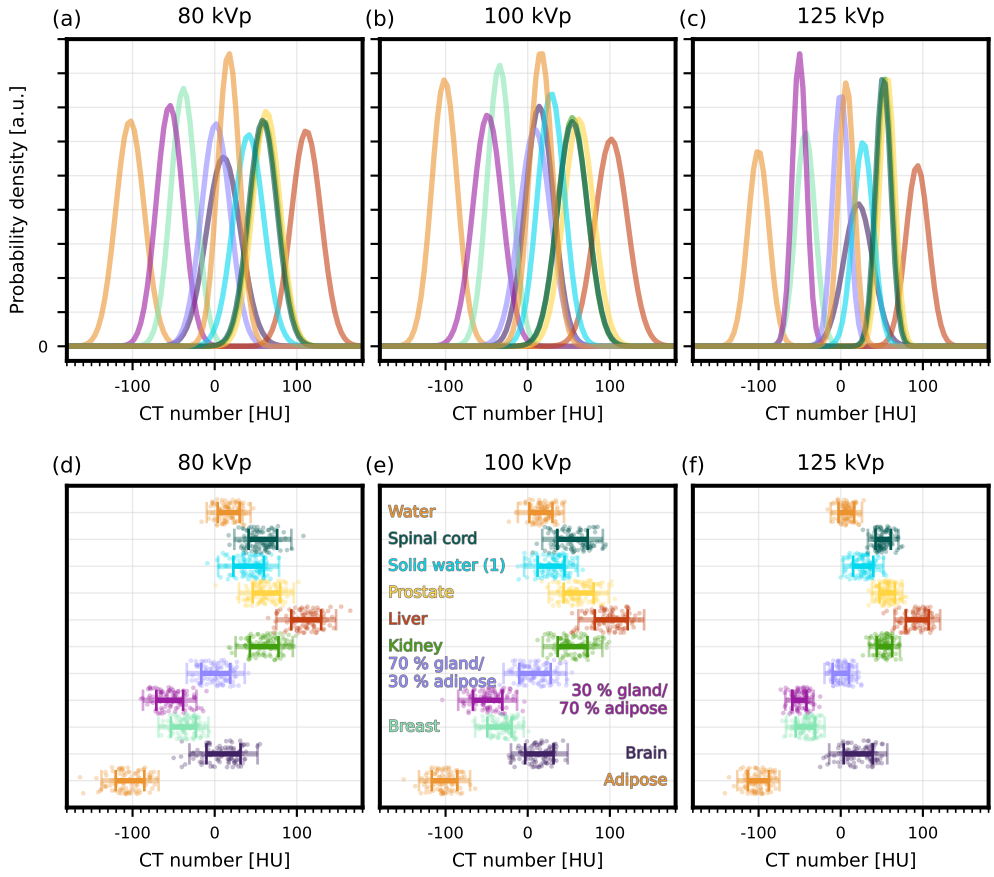

Figure 4.6: CT numbers of inserts mimicking soft tissue and adipose tissue (CIRS and Gammex) for the SE case, plotted for different source voltages. First row: Approximation of CT numbers of each insert by normal distributions (areas under the curves normalised to 1). Second row: For each insert, the CT numbers of 100 randomly selected voxels are depicted; the (semi-transparent) errorbars indicate 1σ (2σ) confidence intervals; the spread in y-direction is merely for illustrative purposes and has no physical meaning.

0.87) % and (3.4 ± 2.7) %, respectively, which differ by a factor of about 1.5. In terms of RRMSE, they achieve values of (2.53 ± 0.73) % and (7.1 ± 6.9) %, respectively, which differ by a factor of about 2.8. While this means that the HS-based method for DE CBCT scans yields more favourable results, the values for both the HS and HLUT method agree within their error margins.

Hence, additional research will be needed before definite conclusions can be drawn about the performance of SE and DE CBCT for SPR extraction, as this study has several limitations: First, differences in HU units due to different phantom sizes or even an absent phantom body, resulting in a varying degree of beam hardening correction. Second, inserts of different material classes being used for either calibration or evaluation, and third, relatively small phantom sizes, limiting the amount of scatter and hence mitigating the most detrimental effect to image quality in CBCT. Each of these limitations is discussed in more detail in the following.

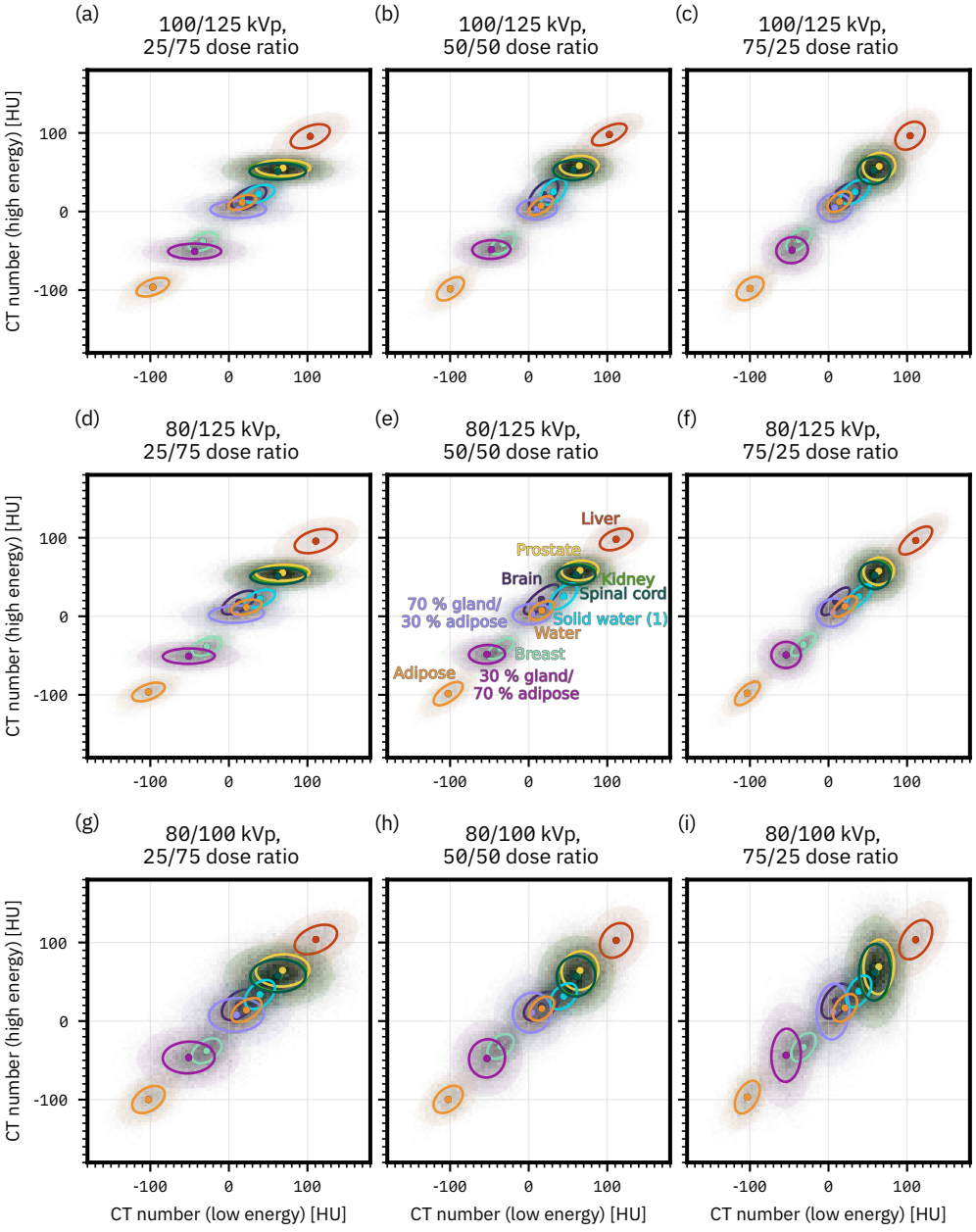

Figure 4.7: CT numbers of inserts mimicking soft tissue and adipose tissue (CIRS and Gammex) for the DE case, plotted for different combinations of LE and HE source voltages and dose ratios. The summed histogram of all inserts is shown in the background, and the ellipses indicate the 1σ (solid line) and 2σ (shaded area) confidence intervals, assuming a normal distribution.

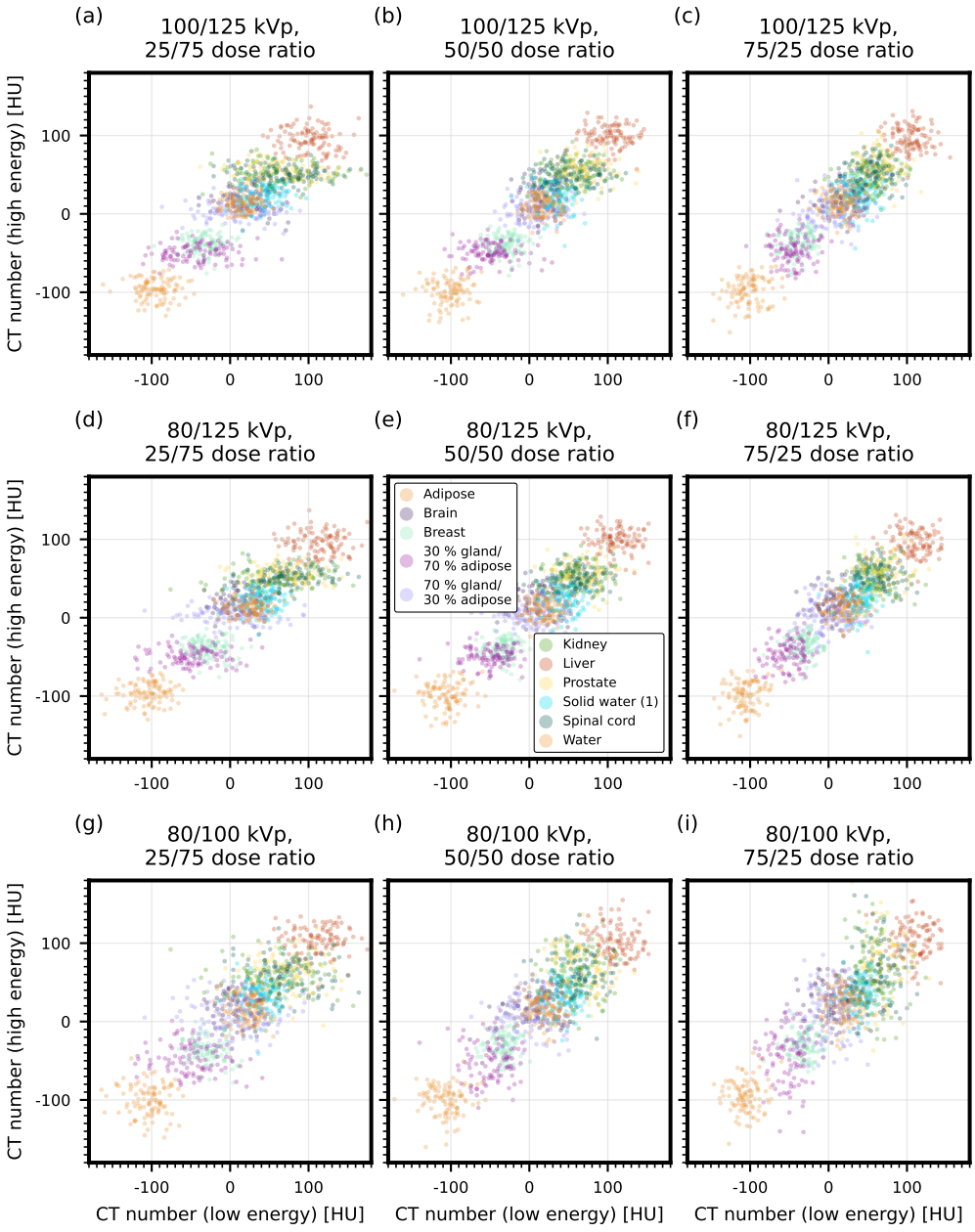

Figure 4.8: CT numbers of inserts mimicking soft tissue and adipose tissue (CIRS and Gammex) for the DE case, plotted for different combinations of LE and HE source voltages and dose ratios. For each insert, the CT numbers of 100 randomly selected voxels are depicted.

To address the first point of different phantom sizes or even an absent phantom body, we evaluated the RRMSE for each phantom separately (see Tables 4.B.25 to 4.B.27 for the HS method). We find that in most cases, using the Gammex phantom for calibration and performing the evaluation using the remaining phantoms, or using either the Catphan or CIRS phantom for calibration and using the Gammex phantom for evaluation, yields the largest RRMSE values. We attribute this to the fact that only slices without the Gammex phantom's body are used, which leads to an over-correction by the beam hardening correction algorithm and hence incorrect HU values. As a consequence, HU values for the same material would hypothetically differ between the Gammex phantom and the Catphan & CIRS phantom, and hence, a HS calibration performed on the Gammex phantom is not applicable to the Catphan & CIRS phantom and vice versa. This behaviour is not limited to RRMSE, yet can also be observed for the RME (Tables 4.B.13 to 4.B.15 for HS method) and RMAE (Tables 4.B.19 to 4.B.21 for HS method). We observe this effect only in case of the HS method, though, which warrants further investigation.

Concerning the second point of different material classes of inserts, we would like to point out that the CIRS and Gammex phantom exclusively exhibit inserts designed to mimic human tissues. In contrast, the Catphan phantom exhibits only three human tissue-like inserts of which one was excluded from evaluation (see Sections 4.2.5 and 4.2.6), whereas its other inserts are commercially available plastics which do not resemble any human tissue with respect to their combination of electron density, effective atomic number or ionisation energy (Figure 4.1). Hence, using the Catphan phantom for calibration and applying it to the CIRS phantom (and vice versa) might lead to suboptimal results. Based on the available data we cannot assess whether this is indeed the case, as confirmation would require another phantom with a similar diameter and inserts made of human tissue-like materials for evaluation; our scans of the Gammex phantom are unsuitable for this assessment. An indication for this, however, might be found in Tables 4.B.7 to 4.B.9 showing the evaluation results of the HLUT method split by each phantom: Regardless of the phantom used for calibration, the evaluation using the Catphan phantom performs consistently worst.

Concerning the third point, since we were able to use only a smaller FOV with our scanner and hence only phantoms comparable in size to a human head, the conclusions in this work apply only to objects with a similar diameter. Although tumours in the head and neck region are among the main indications for proton therapy, larger phantoms introduce a stronger scatter contribution which is one of the main reasons for the inferior image quality of CBCT compared to fan-beam CT. The influence of larger diameters of the object under investigation is therefore yet to be determined and will be discussed in more detail in Section 4.4.3.

While a number of studies have been published comparing DE fan-beam CT (DECT) to SE fan-beam CT (SECT), it is often difficult to directly compare these to the work presented here due to differences in the study design, examples of which are the evaluation of SPR extraction algorithms on fresh tissues vs. evaluation based on phantom inserts, or comparison of predicted SPR values with measured values vs. comparison with values calculated based on elemental composition, etc. A notable exception is the work by Moskvin et al [15], who evaluated both SE and DE SPR estimation algorithms using a dual-layer fan-beam CT and a Gammex 467 phantom for both calibration as well as evaluation. Based on their published data, we calculate a RME of -1.8 % (0.14 %), a RMAE of 2.5 % (0.71 %), and a RRMSE of 2.2 % (0.65 %) for SECT (DECT). In our case, the best values achieved when using the Gammex phantom for both calibration and evaluation are a RME of -0.36 % (0.21 %), a RMAE of 1.37 % (0.72 %), and a RRMSE value of 1.60 % (0.93 %) for SE CBCT (125 kVp) and DE CBCT (80/125 kVp, 75/25 dose ratio), respectively. Hence, our results obtained via SE CBCT are consistently better than those reported by Moskvin et al for SE fan-beam CT, which is unexpected due to the generally worse

image quality of CBCT compared to fan-beam CT. For DE CBCT, our results are consistently worse compared to Moskvin et al, which aligns with our expectations for the same reason. The unexpected findings in case of SE acquisitions could be due to the fact that Moskvin et al also used their dual-layer detector for acquiring SE images or due to different HLUT implementations, and requires a more thorough analysis.
See Table 4.4 for more results on SPR extraction reported in literature.

Table 4.4: Reported values in literature for SPR extraction using SE and DE fan-beam CT.

Publication	Results
Hansen et al [5]	RRMSE between 1.6 to 2.7 % for SECT, between 0.5 to 0.9 % for DECT.
Hudobivnik et al [6]	RRMSE values between 1.6 to 3.6 % for SECT and 1.0 to 1.2 % for DECT.
Möhler et al [13]	RME of (-0.84 ± 0.12) % for SECT and (-0.02 ± 0.15) % for DECT, and a RMAE of (1.27 ± 0.12) % for SECT and (0.10 ± 0.15) % for DECT.
Taasti et al [26]	RRMSE of 2.8 % for SECT and between 0.9 to 1.5 % for DECT.
This study	RME, RMAE and RRMSE value of (1.46 ± 3.3) %, (3.42 ± 2.7) % and (7.05 ± 6.9) %, respectively, for SECT; (0.1 ± 1.2) %, (2.23 ± 0.87) % and (2.53 ± 0.73) % for DECT.

4.4.2 Insert Differentiation

The fact that the attenuation coefficient can be approximately described by the sum of two interaction mechanisms with different dependency on energy (see Section 1.2.6) is the basis for the possibility of DE (CB)CT to distinguish between materials with different chemical compositions but with the same attenuation coefficient $\mu(E)$ at a certain energy E. Our evaluation corroborates this, with a lower overlap between CT number distributions in the DE CBCT case (BC = 0.193) compared to the SE CBCT case (BC = 0.220).

We note that while the reported BC value is the mean value of the BC over all pairs of tissues, some pairs lie sufficiently apart to not have any overlap at all (for example, the Gammex inserts 'adipose' and 'liver'). These sufficiently separated pairs of tissues yield a BC of 0 and hence do not influence the mean value of the BC over all pairs of tissues for different operating parameters. The absolute number of the mean BC value has no particular meaning, only its relative change is insightful.

4.4.3 Recommendations for a Follow-Up Study

In our study, we scanned the CIRS phantom in a head configuration using a single arrangement of inserts. While the body ring of the CIRS phantom does not fit inside the FOV and was hence not used, it contains 8 additional removable inserts (16 CIRS inserts in total) not included in this study. Furthermore, the Gammex inserts have a slightly smaller diameter than the CIRS inserts and are removable as well. This might allow to place the Gammex inserts inside the CIRS phantom (head configuration), at the expense of introducing air gaps. Placing the so far unused 8 inserts of the CIRS phantom and the 16 inserts of the Gammex phantom[2] inside the CIRS phantom (head configuration) would make for 4 phantom configurations with distinct sets of inserts. Furthermore, for each of the 4 sets of inserts their arrangement can be varied in order to quantify the measurement uncertainty due to beam hardening, as recommended by Peters,

[2]The Gammex phantom features 16 inserts in total, with 4 of them being 'solid water' inserts, which brings the total number of unique inserts to 13. Please note that one insert is a water container.

Taasti et al [18]. Furthermore, for calibration they recommend to scan bone inserts individually to avoid highly attenuating inserts from influencing each other, using the centre position of the phantom while filling all other insert positions with materials similar to water.

While in principle it is possible to acquire scans in half-fan beam mode, our clinical system does not and will not for the foreseeable future support the half-fan beam mode for all three kVp voltages, which excludes the use of the Gammex phantom in a configuration as intended by its manufacturer. With the FOV of the full-fan beam mode featuring a diameter of 289.5 mm, it would be possible to add a ring to the CIRS phantom (180 mm diameter) or construct a custom-made phantom such that the phantom's diameter is increased, and, as a consequence the scatter-to-primary ratio. This would then allow to conduct a study with a greater contribution of scatter while still using the full-fan beam mode of our system, and it would allow to compare the robustness of a chosen SPR extraction method with respect to the phantom diameter.
If it is desired to conduct a study using a bigger phantom, either custom made or using an extension ring, it is crucial to prepare it by first testing the acceptance range of the beam hardening correction: Different disks made of water-like material with diameters between 180 mm and up to around 289.5 mm should be scanned and analysed based on HU accuracy and the presence of artefacts.

In this study we relied on the CTDI values as given by the CBCT's user interface as an indication of the radiation output by the system. Ideally, though, one would validate these CTDI values with an approved methodology[3] to make sure the scans emit indeed the radiation dose as stated by the machine parameters.

Moreover, the significance of a future study could furthermore be enhanced by investigating a larger selection of methods for SPR extraction, a comparison of which was published by Bär et al [1], as well as by including a comparison between CBCT scans to fan-beam CT scans.

Finally, we would like to note that in our study we reconstructed the images for each voltage independently using a standard FDK algorithm. However, more information can potentially be extracted by reconstructing the images at two energies jointly. In theory, this allows to achieve a better HU accuracy due to better beam-hardening correction [14].

4.5 Conclusion

In this study we investigated the use of dual-energy cone-beam CT for extraction of proton stopping power ratios for proton therapy planning. We emulated a dual-energy CBCT setup by sequentially scanning three phantoms at different tube voltages. SPR values from dual-energy scans were extracted using the Hünemohr-Saito method, and compared to SPR values extracted from single-energy scans using a Hounsfield look-up table.

Comparing the predicted SPR values by either HS and HLUT method based on the achieved RME, RMAE and RRMSE values, the HS method consistently performed better in this study. However, we pointed out that these results need to be considered cautiously, due to the large measurement uncertainties, the use of phantoms with different diameters, different and sometimes incompatible material classes of inserts, and the small size of phantoms (comparable to the size of a human head). This warrants further research before definitive conclusions can be drawn about the performance of SE and DE CBCT for SPR extraction, and we laid down recommendations for an improved follow-up study to overcome these limitations.

[3] An appropriate standard to measure CTDI values for CBCT might be the IEC 60601-2-68 standard [8].

Finally, we would like to note that we compared the performance of DE and SE CBCT only with respect to their ability to extract SPR values. If CBCT is to supplement or even replace fan-beam CT in treatment planning for proton therapy, it is necessary to also examine the soft tissue contrast achieved with CBCT.

Data Availability

The data used in this work can be found here: https://doi.org/10.4121/c90c9688-403a-4685-9c4f-bf9854008616.

Acknowledgements

A large number of people was involved in the planning and execution of this study, all of whom made this research possible. We would therefore like to express our sincere gratitude to everyone, and we appreciate all the generous help and support we received.

More specifically, we would like to thank the staff at HollandPTC for supporting us in both technical and operational manner (in alphabetical order): Astrid Moerman, Charlotte van der Vos, Hansjoerg Wertz, Lilian Koster-Munsterman, Mischa Hoogeman, Patricia Lopes, Paola Flores Sanchez, Paul van Beers, Petra Assems, and Rob Louwe.
A special thanks goes to Henry Noordmans and Vera Schroen for spending two long evenings performing the CBCT scans for us, and for being willing to answer our many follow-up questions.
Furthermore, we would like to thank the staff at Varian who was always readily answering our technical questions (in alphabetical order): Adam Harrington, Erik Visser, Mitchel Low, Radek Ofierzynski, Roberto Cassetta, Vladimir Balaz, and the on-site Varian engineers at HPTC.
Furthermore, we would like to thank the staff at Erasmus MC for their support (in alphabetical order): Marcel van Straaten, Michelle Oud, Miriam Both, Paulette Prins, and Sophie Huijskens, During this study we annoyed a lot of people with our many questions, which is why we would like to particularly thank (in alphabetical order) Erik Visser, Patricia Lopes, Paul van Beers, Rob Louwe and Roberto Cassetta for their patience.
We would like to especially thank Roberto Cassetta for providing us with scatter-corrected projection data.
Furthermore, we would like to thank Esther Plomp for her support and Lukas Schroeder for helpful discussions, and the staff at The Phantom Laboratory, manufacturer of the Catphan phantom, for their support. We would like to apologise in case we forgot to mention anyone who was directly or indirectly involved in this study. A special thank goes to Bob Duivestein, whose work [4] paved the way for this study. Finally, our implementation of the HLUT specification relies heavily on the consensus guide by Peters, Taasti et al [18]. We would like to thank the authors for providing their tools and their implementation as open source.

References

[1] E. Bär, A. Lalonde, G. Royle, H.-M. Lu, and H. Bouchard, "The potential of dual-energy CT to reduce proton beam range uncertainties", *Medical Physics*, vol. 44, no. 6, pp. 2332–2344, 2017. DOI: 10.1002/mp.12215.

[2] A. Bolsi, M. Peroni, D. Amelio, *et al.*, "Practice patterns of image guided particle therapy in Europe: A 2016 survey of the European Particle Therapy Network (EPTN)", *Radiotherapy and Oncology*, vol. 128, no. 1, pp. 4–8, 2018. DOI: 10.1016/j.radonc.2018.03.017.

[3] Z. Chen, M. M. Dominello, M. C. Joiner, and J. W. Burmeister, "Proton versus photon radiation therapy: A clinical review", *Frontiers in Oncology*, vol. 13, p. 1 133 909, 2023. DOI: 10.3389/fonc.2023.1133909.

[4] R. A. Duivestein, "Simulating and evaluating different implementations of dual energy cone-beam CT for proton therapy treatment planning", M.S. thesis, Delft University of Technology, Delft, 2024.

[5] D. C. Hansen, J. Seco, T. S. Sørensen, *et al.*, "A simulation study on proton computed tomography (CT) stopping power accuracy using dual energy CT scans as benchmark", *Acta Oncologica*, vol. 54, no. 9, pp. 1638–1642, 2015. DOI: 10.3109/0284186X.2015.1061212.

[6] N. Hudobivnik, F. Schwarz, T. Johnson, *et al.*, "Comparison of proton therapy treatment planning for head tumors with a pencil beam algorithm on dual and single energy CT images: DECT proton therapy treatment planning for head tumors", *Medical Physics*, vol. 43, no. 1, pp. 495–504, 2016. DOI: 10.1118/1.4939106.

[7] N. Hünemohr, B. Krauss, C. Tremmel, B. Ackermann, O. Jäkel, and S. Greilich, "Experimental verification of ion stopping power prediction from dual energy CT data in tissue surrogates", *Physics in Medicine and Biology*, vol. 59, no. 1, pp. 83–96, 2014. DOI: 10.1088/0031-9155/59/1/83.

[8] *IEC 60601-2-68:2025 : Medical electrical equipment - Part 2-68: Particular requirements for the basic safety and essential performance of X-ray-based image-guided radiotherapy equipment for use with electron accelerators, light ion beam therapy equipment and radionuclide beam therapy equipment*, https://webstore.iec.ch/en/publication/67429, 2025.

[9] T. Inaniwa and N. Kanematsu, "Effective particle energies for stopping power calculation in radiotherapy treatment planning with protons and helium, carbon, and oxygen ions", *Physics in Medicine and Biology*, vol. 61, no. 20, N542–N550, 2016. DOI: 10.1088/0031-9155/61/20/n542.

[10] International Commission on Radiation Units and Measurements, Ed., *ICRU Report 49: Stopping Powers and Ranges for Protons and Alpha Particles* (ICRU Report 49). Bethesda, MD: International Commission on Radiation Units and Measurements, 1993.

[11] G. Landry and C.-h. Hua, "Current state and future applications of radiological image guidance for particle therapy", *Medical Physics*, vol. 45, no. 11, 2018. DOI: 10.1002/mp.12744.

[12] B. Li, H. C. Lee, X. Duan, *et al.*, "Comprehensive analysis of proton range uncertainties related to stopping-power-ratio estimation using dual-energy CT imaging", *Physics in Medicine & Biology*, vol. 62, no. 17, pp. 7056–7074, 2017. DOI: 10.1088/1361-6560/aa7dc9.

[13] C. Möhler, T. Russ, P. Wohlfahrt, *et al.*, "Experimental verification of stopping-power prediction from single- and dual-energy computed tomography in biological tissues", *Physics in Medicine & Biology*, vol. 63, no. 2, p. 025 001, 2018. DOI: 10.1088/1361-6560/aaa1c9.

[14] C. Mory, B. Sixou, S. Si-Mohamed, L. Boussel, and S. Rit, "Comparison of five one-step reconstruction algorithms for spectral CT", *Physics in Medicine & Biology*, vol. 63, no. 23, p. 235 001, 2018. DOI: 10.1088/1361-6560/aaeaf2.

[15] V. P. Moskvin, F. Pirlepesov, Y. Yan, *et al.*, "Accuracy of stopping power ratio calculation and experimental validation of proton range with dual-layer computed tomography", *Acta Oncologica*, vol. 61, no. 7, pp. 864–868, 2022. DOI: 10.1080/0284186X.2022.2069477.

[16] W. D. Newhauser and R. Zhang, "The physics of proton therapy", *Physics in Medicine and Biology*, vol. 60, no. 8, R155–R209, 2015. DOI: 10.1088/0031-9155/60/8/R155.

[17] J. Ödén, J. Zimmerman, R. Bujila, P. Nowik, and G. Poludniowski, "Technical Note: On the calculation of stopping-power ratio for stoichiometric calibration in proton therapy", *Medical Physics*, vol. 42, no. 9, pp. 5252–5257, 2015. DOI: 10.1118/1.4928399.

[18] N. Peters, V. Trier Taasti, B. Ackermann, *et al.*, "Consensus guide on CT-based prediction of stopping-power ratio using a Hounsfield look-up table for proton therapy", *Radiotherapy and Oncology*, vol. 184, p. 109 675, 2023. DOI: 10.1016/j.radonc.2023.109675.

[19] N. Peters, P. Wohlfahrt, C. Hofmann, *et al.*, "Reduction of clinical safety margins in proton therapy enabled by the clinical implementation of dual-energy CT for direct stopping-power prediction", *Radiotherapy and Oncology*, vol. 166, pp. 71–78, 2022. DOI: 10.1016/j.radonc.2021.11.002.

[20] R. A. Rutherford, B. R. Pullan, and I. Isherwood, "Measurement of effective atomic number and electron density using an EMI scanner", *Neuroradiology*, vol. 11, no. 1, pp. 15–21, 1976. DOI: 10.1007/BF00327253.

[21] M. Saito, "Potential of dual-energy subtraction for converting CT numbers to electron density based on a single linear relationship: Conversion of energy-subtracted CT number to electron density", *Medical Physics*, vol. 39, no. 4, pp. 2021–2030, 2012. DOI: 10.1118/1.3694111.

[22] U. Schneider, E. Pedroni, and A. Lomax, "The calibration of CT Hounsfield units for radiotherapy treatment planning", *Physics in Medicine and Biology*, vol. 41, no. 1, pp. 111–124, 1996. DOI: 10.1088/0031-9155/41/1/009.

[23] J. Seco and M. F. Spadea, "Imaging in particle therapy: State of the art and future perspective", *Acta Oncologica*, vol. 54, no. 9, pp. 1254–1258, 2015. DOI: 10.3109/0284186X.2015.1075665.

[24] S. M. Seltzer and M. J. Berger, "Evaluation of the collision stopping power of elements and compounds for electrons and positrons", *The International Journal of Applied Radiation and Isotopes*, vol. 33, no. 11, pp. 1189–1218, 1982. DOI: 10.1016/0020-708X(82)90244-7.

[25] J. H. Siewerdsen, M. J. Daly, B. Bakhtiar, *et al.*, "A simple, direct method for x-ray scatter estimation and correction in digital radiography and cone-beam CT: X-ray scatter correction", *Medical Physics*, vol. 33, no. 1, pp. 187–197, 2005. DOI: 10.1118/1.2148916.

[26] V. T. Taasti, G. J. Michalak, D. C. Hansen, *et al.*, "Validation of proton stopping power ratio estimation based on dual energy CT using fresh tissue samples", *Physics in Medicine & Biology*, vol. 63, no. 1, p. 015 012, 2017. DOI: 10.1088/1361-6560/aa952f.

[27] V. T. Taasti, L. P. Muren, K. Jensen, *et al.*, "Comparison of single and dual energy CT for stopping power determination in proton therapy of head and neck cancer", *Physics and Imaging in Radiation Oncology*, vol. 6, pp. 14–19, 2018. DOI: 10.1016/j.phro.2018.04.002.

[28] D. R. White, J. Booz, R. V. Griffith, J. J. Spokas, and I. J. Wilson, "Report 44", *Journal of the International Commission on Radiation Units and Measurements (ICRU)*, vol. os23, no. 1, NP–NP, 1989. DOI: 10.1093/jicru/os23.1.Report44.

[29] D. R. White, H. Q. Woodard, and S. M. Hammond, "Average soft-tissue and bone models for use in radiation dosimetry", *The British Journal of Radiology*, vol. 60, no. 717, pp. 907–913, 1987. DOI: 10.1259/0007-1285-60-717-907.

[30] P. Wohlfahrt, C. Möhler, C. Richter, and S. Greilich, "Evaluation of Stopping-Power Prediction by Dual- and Single-Energy Computed Tomography in an Anthropomorphic Ground-Truth Phantom", *International Journal of Radiation Oncology*Biology*Physics*, vol. 100, no. 1, pp. 244–253, 2018. DOI: 10.1016/j.ijrobp.2017.09.025.

[31] H. Q. Woodard and D. R. White, "The composition of body tissues", *British Journal of Radiology*, vol. 59, no. 708, pp. 1209–1218, 1986. DOI: 10.1259/0007-1285-59-708-1209.

[32] Y. Xie, C. Ainsley, L. Yin, *et al.*, "*Ex vivo* validation of a stoichiometric dual energy CT proton stopping power ratio calibration", *Physics in Medicine & Biology*, vol. 63, no. 5, p. 055 016, 2018. DOI: 10.1088/1361-6560/aaae91.

[33] M. Yang, G. Virshup, J. Clayton, X. R. Zhu, R. Mohan, and L. Dong, "Theoretical variance analysis of single- and dual-energy computed tomography methods for calculating proton stopping power ratios of biological tissues", *Physics in Medicine and Biology*, vol. 55, no. 5, pp. 1343–1362, 2010. DOI: 10.1088/0031-9155/55/5/006.

Appendix

4.A Supplementary Methods

4.A.1 Number of Voxels per ROI

Table 4.A.1: Number of voxels per ROI. The number of voxels is specified as the product of number of voxels in one slice (same for all slices) times the number of evaluated slices.

Insert	Number of voxels
Catphan	
Acrylic	242 × 16
Air	242 × 16
20 % Bone	242 × 16
50 % Bone	248 × 16
Delrin	242 × 16
LDPE	248 × 16
Lung Foam	241 × 16
PMP	241 × 16
Polystyrene	242 × 16
Teflon	248 × 16
Air (empty water container)	420 × 16
CIRS	
70 % Cort./30 % Trab. Bone	1264 × 21
30 % Gland/70 % Adipose	1245 × 21
70 % Gland/30 % Adipose	1264 × 21
Kidney	1245 × 21
Lung (inhale)	1245 × 21
Prostate	1245 × 21
Spinal Cord	1252 × 21
Spinal Disk	1252 × 21
Gammex, inserts only	
Adipose	1252 × 8
Brain	1264 × 8
Breast	1264 × 8
B200 Bone Mineral	1252 × 8
CB2-30 % $CaCO_3$ Bone	1264 × 8
CB2-50 % $CaCO_3$ Bone	1264 × 8
Cortical Bone	1252 × 8
Inner Bone	1252 × 8
Liver	1264 × 8
LN300 Lung	1245 × 8
LN450 Lung	1252 × 8
Solid Water (1–4)	1252 × 8
Water	880 × 8

4.A.2 Elemental Data

Table 4.A.2: Atomic number Z, mass number A and ionisation energy I for each element used in this study.

Element	Z	A	I [eV]
H	1	1.008	19.20
C	6	12.011	81.00
N	7	14.007	82.00
O	8	15.999	106.00
Na	11	22.990	168.37
Mg	12	24.305	176.28
P	15	30.974	195.49
S	16	32.060	203.40
Cl	17	35.453	180.00
K	19	39.098	214.70
Ca	20	40.078	215.83
Fe	26	55.845	323.18

4.A.3 Comparison Between Measured and Calculated SPR Values

Since SPR data measured at the HollandPTC proton treatment facility is only available for the Gammex and CIRS phantom but not the Catphan phantom, we hence compare the predicted SPR values to SPR values calculated based on the available elemental composition and mass density data of phantom inserts, as this data is available for all three phantoms. Table 4.A.3 compares SPR values calculated based on composition and mass density to the measured values, and we observe a mean relative difference of (1.24 ± 0.46) % for the CIRS and (1.50 ± 2.26) % for the Gammex phantom.

Table 4.A.3: SPR values as calculated based on the elemental composition and electron density of the inserts as specified by the manufacturers (SPR_{comp}, calculated based on Equation 4.4), and compared to SPR values measured at HollandPTC (SPR_{meas}). The table compares the relative and absolute differences between SPR_{comp} and SPR_{meas}, and the mean, standard deviation, minimum and maximum values for the relative and absolute differences.

Insert	SPR_{comp}	SPR_{meas}	relative diff. [%]	absolute diff.
CIRS				
70 % cort./30 % trab. bone	1.47	1.49	0.95	0.014
30 % gland/70 % adipose	0.975	0.987	1.17	0.011
70 % gland/30 % adipose	1.01	1.03	1.98	0.020
Kidney	1.05	1.05	0.52	0.005
Lung (inhale)	0.203	0.207	1.80	0.004
Prostate	1.04	1.05	1.14	0.012
Spinal cord	1.03	1.05	1.49	0.015
Spinal disk	1.07	1.08	0.85	0.009
Mean			**1.24**	**0.011**
Std			**0.46**	**0.005**
Min			**0.52**	**0.004**
Max			**1.98**	**0.020**
Gammex				
Adipose	0.948	0.951	0.35	0.003
Brain	1.05	1.03	−2.13	−0.022
Breast	0.976	0.979	0.33	0.003
CB2-30 % $CaCO_3$ bone	1.25	1.29	2.94	0.037
CB2-50 % $CaCO_3$ bone	1.42	1.45	2.13	0.030
Cortical bone	1.61	1.58	−1.72	−0.028
Inner bone	1.09	1.11	1.86	0.020
Liver	1.07	1.09	1.82	0.020
LN300 lung	0.270	0.280	3.82	0.010
LN450 lung	0.443	0.468	5.59	0.025
Mean			**1.50**	**0.010**
Std			**2.26**	**0.020**
Min			**-2.13**	**-0.028**
Max			**5.59**	**0.037**

4.A.4 HLUT Calibration Parameters

Table 4.A.4 states the HLUT calibration parameters for each of the three calibration phantoms, but only for the source voltage of 125 kVp that achieved the best results.

Table 4.A.4: HLUT calibration parameters for each of the calibration phantoms.

Phantom	Stoichiometric calib. coeff.			HLUT connection points	
	K^{ph}	K^{coh}	K^{KN}	CT number	SPR
Catphan	2.434e-05	1.142e-4	0.4998	−1024	0.0011
				−999	0.0011
				−950	0.0663
				−159	0.8416
				−139	0.9301
				−40	0.9972
				0	0.9974
				70	1.0660
				158	1.0674
				2000	1.7582
CIRS	2.089e-05	2.389e-17	0.5027	−1024	0.0011
				−999	0.0011
				−950	0.0705
				−153	0.8476
				−133	0.9267
				−34	0.9961
				0	0.9968
				68	1.0631
				155	1.0878
				2000	1.8304
Gammex	2.448-05	2.913-18	0.5047	−1024	0.0011
				−999	0.0011
				−950	0.0796
				−160	0.8426
				−140	0.9228
				−36	0.9964
				0	0.9971
				103	1.0966
				235	1.0969
				2000	1.7600

4.A.5 HS Calibration Parameters

Table 4.A.5 states the HS calibration parameters for each of the three calibration phantoms, but only for the optimum source voltage combination of 80/125 kVp and a 75/25 dose ratio.

Table 4.A.5: HS calibration parameters for each of the calibration phantoms.

Parameter	Phantom		
	Catphan	CIRS	Gammex
α	2.16 ± 0.01	2.048 ± 0.008	2.212 ± 0.004
a	0.9303 ± 0.0072	0.9184 ± 0.0036	0.8988 ± 0.0057
b	0.9829 ± 0.0034	0.9983 ± 0.0014	1.0036 ± 0.0020
β	-14.65 ± 0.05	-17.22 ± 0.003	-18.3 ± 0.07
c	638 ± 13	617.3 ± 5.1	535.7 ± 5.1
d	447 ± 15	413.0 ± 6.7	362.4 ± 9.2

Table 4.A.6 lists the calibration parameter for the conversion from effective atomic number to ionisation potential for the same optimum parameters.

Table 4.A.6: HS calibration parameters for the conversion from effective atomic number to ionisation potential.

Parameter	Value
c_1	0.1217 ± 0.0054
c_2	3.400 ± 0.040
c_3	0.1022 ± 0.0043
c_4	3.331 ± 0.051

4.B Supplementary Results

Please note that in this section, the number of digits (after the decimal point) for stated uncertainties is kept constant and not adapted to the value it quantifies the uncertainty of; this is not to be understood as an indication for the number of reliably known digits.

Furthermore, please note that uncertainties are specified as 1σ standard deviation.

4.B.1 Hounsfield Unit Values for All Phantoms, Inserts, Voltages and Dose Percentages

Table 4.B.1: HU values (mean ± stdev.) for all inserts of the Catphan phantom, for all source voltages and percentages of the maximum dose.

Insert	kVp [kV]	Percentage of max. dose [%]	Attenuation [HU]
Acrylic	80	25	129.9 ± 40.1
	80	50	125.1 ± 27.5
	80	75	122.3 ± 22.9
	80	100	121.4 ± 19.3
	100	25	140.4 ± 40.3
	100	50	135.7 ± 29.7
	100	75	132.9 ± 23.5
	100	100	132.3 ± 21.3
	125	25	139.6 ± 20.3
	125	50	139.4 ± 14.8
	125	75	137.3 ± 11.9
	125	100	136.8 ± 10.6
Air	80	25	−995.4 ± 10.7
	80	50	−995.9 ± 8.4
	80	75	−996.1 ± 7.8
	80	100	−996.8 ± 6.4
	100	25	−996.0 ± 9.7
	100	50	−997.0 ± 6.8
	100	75	−997.6 ± 5.4
	100	100	−997.7 ± 5.1
	125	25	−998.3 ± 4.5
	125	50	−999.0 ± 3.3
	125	75	−999.2 ± 2.8
	125	100	−999.3 ± 2.4
Air (2) (empty water container)	80	25	−995.6 ± 9.8
	80	50	−996.0 ± 7.8
	80	75	−996.3 ± 6.7
	80	100	−997.0 ± 5.8
	100	25	−997.1 ± 6.9
	100	50	−997.8 ± 4.9
	100	75	−998.3 ± 3.7
	100	100	−998.7 ± 2.5
	125	25	−998.7 ± 2.3
	125	50	−999.1 ± 1.4

Table 4.B.1: *(continued)*

Insert	kVp [kV]	Percentage of max. dose [%]	Attenuation [HU]
	125	75	−999.3 ± 1.3
	125	100	−999.3 ± 1.2
20 % Bone	80	25	335.1 ± 45.1
	80	50	324.4 ± 33.4
	80	75	323.1 ± 28.5
	80	100	319.6 ± 25.4
	100	25	291.6 ± 46.4
	100	50	285.9 ± 32.7
	100	75	284.0 ± 28.1
	100	100	283.5 ± 25.6
	125	25	262.0 ± 23.8
	125	50	261.8 ± 17.6
	125	75	260.1 ± 16.1
	125	100	257.3 ± 14.7
50 % Bone	80	25	960.4 ± 49.4
	80	50	938.3 ± 34.4
	80	75	931.7 ± 29.1
	80	100	927.4 ± 26.1
	100	25	840.5 ± 46.6
	100	50	825.2 ± 33.1
	100	75	818.2 ± 28.7
	100	100	815.3 ± 25.3
	125	25	747.9 ± 23.5
	125	50	747.7 ± 18.0
	125	75	743.2 ± 15.0
	125	100	742.1 ± 14.3
Delrin	80	25	380.2 ± 41.5
	80	50	373.9 ± 28.8
	80	75	364.6 ± 23.4
	80	100	368.0 ± 20.3
	100	25	389.5 ± 42.2
	100	50	377.9 ± 30.2
	100	75	379.4 ± 24.8
	100	100	371.6 ± 20.9
	125	25	379.5 ± 20.7
	125	50	384.5 ± 15.0
	125	75	376.7 ± 12.1
	125	100	380.8 ± 11.3
LDPE	80	25	−104.4 ± 39.3
	80	50	−106.5 ± 27.2
	80	75	−107.0 ± 21.8
	80	100	−107.2 ± 19.4
	100	25	−91.8 ± 41.4
	100	50	−95.3 ± 27.5

Table 4.B.1: *(continued)*

Insert	kVp [kV]	Percentage of max. dose [%]	Attenuation [HU]
	100	75	−95.0 ± 23.3
	100	100	−95.5 ± 19.7
	125	25	−86.4 ± 20.5
	125	50	−84.5 ± 14.4
	125	75	−87.6 ± 11.9
	125	100	−87.6 ± 10.5
Lung Foam	80	25	−852.2 ± 35.7
	80	50	−841.4 ± 25.0
	80	75	−837.2 ± 19.8
	80	100	−836.8 ± 17.7
	100	25	−856.7 ± 37.2
	100	50	−848.4 ± 26.2
	100	75	−845.4 ± 21.1
	100	100	−843.3 ± 18.2
	125	25	−849.2 ± 19.2
	125	50	−847.3 ± 13.9
	125	75	−847.6 ± 11.7
	125	100	−847.7 ± 10.8
PMP	80	25	−197.0 ± 39.1
	80	50	−194.8 ± 26.0
	80	75	−195.2 ± 21.4
	80	100	−194.7 ± 18.8
	100	25	−182.5 ± 39.3
	100	50	−183.8 ± 28.2
	100	75	−182.5 ± 23.4
	100	100	−183.8 ± 19.5
	125	25	−177.5 ± 19.2
	125	50	−175.0 ± 14.0
	125	75	−177.9 ± 11.9
	125	100	−177.4 ± 10.2
Polystyrene	80	25	−42.0 ± 39.6
	80	50	−41.2 ± 28.5
	80	75	−45.0 ± 22.7
	80	100	−43.1 ± 19.6
	100	25	−28.1 ± 41.2
	100	50	−33.6 ± 28.9
	100	75	−30.9 ± 23.8
	100	100	−34.2 ± 20.0
	125	25	−24.8 ± 20.3
	125	50	−21.4 ± 14.5
	125	75	−26.3 ± 11.5
	125	100	−24.2 ± 10.6
Teflon	80	25	1060.3 ± 45.9
	80	50	1039.5 ± 32.4

Table 4.B.1: *(continued)*

Insert	kVp [kV]	Percentage of max. dose [%]	Attenuation [HU]
	80	75	1027.7 ± 27.0
	80	100	1026.0 ± 23.4
	100	25	1037.0 ± 48.8
	100	50	1016.3 ± 33.2
	100	75	1013.1 ± 27.8
	100	100	1004.0 ± 23.5
	125	25	999.1 ± 23.4
	125	50	999.7 ± 17.5
	125	75	992.8 ± 13.8
	125	100	994.1 ± 13.0

Table 4.B.2: HU values (mean ± stdev.) for all inserts of the CIRS phantom, for all source voltages and percentages of the maximum dose.

Insert	kVp [kV]	Percentage of max. dose [%]	Attenuation [HU]
70 % Cort./30 % Trab. Bone	80	25	1390.8 ± 52.5
	80	50	1370.9 ± 38.2
	80	75	1360.9 ± 32.3
	80	100	1363.0 ± 29.8
	100	25	1232.7 ± 49.4
	100	50	1210.2 ± 35.9
	100	75	1205.8 ± 30.5
	100	100	1196.2 ± 27.3
	125	25	1100.5 ± 24.9
	125	50	1100.6 ± 20.1
	125	75	1095.2 ± 17.7
	125	100	1100.7 ± 16.7
30 % Gland/70 % Adipose	80	25	−51.1 ± 33.0
	80	50	−53.0 ± 23.0
	80	75	−54.0 ± 18.8
	80	100	−54.8 ± 16.3
	100	25	−43.5 ± 33.8
	100	50	−47.5 ± 24.3
	100	75	−46.4 ± 20.1
	100	100	−48.8 ± 17.9
	125	25	−49.2 ± 16.6
	125	50	−48.4 ± 11.9
	125	75	−50.7 ± 9.8
	125	100	−50.3 ± 8.6
70 % Gland/30 % Adipose	80	25	9.6 ± 35.0

Table 4.B.2: *(continued)*

Insert	kVp [kV]	Percentage of max. dose [%]	Attenuation [HU]
	80	50	4.2 ± 24.6
	80	75	5.7 ± 20.7
	80	100	1.3 ± 17.6
	100	25	11.9 ± 35.4
	100	50	10.8 ± 25.4
	100	75	7.9 ± 21.4
	100	100	8.8 ± 19.1
	125	25	4.8 ± 17.8
	125	50	3.1 ± 13.0
	125	75	2.6 ± 11.0
	125	100	0.1 ± 9.9
Kidney	80	25	64.4 ± 35.6
	80	50	61.7 ± 25.1
	80	75	60.2 ± 20.2
	80	100	60.2 ± 17.4
	100	25	62.2 ± 36.1
	100	50	57.7 ± 25.5
	100	75	58.1 ± 20.8
	100	100	54.6 ± 18.1
	125	25	53.4 ± 17.6
	125	50	53.8 ± 13.0
	125	75	53.2 ± 10.6
	125	100	53.2 ± 9.4
Lung (inhale)	80	25	−820.1 ± 29.0
	80	50	−811.2 ± 21.6
	80	75	−813.0 ± 17.7
	80	100	−809.7 ± 16.4
	100	25	−825.4 ± 29.7
	100	50	−824.1 ± 21.6
	100	75	−818.4 ± 18.5
	100	100	−821.2 ± 16.3
	125	25	−831.2 ± 15.8
	125	50	−825.8 ± 13.0
	125	75	−829.6 ± 11.1
	125	100	−828.5 ± 10.8
Prostate	80	25	68.4 ± 34.1
	80	50	65.3 ± 23.6
	80	75	63.9 ± 19.4
	80	100	63.0 ± 16.7
	100	25	69.0 ± 34.6
	100	50	64.3 ± 24.7
	100	75	64.5 ± 20.5
	100	100	62.0 ± 18.3
	125	25	57.4 ± 17.3

Table 4.B.2: *(continued)*

Insert	kVp [kV]	Percentage of max. dose [%]	Attenuation [HU]
	125	50	58.3 ± 12.6
	125	75	55.4 ± 10.3
	125	100	56.6 ± 9.3
Spinal Cord	80	25	62.5 ± 35.3
	80	50	60.2 ± 24.6
	80	75	58.7 ± 19.9
	80	100	58.6 ± 17.4
	100	25	62.2 ± 35.9
	100	50	57.1 ± 25.7
	100	75	57.7 ± 20.9
	100	100	54.6 ± 18.4
	125	25	52.2 ± 17.4
	125	50	52.6 ± 12.7
	125	75	51.0 ± 10.5
	125	100	51.7 ± 9.3
Spinal Disk	80	25	135.9 ± 35.8
	80	50	132.9 ± 25.3
	80	75	131.7 ± 20.4
	80	100	131.6 ± 17.8
	100	25	129.8 ± 35.8
	100	50	124.9 ± 25.7
	100	75	124.9 ± 21.1
	100	100	121.5 ± 18.6
	125	25	118.5 ± 17.9
	125	50	119.3 ± 13.2
	125	75	118.6 ± 10.9
	125	100	119.0 ± 9.7

Table 4.B.3: HU values (mean ± stdev.) for all inserts of the Gammex phantom (slices with inserts only), for all source voltages and percentages of the maximum dose.

Insert	kVp [kV]	Percentage of max. dose [%]	Attenuation [HU]
Adipose	80	25	−102.4 ± 20.7
	80	50	−102.5 ± 18.6
	80	75	−103.4 ± 15.9
	80	100	−103.1 ± 17.4
	100	25	−96.8 ± 20.8
	100	50	−99.7 ± 17.3
	100	75	−99.8 ± 17.3
	100	100	−101.3 ± 15.6

Table 4.B.3: *(continued)*

Insert	kVp [kV]	Percentage of max. dose [%]	Attenuation [HU]
	125	25	−98.1 ± 15.0
	125	50	−98.4 ± 14.9
	125	75	−96.3 ± 11.9
	125	100	−100.3 ± 12.8
Brain	80	25	12.5 ± 21.5
	80	50	16.2 ± 22.2
	80	75	9.1 ± 18.0
	80	100	10.7 ± 20.7
	100	25	25.4 ± 22.2
	100	50	18.9 ± 18.6
	100	75	20.6 ± 19.5
	100	100	14.2 ± 17.3
	125	25	19.0 ± 17.6
	125	50	21.5 ± 18.9
	125	75	17.4 ± 15.0
	125	100	21.3 ± 17.7
Breast	80	25	−28.2 ± 18.8
	80	50	−35.9 ± 16.7
	80	75	−31.9 ± 15.6
	80	100	−38.1 ± 15.2
	100	25	−33.2 ± 18.2
	100	50	−32.3 ± 15.8
	100	75	−37.9 ± 15.9
	100	100	−34.4 ± 14.8
	125	25	−36.0 ± 14.4
	125	50	−41.2 ± 13.2
	125	75	−38.5 ± 11.9
	125	100	−43.1 ± 11.8
B200 Bone Mineral	80	25	377.0 ± 26.4
	80	50	380.9 ± 21.7
	80	75	379.6 ± 20.4
	80	100	382.5 ± 18.7
	100	25	331.3 ± 24.8
	100	50	326.0 ± 21.1
	100	75	328.0 ± 18.5
	100	100	323.0 ± 18.2
	125	25	296.1 ± 15.1
	125	50	301.8 ± 13.0
	125	75	300.4 ± 14.2
	125	100	297.9 ± 12.2
CB2-30 % $CaCO_3$ Bone	80	25	738.7 ± 25.0
	80	50	744.5 ± 23.6
	80	75	740.4 ± 21.3
	80	100	741.0 ± 21.3

Table 4.B.3: *(continued)*

Insert	kVp [kV]	Percentage of max. dose [%]	Attenuation [HU]
	100	25	665.0 ± 24.2
	100	50	660.5 ± 20.7
	100	75	661.7 ± 20.3
	100	100	654.0 ± 18.2
	125	25	606.5 ± 17.5
	125	50	603.5 ± 17.2
	125	75	598.9 ± 17.2
	125	100	603.2 ± 14.9
CB2-50 % $CaCO_3$ Bone	80	25	1332.0 ± 33.6
	80	50	1337.2 ± 30.4
	80	75	1339.3 ± 29.8
	80	100	1336.5 ± 27.6
	100	25	1183.9 ± 29.4
	100	50	1182.9 ± 26.8
	100	75	1181.9 ± 25.7
	100	100	1177.1 ± 24.8
	125	25	1081.8 ± 24.0
	125	50	1073.6 ± 19.4
	125	75	1072.9 ± 22.3
	125	100	1070.8 ± 22.3
Cortical Bone	80	25	2022.3 ± 41.9
	80	50	2036.6 ± 42.5
	80	75	2034.5 ± 39.6
	80	100	2040.3 ± 38.2
	100	25	1801.0 ± 38.6
	100	50	1791.9 ± 34.6
	100	75	1798.7 ± 34.6
	100	100	1790.5 ± 30.0
	125	25	1633.9 ± 30.2
	125	50	1632.1 ± 27.5
	125	75	1620.3 ± 27.5
	125	100	1624.3 ± 30.2
Inner Bone	80	25	369.6 ± 29.8
	80	50	368.0 ± 24.5
	80	75	369.6 ± 22.7
	80	100	368.2 ± 21.1
	100	25	314.4 ± 26.9
	100	50	315.7 ± 23.2
	100	75	312.5 ± 21.5
	100	100	313.5 ± 20.7
	125	25	282.4 ± 19.3
	125	50	281.5 ± 17.1
	125	75	284.3 ± 19.2
	125	100	278.3 ± 15.9

Table 4.B.3: *(continued)*

Insert	kVp [kV]	Percentage of max. dose [%]	Attenuation [HU]
Liver	80	25	110.7 ± 27.0
	80	50	111.3 ± 20.8
	80	75	111.0 ± 21.0
	80	100	111.4 ± 18.2
	100	25	103.5 ± 24.9
	100	50	102.6 ± 22.1
	100	75	103.8 ± 18.8
	100	100	101.6 ± 20.0
	125	25	96.5 ± 17.8
	125	50	97.9 ± 13.9
	125	75	95.7 ± 15.4
	125	100	93.2 ± 13.9
LN300 Lung	80	25	−748.3 ± 25.8
	80	50	−748.9 ± 24.0
	80	75	−747.5 ± 22.1
	80	100	−748.3 ± 21.8
	100	25	−762.7 ± 26.1
	100	50	−763.9 ± 23.4
	100	75	−763.1 ± 22.4
	100	100	−765.2 ± 22.1
	125	25	−768.0 ± 18.2
	125	50	−768.9 ± 18.2
	125	75	−766.3 ± 16.9
	125	100	−766.9 ± 17.1
LN450 Lung	80	25	−556.0 ± 24.4
	80	50	−559.6 ± 20.9
	80	75	−556.6 ± 20.8
	80	100	−558.6 ± 19.1
	100	25	−570.5 ± 23.8
	100	50	−570.5 ± 22.1
	100	75	−571.6 ± 20.0
	100	100	−570.1 ± 20.1
	125	25	−576.5 ± 17.3
	125	50	−576.4 ± 15.9
	125	75	−578.9 ± 15.8
	125	100	−585.0 ± 14.7
Solid Water (1)	80	25	39.5 ± 19.1
	80	50	44.5 ± 17.1
	80	75	38.5 ± 16.0
	80	100	41.3 ± 18.5
	100	25	37.7 ± 20.2
	100	50	31.5 ± 16.6
	100	75	33.8 ± 18.5
	100	100	28.4 ± 16.4

Table 4.B.3: *(continued)*

Insert	kVp [kV]	Percentage of max. dose [%]	Attenuation [HU]
	125	25	25.0 ± 15.6
	125	50	25.2 ± 16.6
	125	75	22.4 ± 11.4
	125	100	27.4 ± 12.3
Solid Water (2)	80	25	21.3 ± 22.7
	80	50	19.5 ± 20.0
	80	75	19.4 ± 17.3
	80	100	18.9 ± 18.0
	100	25	10.6 ± 23.1
	100	50	12.1 ± 18.8
	100	75	10.9 ± 18.7
	100	100	10.9 ± 16.9
	125	25	4.5 ± 15.1
	125	50	6.1 ± 16.2
	125	75	−2.4 ± 13.9
	125	100	−4.1 ± 14.0
Solid Water (3)	80	25	27.8 ± 25.7
	80	50	35.0 ± 24.2
	80	75	29.3 ± 20.2
	80	100	34.9 ± 21.0
	100	25	25.9 ± 26.7
	100	50	20.1 ± 21.6
	100	75	25.4 ± 21.3
	100	100	18.7 ± 18.7
	125	25	17.5 ± 16.7
	125	50	22.0 ± 17.5
	125	75	17.0 ± 16.5
	125	100	18.6 ± 16.7
Solid Water (4)	80	25	26.6 ± 25.4
	80	50	29.2 ± 19.8
	80	75	27.7 ± 20.0
	80	100	29.6 ± 17.1
	100	25	20.9 ± 22.1
	100	50	17.9 ± 21.0
	100	75	19.9 ± 16.6
	100	100	17.2 ± 17.8
	125	25	11.7 ± 17.0
	125	50	17.3 ± 12.6
	125	75	7.2 ± 16.5
	125	100	5.8 ± 11.8
Water	80	25	22.3 ± 19.3
	80	50	16.7 ± 15.5
	80	75	21.0 ± 15.4
	80	100	17.0 ± 13.4

Table 4.B.3: *(continued)*

Insert	kVp [kV]	Percentage of max. dose [%]	Attenuation [HU]
	100	25	16.8 ± 17.7
	100	50	15.8 ± 15.2
	100	75	14.0 ± 15.3
	100	100	16.1 ± 14.0
	125	25	12.5 ± 13.1
	125	50	7.4 ± 12.0
	125	75	11.6 ± 9.5
	125	100	6.8 ± 9.5

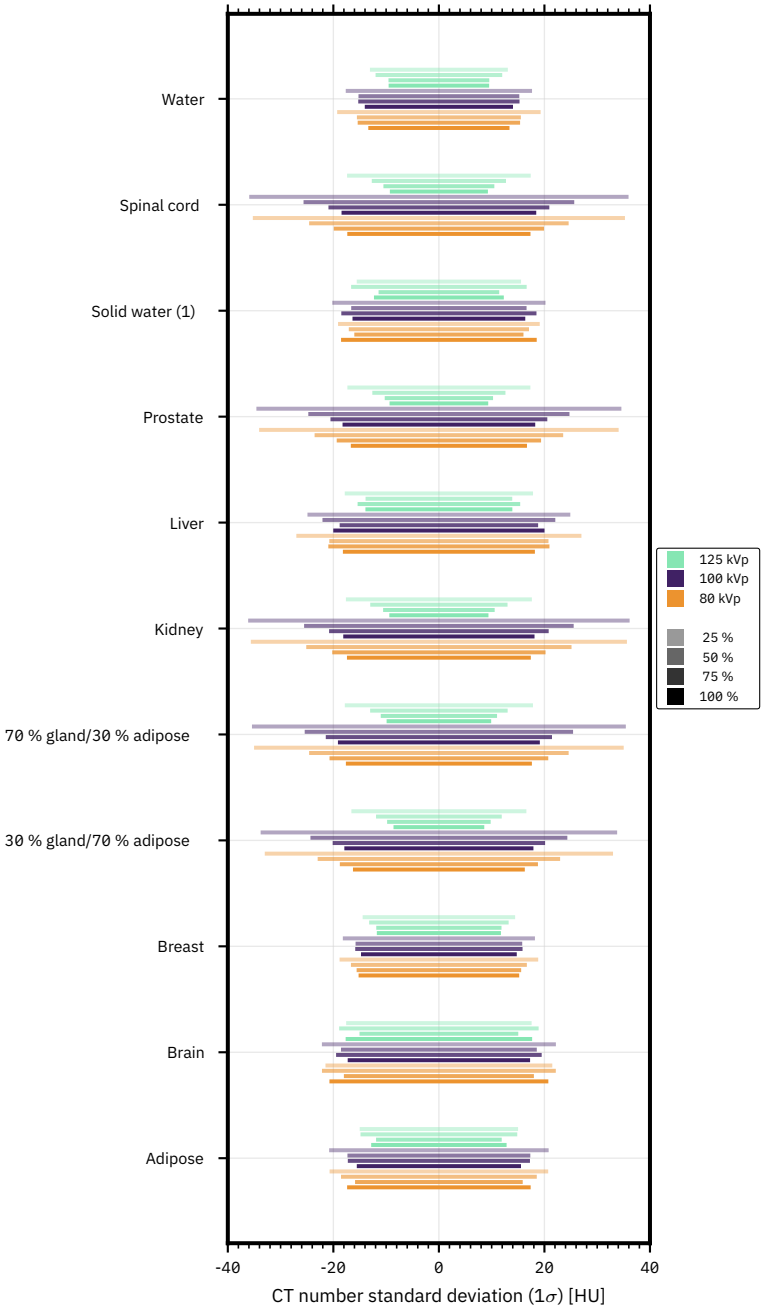

Figure 4.B.1: CT numbers noise levels of both Gammex and CIRS inserts (soft tissue and adipose), for different source voltages and dose ratios. The errorbars indicate 1σ confidence intervals.

4.B.2 Additional Results for the Hounsfield Look-Up Table Method

Table 4.B.4: Results for the HLUT method, using different values for the source voltage and different choices of calibration phantom. Results are shown as the RME on SPR in percent, either including only the calibration phantom in the calculation of the RME, or all phantoms except the calibration phantom, or all phantoms.

kVp [kV]	Calibration phantom	Evaluation phantom(s)		
		Only calibration phantom	All phantoms excl. calibr. phantom	All phantoms
80	Catphan	8.4 ± 10.6	-0.76 ± 2.07	1.44 ± 6.55
	CIRS	-0.51 ± 1.14	0.86 ± 7.38	0.53 ± 6.44
	Gammex	-0.99 ± 2.08	3.84 ± 8.61	1.34 ± 6.53
100	Catphan	7.74 ± 9.86	-0.40 ± 1.82	1.56 ± 5.99
	CIRS	-0.555± 0.859	0.90 ± 6.71	0.55 ± 5.86
	Gammex	-0.69 ± 1.75	3.49 ± 7.94	1.33 ± 5.95
125	Catphan	7.22 ± 9.23	-0.07 ± 1.88	1.69 ± 5.57
	CIRS	-0.317± 0.966	1.08 ± 6.21	0.74 ± 5.43
	Gammex	-0.36 ± 1.71	3.35 ± 7.35	1.43 ± 5.49

Table 4.B.5: Results for the HLUT method, using different values for the source voltage and different choices of calibration phantom. Results are shown as the RMAE on SPR in percent, either including only the calibration phantom in the calculation of the RMAE, or all phantoms except the calibration phantom, or all phantoms.

kVp [kV]	Calibration phantom	Evaluation phantom(s)		
		Only calibration phantom	All phantoms excl. calibr. phantom	All phantoms
80	Catphan	9.51 ± 9.36	1.83 ± 1.18	3.68 ± 5.57
	CIRS	0.998 ± 0.661	4.90 ± 5.49	3.96 ± 5.06
	Gammex	1.88 ± 1.26	5.52 ± 7.56	3.64 ± 5.54
100	Catphan	8.85 ± 8.71	1.53 ± 1.00	3.30 ± 5.21
	CIRS	0.793 ± 0.603	4.42 ± 5.05	3.54 ± 4.66
	Gammex	1.49 ± 1.09	5.06 ± 6.98	3.21 ± 5.15
125	Catphan	8.28 ± 8.13	1.45 ± 1.15	3.10 ± 4.90
	CIRS	0.775 ± 0.591	4.10 ± 4.71	3.29 ± 4.34
	Gammex	1.37 ± 1.04	4.73 ± 6.49	2.99 ± 4.80

Table 4.B.6: Results for the HLUT method, using different values for the source voltage and different choices of calibration phantom. Results are shown as the RRMSE on SPR in percent, either including only the calibration phantom in the calculation of the RRMSE, or all phantoms except the calibration phantom, or all phantoms.

kVp [kV]	Calibration phantom	Evaluation phantom(s)		
		Only calibration phantom	All phantoms excl. calibr. phantom	All phantoms
80	Catphan	16.9 ± 16.5	2.21 ± 1.35	9.3 ± 18.5
	CIRS	1.096 ± 0.509	10.0 ± 16.1	8.8 ± 16.3
	Gammex	2.23 ± 1.41	12.7 ± 18.0	9.3 ± 18.7
100	Catphan	15.8 ± 15.3	1.90 ± 1.47	8.7 ± 17.3
	CIRS	0.910 ± 0.442	9.2 ± 14.7	8.0 ± 14.8
	Gammex	1.84 ± 1.29	11.7 ± 16.7	8.6 ± 17.4
125	Catphan	14.7 ± 14.3	1.74 ± 1.32	8.1 ± 16.1
	CIRS	0.888 ± 0.436	8.5 ± 13.7	7.4 ± 13.8
	Gammex	1.60 ± 1.03	10.9 ± 15.5	8.0 ± 16.2

Table 4.B.7: Results for the HLUT method and different choices of calibration phantom. Results are shown as the RME on SPR in percent, using only one phantom for evaluation at a time.

kVp [kV]	Calibration phantom	Catphan	CIRS	Gammex
80	Catphan	8.4 ± 10.6	-0.09 ± 1.95	-1.07 ± 2.12
	CIRS	7.0 ± 10.5	-0.51 ± 1.14	-1.99 ± 2.59
	Gammex	8.0 ± 10.7	-0.30 ± 2.36	-0.99 ± 2.08
100	Catphan	7.74 ± 9.86	-0.07 ± 1.86	-0.56 ± 1.84
	CIRS	6.19 ± 9.77	-0.555± 0.859	-1.57 ± 2.47
	Gammex	7.34 ± 9.89	-0.36 ± 2.11	-0.69 ± 1.75
125	Catphan	7.22 ± 9.23	0.16 ± 1.72	-0.17 ± 1.99
	CIRS	5.72 ± 9.09	-0.317± 0.966	-1.08 ± 2.58
	Gammex	6.85 ± 9.21	-0.14 ± 1.91	-0.36 ± 1.71

Table 4.B.8: Results for the HLUT method and different choices of calibration phantom. Results are shown as the RMAE on SPR in percent, using only one phantom for evaluation at a time.

kVp [kV]	Calibration phantom	Catphan	CIRS	Gammex
80	Catphan	9.51 ± 9.36	1.558 ± 0.989	1.95 ± 1.27
	CIRS	9.72 ± 7.60	0.998 ± 0.661	2.64 ± 1.86
	Gammex	9.20 ± 9.52	1.85 ± 1.29	1.88 ± 1.26
100	Catphan	8.85 ± 8.71	1.37 ± 1.13	1.611 ± 0.969
	CIRS	8.92 ± 6.89	0.793 ± 0.603	2.32 ± 1.73
	Gammex	8.47 ± 8.76	1.64 ± 1.20	1.49 ± 1.09
125	Catphan	8.28 ± 8.13	1.29 ± 1.03	1.52 ± 1.23
	CIRS	8.28 ± 6.40	0.775 ± 0.591	2.14 ± 1.72
	Gammex	7.95 ± 8.11	1.50 ± 1.03	1.37 ± 1.04

Table 4.B.9: Results for the HLUT method and different choices of calibration phantom. Results are shown as the RRMSE on SPR in percent, using only one phantom for evaluation at a time.

kVp [kV]	Calibration phantom	Catphan	CIRS	Gammex
80	Catphan	16.9 ± 16.5	2.07 ± 1.66	2.27 ± 1.25
	CIRS	15.5 ± 14.8	1.096 ± 0.509	3.61 ± 2.36
	Gammex	16.8 ± 16.8	2.44 ± 1.66	2.23 ± 1.41
100	Catphan	15.8 ± 15.3	2.05 ± 1.91	1.83 ± 1.19
	CIRS	14.2 ± 13.5	0.910 ± 0.442	3.33 ± 2.52
	Gammex	15.6 ± 15.5	2.27 ± 1.74	1.84 ± 1.29
125	Catphan	14.7 ± 14.3	1.90 ± 1.78	1.647 ± 0.962
	CIRS	13.2 ± 12.5	0.888 ± 0.436	3.00 ± 2.24
	Gammex	14.5 ± 14.5	2.03 ± 1.57	1.60 ± 1.03

4.B.3 Additional Results for the Hünemohr-Saito Method

Results using RME as error metric

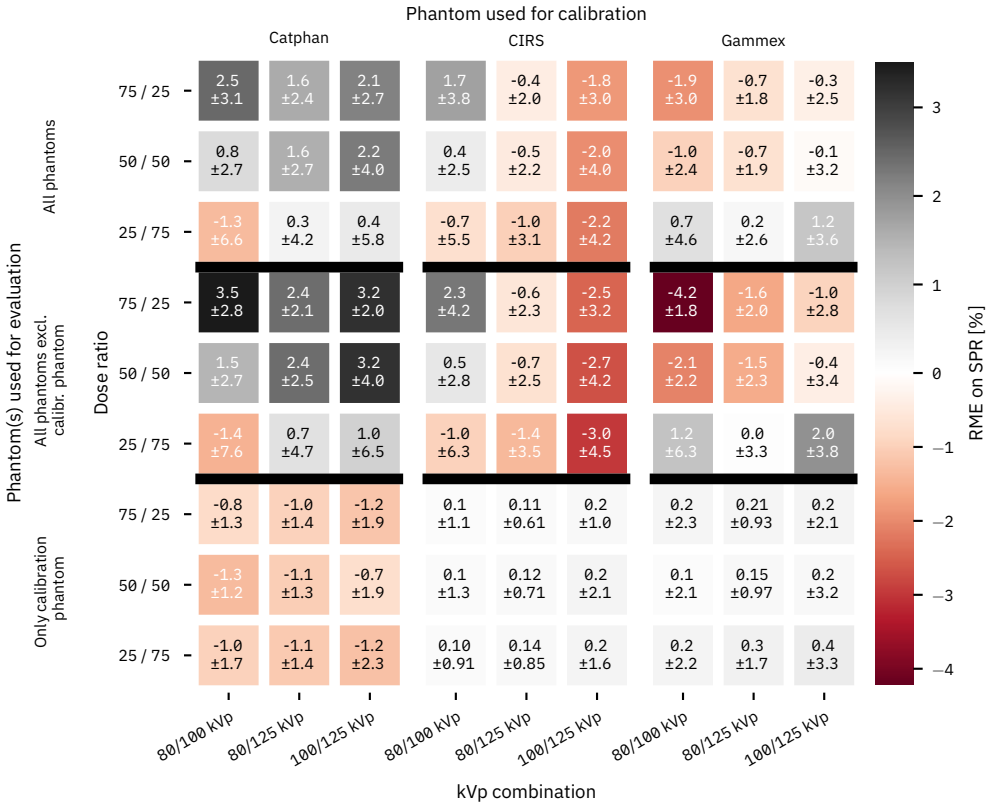

Figure 4.B.2: RME on SPR for different kVp combinations, dose ratios, and phantoms used for calibration as obtained by the HS method. The results are grouped by case: Evaluation of RME using the same phantom that was used for calibration, evaluation using all phantoms except the calibration phantom, and evaluation using all phantoms. See also Tables 4.B.10 to 4.B.12.

Table 4.B.10: Results for the HS method using a kVp combination of 80/100 kVp and different choices of calibration phantom. Results are shown as the RME on SPR in percent, either including only the calibration phantom in the calculation of the RME, or all phantoms except the calibration phantom, or all phantoms.

Dose ratio	Calibration phantom	Evaluation phantom(s)		
		Only calibration phantom	All phantoms excl. calibr. phantom	All phantoms
25/75	Catphan	-0.98 ± 1.69	-1.45 ± 7.61	-1.33 ± 6.64
	CIRS	0.10 ± 0.91	-0.96 ± 6.33	-0.70 ± 5.52
	Gammex	0.23 ± 2.15	1.23 ± 6.33	0.71 ± 4.60
50/50	Catphan	-1.34 ± 1.23	1.47 ± 2.70	0.79 ± 2.70
	CIRS	0.09 ± 1.34	0.54 ± 2.79	0.43 ± 2.50
	Gammex	0.08 ± 2.07	-2.08 ± 2.20	-0.96 ± 2.36
75/25	Catphan	-0.82 ± 1.32	3.52 ± 2.80	2.47 ± 3.13
	CIRS	0.08 ± 1.06	2.28 ± 4.22	1.75 ± 3.81
	Gammex	0.19 ± 2.29	-4.21 ± 1.82	-1.93 ± 3.03

Table 4.B.11: Results for the HS method using a kVp combination of 80/125 kVp and different choices of calibration phantom. Results are shown as the RME on SPR in percent, either including only the calibration phantom in the calculation of the RME, or all phantoms except the calibration phantom, or all phantoms.

Dose ratio	Calibration phantom	Evaluation phantom(s)		
		Only calibration phantom	All phantoms excl. calibr. phantom	All phantoms
25/75	Catphan	-1.09 ± 1.40	0.69 ± 4.70	0.26 ± 4.20
	CIRS	0.14 ± 0.85	-1.36 ± 3.49	-1.00 ± 3.11
	Gammex	0.32 ± 1.71	0.03 ± 3.34	0.18 ± 2.58
50/50	Catphan	-1.05 ± 1.28	2.39 ± 2.54	1.56 ± 2.73
	CIRS	0.12 ± 0.71	-0.67 ± 2.45	-0.48 ± 2.18
	Gammex	0.15 ± 0.97	-1.55 ± 2.33	-0.67 ± 1.93
75/25	Catphan	-0.96 ± 1.39	2.41 ± 2.08	1.60 ± 2.41
	CIRS	0.11 ± 0.61	-0.57 ± 2.28	-0.41 ± 2.01
	Gammex	0.21 ± 0.93	-1.64 ± 2.01	-0.68 ± 1.79

Table 4.B.12: Results for the HS method using a kVp combination of 100/125 kVp and different choices of calibration phantom. Results are shown as the RME on SPR in percent, either including only the calibration phantom in the calculation of the RME, or all phantoms except the calibration phantom, or all phantoms.

Dose ratio	Calibration phantom	Evaluation phantom(s)		
		Only calibration phantom	All phantoms excl. calibr. phantom	All phantoms
25/75	Catphan	-1.23 ± 2.34	0.98 ± 6.52	0.45 ± 5.83
	CIRS	0.22 ± 1.63	-2.97 ± 4.53	-2.20 ± 4.23
	Gammex	0.44 ± 3.31	1.96 ± 3.83	1.17 ± 3.59
50/50	Catphan	-0.73 ± 1.90	3.18 ± 4.01	2.24 ± 3.96
	CIRS	0.23 ± 2.05	-2.67 ± 4.21	-1.97 ± 3.98
	Gammex	0.15 ± 3.18	-0.39 ± 3.38	-0.11 ± 3.23
75/25	Catphan	-1.16 ± 1.90	3.20 ± 1.96	2.14 ± 2.69
	CIRS	0.16 ± 1.00	-2.46 ± 3.17	-1.83 ± 3.00
	Gammex	0.22 ± 2.07	-0.95 ± 2.81	-0.34 ± 2.48

Table 4.B.13: Results for the HS method using a kVp combination of 80/100 kVp and different choices of calibration phantom. Results are shown as the RME on SPR in percent, using only one phantom for evaluation at a time.

Dose ratio	Calibration phantom	Catphan	CIRS	Gammex
25/75	Catphan	-0.98 ± 1.69	-0.63 ± 1.22	-1.83 ± 9.26
	CIRS	-0.55 ± 1.97	0.10 ± 0.91	-1.16 ± 7.64
	Gammex	1.08 ± 7.48	1.38 ± 5.55	0.23 ± 2.15
50/50	Catphan	-1.34 ± 1.23	-0.16 ± 1.94	2.24 ± 2.71
	CIRS	-1.16 ± 1.80	0.09 ± 1.34	1.33 ± 2.86
	Gammex	-2.46 ± 1.81	-1.70 ± 2.61	0.08 ± 2.07
75/25	Catphan	-0.82 ± 1.32	1.06 ± 1.01	4.66 ± 2.62
	CIRS	-2.44 ± 2.33	0.08 ± 1.06	4.49 ± 2.84
	Gammex	-5.24 ± 1.67	-3.18 ± 1.37	0.19 ± 2.29

Table 4.B.14: Results for the HS method using a kVp combination of 80/125 kVp and different choices of calibration phantom. Results are shown as the RME on SPR in percent, using only one phantom for evaluation at a time.

Dose ratio	Calibration phantom	Catphan	CIRS	Gammex
25/75	Catphan	-1.09 ± 1.40	1.07 ± 1.02	0.51 ± 5.71
	CIRS	-2.11 ± 1.47	0.14 ± 0.85	-1.00 ± 4.11
	Gammex	-0.99 ± 3.47	1.06 ± 3.09	0.32 ± 1.71
50/50	Catphan	-1.05 ± 1.28	1.97 ± 0.77	2.59 ± 3.05
	CIRS	-2.73 ± 1.07	0.12 ± 0.71	0.29 ± 2.33
	Gammex	-2.93 ± 1.99	-0.17 ± 1.83	0.15 ± 0.97
75/25	Catphan	-0.96 ± 1.39	1.94 ± 0.67	2.63 ± 2.48
	CIRS	-2.71 ± 1.00	0.11 ± 0.61	0.42 ± 2.00
	Gammex	-3.01 ± 1.42	-0.27 ± 1.53	0.21 ± 0.93

Table 4.B.15: Results for the HS method using a kVp combination of 100/125 kVp and different choices of calibration phantom. Results are shown as the RME on SPR in percent, using only one phantom for evaluation at a time.

Dose ratio	Calibration phantom	Catphan	CIRS	Gammex
25/75	Catphan	-1.23 ± 2.34	2.56 ± 2.18	0.25 ± 7.74
	CIRS	-3.01 ± 2.74	0.22 ± 1.63	-2.95 ± 5.25
	Gammex	0.45 ± 3.88	3.47 ± 3.36	0.44 ± 3.31
50/50	Catphan	-0.73 ± 1.90	4.18 ± 2.27	2.71 ± 4.60
	CIRS	-5.92 ± 2.60	0.23 ± 2.05	-1.15 ± 4.00
	Gammex	-2.75 ± 2.76	1.97 ± 2.03	0.15 ± 3.18
75/25	Catphan	-1.16 ± 1.90	3.64 ± 1.43	2.99 ± 2.18
	CIRS	-4.00 ± 2.32	0.16 ± 1.00	-1.74 ± 3.31
	Gammex	-3.21 ± 1.82	1.31 ± 1.35	0.22 ± 2.07

Results using RMAE as error metric

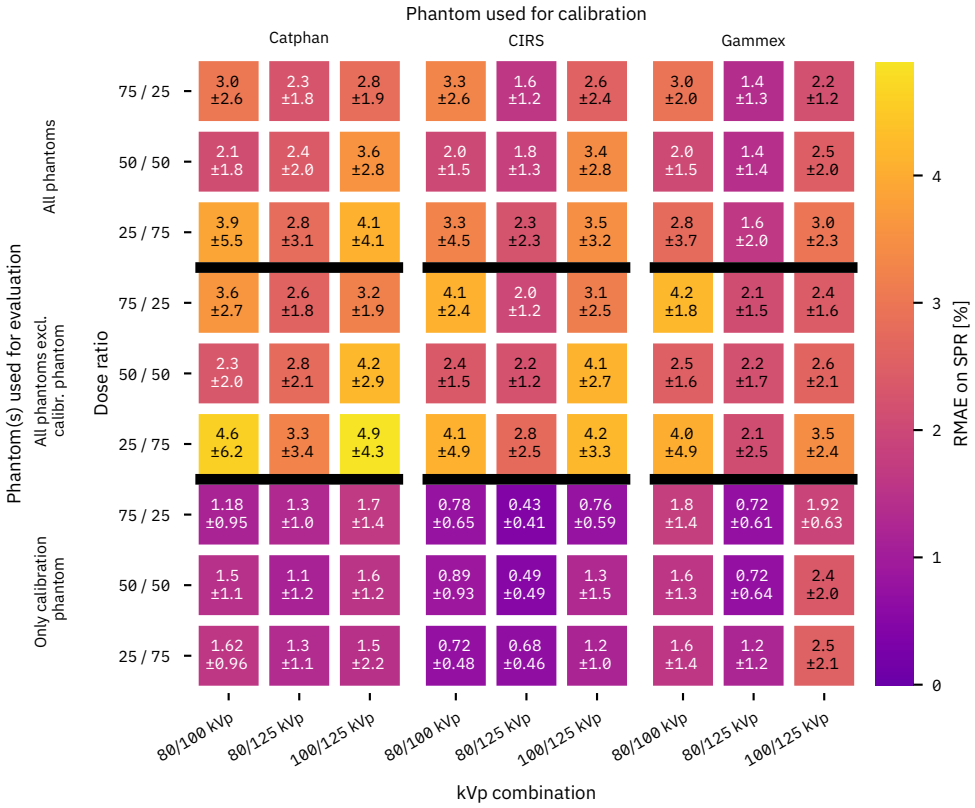

Figure 4.B.3: RMAE on SPR for different kVp combinations, dose ratios, and phantoms used for calibration as obtained by the HS method. The results are grouped by case: Evaluation of RMAE using the same phantom that was used for calibration, evaluation using all phantoms except the calibration phantom, and evaluation using all phantoms. See also Tables 4.B.16 to 4.B.18.

Table 4.B.16: Results for the HS method using a kVp combination of 80/100 kVp and different choices of calibration phantom. Results are shown as the RMAE on SPR in percent, either including only the calibration phantom in the calculation of the RMAE, or all phantoms except the calibration phantom, or all phantoms.

Dose ratio	Calibration phantom	Evaluation phantom(s)		
		Only calibration phantom	All phantoms excl. calibr. phantom	All phantoms
25/75	Catphan	1.62 ± 0.96	4.60 ± 6.16	3.88 ± 5.51
	CIRS	0.72 ± 0.48	4.07 ± 4.87	3.26 ± 4.46
	Gammex	1.60 ± 1.40	4.04 ± 4.91	2.78 ± 3.70
50/50	Catphan	1.46 ± 1.06	2.32 ± 1.98	2.11 ± 1.82
	CIRS	0.89 ± 0.93	2.36 ± 1.49	2.01 ± 1.51
	Gammex	1.58 ± 1.26	2.51 ± 1.65	2.03 ± 1.51
75/25	Catphan	1.18 ± 0.95	3.61 ± 2.67	3.02 ± 2.58
	CIRS	0.78 ± 0.65	4.07 ± 2.43	3.28 ± 2.56
	Gammex	1.79 ± 1.37	4.21 ± 1.82	2.96 ± 2.00

Table 4.B.17: Results for the HS method using a kVp combination of 80/125 kVp and different choices of calibration phantom. Results are shown as the RMAE on SPR in percent, either including only the calibration phantom in the calculation of the RMAE, or all phantoms except the calibration phantom, or all phantoms.

Dose ratio	Calibration phantom	Evaluation phantom(s)		
		Only calibration phantom	All phantoms excl. calibr. phantom	All phantoms
25/75	Catphan	1.34 ± 1.12	3.26 ± 3.38	2.80 ± 3.09
	CIRS	0.68 ± 0.46	2.76 ± 2.47	2.26 ± 2.33
	Gammex	1.21 ± 1.21	2.11 ± 2.52	1.64 ± 1.97
50/50	Catphan	1.15 ± 1.18	2.79 ± 2.08	2.39 ± 2.01
	CIRS	0.49 ± 0.49	2.22 ± 1.16	1.80 ± 1.27
	Gammex	0.72 ± 0.64	2.19 ± 1.69	1.43 ± 1.45
75/25	Catphan	1.29 ± 1.03	2.59 ± 1.84	2.28 ± 1.76
	CIRS	0.43 ± 0.41	2.00 ± 1.16	1.62 ± 1.23
	Gammex	0.72 ± 0.61	2.11 ± 1.46	1.39 ± 1.30

Table 4.B.18: Results for the HS method using a kVp combination of 100/125 kVp and different choices of calibration phantom. Results are shown as the RMAE on SPR in percent, either including only the calibration phantom in the calculation of the RMAE, or all phantoms except the calibration phantom, or all phantoms.

Dose ratio	Calibration phantom	Evaluation phantom(s)		
		Only calibration phantom	All phantoms excl. calibr. phantom	All phantoms
25/75	Catphan	1.49 ± 2.16	4.89 ± 4.30	4.07 ± 4.13
	CIRS	1.19 ± 1.04	4.21 ± 3.34	3.48 ± 3.21
	Gammex	2.52 ± 2.09	3.45 ± 2.43	2.97 ± 2.27
50/50	Catphan	1.56 ± 1.17	4.21 ± 2.85	3.57 ± 2.78
	CIRS	1.28 ± 1.53	4.11 ± 2.74	3.43 ± 2.76
	Gammex	2.36 ± 2.03	2.62 ± 2.05	2.49 ± 2.01
75/25	Catphan	1.65 ± 1.41	3.21 ± 1.94	2.83 ± 1.93
	CIRS	0.76 ± 0.59	3.14 ± 2.45	2.57 ± 2.38
	Gammex	1.92 ± 0.63	2.43 ± 1.58	2.17 ± 1.19

Table 4.B.19: Results for the HS method using a kVp combination of 80/100 kVp and different choices of calibration phantom. Results are shown as the RMAE on SPR in percent, using only one phantom for evaluation at a time.

Dose ratio	Calibration phantom	Catphan	CIRS	Gammex
25/75	Catphan	1.62 ± 0.96	1.16 ± 0.63	6.20 ± 6.93
	CIRS	1.74 ± 0.83	0.72 ± 0.48	5.16 ± 5.59
	Gammex	5.12 ± 5.17	2.96 ± 4.78	1.60 ± 1.40
50/50	Catphan	1.46 ± 1.06	1.42 ± 1.20	2.74 ± 2.16
	CIRS	1.76 ± 1.09	0.89 ± 0.93	2.64 ± 1.61
	Gammex	2.46 ± 1.81	2.55 ± 1.61	1.58 ± 1.26
75/25	Catphan	1.18 ± 0.95	1.13 ± 0.92	4.77 ± 2.41
	CIRS	2.47 ± 2.30	0.78 ± 0.65	4.82 ± 2.16
	Gammex	5.24 ± 1.67	3.18 ± 1.37	1.79 ± 1.37

Table 4.B.20: Results for the HS method using a kVp combination of 80/125 kVp and different choices of calibration phantom. Results are shown as the RMAE on SPR in percent, using only one phantom for evaluation at a time.

Dose ratio	Calibration phantom	Catphan	CIRS	Gammex
25/75	Catphan	1.34 ± 1.12	1.33 ± 0.55	4.17 ± 3.78
	CIRS	2.11 ± 1.47	0.68 ± 0.46	3.06 ± 2.81
	Gammex	2.55 ± 2.37	1.66 ± 2.77	1.21 ± 1.21
50/50	Catphan	1.15 ± 1.18	1.97 ± 0.77	3.17 ± 2.39
	CIRS	2.73 ± 1.07	0.49 ± 0.49	1.98 ± 1.15
	Gammex	3.01 ± 1.83	1.36 ± 1.11	0.72 ± 0.64
75/25	Catphan	1.29 ± 1.03	1.94 ± 0.67	2.90 ± 2.14
	CIRS	2.71 ± 1.00	0.43 ± 0.41	1.67 ± 1.10
	Gammex	3.01 ± 1.42	1.21 ± 0.85	0.72 ± 0.61

Table 4.B.21: Results for the HS method using a kVp combination of 100/125 kVp and different choices of calibration phantom. Results are shown as the RMAE on SPR in percent, using only one phantom for evaluation at a time.

Dose ratio	Calibration phantom	Catphan	CIRS	Gammex
25/75	Catphan	1.49 ± 2.16	3.04 ± 1.27	5.75 ± 4.95
	CIRS	3.23 ± 2.42	1.19 ± 1.04	4.67 ± 3.67
	Gammex	3.29 ± 1.63	3.61 ± 3.18	2.52 ± 2.09
50/50	Catphan	1.56 ± 1.17	4.18 ± 2.27	4.22 ± 3.16
	CIRS	5.92 ± 2.60	1.28 ± 1.53	3.27 ± 2.44
	Gammex	3.01 ± 2.42	2.23 ± 1.70	2.36 ± 2.03
75/25	Catphan	1.65 ± 1.41	3.64 ± 1.43	3.00 ± 2.16
	CIRS	4.00 ± 2.32	0.76 ± 0.59	2.74 ± 2.48
	Gammex	3.21 ± 1.82	1.65 ± 0.80	1.92 ± 0.63

Results using RRMSE as error metric

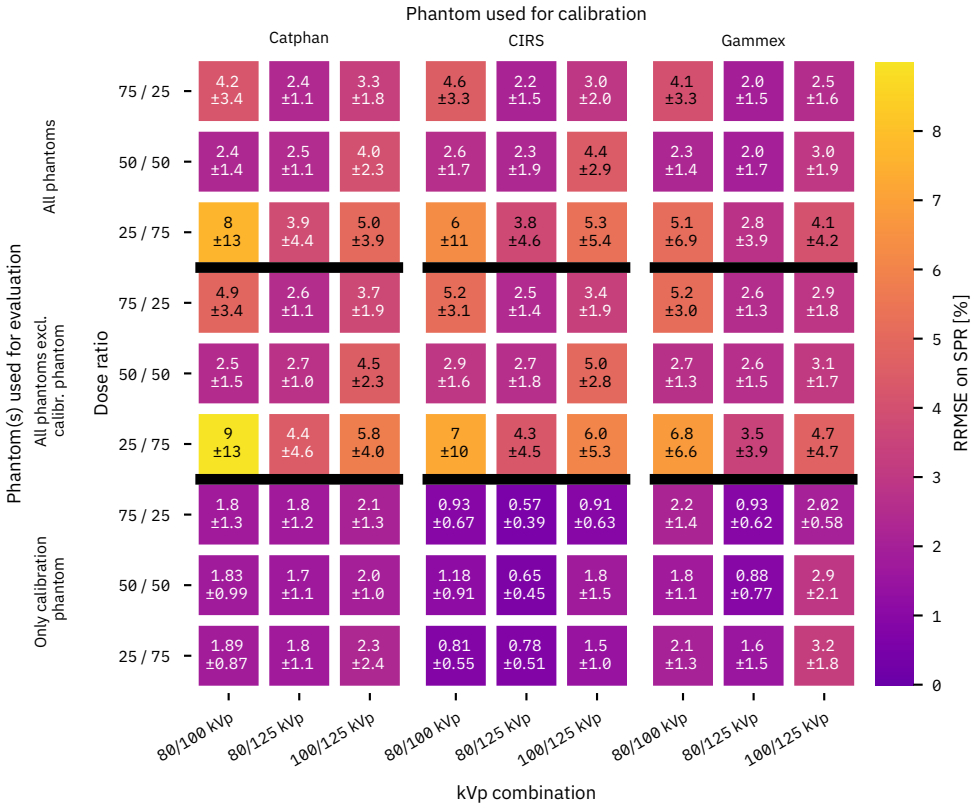

Figure 4.B.4: RRMSE on SPR for different kVp combinations, dose ratios, and phantoms used for calibration as obtained by the HS method. The results are grouped by case: Evaluation of RRMSE using the same phantom that was used for calibration, evaluation using all phantoms except the calibration phantom, and evaluation using all phantoms. See also Tables 4.B.22 to 4.B.24.

Table 4.B.22: Results for the HS method using a kVp combination of 80/100 kVp and different choices of calibration phantom. Results are shown as the RRMSE on SPR in percent, either including only the calibration phantom in the calculation of the RRMSE, or all phantoms except the calibration phantom, or all phantoms.

Dose ratio	Calibration phantom	Evaluation phantom(s)		
		Only calibration phantom	All phantoms excl. calibr. phantom	All phantoms
25/75	Catphan	1.89 ± 0.87	9.00 ± 13.28	7.66 ± 12.84
	CIRS	0.81 ± 0.55	7.22 ± 10.41	6.32 ± 10.53
	Gammex	2.05 ± 1.32	6.83 ± 6.60	5.15 ± 6.90
50/50	Catphan	1.83 ± 0.99	2.53 ± 1.50	2.35 ± 1.39
	CIRS	1.18 ± 0.91	2.92 ± 1.62	2.62 ± 1.70
	Gammex	1.76 ± 1.13	2.73 ± 1.27	2.32 ± 1.36
75/25	Catphan	1.78 ± 1.31	4.90 ± 3.43	4.25 ± 3.37
	CIRS	0.93 ± 0.67	5.19 ± 3.12	4.56 ± 3.35
	Gammex	2.20 ± 1.43	5.19 ± 3.01	4.05 ± 3.29

Table 4.B.23: Results for the HS method using a kVp combination of 80/125 kVp and different choices of calibration phantom. Results are shown as the RRMSE on SPR in percent, either including only the calibration phantom in the calculation of the RRMSE, or all phantoms except the calibration phantom, or all phantoms.

Dose ratio	Calibration phantom	Evaluation phantom(s)		
		Only calibration phantom	All phantoms excl. calibr. phantom	All phantoms
25/75	Catphan	1.76 ± 1.12	4.43 ± 4.57	3.86 ± 4.35
	CIRS	0.78 ± 0.51	4.30 ± 4.48	3.78 ± 4.57
	Gammex	1.60 ± 1.48	3.49 ± 3.94	2.76 ± 3.87
50/50	Catphan	1.71 ± 1.12	2.74 ± 1.03	2.49 ± 1.06
	CIRS	0.65 ± 0.45	2.66 ± 1.84	2.35 ± 1.93
	Gammex	0.88 ± 0.77	2.63 ± 1.48	2.00 ± 1.70
75/25	Catphan	1.77 ± 1.16	2.56 ± 1.07	2.36 ± 1.08
	CIRS	0.57 ± 0.39	2.46 ± 1.39	2.17 ± 1.50
	Gammex	0.93 ± 0.62	2.56 ± 1.28	1.97 ± 1.50

Table 4.B.24: Results for the HS method using a kVp combination of 100/125 kVp and different choices of calibration phantom. Results are shown as the RRMSE on SPR in percent, either including only the calibration phantom in the calculation of the RRMSE, or all phantoms except the calibration phantom, or all phantoms.

Dose ratio	Calibration phantom	Evaluation phantom(s)		
		Only calibration phantom	All phantoms excl. calibr. phantom	All phantoms
25/75	Catphan	2.34 ± 2.36	5.78 ± 3.98	5.04 ± 3.91
	CIRS	1.46 ± 1.04	6.04 ± 5.29	5.33 ± 5.43
	Gammex	3.25 ± 1.84	4.74 ± 4.70	4.10 ± 4.24
50/50	Catphan	2.00 ± 1.03	4.54 ± 2.34	3.98 ± 2.33
	CIRS	1.81 ± 1.53	4.97 ± 2.75	4.43 ± 2.91
	Gammex	2.92 ± 2.12	3.08 ± 1.69	3.01 ± 1.87
75/25	Catphan	2.12 ± 1.34	3.71 ± 1.86	3.33 ± 1.81
	CIRS	0.91 ± 0.63	3.38 ± 1.87	2.99 ± 2.01
	Gammex	2.02 ± 0.58	2.92 ± 1.76	2.53 ± 1.63

Table 4.B.25: Results for the HS method using a kVp combination of 80/100 kVp and different choices of calibration phantom. Results are shown as the RRMSE on SPR in percent, using only one phantom for evaluation at a time.

Dose ratio	Calibration phantom	Catphan	CIRS	Gammex
25/75	Catphan	1.89 ± 0.87	1.52 ± 1.27	10.94 ± 13.25
	CIRS	2.07 ± 1.30	0.81 ± 0.55	9.00 ± 10.92
	Gammex	6.66 ± 4.82	7.01 ± 8.91	2.05 ± 1.32
50/50	Catphan	1.83 ± 0.99	1.95 ± 1.32	2.77 ± 1.53
	CIRS	2.26 ± 1.47	1.18 ± 0.91	3.25 ± 1.71
	Gammex	2.52 ± 1.23	2.96 ± 1.41	1.76 ± 1.13
75/25	Catphan	1.78 ± 1.31	1.41 ± 0.95	5.91 ± 3.15
	CIRS	4.09 ± 3.20	0.93 ± 0.67	5.75 ± 3.18
	Gammex	6.10 ± 2.76	3.73 ± 2.24	2.20 ± 1.43

Table 4.B.26: Results for the HS method using a kVp combination of 80/125 kVp and different choices of calibration phantom. Results are shown as the RRMSE on SPR in percent, using only one phantom for evaluation at a time.

Dose ratio	Calibration phantom	Catphan	CIRS	Gammex
25/75	Catphan	1.76 ± 1.12	1.37 ± 0.43	5.33 ± 4.51
	CIRS	2.63 ± 1.77	0.78 ± 0.51	5.04 ± 4.97
	Gammex	2.93 ± 2.02	4.06 ± 5.24	1.60 ± 1.48
50/50	Catphan	1.71 ± 1.12	2.14 ± 0.80	3.00 ± 1.03
	CIRS	2.79 ± 1.02	0.65 ± 0.45	2.57 ± 2.33
	Gammex	2.99 ± 1.01	2.09 ± 2.16	0.88 ± 0.77
75/25	Catphan	1.77 ± 1.16	2.12 ± 0.86	2.75 ± 1.12
	CIRS	2.89 ± 1.08	0.57 ± 0.39	2.14 ± 1.51
	Gammex	3.07 ± 0.84	1.72 ± 1.62	0.93 ± 0.62

Table 4.B.27: Results for the HS method using a kVp combination of 100/125 kVp and different choices of calibration phantom. Results are shown as the RRMSE on SPR in percent, using only one phantom for evaluation at a time.

Dose ratio	Calibration phantom	Catphan	CIRS	Gammex
25/75	Catphan	2.34 ± 2.36	3.27 ± 1.19	6.68 ± 4.02
	CIRS	3.54 ± 2.42	1.46 ± 1.04	7.13 ± 5.75
	Gammex	3.71 ± 1.59	5.76 ± 6.15	3.25 ± 1.84
50/50	Catphan	2.00 ± 1.03	4.41 ± 2.09	4.60 ± 2.53
	CIRS	6.05 ± 1.95	1.81 ± 1.53	4.15 ± 2.98
	Gammex	3.16 ± 1.44	2.96 ± 2.12	2.92 ± 2.12
75/25	Catphan	2.12 ± 1.34	4.08 ± 1.91	3.51 ± 1.85
	CIRS	4.08 ± 1.74	0.91 ± 0.63	2.85 ± 1.51
	Gammex	3.47 ± 1.58	2.01 ± 1.35	2.02 ± 0.58

Chapter 5

Conclusion and Outlook

5.1 Conclusion

The purpose of this thesis was to investigate whether the performance of spectral cone-beam computed tomography can be improved over conventional single-energy energy-integrating CBCT, such that its images can be directly used for treatment plan updates or maybe even for online adaptive radiotherapy. It was motivated by a range of studies that showed a better performance of dual-energy fan-beam CT for proton stopping power ratio extraction compared to single-energy fan-beam CT in the context of proton therapy [2, 18, 21, 22, 24, 35, 36, 43, 44, 46]. This thesis focused on hardware-based improvements, and investigated (1) which figure(s) of merit can be used to compare spectral CBCT setups, (2) which spectral CBCT setup is best suited for SPR extraction as well as to optimise the parameters of such a setup, and (3) to test SPR extraction experimentally using a clinical CBCT system.

In order to address the first research question, we considered photon-counting detectors as a way to implement spectral CBCT, for the assessment of which a quality metric is needed. Typically, common quality metrics for detector performance assume a linear behaviour under low fluence rate conditions and are not directly applicable to PCDs under pulse pile-up. Chapter 2 proposes to adapt quality metrics for the non-linear case under pulse pile-up using a small-signal analysis approach. It approximates the non-linear behaviour of PCDs by a linear response around a given operating point, which is determined by the spectral shape and the total fluence rate of the spectrum incident on the detector. The response around this operating point is described by a so-called perturbation point spread function, which captures the spectral and spatial response of a PCD around that operating point. Furthermore, we investigated how this can be used to determine the contrast and contrast-to-noise ratio for an arbitrary lesion in the projection path, and we show how an increasing fluence rate can cause nonintuitive effects such as inversion or cancellation of contrast and contrast-to-noise ratio between/within energy bins. Our framework could be applied to adopt detector quality measures, such as the modulation transfer function, to the case of non-linear PCDs.
While pile-up is relevant for detectors with a response time comparable to the rate of incoming photons, Thomas Flohr, former *Senior Principal Key Expert CT* at SIEMENS HEALTHINEERS, stated that pulse pile-up is not an issue in their SIEMENS photon-counting CT scanner under any clinically relevant condition; as a consequence, their PCD CT scanner does not feature pulse pile-up correction [7]. It is a reminder that, from the standpoint of building a detection system, it is preferable to choose a detector with a fast enough characteristic response time and/or sufficiently small pixels to avoid pile-up, instead of a detector suffering from pile-up that needs to be accounted for.

Addressing the second research question, Chapter 3 compared a wide range of spectral CBCT setups with respect to their performance of extracting SPR values, including, but not limited to, PCD-based setups. Our Cramér-Rao Lower Bound-based approach is a powerful methodology enabling a comparison based on the theoretically achievable performance limits in a simulation study, without being influenced by the limitations of a particular reconstruction algorithm or by the method of converting reconstructed images to SPR values. It should be noted that within the scope of Chapter 3, PCD-based setups are assumed to operate in the linear regime. We found that, assuming a realistic detector response, setups with a kVp-switching source perform best, with the kVp-switching setup paired with an energy-integrating detector performing slightly better than the PCD-based kVp-switching setup. We attribute the worse performance of the PCD-based setup to the degradation of the registered spectrum in the PCD. However, the kVp-switching setup with an EID performs only best as long as the mAs ratio of the kVp-switching source can assume any value; if it is fixed to a ratio of 1, the performance of the kVp-switching setup with an EID is significantly degraded and outperformed by any PCD-based

setup. Furthermore, we found that a higher source voltage or a greater separation between source spectra in general yield better performance. Comparing PCDs with charge sharing to such without, we find that the latter might offer substantially improved SPR extraction.
The main drawback of the CRLB approach is that it can only compare spectral CBCT setups amongst themselves, hence, it can unfortunately not draw a comparison between spectral CBCT and single-energy energy-integrating CBCT setups, since there exists no unbiased estimator for extracting SPR via electron density and ionisation potential from a single-energy measurement.
While Chapter 3 resulted in a clear indication which setup performs best, based on either an ideal or realistic detector response function, it did so only with respect to a setup's ability of extracting SPRs. While this is undeniably an important aspect for proton therapy planning, another crucial aspect is the achievable soft tissue contrast necessary for the task of tissue delineation (including the tumour and organs at risk), and which also benefits from spectral capabilities as shown by Bazalova et al [3]. Such an investigation into soft tissue contrast would clearly go beyond the scope of Chapter 3 and is worthy of a dedicated study. We would like to note, though, that the same CRLB-based approach can be adapted for the optimisation with respect to soft tissue contrast instead of SPR extraction, as well as for other imaging tasks such as K-edge imaging of contrast agents, if desired. Based on our findings, we also recommend considering to extend the investigated X-ray energy range to both larger spectral separation (in case that two independent X-ray source spectra are used) or spectra with higher energy (in case a single X-ray source spectrum is used), thus going beyond the X-ray energy range typically used in medical X-ray imaging.
Furthermore, the same CRLB optimisation for CBCT can also be repeated for fan-beam CT using an appropriate scatter model. Such a study would be able to relate CBCT performance to a fan-beam CT reference.
While both extraction of SPR values and the achieved soft tissue contrast are important aspects in the choice of a spectral CBCT setup for proton therapy planning, the decision will also need to consider economical aspects. For example, PCDs are at the moment still very expensive, and a dual-source system is more costly than a single-source system. Our study indicates that dual-layer detectors, while being relatively cost-effective due to their detector consisting of two layers of conventional EIDs, perform worst with respect to dual-energy SPR extraction and we therefore discourage their use in imaging for proton treatment planning.

The last research question is addressed via the experimental study in Chapter 4, comparing single- and dual-energy CBCT. While the results indicate that dual-energy CBCT might perform better than single-energy CBCT with respect to extracting SPR values, unfortunately, though, due to limitations in the study design and the large uncertainties on the obtained figure of merit values, no definite answer can be given. We outline improvements necessary for a future study to yield more significant results; however, we would also like to caution the reader to accept the results of a study with an improved design as final: Reconstruction algorithms are only as good as the underlying model, and, for example, an algorithm reconstructing attenuation maps for each energy separately will always perform suboptimal compared to an algorithm that incorporates data of both energies and hence all available information during the reconstruction process.
To conclude, Chapter 4 is an indication that spectral CBCT might perform better than single-energy energy-integrating CBCT, but more research is needed.

5.2 Outlook

Proton tomography is an alternative to X-ray (CB)CT. Its appeal lies in the direct extraction of proton SPR values [4, 23, 38], hence, circumventing the conversion methods necessary in the case of X-ray-based SPR extraction. This might also allow for real-time online adaptive proton therapy, for example by interleaving high energy proton beams for imaging with lower energy proton beams for therapeutic dose deposition. Challenges for proton imaging are the higher proton energies necessary, since the proton energies used for treatment are adjusted for the beam to stop inside the patient. Moreover, due to scatter, proton tomography has lower spatial resolution than X-ray imaging [5, 31]. Nonetheless, a study by DeJongh et al [6] on porcine models as well as a study by Terakawa et al [37] on small animals compared single-energy CT to proton CT, and in both cases found proton CT to deliver improved results over X-ray CT. Furthermore, Dedes et al [4] compared proton CT to dual-energy CT, achieving a mean absolute percent error of 0.55 % and 0.67 % for proton CT and dual-energy CT, respectively.

Ultimately, the goal is an imaging modality that allows to image the patient in treatment position, perhaps even during proton beam delivery itself. This distinction is important, since one can imagine a retractable imaging modality that is able to image the patient in treatment position, but that would block the path of the proton beam during imaging. Based on the geometry of the gantry in our proton therapy centre, a (fan-beam) CT or MRI scanner on rails does not fit between patient couch and proton nozzle. In contrast to that, a CBCT system mounted onto a proton therapy gantry would in principle allow simultaneous imaging of the patient, although not independent of gantry rotation. An example of an imaging system independent of gantry rotation and small enough to fit between patient couch and proton nozzle is a CBCT-like system developed by the company MEDPHOTON [27, 48] with both the source and detector mounted onto a ring instead of a C-arm. In the MedAustron ion therapy treatment facility, this system is directly mounted onto the patient couch and can translate along it.

Future improvements of X-ray (spectral) CBCT are possible via improvements in software or hardware, based on the conventional design of CBCT.
In terms of software, iterative algorithms [20] can incorporate in principle an arbitrarily complex physics model and prior knowledge, and in principle also allow to reconstruct the attenuation maps at more than one energy simultaneously. VARIAN recently introduced an iterative reconstruction software specifically for CBCT [9, 13, 15], being able to reduce image noise and artefacts. Moreover, with graphics processing units (GPUs) becoming more powerful and affordable, deep learning algorithms became feasible to be implemented for (CB)CT reconstruction [28, 34, 39].
Progress in terms of hardware concerns the use of improved detectors, such as PCDs. Direct-conversion PCDs have now reached technical maturity, as proven by their usage in the latest clinical and commercially available fan-beam PCD CT by SIEMENS. However, PCDs are still prohibitively expensive for their use in flat-panel detectors, although a stronger market penetration of PCDs could lead to a decrease in price.
Our results in Chapter 3 show that addressing the charge sharing in PCDs promises significant performance gains in terms of SPR estimation. An alternative to direct-conversion PCDs might be to use indirect-conversion PCDs [19, 40, 41] if the characteristic detector response time of initial prototypes can be decreased by a factor of 0.8 to reach the same count rate capability as direct-conversion PCDs [33], and if their pixel area can be reduced significantly.[1]

Since scatter is one of the primary effects that degrade CBCT image quality in comparison to

[1] Prototypes of indirect-conversion detectors featured a size of $1 \times 1\ \mathrm{mm}^2$. The current clinical PCD CT scanner by SIEMENS features a pixel size of around $0.275 \times 0.322\ \mathrm{mm}^2$ [26, 16]; the pixel size of CBCT systems is comparable.

fan-beam CT, much research has been devoted to reducing its influence. Both hardware- and software-based methods or a combination thereof have been explored.
Instead of estimating the scatter field purely by software-based methods, Zhu et al [8, 51, 52] introduced a hybrid approach to estimate the scatter field. They proposed to insert a so-called primary modulator, a chequerboard pattern of high and low attenuating fields, between the source and the object. This technique makes use of the fact that the scatter field can be sufficiently described with a set of low spatial frequencies only, and by reducing the number of primaries transmitted by half of the fields of the chequerboard both primary and scatter component can be extracted. This methodology was reported to decrease the CT number error from 222 to 15 HU in a Catphan phantom and from 278 to 4 HU in a Rando phantom, to substantially reduce cupping artefacts,[2] and to increase contrast by a factor of 2 [51]. The approach of primary modulators has the disadvantage of introducing additional scatter originating in the primary modulator itself, but it has the advantage that it modulates the primary photon distribution before the object under the investigation, therefore avoiding the sacrifice of primary photons at the detector side as in the case of anti-scatter grids. Moreover, this technique is compatible with all spectral CBCT setups considered in this thesis, and allows to be installed with only minor modifications to the hardware.
Anti-scatter grids might appear as an obvious choice for a hardware-based scatter solution. However, earlier studies by Schafer et al [30] and Wiegert et al [42] concluded that anti-scatter grids in the case of somewhat larger isocenter-to-detector distances, as common for, e.g., C-arm CBCTs, lead to an unfavourable reduction in the number of primary photons, increasing image noise. More recent studies, on the other hand, showed that better performance can be achieved with two-dimensional anti-scatter grids [1, 11, 29]. In particular, we would like to mention the study by Pyakurel et al [25] who mounted an anti-scatter grid to a CBCT in a proton treatment gantry. They report an increase in CT number uniformity from 134 to 45 HU, an increase in contrast-to-noise ratio by a factor of 2.5, and a significant reduction in cupping artefacts, outperforming their clinical software-based scatter correction in terms of HU uniformity, CNR as well as cupping artefacts. As is the case with a primary modulator, anti-scatter grids are compatible with all spectral CBCT setups we considered in this work.

The aforementioned techniques focus on reducing the influence of scatter based on the classic CBCT design of a single source and a flat-panel detector. More recently, some profoundly different concepts have been developed.
For example, Yin et al [47] proposed the concept of using multiple sources or a moving source combined with a stationary detector. The concept of arrays of X-ray sources became feasible with carbon-nanotube (CNT) emitter-based X-ray tubes developed by O. Zhou et al [49, 50], which allows to integrate multiple, individually addressable focal spots into a compact housing. Xu et al employed such a source array to create multiple narrowly collimated fan-beams in combination with a conventional flat-panel detector [45], essentially replacing the X-ray cone-beam by a stack of fan-beams, and they reported an improved soft tissue contrast-to-noise ratio by 30 to 50 %. In the same study, they use the areas of the flat-panel detector that are not directly illuminated by the currently active X-ray source beamlet to estimate the scatter field and subtract it from the primary component. Due to their compact size, CNT-based X-ray tubes allow to integrate multiple sources with different filtration into the same housing, therefore improving spectral separation for multi-energy imaging [12].
The small footprint of CNT-based X-ray sources offers the possibility to realise the concept of an arc of sources proposed by Yin et al: Lopez-Montes et al [14] and McSkimming et al [17]

[2] *Cupping artefacts* are a result of beam hardening and of conventional reconstruction algorithms assuming a monoenergetic X-ray beam. If beam hardening is not corrected for, the reconstructed attenuation coefficient of, e.g., a cylindrical, homogeneous object decreases towards the centre of the object.

report research on a mobile stroke unit with a stationary array of sources and a stationary detector ring. While in their design the source array covers a limited angle of 160 degrees, a more complete coverage might be achievable with reasonable added complexity. As mentioned before, the individual control of sources enables the simultaneous registration of scatter, and could offer a way to reduce motion artefacts compared to CBCT. Furthermore, this setup could be fitted with either a PCD panel and/or two sets of sources for different energies, and/or kVp-switching sources to allow for spectral imaging.
Translating this concept to proton therapy, one could imagine the stationary ring mounted to the patient couch. Moreover, it might be feasible to use a slit ring instead, which would allow for isocentric imaging with the proton beam during treatment, and without a fast rotating CT gantry. Sacrificing a small part of the angular coverage is feasible [32], even more so when a prior planning CT scan is available [10].

In conclusion, there is still a plethora of interesting options to be explored to advance in-room imaging for proton therapy, improving treatment workflow and patient outcome.

References

[1] T. Alexeev, B. Kavanagh, M. Miften, and C. Altunbas, "Two-dimensional antiscatter grid: A novel scatter rejection device for Cone-beam computed tomography", *Medical Physics*, vol. 45, no. 2, pp. 529–534, 2018. DOI: 10.1002/mp.12724.

[2] E. Bär, A. Lalonde, G. Royle, H.-M. Lu, and H. Bouchard, "The potential of dual-energy CT to reduce proton beam range uncertainties", *Medical Physics*, vol. 44, no. 6, pp. 2332–2344, 2017. DOI: 10.1002/mp.12215.

[3] M. Bazalova, J.-F. Carrier, L. Beaulieu, and F. Verhaegen, "Dual-energy CT-based material extraction for tissue segmentation in Monte Carlo dose calculations", *Physics in Medicine and Biology*, vol. 53, no. 9, pp. 2439–2456, 2008. DOI: 10.1088/0031-9155/53/9/015.

[4] G. Dedes, J. Dickmann, K. Niepel, *et al.*, "Experimental comparison of proton CT and dual energy x-ray CT for relative stopping power estimation in proton therapy", *Physics in Medicine & Biology*, vol. 64, no. 16, p. 165 002, 2019. DOI: 10.1088/1361-6560/ab2b72.

[5] S. Deffet, P. Farace, and B. Macq, "Sparse deconvolution of proton radiography data to estimate water equivalent thickness maps", *Medical Physics*, vol. 47, no. 2, pp. 509–517, 2020. DOI: 10.1002/mp.13917.

[6] D. F. DeJongh, E. A. DeJongh, V. Rykalin, *et al.*, "A comparison of proton stopping power measured with proton CT and x-ray CT in fresh postmortem porcine structures", *Medical Physics*, vol. 48, no. 12, pp. 7998–8009, 2021. DOI: 10.1002/mp.15334.

[7] T. Flohr, *Basic short course: Photon-counting CT*, Bamberg, Germany, 2024.

[8] H. Gao, R. Fahrig, N. R. Bennett, M. Sun, J. Star-Lack, and L. Zhu, "Scatter correction method for x-ray CT using primary modulation: Phantom studies: Phantom studies for primary modulation method", *Medical Physics*, vol. 37, no. 2, pp. 934–946, 2010. DOI: 10.1118/1.3298014.

[9] S. J. Gardner, W. Mao, C. Liu, *et al.*, "Improvements in CBCT Image Quality Using a Novel Iterative Reconstruction Algorithm: A Clinical Evaluation", *Advances in Radiation Oncology*, vol. 4, no. 2, pp. 390–400, 2019. DOI: 10.1016/j.adro.2018.12.003.

[10] C. Gong, L. Zeng, and C. Wang, "Image reconstruction model for limited-angle CT based on prior image induced relative total variation", *Applied Mathematical Modelling*, vol. 74, pp. 586–605, 2019. DOI: 10.1016/j.apm.2019.05.020.

[11] J. Kim, Y. Kang, T. Hwang, M. Park, and W. Chung, "Evaluation of a two-dimensional Moire-free antiscatter grid for cone-beam computed tomography", *Medical Physics*, vol. 50, no. 6, pp. 3435–3444, 2023. DOI: 10.1002/mp.16243.

[12] B. Li, Y. Hu, C. R. Inscoe, *et al.*, "Dual-energy CBCT by spectral filtration of a dual-focus CNT x-ray source", in *Medical Imaging 2024: Physics of Medical Imaging*, R. Fahrig, J. M. Sabol, and K. Li, Eds., San Diego, United States: SPIE, 2024, p. 43. DOI: 10.1117/12.3006588.

[13] R. Lim, G. P. Penoncello, D. Hobbis, D. P. Harrington, and Y. Rong, "Technical note: Characterization of novel iterative reconstructed cone beam CT images for dose tracking and adaptive radiotherapy on L-shape linacs", *Medical Physics*, vol. 49, no. 12, pp. 7715–7732, 2022. DOI: 10.1002/mp.15943.

[14] A. Lopez Montes, T. McSkimming, W. Zbijewski, *et al.*, "Stationary x-ray tomography for hemorrhagic stroke imaging: Sampling and resolution properties", in *7th International Conference on Image Formation in X-Ray Computed Tomography*, J. W. Stayman, Ed., Baltimore, United States: SPIE, 2022, p. 73. DOI: 10.1117/12.2646858.

[15] W. Mao, C. Liu, S. J. Gardner, *et al.*, "Evaluation and Clinical Application of a Commercially Available Iterative Reconstruction Algorithm for CBCT-Based IGRT", *Technology in Cancer Research & Treatment*, vol. 18, p. 1 533 033 818 823 054, 2019. DOI: 10.1177/1533033818823054.

[16] J. F. Marsh, P. D. VanMeter, K. Rajendran, S. Leng, and C. H. McCollough, "Ex vivo coronary calcium volume quantification using a high-spatial-resolution clinical photon-counting-detector computed tomography", *Journal of Medical Imaging*, vol. 10, no. 04, 2023. DOI: 10.1117/1.JMI.10.4.043501.

[17] T. McSkimming, A. Lopez-Montes, A. Skeats, *et al.*, "Multi-source semi-stationary CT for brain imaging: Development and assessment of a prototype system and image formation algorithms", in *Medical Imaging 2024: Physics of Medical Imaging*, R. Fahrig, J. M. Sabol, and K. Li, Eds., San Diego, United States: SPIE, 2024, p. 42. DOI: 10.1117/12.3006970.

[18] C. Möhler, T. Russ, P. Wohlfahrt, *et al.*, "Experimental verification of stopping-power prediction from single- and dual-energy computed tomography in biological tissues", *Physics in Medicine & Biology*, vol. 63, no. 2, p. 025 001, 2018. DOI: 10.1088/1361-6560/aaa1c9.

[19] H. Morita, T. Oshima, J. Kataoka, M. Arimoto, and H. Nitta, "Novel photon-counting low-dose computed tomography using a multi-pixel photon counter", *Nuclear Instruments and Methods in Physics Research Section A: Accelerators, Spectrometers, Detectors and Associated Equipment*, vol. 857, pp. 58–65, 2017. DOI: 10.1016/j.nima.2017.02.015.

[20] C. Mory, B. Sixou, S. Si-Mohamed, L. Boussel, and S. Rit, "Comparison of five one-step reconstruction algorithms for spectral CT", *Physics in Medicine & Biology*, vol. 63, no. 23, p. 235 001, 2018. DOI: 10.1088/1361-6560/aaeaf2.

[21] V. P. Moskvin, F. Pirlepesov, Y. Yan, *et al.*, "Accuracy of stopping power ratio calculation and experimental validation of proton range with dual-layer computed tomography", *Acta Oncologica*, vol. 61, no. 7, pp. 864–868, 2022. DOI: 10.1080/0284186X.2022.2069477.

[22] N. Peters, P. Wohlfahrt, C. Hofmann, *et al.*, "Reduction of clinical safety margins in proton therapy enabled by the clinical implementation of dual-energy CT for direct stopping-power prediction", *Radiotherapy and Oncology*, vol. 166, pp. 71–78, 2022. DOI: 10.1016/j.radonc.2021.11.002.

[23] G. Poludniowski, N. M. Allinson, and P. M. Evans, "Proton radiography and tomography with application to proton therapy", *The British Journal of Radiology*, vol. 88, no. 1053, p. 20 150 134, 2015. DOI: 10.1259/bjr.20150134.

[24] A. Popper, *Practical Excercises for Young Magicians*. Whitespire: Fillory Press, 2015.

[25] U. Pyakurel, Y. Zhang, R. Sabounchi, *et al.*, "Investigation of 2D anti-scatter grid implementation in a gantry-mounted cone beam computed tomography system for proton therapy", *Physics and Imaging in Radiation Oncology*, vol. 33, p. 100 730, 2025. DOI: 10.1016/j.phro.2025.100730.

[26] K. Rajendran, M. Petersilka, A. Henning, *et al.*, "First Clinical Photon-counting Detector CT System: Technical Evaluation", *Radiology*, vol. 303, no. 1, pp. 130–138, 2022. DOI: 10.1148/radiol.212579.

[27] S. Rit, R. Clackdoyle, P. Keuschnigg, and P. Steininger, "Filtered-backprojection reconstruction for a cone-beam computed tomography scanner with independent source and detector rotations: FBP reconstruction with independent source and detector rotations", *Medical Physics*, vol. 43, no. 5, pp. 2344–2352, 2016. DOI: 10.1118/1.4945418.

[28] B. Rusanov, G. M. Hassan, M. Reynolds, *et al.*, "Deep learning methods for enhancing cone-beam CT image quality toward adaptive radiation therapy: A systematic review", *Medical Physics*, vol. n/a, no. n/a, 2022. DOI: 10.1002/mp.15840.

[29] R. Sabounchi, U. Pyakurel, F. Bayat, M. Eldib, and C. Altunbas, "Effect of scatter suppression with 2D antiscatter grids in photon counting compact CBCT", in *Medical Imaging 2024: Physics of Medical Imaging*, R. Fahrig, J. M. Sabol, and K. Li, Eds., San Diego, United States: SPIE, 2024, p. 101. DOI: 10.1117/12.3006524.

[30] S. Schafer, J. W. Stayman, W. Zbijewski, C. Schmidgunst, G. Kleinszig, and J. H. Siewerdsen, "Antiscatter grids in mobile C-arm cone-beam CT: Effect on image quality and dose: Antiscatter grids in mobile C-arm cone-beam CT", *Medical Physics*, vol. 39, no. 1, pp. 153–159, 2011. DOI: 10.1118/1.3666947.

[31] U. Schneider, J. Besserer, and M. Hartmann, "Technical Note: Spatial resolution of proton tomography: Impact of air gap between patient and detector: Impact of air gap in proton tomography", *Medical Physics*, vol. 39, no. 2, pp. 798–800, 2012. DOI: 10.1118/1.3676739.

[32] E. Y. Sidky, C.-M. Kao, and X. Pan, "Accurate image reconstruction from few-views and limited-angle data in divergent-beam CT", *Journal of X-Ray Science and Technology: Clinical Applications of Diagnosis and Therapeutics*, vol. 14, no. 2, pp. 119–139, 2006. DOI: 10.3233/XST-2006-00155.

[33] Stefan van der Sar, "Exploring X-ray photon-counting scintillation detectors with silicon photomultiplier readout for medical imaging", Ph.D. dissertation, TU Delft, Delft, 2023.

[34] T. P. Szczykutowicz, G. V. Toia, A. Dhanantwari, and B. Nett, "A Review of Deep Learning CT Reconstruction: Concepts, Limitations, and Promise in Clinical Practice", *Current Radiology Reports*, vol. 10, no. 9, pp. 101–115, 2022. DOI: 10.1007/s40134-022-00399-5.

[35] V. T. Taasti, G. J. Michalak, D. C. Hansen, *et al.*, "Validation of proton stopping power ratio estimation based on dual energy CT using fresh tissue samples", *Physics in Medicine & Biology*, vol. 63, no. 1, p. 015 012, 2017. DOI: 10.1088/1361-6560/aa952f.

[36] V. T. Taasti, L. P. Muren, K. Jensen, *et al.*, "Comparison of single and dual energy CT for stopping power determination in proton therapy of head and neck cancer", *Physics and Imaging in Radiation Oncology*, vol. 6, pp. 14–19, 2018. DOI: 10.1016/j.phro.2018.04.002.

[37] A. Terakawa, H. Hosokawa, M. Nogami, K. Hitomi, and K. Ishii, "Experimental comparison of relative stopping power evaluation between proton CT and x-ray CT for pre-clinical proton irradiation studies of small animals", *Physics in Medicine & Biology*, vol. 68, no. 9, p. 095 023, 2023. DOI: 10.1088/1361-6560/acc9fa.

[38] M. Testa, J. M. Verburg, M. Rose, *et al.*, "Proton radiography and proton computed tomography based on time-resolved dose measurements", *Physics in Medicine & Biology*, vol. 58, no. 22, pp. 8215–8233, 2013. DOI: 10.1088/0031-9155/58/22/8215.

[39] The Association for Computational Heresy, *A Record of the Proceedings of SIGBOVIK 2024*. April 0, 2024, https://www.sigbovik.org/2024/proceedings.pdf.

[40] S. J. Van Der Sar, S. E. Brunner, and D. R. Schaart, "Silicon photomultiplier-based scintillation detectors for photon-counting CT: A feasibility study", *Medical Physics*, vol. 48, no. 10, pp. 6324–6338, 2021. DOI: 10.1002/mp.14886.

[41] S. J. Van Der Sar, D. Leibold, S. Brunner, and D. Schaart, "LaBr3:Ce and silicon photomultipliers: Towards the optimal scintillating photon-counting detector", in *7th International Conference on Image Formation in X-Ray Computed Tomography*, J. W. Stayman, Ed., vol. 12304, Baltimore, United States: Proc. SPIE, 2022, 123040A. DOI: 10.1117/12.2646519.

[42] J. Wiegert, M. Bertram, D. Schaefer, *et al.*, "Performance of standard fluoroscopy antiscatter grids in flat-detector-based cone-beam CT", in *Medical Imaging 2004*, M. J. Yaffe and M. J. Flynn, Eds., San Diego, CA, 2004, p. 67. DOI: 10.1117/12.535387.

[43] P. Wohlfahrt, C. Möhler, C. Richter, and S. Greilich, "Evaluation of Stopping-Power Prediction by Dual- and Single-Energy Computed Tomography in an Anthropomorphic Ground-Truth Phantom", *International Journal of Radiation Oncology*Biology*Physics*, vol. 100, no. 1, pp. 244–253, 2018. DOI: 10.1016/j.ijrobp.2017.09.025.

[44] Y. Xie, C. Ainsley, L. Yin, *et al.*, "*Ex vivo* validation of a stoichiometric dual energy CT proton stopping power ratio calibration", *Physics in Medicine & Biology*, vol. 63, no. 5, p. 055 016, 2018. DOI: 10.1088/1361-6560/aaae91.

[45] S. Xu, Y. Hu, B. Li, *et al.*, "Volumetric computed tomography with carbon nanotube X-ray source array for improved image quality and accuracy", *Communications Engineering*, vol. 2, no. 1, p. 71, 2023. DOI: 10.1038/s44172-023-00123-x.

[46] M. Yang, G. Virshup, J. Clayton, X. R. Zhu, R. Mohan, and L. Dong, "Theoretical variance analysis of single- and dual-energy computed tomography methods for calculating proton stopping power ratios of biological tissues", *Physics in Medicine and Biology*, vol. 55, no. 5, pp. 1343–1362, 2010. DOI: 10.1088/0031-9155/55/5/006.

[47] Z. Yin, B. De Man, and J. Pack, "3D Analytic Cone-Beam Reconstruction for Multiaxial CT Acquisitions", *International Journal of Biomedical Imaging*, vol. 2009, no. 1, Y. Zheng, Ed., p. 538 389, 2009. DOI: 10.1155/2009/538389.

[48] A. Zechner, M. Stock, D. Kellner, *et al.*, "Development and first use of a novel cylindrical ball bearing phantom for 9-DOF geometric calibrations of flat panel imaging devices used in image-guided ion beam therapy", *Physics in Medicine and Biology*, vol. 61, no. 22, N592–N605, 2016. DOI: 10.1088/0031-9155/61/22/N592.

[49] J. Zhang, G. Yang, Y. Cheng, *et al.*, "Stationary scanning x-ray source based on carbon nanotube field emitters", *Applied Physics Letters*, vol. 86, no. 18, p. 184 104, 2005. DOI: 10.1063/1.1923750.

[50] O. Zhou, J. Lu, Y. Lee, W. Lin, Y. Cheng, and J. Zhang, "Computed tomography system for imaging of human and small animal", US Patent 7,082,182, 2006.

[51] L. Zhu, "Local filtration based scatter correction for cone-beam CT using primary modulation: Local filtration based scatter correction using primary modulation", *Medical Physics*, vol. 43, no. 11, pp. 6199–6209, 2016. DOI: 10.1118/1.4965042.

[52] L. Zhu, N. R. Bennett, and R. Fahrig, "Scatter Correction Method for X-Ray CT Using Primary Modulation: Theory and Preliminary Results", *IEEE Transactions on Medical Imaging*, vol. 25, no. 12, pp. 1573–1587, 2006. DOI: 10.1109/TMI.2006.884636.

This page is unintentionally left blank due to a lack of results.

List of Publications

Peer-reviewed publications related to this thesis:

- S. J. van der Sar, **DL**, and D. R. Schaart, "Experimental investigation of the potential of $LaBr_3$:Ce, LYSO:Ce, and YAP:Ce for scintillator-based x-ray photon-counting detectors", Physics in Medicine & Biology, 71 (2), 025003 (2026). doi: 10.1088/1361-6560/ae1bf4.

- **DL**, D. R. Schaart, and M. C. Goorden, "Optimising proton stopping power ratio prediction with spectral cone-beam CT", Physics in Medicine & Biology, 70 (14), 145023 (2025). doi: 10.1088/1361-6560/adebd6.
  DL, D. R. Schaart, and M. C. Goorden, "Data and code underlying the publication: 'Optimising proton stopping power ratio prediction with spectral cone-beam CT'", 4TU.ResearchData (2025). doi: 10.4121/BD754669-5AF8-4E2D-9A70-37AC56BD6674.

- **DL**, S. J. van der Sar, M. C. Goorden, and D. R. Schaart, "Framework for evaluating photon-counting detectors under pile-up conditions", Journal of Medical Imaging, 11 (S1), S12802 (2024). doi: 10.1117/1.JMI.11.S1.S12802.
  DL, S. J. van der Sar, M. C. Goorden, and D. R. Schaart, "Data and code underlying the publication: 'Framework for evaluating photon-counting detectors under pile-up conditions'", 4TU.ResearchData (2024).
  doi: 10.4121/8CE1A22F-16A4-450E-B24A-775278CAD7A1.

Conference contributions related to this thesis:

- **DL**, M. C. Goorden, and D. R. Schaart, "Experimental study on dual-energy cone-beam CT for proton therapy planning", Proceedings of SPIE, Medical Imaging 2026: Physics of Medical Imaging. *In press*.

- **DL**, M. C. Goorden, and D. R. Schaart, "Optimizing spectral cone-beam CT for in-room proton stopping power ratio estimation: towards an adaptive treatment workflow", International Journal of Particle Therapy, 17, 101116 (2025). doi: 10.1016/j.ijpt.2025.101116.

- **DL**, J. van Leenen, D. R. Schaart, and M. C. Goorden, "Initial results for joint reconstruction/decomposition of spectral cone-beam computed tomography data", Proceedings of the 8th international conference on image formation in X-ray computed tomography (CT meeting), Marc Kachelrieß (Ed.), Bamberg, Germany, 288–291 (2024).

- **DL**, M. C. Goorden, and D. Schaart, "Direct estimation of proton stopping power ratios from dual-energy cone-beam CT: What are the physical limits?", International Journal of Particle Therapy, 12, 100207 (2024). doi: 10.1016/j.ijpt.2024.100207.

- **DL**, D. R. Schaart, and M. C. Goorden, "Optimizing proton stopping power ratio prediction with dual-energy cone-beam CT using the Cramér-Rao lower bound", Proceedings of SPIE 12925, Medical Imaging 2024: Physics of Medical Imaging, 129253N (2024). doi: 10.1117/12.3006731.

- S. J. van der Sar, **DL**, S. E. Brunner, and D. R. Schaart, "$LaBr_3$:Ce and silicon photomultipliers: towards the optimal scintillating photon-counting detector", 7th International

conference on image formation in X-ray computed tomography (CT meeting), J. W. Stayman (Ed.), Baltimore, United States, Proceedings of SPIE 12304, 123040A (2022). doi: 10.1117/12.2646519.

- **DL**, S. J. van der Sar, M. C. Goorden, and D. R. Schaart, "Point spread function of photon-counting detectors under pile-up conditions: a proposed framework", Proceedings of SPIE 12031, Medical Imaging 2022: Physics of Medical Imaging, 120314R (2022). doi: 10.1117/12.2612861.

Publications prior to this thesis:

- **DL**, V. Lami, Y. V. Hofstetter, D. Becker-Koch, A. Weu, P. Biegger, F. Paulus, U. H. F. Bunz, P. E. Hopkinson, A. A. Bakulin, and Y. Vaynzof, "Triptycenyl-phenazino-thiadiazole as acceptor in organic bulk-heterojunction solar cells", Organic Electronics, 57, 285–291 (2018). doi: 10.1016/j.orgel.2018.03.001.
- E. H. Menke, **DL**, A. P. Ullrich, Y. Vaynzof, and M. Mastalerz, "Planar versus triptycenylene end-capped aroyleneimidazoles as electron acceptors in organic photovoltaics", Organic Chemistry Frontiers, 4, 834–838 (2017). doi: 10.1039/C7QO00231A.
- V. Lami, **DL**, P. Fassl, Y. J. Hofstetter, D. Becker-Koch, P. Biegger, F. Paulus, P. E. Hopkinson, M. Adams, U. H. F. Bunz, S. Huettner, I. Howard, A. A. Bakulin, and Y. Vaynzof, "*N*-Heteroacenes as a new class of non-fullerene electron acceptors for organic bulk-heterojunction photovoltaic devices", Solar RRL, 1, 1700053 (2017). doi: 10.1002/solr.201700053.
- E. H. Menke, **DL**, V. Lami, Y. J. Hofstetter, M. Mastalerz, and Y. Vaynzof, "Triptycene-trisaroyleneimidazoles as non-fullerene acceptors — Influence of side-chains on solubility, device morphology and performance", Organic Electronics, 47, 211–219 (2017). doi: 10.1016/j.orgel.2017.05.004.
- E. H. Menke, **DL**, F. J. Berger, F. Rominger, Y. Vaynzof, and M. Mastalerz, "Triptycene-bis(aroyleneimidazole)s as non-fullerene acceptors: The missing links", ChemPlusChem, 82, 1390–1395 (2017). doi: 10.1002/cplu.201700428.

About the Author

David Leibold was born in 1991 in Germany and obtained his bachelor's degree in physics at Heidelberg University, Heidelberg, Germany. He wrote his thesis in the group of Prof. Christian Enss in the field of low-temperature microcalorimeters under the supervision of JProf. Loredana Gastaldo. He then proceeded to obtain a master's degree in physics at the same university, specialising in solid state physics. His master's thesis on organic solar cells was performed under the supervision of Prof. Yana Vaynzof. David then worked as a research technician in the lab by Associate Prof. Fiona Beck at the Australian National University School of Engineering, Canberra, Australia. After an internship at a company for industrial cameras, he proceeded to pursue a PhD at the department of Radiation Science & Technology at the Technische Universiteit Delft, Delft, The Netherlands, under the supervision of Dr. ir. Marlies C. Goorden and Dr. ir. Dennis R. Schaart.

Colophon

Template

This dissertation builds upon the LaTeXtemplate created by K. P. Hart, which can be found here: https://www.overleaf.com/latex/templates/tud-dissertation/tcddkjggskqx

Font

The main font used in this document is the font 'IBM Plex Sans', which is open source and can be obtained from https://github.com/IBM/plex

Set of colours

Figure C.1 shows the (primary) set of ten colours used for figures in this thesis. The colours were chosen such that their lightness values are evenly spread in order to make them clearly distinguishable when converted to grey scale. Furthermore, the colours were chosen such that they are distinct from each other as much as possible, especially colours right next to each other on the lightness scale. However, note that it is not guaranteed that a particular software performs the conversion into grey scale correctly, which might lead to vanishing grey scale differences between colours. For more information on colour space conversion see the tutorial at https://colorspacious.readthedocs.io/en/latest/tutorial.html

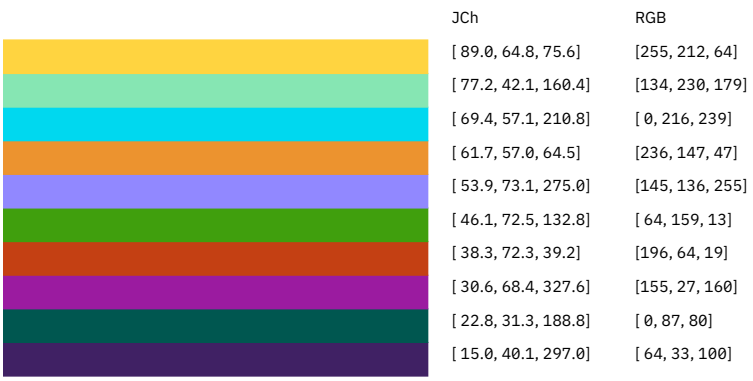

Figure C.1: Set of colours used. Colours are specified in "JCh" (lightness, chroma, hue) and in RGB.

Cover art (front and back):

Artistic impression of an X-ray cone-beam computed tomography acquisition during a proton radiotherapy treatment of a patient (proton beam shown in red). The X-ray beam (light green) is registered by an indirect, scintillation crystal-based photon-counting detector with two energy bins, leading to the registration of X-ray projections at two energies (arc of projections around the patient).

The 3D model of the proton therapy gantry was obtained from CGtrader and was created by the author ”kudim”, see
https://www.cgtrader.com/3d-models/science/medical/varian-proton-therapy-system-probeam-360.

TU Delft Delft University of Technology